INAUGURAL–DISSERTATION

zur

Erlangung der Doktorwürde

der

Naturwissenschaftlich–Mathematischen Gesamtfakultät

der

RUPRECHT–KARLS–UNIVERSITÄT

HEIDELBERG

vorgelegt von

M.Sc. Enrique Eduardo Guerrero Merino

aus Santiago, Chile

Tag der mündlichen Prüfung

. . . .

Real-Time Optimization for Estimation and Control:

Application to Waste Heat Recovery for Heavy Duty Trucks

Gutachter

PROFESSOR DR. CHRISTIAN KIRCHES

With all my heart, to my mother, Viviana Merino Villagra; to my father, Luis Enrique Guerrero Pavez, and to my beloved Salome Zilke.

Also, to anyone that, without resigning to the world's current state, strives by means of his gifts and talents for the realization of that what still remains to be done, knowing that the mistakes he or she may make along the way find forgiveness and mercy in Jesus Christ, my Lord.

Zusammenfassung

Das Ziel dieser Doktorarbeit sind die Erforschung und Entwicklung von Regelungtechniken für die auf dem organischen Rankine-Kreislauf basierten Abwärmerückgewinnungsyteme (WHR) für Lastkraftwagen. Die Systeme sollen so geregelt werden, dass sie möglichst viel Energie rückgewinnen. Allerdings ist das keine triviale Aufgabe, denn ihre höchst nichtlineare Dynamik ist von externen Eingängen (Störungen) sehr stark beeinflusst. Zusätzlich müssen nichtlineare Nebenbedingungen eingehalten werden. Um dieses Problem zu behandeln, ist in dieser Doktorarbeit ein dynamisches Modell formuliert, das auf Grundsätzen und empirischen Beziehungen der Thermodynamik und der Wärmeübertragung basiert. Dieses Modell entspricht einer DAE von Index 1. Im Hinblick auf die Anforderungen der verwendeten numerischen Methoden, es wurde mit einer für die Modellauswertung erforderlichen thermophysikalischen Eigenschaften Auswertemethodik versehen, die auf Splines beruht. Damit wurde die stetige Differenzierbarkeit der Zustandstrajektorien bezüglich Steuerungen und Zustände innerhalb des Modellauswertungsbereichs erreicht. Im Anschluss sind ein Optimalsteuerungsproblem (OCP), ein nichtlineares modell-prädiktives Regelungsschema (NMPC) und ein Zustandsschätzer in der Form eines bewegten-Horizont-Schätzungsschemas (MHE) formuliert. In dieser Doktorarbeit werden effiziente numerische Methoden benutzt, um das OCP näherungsweise zu lösen und die MHE- und NMPC-Schemata zu implementieren. Diese Methoden beruhen auf dem direkten Mehrzielverfahren für Optimalsteuerungsprobleme (DMS), den Rückwärts-Differenzenformeln zur Lösung von DAE-Anfangswertproblemen und den entsprechenden Versionen des Echtzeititerationsschemas (RTI). Die Stabilität einer gleichzeitigen Anwendung von auf RTI basierten NMPC- und MHE-Schemata ist bereits bekannt.

Mehrere numerische Instanzen der DMS-Methode werden für die vorgeschlagene OCP-, NMPC- und MHE-Schemata für ein reales Betriebsszenario getestet, das Lastkraftwagenabgasdaten, die während einer tatsächlich durchgeführten Fahrt aufgenommen worden sind, verwendet. Diese Daten wurden von unserem Industriekooperationspartner Daimler AG zur Verfügung gestellt. Zudem werden PI- und LQGI-Regelungstrategien, die innerhalb der regelungstechnischen Literatur von WHR-Systemen weit verbreitet sind, mit dem vorgeschlagenen Schema verglichen. Ein wichtiges Ergebnis dieser Arbeit ist, dass das vorgeschlagene NMPC-Schema circa $3\,[\%]$ mehr Energie rückgewinnen kann als die PI- und LQGI-Strategien, wenn der Zustandsvektor als bekannt angenommen wird. Darüber hinaus lassen die Rechenzeiten des NMPC-Schemas zu, dass die Steuerung in Echtzeit aktualisiert werden kann, wenn die Abtastzeit $100\,[\mathrm{ms}]$ ist. In einem realistischeren Szenario, in welchem der Zustand aus verrauschten Signalen geschätzt werden muss, führt eine Kombination aus beiden vorgenannten NMPC- und MHE-Schemata zu einer zusätzlichen Energierückgewinnung von circa $2\,[\%]$.

Konkret stellt diese Doktorarbeit neue Ergebnisse und Fortschritte in den folgenden Gebieten vor:

- Ein DAE-Modell für das WHR wurde entwickelt, das aus den Gesetzen der Energie- und Massenerhaltung sowie Wärmeübertragungsbeziehungen hervorgeht. Es ist mit einer Auswertungsmethode für die thermophysikalischen Eigenschaften ausgestattet, womit es die Eigenschaft der stetigen Differenzierbarkeit bezüglich seiner Steuerungen und Zustände innerhalb seines ganzen Auswertungsbereichs besitzt.

- Eine neue, auf Echtzeitoptimierung beruhende Regelungstrategie für das WHR wurde entwickelt. Es besteht aus einer NMPC-Strategie, die auf effizienten Simulations-, Optimierungs- und Regelungswerkzeugen gründet. Das Schema ist imstande nichtlineare Zustands- und Steuerungsnebenbedingungen zu behandeln. Im Gegensatz zu anderen in der Literatur zu findenden Instanzen von NMPC-Ansätze für WHR, wird unser Schema durch seine effiziente numerische Behandlung echtzeitfähig, sogar wenn die volle nichtlineare WHR-Dynamik berücksichtigt wird.

- Das ist die erste Implementierung, die gleichzeitig NMPC- und MHE-Ansätze für die WHR-Steuerung miteinbezieht. Die Kombination aus NMPC und MHE führt zu einem stabilen modellbasierten Regelkreis, der aus realistischen Messungen die Steuerung berechnen kann.

Abstract

This thesis aims at the investigation and development of the control of waste heat recovery systems (WHR) for heavy duty trucks based on the organic Rankine cycle. It is desired to control these systems in real time so that they recover as much energy as possible, but this is no trivial task since their highly nonlinear dynamics are strongly affected by external inputs (disturbances). Additionally, nonlinear operational constraints must be satisfied. To deal with this problem, in this thesis a dynamic model of a WHR that is based on first principles and empirical relationships from thermodynamics and heat transfer is formulated. This model corresponds to a DAE of index 1. In view of the requirements of the employed numerical methods, it includes a spline-based evaluation method for the thermophysical properties needed to evaluate the model. Therewith, the continuous differentiability of the state trajectories with respect to controls and states on its domain of evaluation is achieved. Next, an optimal control problem (OCP) for a fixed time horizon is formulated. From the OCP, a nonlinear model-predictive control (NMPC) scheme is formulated as well. Since NMPC corresponds to a state feedback strategy, a state estimator is also formulated in the form of a moving horizon estimation (MHE) scheme. In this thesis, we make use of efficient numerical methods based on the direct multiple shooting (DMS) method for optimal control, backward differentiation formulae for the solution of initial value problems for DAEs, and the corresponding versions of the real-time iteration (RTI) scheme in order to approximately solve the OCP and implement the MHE and NMPC schemes. The simultaneous implementation of NMPC and MHE schemes based on RTI has been already proven to be stable in the control literature.

Several numerical instances of the DMS method for the proposed OCP, NMPC and MHE schemes are tested assuming a given real-world operation scenario consisting of truck exhaust gas data recorded during a real trip. These data have been kindly provided by our industry cooperation partner Daimler AG. Additionally, the PI and LQGI control strategies, of wide-spread use in the literature of control of WHR, are also considered for comparison with the proposed scheme. An important result of this thesis is that, considering the highest energy recovery obtained from both strategies as a reference for the given operation scenario, the proposed NMPC scheme is able to reach an additional energy generation of around $3\,[\%]$ when the full state vector is assumed to be known, and its computational speed allows it to update the control function in times shorter than the considered sampling time of $100\,[\text{ms}]$, which makes it a suitable candidate for real-time implementation. In a more realistic scenario in which the state has to be estimated from noisy measurements, a combination of both aforementioned NMPC and MHE schemes yields an additional energy generation of around $2\,[\%]$.

Concretely, this thesis presents novel results and advances in the following areas:

- A first principles DAE model of the WHR is presented. The model is derived from the energy and mass conservation considerations and empirical heat transfer relationships; and features a tailored evaluation method of thermophysical properties with which it possesses the property of being at least continuously differentiable with respect to its controls and states on its whole domain of evaluation.

- A new real-time optimization control strategy for the WHR is developed. It consists of an NMPC strategy based on efficient simulation, optimization and control tools developed in previous works. The scheme is able to explicitly handle nonlinear constraints on controls and states. In contrast to other NMPC instances for the WHR found in the literature, our scheme's efficient numerical treatment make it real-time feasible even if the full nonlinear WHR dynamics are considered.

- To the author's knowledge, this is the first implementation that considers both the NMPC and the MHE approaches used simultaneously in the control of the WHR. The combination of NMPC and MHE produces a closed-loop, model-based implementation that can treat realistic measurements as inputs and calculates the corresponding control functions as outputs.

Danksagung (Agradecimientos, Thanks)

Contents

1 Introduction

In recent decades the urgency to develop strategies to decrease energy and fuel consumption in the transport sector, in particular for heavy duty trucks, has become clear. Heavy duty trucks combust oil derived fuels, which is associated to air pollution, ozone layer depletion, greenhouse gases emissions and economic dependency, but at the same time are of crucial importance to economy. Concretely, in 2015 oil derived fuels supplied 95% of the energy consumed by the transport sector. In turn, the transport sector alone consumed about a third of the European Union's final energy consumption[1] [148, 149]. Moreover, that same year 75% of the total freight transport (measured in tonnes-kilometers) was transported on roads, and 79% of the European Union's road freight transport was performed by heavy duty trucks (road tractors and semi-trailers) [148].

With regard to the internal fuel consumption of heavy duty vehicles (both trucks and buses), around one third of the fuel energy is used to effectively move the vehicle, one third is lost as heat in the vehicle's cooling system and one third is wasted as warm exhaust gas (see e.g. [26, 71]). This gives a great potential for energy efficiency improvement in such vehicles. Several alternatives have been introduced and analyzed, see [26] for an overview. In particular, the Waste Heat Recovery Systems (WHR) have been introduced to recapture the energy wasted in the exhaust gases. The recaptured energy can be directly incorporated to the powertrain so as to ease the engine's burden or, if the vehicle is hybrid, used to feed its electrical circuit. Specifically, in this thesis we are interested in WHR based on the organic Rankine cycle (ORC). We proceed to introduce it briefly for reference in the following discussion, and leave deeper technical details for Chapters 2 and 3.

Let us consider the most simple system configuration of a WHR based on a Rankine cycle, illustrated in Fig. 1.1. Therein, the warm exhaust gas coming from the engine enters the evaporator, along which some heat at a rate $\dot{Q}_{\mathrm{in}}$ is extracted from it. As a result, the exhaust gas temperature is lower at the evaporator output. The extracted heat is used to evaporate a second fluid, called the *working fluid*. For applications of a Rankine cycle of low to medium evaporating temperatures, the working fluid is typically chosen to be of organic nature, thus justifying the name *organic* Rankine cycle. The working fluid is expected to enter the evaporator in a liquid phase[2] at its inlet (B), and is expected to leave it in a vapor phase[3] at (C). This vapor undergoes an increment of its volume as it passes through the expander, thus transferring mechanical power $\dot{W}_{\mathrm{out}}$ to the latter's shaft, which in turn can be connected to an electrical generator or to the vehicle's powertrain directly. The working fluid, mostly in vapor phase at the expander outlet (D), is afterwards passed through a condenser, in which some additional heat is extracted from it at a rate $\dot{Q}_{\mathrm{out}}$. At the condenser output (A), the working fluid is expected to be found in a liquid phase in order to be pumped again, by means of some energy input $\dot{W}_{\mathrm{in}}$, towards the evaporator.

This technology has been also used for waste heat recovery in industry [4, 88, 129, 134, 153], renewable energy generation [80, 90, 129, 133, 134, 151, 152, 153] and automotive applica-

---

[1]Final energy consumption is the total energy consumed by end users, such as households, industry and agriculture. It is the energy which reaches the final consumer's door and excludes that which is used by the energy sector itself.

[2]We will define the concept of a phase more precisely in Chapter 2.

[3]Idem.
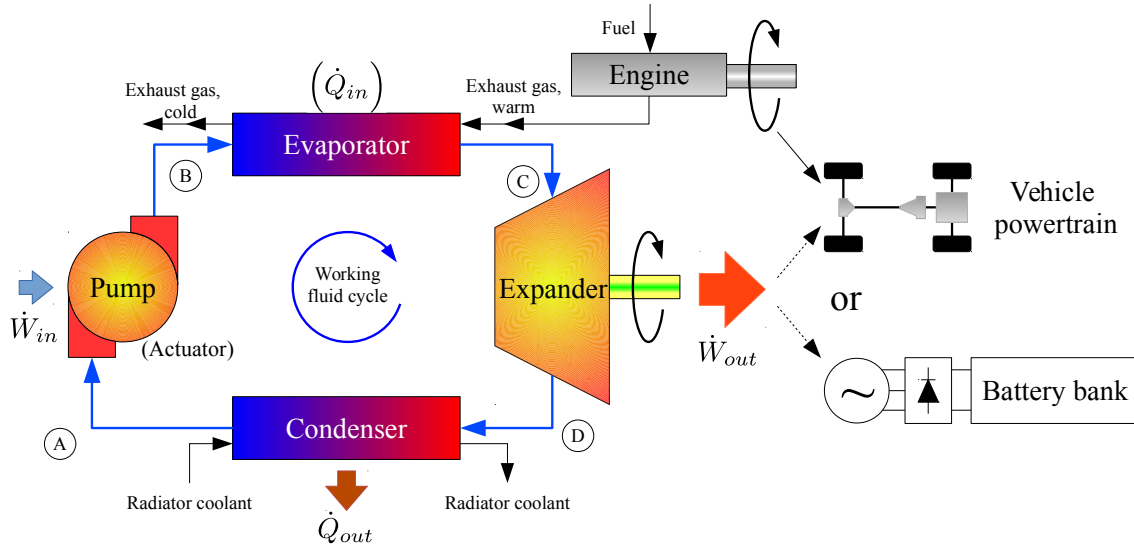
Figure 1.1: Organic Rankine cycle schematic diagram

tions [129, 147, 155, 156, 162]. In heavy duty and passenger vehicles, WHR systems based on the ORC have been reported to produce reductions of 5-10% in the fuel consumptions depending on the system and the driving cycle [26, 147]. This roughly corresponds to a 4-5% recovery of the total fuel energy.

An important contrast between WHR for industrial and automotive applications, is that in the latter the exhaust gas conditions can vary rapidly and in a very wide range. This affects the whole ORC operation due to the strong coupling between the working fluid and the exhaust gas taking place in the evaporator. Further, the ORC needs safeguard measures for its operation: the working fluid at the expander inlet should be in a dry vapor state, since the latter's blades could suffer severe damage if impacted by droplets. On the other hand, too high a working fluid temperature at the expander inlet leads to inefficient operation, and if at some point in the cycle the working fluid is hotter than a certain maximum temperature, it will degrade due to its organic nature. Moreover, the pump should receive only subcooled liquid, so as to eliminate the risk of cavitation[4]. If the ORC is at risk of entering one of these conditions, the energy recovery should be stopped, which is not desirable. As pointed out by [60, 106, 156], the ORC transient effects should be taken into consideration in the efforts towards its performance optimization. In the literature, the maximization of the ORC performance for a given application has been done through component-wise experimental analysis [7, 68, 94, 116, 130, 168], component design [132, 133], working fluid selection [75, 97, 142, 151, 160], and steady state thermodynamic analysis [111, 140, 141, 139, 161, 163, 168]. Economic criteria have also been considered [89, 132]. None of these approaches takes transient effects into consideration. In contrast, the context of control systems offers a natural environment for the inclusion of transient effects. As indicated in e.g. [131], important gains in the energy recovery can be achieved with an appropriate choice of a control strategy for the WHR.

The main focus of this thesis is the application of model-based optimizing real-time control techniques to the WHR for pursuing the maximization of its energy recovery during a given driving cycle, while safeguarding the WHR components. In our analyses we explicitly consider the transient behavior of the ORC. We proceed as follows:

1. To represent the WHR dynamics, a mathematical model is developed. The model is based on concepts belonging to thermodynamics and heat transfer, and consists of an appropriate connection of models corresponding to each component of the WHR. The resulting

---

[4]See Chapters 2 and 3.

model posseses the structure of a differential-algebraic equation (DAE) of index 1. Essentially this structure arises from a spatial discretization applied to the partial differential equations corresponding to mass and energy conservation of the working fluid inside the evaporator, an approach known in the literature as the *moving boundary* (MB).

The functions constituting the model's right-hand side as well as its left-hand side matrix depend on the thermophysical properties of the working fluid and the exhaust gas, which leads to several challenges:

- Due to the phase change taking place inside the evaporator, some of the working fluid's thermophysical properties have non-differentiabilities or even discontinuities with respect to the model's state vector along certain curves contained in the evaluation domain. Moreover, the shape of these curves complicates the direct application of interpolation methods.

- The evaluation of these properties by means of standard computational methods involve the solution of nonlinear systems of equations, which can lead to a big computational effort on each model evaluation.

In order to treat these challenges, in this thesis a special evaluation method for the thermophysical properties of the fluid and the exhaust gas is proposed. The method is based on cubic and bicubic spline interpolation and on the definition of a special partition of the properties' evaluation domain. Moreover, a careful implementation of an extrapolation technique allows for the evaluation of the thermophysical properties outside their domains of definition without losing differentiability at the latters' borders. With these improvements the model's evaluation speed is increased and its differentiability properties are enhanced: all functions constituting it are at least continuously differentiable with respect to the state vector, control, parameters and external inputs.

2. Based on the mathematical model of the WHR, mathematical expressions for the operational constraints are formulated. The result is the definition of a vector function which depends non-linearly on the state vector and control. This function defines a feasible region in the state-control space which is not convex for the working fluid considered in our studies. Additionally, a mathematical expression for the recovered energy during a fixed time interval is given in terms of the state vector and control and used as a cost function. It consists of a Lagrange term whose integrand is a non-linear function of the state vector and the control.

3. Taking into account the mathematical model of the WHR, the constraints and the cost function, an *optimal control problem* (OCP) is mathematically formulated for the WHR. The problem presents a structure that is challenging to solve by means of analytical methods. Therefore, a numerical solution is pursued.

4. For these means, the Direct Multiple Shooting (DMS) method (see e.g. [18, 92, 124]) is used. Therewith the OCP can be represented by a *non-linear programming problem* (NLP) which is solved numerically instead of the original OCP. In our scheme we solve the NLP by means of derivative-based methods, in particular the *sequential quadratic programming* (SQP). In order to evaluate the functions and derivatives required by it, we make use of an efficient DAE solver based on the *backward differentiation formulae* (BDF). In addition, the computational effort is further reduced in our scheme by resorting to partial reduction and condensing techniques, see [18, 92] and Chapter 4.

5. In addition, we consider a *non-linear model-predictive control* (NMPC) strategy for the WHR. The strategy is attractive for this application for its closeness to the OCP for-

mulation. Concretely, it is a *state feedback* control strategy that offers the possibility of defining an objective function, whose minimization is pursued during the system operation. Further, NMPC is also able to deal with non-linear dynamic models and non-linear constraints and it permits the incorporation of predictions of the future exhaust gas conditions. For the numerical realization of this technique we resort to the DMS method explained in the previous item and to the Real-time Iteration scheme (RTI), see [36].

6. Since the dynamic model's state vector cannot be directly measured, a *moving horizon estimator* (MHE) is implemented in order to estimate it from practical sensor measurements[5]. In contrast to implementations based on the Kalman filter (cf. [79, 28, 102, 103, 104, 121, 123, 170]), in MHE several past measurements are explicitly considered in the estimation. Moreover, the approach is appealing for our purposes due to its capability to cope with our nonlinear DAE model explicitly. In our formulation it is assumed that noise affects the measurements, but the dynamics are undisturbed. In addition, noise is assumed to be white and Gaussian. Therefore, we choose a least-squares approach to formulate the MHE, with which the joint maximum likelihood estimates are obtained under the aforementioned hypothesis [76]. In order to implement the MHE we formulate a tailored instance of the RTI scheme of [42, 86] based on the DMS method previously mentioned. In [86] it is shown that the MHE scheme is more effective than an extended Kalman filter (EKF) implementation, with similar computational effort. The stability of NMPC and MHE working together in an RTI framework has been shown in [166].

7. The proposed strategies are implemented in a simulation environment. In all simulations a scenario comprising exhaust gas massflow and temperature profiles at the WHR evaporator inlet is considered. The profiles consist of real-world measurements carried out by our industry cooperation partner Daimler AG during a heavy duty truck trip in Baden-Württemberg, Germany, in 2015. Firstly, numerical experiments are performed in which several instances of the DMS method's time discretization for OCP and NMPC are considered. These studies yield results on the computational times, feasibility and objective function values obtained with the different instances. Further, experiments are performed for evaluating the potential benefit of counting on exact predictions of the future exhaust gas conditions in the NMPC case. Also, the best approximate OCP and NMPC trajectories are qualitatively compared. Next, the NMPC implementation is compared with other control strategies frequently applied to WHR in the literature. Specifically, we consider LQGI (cf. [103, 104, 105, 169, 170]) and PI (cf. [6, 59, 74, 103, 104, 119, 120, 121, 122, 123, 131, 144, 156, 167]) implementations. Finally, the case in which the state is estimated from practical measurements using the MHE is regarded. First, the estimation quality of the MHE is analyzed for a particular numerical instance. Next, the results yielded by the NMPC when the state is assumed to be known are compared with those yielded while using both the NMPC and the MHE simultaneously. Lastly, the latter results are contrasted with those yielded by the aforementioned PI and LQGI strategies.

In summary, the numerical results highlight the following:

- The proposed NMPC scheme is capable of controlling the WHR in real-time under a sampling time of 100 [ms], a typical sampling time for an on-board controller.

- The exact knowledge of the future exhaust gas conditions improves the NMPC performance, but not drastically if the prediction horizon is short.

---

[5]Namely, pressure, temperature and massflow measurements of the working fluid and the exhaust gas.

- MHE can produce precise state vector estimations, resorting to this end to quantities that are easily measurable in realistic implementations.

- The NMPC-MHE scheme and the NMPC scheme with full state knowledge behave almost identically.

- The proposed scheme drives the WHR safely, keeping the operational constraints. Moreover, more energy is recovered using it than using PI or LQGI controllers. In comparison to the highest energy recovery of the last two, the proposed scheme recovers around $2\,[\%]$ more when the MHE is used and around $3\,[\%]$ more when the state is fully known.

1.1 Aims and Contributions of this Thesis

As previously mentioned, the main goal of this thesis is the control of the WHR of a heavy duty truck in a real time environment using model-based techniques based on numerical optimization. The achievement of this goal brings with itself the innovations and advantages with respect to other state-of-the-art solutions listed next.

A tailored evaluation method for an MB model of the WHR: In this work, due to its good precision with a small number of state variables [164], we make use of a nonlinear, first-principles based model obtained through the MB approach. In contrast to most works, we make use of the full nonlinear dynamics in our control formulation. Since, as explained in Chapter 4, our methods impose differentiability requirements on the model, this aspect has been carefully investigated, and a tailored scheme for evaluating the model has been developed (see Section 3.3, cf. [62]). The scheme builds upon the one found in [58], extending it by means of an additional extrapolation feature.

A new real-time optimization control strategy for the WHR: In [49, 131, 167, 168, 173] it has been concluded, under the assumption of a steady state, that the ORC reaches an optimal efficiency when the working fluid at the expander inlet (point (C) of Fig. 1.1) is in a saturated vapor state[6] while keeping a high evaporating pressure. Under the additional consideration of an appropriate safety margin, set points for the corresponding controllers are generated. In some articles, the set points are fixed [50, 49, 48, 51, 103, 131, 167, 168]. This approach is suitable when the WHR is used in industrial processes, in which waste heat conditions can be precisely controlled. However, in automotive applications, where the exhaust gas exhibits a highly dynamic behavior and thus a steady state is hardly reachable, it is more suitable that the controller leverages transient conditions. To this end, in [119, 122, 131, 156, 173, 174] the set point is varied in accordance to the current working fluid and exhaust gas conditions. As pointed out in [30, 48], these enhancements can be further improved if an NMPC strategy is considered. In this thesis we propose an NMPC scheme based on efficient simulation, optimization and control tools developed in previous works (see e.g. [124, 17, 8, 92, 36]). Our scheme is able to explicitly handle nonlinear constraints on controls and states. In contrast to other NMPC instances for the WHR found in the literature, our scheme's efficient numerical treatment make it real-time feasible even if the full nonlinear WHR dynamics are considered. To illustrate this, a test scenario consisting of real-world data provided by Daimler AG is presented in which the scheme reaches computational times faster than $100\,[\mathrm{ms}]$ (a typical sampling time for an on-board controller) for different configuration settings.

---

[6]See Chapter 2.

The first NMPC-MHE control scheme for WHR: To the author's knowledge, this is the first implementation that considers both the NMPC and the MHE approaches used simultaneously in the control of the WHR. The combination of NMPC and MHE produces a closed-loop, model-based implementation that can treat realistic measurements as inputs and calculates the corresponding control functions as outputs.

1.2 Structure of this Thesis

In Chapter 2 the thermodynamic concepts that allow us to evaluate the system's performance are introduced. In particular, mass and energy conservation laws are introduced, as well as the role that main thermophysical properties play in the aforementioned processes. Numerical methods for the evaluation of those properties are briefly explained. Additionally, a brief introduction to the phenomena of forced convection and two-phase flow is done. The Rankine cycle in its original version is described and analyzed.

In Chapter 3, the general principles of Chapter 2 are applied to a specific case of the WHR. First, the topology of the WHR under consideration is introduced, and afterwards a phenomenological dynamic model for it is derived. The resulting model has the structure of a differential-algebraic equation system (DAE) of index 1. The properties of this model are discussed, after which an optimal control problem (OCP) based on it is stated. The problem solution depends continuously on the initial value of the WHR state and on the driving pattern. The latter is represented by the massflow and temperature of the exhaust gas entering the evaporator. With the OCP formulation as a basis, a nonlinear model-predictive control (NMPC) strategy is proposed for implementing a state-feedback controller for the WHR. Since the involved state cannot be fully measured, a state estimation problem is defined, and a moving horizon estimation (MHE) approach is proposed to address it. At this point, the OCP and NMPC problems are still formulated in function space.

Since the infinite dimensional problems introduced in Chapter 3 are difficult to solve analytically with the desired level of detail, in Chapter 4 the numerical methods used in this thesis for their approximate solution are revised. First, the direct multiple shooting method is introduced to parametrize the problems in a suitable way. As a result, finite dimensional nonlinear programming problems (NLP) arise. These NLPs can be efficiently solved using the structure-exploiting techniques that are described subsequently. Then, the real-time iteration scheme (RTI) is introduced for the NMPC and MHE problems. The scheme is introduced to improve the response speed of the NMPC and MHE schemes by exploiting the continuous dependency of the optimal control and state estimation problems on the differential state and the measurement data, respectively. Additionally, the PI and LQGI control strategies are introduced for later comparison with our scheme.

Chapter 5 shows the results obtained from applying the procedures described in Chapter 4 to the problems defined in Chapter 3, using a typical instance of the WHR model and a representative vehicle driving profile (scenario). Several numerical solutions of the OCP, obtained using different instances of the direct multiple shooting method's time discretization, are analyzed. An analog procedure is followed for an NMPC instance which does not include a MHE, i.e. in which it is assumed that the full state vector is available. The results are compared with the solutions of the OCP. Additionally, the effect of the prediction quality of the vehicle driving profile on the results is analyzed. To this end, two scenarios are presented whose only difference is the degree of knowledge of the vehicle driving profile. In one scenario, the prediction matches the actual profile perfectly, and in the second the prediction is made by extrapolating the profile along a given prediction horizon by a constant function whose value equals to the last profile measurement.

Later in Chapter 5, a brief study on the speed of response of the NMPC is done, with the aim of assessing the method's feasibility for real-time applications. Finally, the state uncertainty is included by considering the use of the MHE. The estimator performance is studied for different window lengths (and thus number of measurements entering it), taking again real-time feasibility into account. Next, the whole MHE-NMPC ensemble performance is evaluated by comparison of the control trajectories and energy recovery against those obtained with the NMPC without MHE, which assumes the state can be measured with perfect accuracy.

Finally, selected results of the tests mentioned above are compared with those obtained using the alternative strategies defined in Chapter 4.

Chapter 6 states this thesis' main conclusions and gives an outlook of future development possibilities.

2 Thermodynamics and Heat Transfer

In this chapter, we give basic concepts on thermodynamics. They will be used extensively throughout this work in order to define the model in Chapter 3, explain the considered methods for the evaluation of thermophysical properties in Section 3.3 and to physically analyze the numerical results in Chapter 5. We begin by introducing fundamental definitions. Afterwards, rather intuitive thermophysical fluid properties such as pressure, temperature and specific volume are introduced. Afterwards, the laws of thermodynamics are introduced, with which the horizon opens and further properties might be introduced, such as enthalpy and entropy. Finally, the Rankine cycle is introduced. An idealized version of it is analyzed, in the search for theoretical maximum efficiencies. This Chapter is largely based on the textbooks [24] and [113].

2.1 Basic Definitions

In thermodynamics, a *system* is nothing more than the physical object of study. It is distinguished from its *surroundings* by means of an arbitrarily chosen *boundary*. This boundary may be fixed or moving. If mass transfers through the boundary are allowed, the system is said to be an *control volume*. Otherwise it will be denoted as a *closed system*. In particular, an *isolated system* is one that does not interact with its surroundings in any way.

A *thermophysical property* is a macroscopic characteristic of a system to which a numerical value can be assigned at a given time without knowledge of the previous history of the system. The different thermophysical properties give information about the *thermodynamic state* of the system, which is the condition it is found at a given time. Often, relationships between the different thermophysical properties exist, so only a reduced amount of them are sufficient to determine the state of a system.

A thermodynamic system is said to be in *steady state* if none of the system's properties changes with time. If any system properties change, the system is said to have undergone a *process*. A sequence of processes that begins and ends at the same thermodynamic state is called a *thermodynamic cycle*.

From the definition of thermophysical property, a quantity can only be considered as such if its change in value between two states is independent of the process.

A thermophysical property is said to be *extensive* if its value for a given system equals the sum of the property's values for its constituting parts. A thermophysical property is said to be *intensive* if its value does not depend on the extent or size of a system and may vary from place to place within the system at any time. As a consequence, intensive properties may be functions of position and time, whereas extensive properties may be only functions of time.

A *phase* is a quantity of matter that is homogeneous throughout in chemical composition and physical structure (i.e. all the matter is solid, or all liquid, or all gas). In a system, one or more phases may be found. If there are more than one, they are separated by the corresponding *phase boundaries*. A *pure substance* is one that is uniform and invariable in chemical composition. It can have many phases, but the chemical composition must be the same for each phase.

An *equilibrium state* is one in which no macroscopically observable changes would take place if the system was isolated from its surroundings. A *quasiequilibrium processes* is a process in

which the departure from a thermodynamic equilibrium is at most infinitesimal.

2.2 First Thermophysical Properties

In this section, the particular thermophysical properties known as specific volume, pressure and temperature are defined. Their simplicity and intuitiveness allow the reader to have a quick understanding of many phenomena studied in this work and give a solid ground to continue the definition of other important thermophysical properties and laws in further sections.

In this work all mathematical modeling of matter is done under *the continuum hypothesis*, which is the assumption that matter is distributed continuously throughout a region. This assumption is of practical usefulness for macroscopic analysis. Moreover, experience indicate that the resulting description of the behavior of matter is in agreement with experimental data at the scales relevant in this work. This assumption allows to speak of intensive properties "at a point" of the system.

If around a point in space a small volume V is considered, and the mass contained in this volume is denoted by m, the *density* of matter at that point is defined as

$$\varrho = \lim_{V \to V'} (m/V),$$

where V' represents the smallest volume for which statistical mean values are meaningful and the mass-volume ratio is defined. At that point, the *specific volume* is defined as the reciprocal of the density: $v = 1/\varrho$.

A very important property in fluids (in this work, gases or liquids) is *pressure*. Consider a fluid at rest. If a plane with area A passing through a point in it is considered, this plane, independent from its orientation, is subject to two forces perpendicular to it, of equal magnitude F_{normal} and opposingly directed. The fluid's pressure at that point is defined as

$$p = \lim_{A -> A'} (F_{\text{normal}}/A).$$

In this case, A' is chosen in the same sense as V'.

In order to introduce the concept of temperature, it is necessary to introduce the concept of *thermal equilibrium*. If two systems are brought into contact through a wall, an interaction between both systems might take place (in which case the wall is said to be *thermally conducting*; on the contrary the wall is said to be *adiabatic*), and some properties of both may undergo changes. At some point in time, these changes will cease, and the properties in both systems will reach new values. Both systems are then said to have reached a thermal equilibrium.

Even before introducing temperature, we can introduce the

Theorem 2.2.1 (Zeroth Law of Thermodynamics) *If two systems are in thermal equilibrium with a third one, then they are in thermal equilibrium with each other as well.*

We define thus the *temperature* of a system as the physical property that tells whether two systems are in thermal equilibrium. If two systems are in thermal equilibrium with each other, their temperatures are equal. As stated, the definition of temperature is independent of the sensorial perceptions of "hot" and "cold", but recovers the intuition, as two systems in thermal equilibrium with one another do feel "equally hot".

2.3 First Law of Thermodynamics

This work's main concern is the energy efficiency. Basically, the first law of thermodynamics states that energy is conserved along all processes. This statement is mathematically formalized in this section, and gives a solid background for performing calculations concerning the important concept of energy. The formalization requires a proper definition of work, internal energy and heat, also given.

From Newton's second law of motion it is possible to arrive at the concepts of kinetic energy, potential energy and mechanical work. These establish the basis for the conservation of energy in mechanics. In thermodynamics, the concept of energy and its conservation principles are extended to cover more complex systems and interactions in a tractable way. We give first a thermodynamic definition of *work* as follows: work is defined as any quantity that flows across the boundary of a system during a change in its state and is completely convertible into the lifting of a weight in the surroundings. In this thesis we assign the symbol W to work. The rate of energy transfer by work per unit time is known as *power* and it is assigned the symbol $\dot{W}$. Given the power on a time interval $[t_1, t_2]$, the energy transfer by work during this interval is given by

$$W = \int_{t_1}^{t_2} \dot{W} \, \mathrm{d}t. \tag{2.1}$$

Notice that the definition of work actually includes a variety of energy transfer modes, such as compression or expansion of gases or fluids, extension or compression of solids, mechanical energy transmission through a shaft, electric current within a voltage difference, electric polarization, magnetic polarization, and so on. The inclusion of the corresponding hypothetical converting devices to the aforementioned process allows the intepretation. The application of work implies energy transfer. All energy transfers by work between a given system and its surroundings may be added to yield a net total.

It is clear that work is not a property, since it depends on the process being applied. Also, notice that works appears only at the boundary of a system, appears only during a change of state, and is manifested by an effect on the surroundings. Since an energy transfer by work implies a change of state in the system, we can evaluate the energy transfered by the process between the initial (say, ①) and the final (say, ②) states as

$$W = \int_{①}^{②} \mathrm{đ}W.$$

Since the integral needs in general detailed knowledge about the process involving the energy transfer, we say that the quantity $\mathrm{đ}W$ is an *inexact differential*: the dashed d (đ) has the same mathematical meaning as the usual (exact) differential d, but it is used to denote the need of the knowledge of process details in order to evaluate the integral. Moreover, as with inexact differentials, it makes no sense to talk about the value of the integral above as $W_2 - W_1$: work is not a property, and thus not possible to associate with a state. [1]

We define the *internal energy* of a system as the sum of all energy stored in the system on its different forms. It can include microscopic forms of energy such as molecular kinetic energy in forms of vibration, rotation and motion, chemical linkages on each molecule, intermolecular forces, and so on, but also macroscopic forms. It is an extensive property. Its symbol in this work is U. All extensive properties are proportional to the system's mass. Therefore, dividing

---

[1]Compare with the work definition used in mechanics as the line integral of a force along a given path.

by it, a form of the property, denoted *specific*, may be obtained. The result is independent of the system's mass, thus intensive. In this thesis, the specific form of an extensive property is denoted with the corresponding lower case symbol: the specific internal energy's symbol is thus u.

The next definition corresponds to heat. For clarity, keep in mind the defintion of thermal equilibrium and temperature. We define *heat* as a quantity that flows across the boundary of a system during a change in its state in virtue of a difference of temperature between the system and its surroundings and from a point of higher to a point of lower temperature. In this thesis, we assign heat the symbol Q. As with work, the *rate of heat transfer* is assigned the symbol $\dot{Q}$. Given the rate of heat transfer on a time interval $[t_1, t_2]$, the energy transfer by heat during this interval is equal to

$$Q = \int_{t_1}^{t_2} \dot{Q} \mathrm{d}t. \tag{2.2}$$

The lower case symbol $\dot{q}$ is assigned to the heat transfer rate per unit of system surface area, also known as *heat flux*.

It is again clear that heat cannot be a property since it depends on the details of the process involved. We assign denote thus its inexact differential as $\text{đ}Q$. There are three heat transfer modes: conduction, convection and radiation. These are treated with more detail in 2.7.

After having defined the internal energy, the work and the heat, we can formulate the first law of thermodynamics as follows

Theorem 2.3.1 (First Law of Thermodynamics) *If a system is subject to any thermodynamic cycle, the work produced in the surroundings is equal to the heat withdrawn from its surroundings. Mathematically,*

$$\oint \text{đ}Q = \oint \text{đ}W,$$

where the symbol $\oint$ denotes the integration of the corresponding differentials along all the processes constituting the thermodynamic cycle.

The fact that the integral of $\text{đ}Q - \text{đ}W$ cancels along a closed integral for each possible path suggests that there is a property whose exact differential is precisely that quantity: we recognize here the internal energy. An alternative differential formulation for Theorem 2.3.1 is, therefore,

$$\mathrm{d}U = \text{đ}Q - \text{đ}W.$$

In other words, all changes in a system's internal energy might be summarized as energy transfers to and from the environment by heat and work.

This definition may be also extended to a time rate form as

$$\frac{\mathrm{d}U}{\mathrm{d}t} = \dot{Q} - \dot{W}.$$

So far we have not considered mass transfers across the system's boundary, i.e. we have only treated closed systems in our analysis. To expand the first law of thermodynamics to this important subclass of systems, we consider first the *mass conservation principle*. In a time rate form, if at a given instant the control volume contains an amount of mass m, receives mass through one of its openings at a rate $\dot{m}_\mathrm{i}$ and loses mass through another one at a rate $\dot{m}_\mathrm{o}$, then

it holds that

$$\frac{\mathrm{d}m}{\mathrm{d}t} = \dot{m}_\mathrm{i} - \dot{m}_\mathrm{o}. \tag{2.3}$$

In this work we call quantities $\dot{m}_\mathrm{i}$ and $\dot{m}_\mathrm{o}$ input and output *massflows*, respectively. For the case in which more than one opening exists, we may use i and o as indices for the incoming and outgoing massflows, respectively, and sum along all openings, so the mass conservation principle reads

$$\frac{\mathrm{d}m}{\mathrm{d}t} = \sum_j \dot{m}_{\mathrm{i},j} - \sum_j \dot{m}_{\mathrm{o},j}. \tag{2.4}$$

A given fluid massflow may be obtained by knowing, for example, the fluid's density at the boundary and then multiplying by the volume of fluid displaced by unit of time. If a volume V is displaced with frequency f, then the massflow is given by

$$\dot{m} = \varrho V f. \tag{2.5}$$

Equivalently, if the mass transfer occurs through an opening of area A, and the fluid velocity at the exit is V, it holds that

$$\dot{m}v = A\mathrm{V}. \tag{2.6}$$

Whenever there is mass exchange across the control volume's boundaries at a rate $\dot{m}$, there is an energy transfer which consists of the internal energy contained by the amount of mass being transfered $\dot{m}u$ on the one side, and of work associated with the displacement of fluid under the influence of pressure on the other. If the pressure at which the mass transfer takes place is p, the corresponding force-velocity product is $(pA)\mathrm{V}$. Using Eq. (2.6), the work corresponds to $\dot{m}pv$. Therefore, the mass exchange implies a total energy transfer of $\dot{m}(u + pv)$.

With the previous considerations, we have that the first law of thermodynamics, formulated for a control volume in which mass enters with massflow $\dot{m}_\mathrm{i}$, with internal energy u_i and specific volume v_i, at a pressure p_i; and mass exists the control volume with massflow $\dot{m}_\mathrm{o}$, with internal energy u_o and specific volume v_o, at a pressure p_o, in a time rate form is

$$\frac{\mathrm{d}U_\mathrm{cv}}{\mathrm{d}t} = \dot{Q}_\mathrm{cv} - \dot{W}_\mathrm{cv} + \dot{m}_\mathrm{i}(u_\mathrm{i} + p_\mathrm{i}v_\mathrm{i}) - \dot{m}_\mathrm{o}(u_\mathrm{o} + p_\mathrm{o}v_\mathrm{o}). \tag{2.7}$$

The subscript 'cv' stands for "control volume". U_cv denotes the total internal energy contained inside its boundary; $\dot{Q}_\mathrm{cv}$ denotes the total heat transfer occurring across its boundary and $\dot{W}_\mathrm{cv}$ denotes all energy transfers by work occurring across its boundary that are not related to mass transfer.

At this point it makes sense to define the enthalpy of a system with volume V as the quantity

$$H = U + pV.$$

The enthalpy is an extensive property. Dividing by the system's mass and recognizing the specific volume and the specific internal energy, the specific enthalpy is thus defined as

$$h = u + pv. \tag{2.8}$$

Since on the definition of the specific enthalpy only intensive properties appear, it is also an intensive property. Enthalpy in itself has no physical meaning, and its definition is only for

operational convenience. On the previous equation, the energy balance may be stated as

$$\frac{\mathrm{d}U_{\text{cv}}}{\mathrm{d}t} = \dot{Q}_{\text{cv}} - \dot{W}_{\text{cv}} + \dot{m}_{\text{i}}h_{\text{i}} - \dot{m}_{\text{o}}h_{\text{o}}. \tag{2.9}$$

If there are many openings through which the system may exchange mass with its surroundings, we may sum upon all openings as done before and state

$$\frac{\mathrm{d}U_{\text{cv}}}{\mathrm{d}t} = \dot{Q}_{\text{cv}} - \dot{W}_{\text{cv}} + \sum_{j} \dot{m}_{\text{i},j}h_{\text{i},j} - \sum_{j} \dot{m}_{\text{o},j}h_{\text{o},j}, \tag{2.10}$$

which is the time rate version of the *first law of thermodynamics for control volumes* of preference in this thesis.

2.4 Second Law of Thermodynamics

The first law of thermodynamics is insufficient to treat complex real world problems since it does not provide criteria for distinguishing which processes are possible from those that are not; nor it is able to predict the direction of a given process. Experience shows, however, that some processes do take place instead of others, even if the energy balances are in all cases consistent. The second law of thermodynamics, to be introduced in this section, provides means to make these distinctions. Additionally, it can be used to evaluate the maximum performance of a power cycle, which is of interest in this work.

The second law of thermodynamics can be formulated in several equivalent ways. We start with the Clausius formulation, which is easy to accept, and then state the more practical Planck-Kelvin formulation. That both laws are equivalent is partly demonstrated in [113].

Theorem 2.4.1 (Second Law of Thermodynamics (Clausius)) *It is impossible for any system to operate in such a way that the sole result of its operation would be an energy transfer by heat from a cooler to a hotter body.*

For the Planck-Kelvin formulation, the concept of a thermal reservoir is needed. A *thermal reservoir* is a system whose temperature always remains the same in spite of energy transfers by heat. These are in fact ideal systems, but in nature there are systems that approximate them closely, such as big masses of air or water or two-phase systems (see 2.5).

Theorem 2.4.2 (Second Law of Thermodynamics (Planck-Kelvin)) *It is impossible for any system to operate in a thermodynamic cycle and deliver a net amount of energy by work to its surroundings while receiving energy by heat transfer from a single thermal reservoir.*

Since, from the first law of thermodynamics, we can define the work performed by a system undergoing a thermodynamic cycle on its surroundings as

$$W_{\text{cycle}} = \oint \mathrm{d}W = \oint \mathrm{d}Q = Q_{\text{cycle}},$$

the Planck-Kelvin formulation may be stated mathematically as

$$W_{\text{cycle}} \leqslant 0, \tag{2.11}$$

under its statement's conditions.

We say that a processes is *irreversible* if, after its realization, the initial state of the system considered and its surroundings cannot recovered. A process is *reversible* if both the system

and its surroundings can be returned to their initial states. For example, letting an hot object cool down to a lower atmospheric temperature would take place, increasing the surrounding air's temperature; the spontaneous cooling of the surrounding air for reheating the object to its starting temperature will not take place; and if it was desired to bring the object back to its temperature, additional energy would need to be taken from the surroundings, with the consequent difference in the surrounding's final and initial states. This is basically what the Clausius formulation of the second law of thermodynamics formulates.

All real processes are irreversible. A process will be irreversibly if it is performed in the presence of *irreversibilities*, such as heat transfer through finite temperature differences, electric resistance, free expansion of a gas or liquid into a smaller pressure, diffusion and mixing processes, spontaneous chemical reactions, magnetization under hysteresis, mechanical friction, and so on.

An idealizations of real processes can be introduced to allow an easier mathematical manipulation of complex processes: an *internally reversible process* is one in which no irreversibilities are found within the system. The system's state is assumed to move through a sequence of equilibrium states, and the irreversibilities are assigned to the system's surroundings. Using the Planck-Kelvin statement of the second law of thermodynamics it can be shown that a thermodynamic cycle satisfying its conditions is internally reversible if and only if $W_{\text{cycle}} = 0$.

Continuing the analysis, we state the *Clausius inequality*: For any thermodynamic cycle it holds that

$$\oint (đQ/T)_{\text{boundary}} \overset{\text{def}}{=} -\sigma_{\text{cycle}} \leqslant 0. \tag{2.12}$$

The subscript 'boundary' means that the integral is evaluated at the system's boundary. The closed integral means that the evaluation also takes place along the whole cycle. The proof follows from the Planck-Kelvin formulation of the second law of thermodynamics and is partially done in [113]. Following the reasoning in the previous paragraph, the value of σ_{cycle} is positive for irreversible processes, and zero for reversible processes. We call this term the cycle's *entropy production* due to irreversibilities. Now, since in internally reversible cycles the system is free from irreversibilities (and, in particular, the system's temperature is uniform), a new, extensive property called *entropy* can be defined, and the symbol S can be associated with it, so that its change between states ① and ② is defined as

$$S_2 - S_1 = \left(\int_{①}^{②} đQ/T \right)_{\text{int. rev.}}. \tag{2.13}$$

The subscript 'int. rev.' indicates that the process connecting states ① and ② needs to be an internally reversible process. We define hence the entropy differential as

$$dS = đQ/T.$$

The lower case symbol s denotes the specific entropy.

Remark 2.4.3 *Notice that for an internally reversible process the entropy change (and the entropy differential) can have any sign, or be zero. The Clausius inequality precludes the possibility of a positive integral for the particular case of a cycle only.*

Remark 2.4.4 *Notice as well that, as for the enthalpy, no direct physical meaning is associated to it. The entropy is introduced as a tool for the thermodynamic analysis.*

Given a process between states ① and ②, which may be irreversible, let us think of an internally reversible process that would bring the system from ② back to ①. The sequence of both processes constitutes a thermodynamic cycle, subject to the Clausius inequality. The integral along the whole cycle may be decomposed in accordance to the irreversible and reversible segments, and the definition of entropy may be used to obtain the *entropy balance for closed systems*,

$$S_2 - S_1 = \int_{①}^{②} (đQ/T)_{\text{boundary}} + \sigma, \quad \sigma \geqslant 0. \tag{2.14}$$

Since the theoretical internally reversible process between states ② and ① is free from irreversibilities, the cycle's entropy production σ is due to the first process only, and therefore the subscript 'cycle' is dropped. In accordance to the Clausius inequality, σ is not allowed to be negative. As previously discussed, the equation's left-hand side is the entropy change due to the process. The integral's subscript 'boundary' indicates again that the integral is evaluated at the system's boundary, where the heat transfer $đQ$ is locally transfered at temperature T (not necessarily uniform throughout the system's boundary). Therefore, the whole integral can be interpreted as an entropy transfer between the system and its surroundings, and may have any sign in accordance to the direction of the heat transfer. Essentially, the identity above tells that, for a closed system, the change in its entropy due to the realization of a process equals the amount of entropy transfered to or from the surroundings plus the entropy produced by the process' internal irreversibilities. Notice that in the equation above, energy transfer by work does not appear. Work does not transfer entropy.

The corresponding time rate form of the entropy balance for closed systems is

$$\frac{dS}{dt} = \sum_j \dot{Q}_j/T_j + \dot{\sigma}, \quad \dot{\sigma} \geqslant 0, \tag{2.15}$$

where the sum is made in such a way that the whole system boundary is covered. To index j corresponds a boundary sector in which heat transfer takes place under an instantaneous temperature T_j at a rate $\dot{Q}_j$. $\dot{\sigma}$ corresponds to the time rate of entropy production due to irreversibilities within the system.

A particular case of a closed system is an isolated system. In that case, no heat transfer takes place, and therefore entropy production is only the source of entropy change. Only processes which increase the system's entropy are allowed. Now, since entropy is an extensive property, if the isolated system is divided in a subsystem and its surroundings, then entropy may locally decrease as the result of a process, but the sum of all entropy changes due to that process has to be positive.

Starting from the entropy balance for closed systems, the *entropy balance for control volumes* includes terms for entropy transfer accompanying mass flow. In a time rate form, if at a given instant mass enters the control volume at a boundary region i at time rate flow $\dot{m}_i$ having specific enthalpy s_i; mass leaves the control volume at a boundary region o at time rate flow $\dot{m}_o$ having specific enthalpy s_o; and the heat transfers take place as described for the entropy balance for closed systems, the entropy balance for control volumes in its time rate form is

$$\frac{dS_{\text{cv}}}{dt} = \sum_j \dot{Q}_j/T_j + \sum_j \dot{m}_{i,j} s_{i,j} - \sum_j \dot{m}_{o,j} s_{o,j} + \dot{\sigma}_{\text{cv}}, \quad \dot{\sigma}_{\text{cv}} \geqslant 0, \tag{2.16}$$

where S_{cv} refers to the total entropy contained within the control volume, and $\dot{\sigma}_{\text{cv}}$ indicates the rate of entropy production within the control volume due to the process execution.

After having briefly discussed the first three fundamental laws of thermodynamics in this section, we proceed in the next one to describe the thermophysical properties of matter with further detail. The facts presented in both sections will prepare us to perform thermodynamic analysis on thermodynamic cycles in Section 2.6.

2.5 Thermophysical Properties of Fluid States of Matter

In this section, the concepts, definitions and laws of thermodynamics introduced in Sections 2.3 and 2.4 are applied to systems in gas or liquid forms. Since for such systems mathematical relationships between several of their thermodynamic properties exist, the knowledge of only a reduced subset of them is sufficient to specify their thermodynamic state. This makes it possible to calculate the system's remaining thermodynamic properties and to represent the system's thermodynamic state in a graphical way using diagrams. These two aspects are the topic of this section. They will be of crucial importance for performing the calculations needed in our model, which is to be introduced in Chapter 3, and the corresponding analysis in Chapter 5. We close the section with a brief discussion on the state of the art concerning the search for an optimal fluid for the energy recovery system considered in this thesis.

2.5.1 Degrees of Freedom in Simple Compressible Systems

Retaking from Section 2.1, the state of a closed system is its condition as described by the values of its properties. Nevertheless, from observation of many thermodynamic systems it is known that not all properties are independent of one another. In this thesis, we are particularly interested in *simple compressible systems*: those are systems that consist of pure substances, or uniform mixtures of nonreacting gases. From Gibbs' phase rule (see e.g. [24] for its derivation) it is known that the number of properties F (also known as degrees of freedom) that determine the state of a simple compressible system consisting of C components and a number of phases in thermal equilibrium P must satisfy the relationship

$$F = C - P + 2.$$

Thus, for a pure simple compressible substance, the number of degrees of freedom is two on single-phase thermodynamic states and one in two-phase thermodynamic states.
For the rest of the section, the discussion will cover only pure simple compressible substances. Experience shows that in those systems both the temperature (T) and the specific volume (v) can be considered as independent, and the pressure p can be obtained as a function of both, (i.e. $p = p(T, v)$). This gives rise to the *p-v-T surface*. These are the $p - v - T$ values the substance would assume in thermal equilibrium. Fig. 2.1 shows the *p-v-T surface* for ethanol.

Remark 2.5.1 *The only aspect defining a phase in pure, simple compressible systems is the physical structure matter can assume. Therefore, both terms may be used interchangeably in this case.*

As previously discussed, in single-phase regions of the p-v-T surface it is enough to know the value of any two properties of the set $\{p, v, T\}$ to fix the state and thus be able to obtain the third one. In two-phase regions of the p-v-T surface the pressure is only a function of temperature (i.e. $p = p(T)$), thus the state can only be fixed by means of the specific volume v and a property of the set $\{p, T\}$. There exists also a region in which three phases coexist in equilibrium: this is the so-called triple line. The only degree of freedom along this line corresponds to the specific volume.
On the p-v-T surface, the thermodynamic states at which a phase change begins or ends are are called *saturation states*. The *vapor dome* is the region of the p-v-T surface where liquid
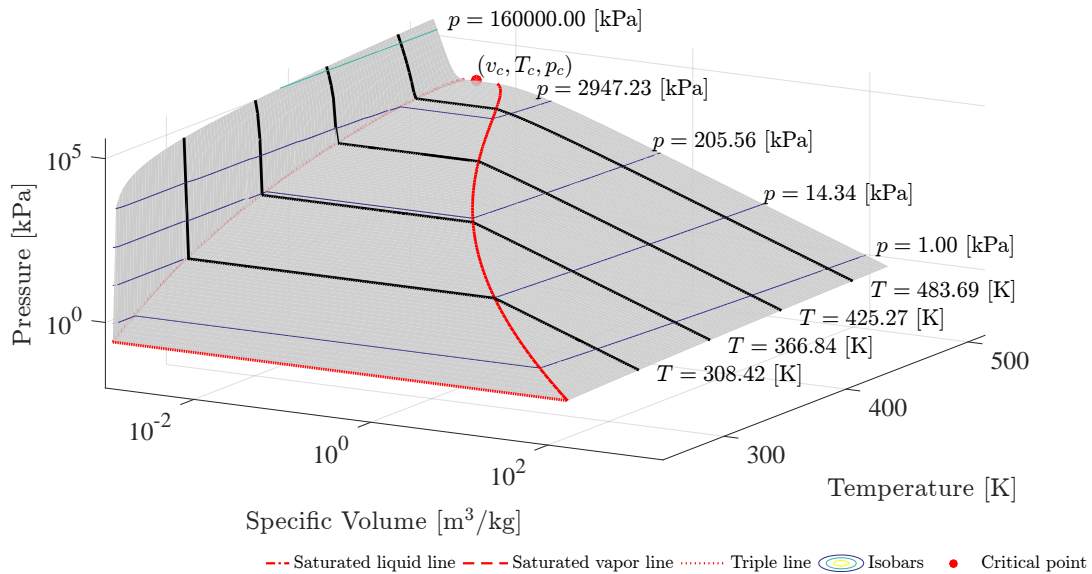
Figure 2.1: p-v-T surface for ethanol

and vapor phases are found in equilibrium. The lines bordering it are called *saturated liquid* and *saturated vapor lines*. They both meet at the critical point, which is characterized by a fixed point (v_c, T_c, p_c) on the p-v-T surface. These coordinates receive the name of *critical pressure*, *critical specific volume* and *critical temperature*, respectively. In practice, two-dimensional projections of the p-v-T surface are often used for representing the thermodynamic state and evaluating some relevant properties. These correspond to the p-v, T-v and the p-T planes. The latter is also known as the *phase diagram*, since the projections of the two-phase regions on this plane take the form of curves, and the triple line reduces to a point. On this plane, any point not belonging to a line corresponds a single-phase state. On Fig. 2.2 the p-v and p-T planes for ethanol are plotted. In this thesis we do not consider the T-v plane.

(a) p-v plane.

(b) p-T plane.
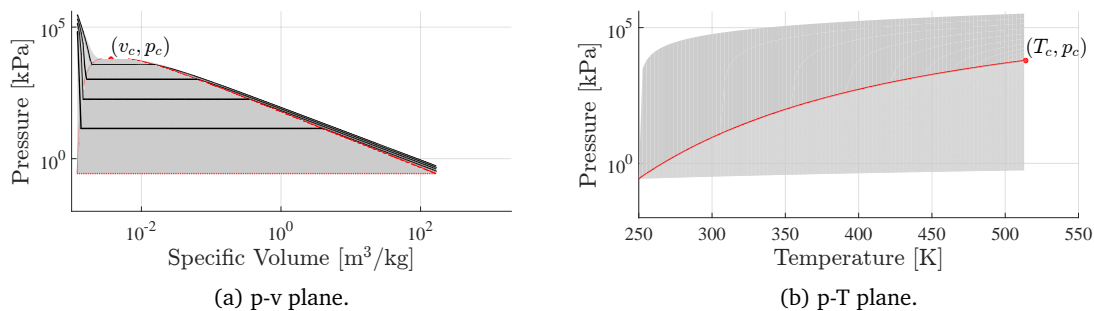
Figure 2.2: p-T and p-v planes for ethanol

On the phase diagram, the (p, T) coordinates corresponding to any of the depicted curves receive the name of *saturation pressure* and *saturation temperature*, respectively, and they designate the pressure and temperature at which a phase change process takes place.

Since we are interested in fluid phases, the p-v plane on Fig. 2.2 does not include information related to solid states. On the p-v plane, the vapor dome is represented by the bell-shaped region. Additional curves known as *isotherms* can be added. They represent the set of thermodynamic states having a particular temperature. Along isotherms corresponding to temperatures lower than the critical temperature, on single-phase regions, pressure decreases at

fixed temperature for increasing specific volume, but it stays constant as the two-phase liquid-vapor region is traversed. On saturation states, these isotherms have no defined slope. For temperatures equal or higher than the critical temperature at the critical point, the associated isotherms do not cross the two-phase liquid-vapor region and the pressure is always decreasing with the specific volume. Moreover, their slope is always defined. For the critical temperature, the coordinates (p_c, v_c) represent an inflection point on the associated isotherm.

2.5.2 Phase Changes

On the following discussion phase changes between liquid and vapor states are considered, and thus only thermodynamic states corresponding to temperatures lower than the critical temperature. In those cases, when pressures are relatively high or the specific volume is relatively low, the system is found in a liquid state, also known as *subcooled liquid state*. If pressure is kept constant, but the substance is, for example, heated until the corresponding saturation temperature is reached, the substance reaches a saturated liquid state. Additional heat addition results in formation of vapor, with considerable increment of volume and no increase of temperature. The new droplets are found in a vapor state, with which the substance is now found in a two-phase liquid-vapor mixture state. In thermal equilibrium, the vapor part reaches a saturated vapor state, whereas the liquid part keeps on a saturated liquid state. If the heating process continues, more and more amount of liquid turns into vapor until the whole system reaches the saturated vapor state (thus becoming single-phase again). If therefrom the heating at constant pressure is continued, the system's temperature would increase again, and the system would enter a *superheated vapor state*.

For two-phase liquid-vapor mixture states, the *quality* x is the ratio of the mass of substance found in a vapor phase to the system's total mass,

$$x = m_{\text{vapor}}/(m_{\text{vapor}} + m_{\text{liquid}}). \tag{2.17}$$

This quantity is useful for evaluating the mixture's intensive properties. For example, if the specific volumes for the saturated liquid and saturated vapor states associated with the same pressure are v' and v'', respectively, then the system's specific volume is given by

$$v = (1-x)v' + xv'' \qquad = v' + x(v'' - v'). \tag{2.18}$$

Similarly, under the same conventions, the system's specific enthalpy, internal energy and entropy are given by

$$u = (1-x)u' + xu'' \qquad = u' + x(u'' - u'), \tag{2.19}$$
$$h = (1-x)h' + xh'' \qquad = h' + x(h'' - h'), \tag{2.20}$$
$$s = (1-x)s' + xs'' \qquad = s' + x(s'' - s'). \tag{2.21}$$

The following relationships hold as well for a phase change at a fixed temperature T (or pressure $p = p(T)$):

$$s'' - s' = (h'' - h')/T, \tag{2.22}$$
$$u'' - u' = (h'' - h') - p(v'' - v'), \tag{2.23}$$
$$\left(\frac{\mathrm{d}p}{\mathrm{d}T}\right)_{\text{sat}} = \frac{h'' - h'}{T(v'' - v')}, \tag{2.24}$$

where the left-hand side of the last identity indicates the slope of the pressure with respect to

the temperature in two-phase liquid-vapor mixture states. The information we are lacking at this moment is where to obtain numerical values the saturated states' properties from, or what to do at single-phase states to evaluate the properties mentioned above, or others. Until now, we have been focused on given qualitative descriptions concerning the physical structure of matter. The goal of the next subsection is to give the elements that also allow a quantitative description of it.

2.5.3 Numerical Evaluation of Thermophysical Properties

From Section 2.1 we have that a property os a macroscopic characteristic of a system to which a numerical value can be assigned. In this work we are interested in using numerical tools to solve model-based problems and thus the concrete numerical values the thermophysical properties of a system under study take are of key importance. The goal of this subsection is to briefly introduce where does each value come from. It is clear that some quantities like pressure, temperature or specific volume can be obtained by direct measurement with appropriate devices, and these data may be summarized in tables for each substance. However, other properties such as entropy, enthalpy and internal energy in their specific variants, also needed for numerical evaluations, are not that easy to obtain. Moreover, since collected data are not continuous, a concrete way must be found to obtain the property values at states not necesarilly included in the collected data.

As seen in Section 2.5.1, pure simple compressible systems can be characterized by their p-v-T surface. This characterization can be done through diagrams and tables (the so-called *steam tables*), but also analytically, in what is called an *equation of state*, which is a functional form relating the three magnitudes. These equations, often deduced empirically, often reach complex forms. The software REFPROP [93], which we make use of in this thesis, provides the computational implementation of several kinds of equations of states for the evaluation of the thermophysical properties of a wide range of substances, which is of great convenience when a large number of high-accuracy evaluations are required. One equation of state implemented in this software for the case of ethanol corresponds to the volume-translated Peng-Robinson equation of state [118]:

$$p = \frac{RT}{v + c_{\mathrm{PR}} - b_{\mathrm{PR}}} - \frac{a_{\mathrm{PR}} \alpha_{\mathrm{PR}}(T, \omega)}{(v + c_{\mathrm{PR}})^2 + 2b_{\mathrm{PR}}(v + c_{\mathrm{PR}}) - b_{\mathrm{PR}}^2}, \tag{2.25}$$

where $R = 8.314472 \left[\mathrm{m^3 Pa/K\,mol}\right]$ is the universal gas constant, T is the temperature in Kelvins, and v is the specific volume. Substance-dependent magnitudes a_{PR} and b_{PR} depend on the respective critical temperature T_c and pressure p_c; c_{PR} corresponds to an empirical constant:

$$a_{\mathrm{PR}} = 0.457235528921 R^2 T_c^2 / p_c; \quad b_{\mathrm{PR}} = O.0777960739039 R T_c / p_c; \quad c_{\mathrm{PR}} = 0.0043733.$$

Function $\alpha_{\mathrm{PR}}(T, \omega_{\mathrm{PR}})$ has the expression

$$\alpha_{\mathrm{PR}}(T, \omega_{\mathrm{PR}}) = \left(1 + \kappa_{\mathrm{PR}}(\omega_{\mathrm{PR}})\left(1 + (T/T_c)^{1/2}\right)^2\right), \tag{2.26}$$

where

$$\kappa_{\mathrm{PR}}(\omega_{\mathrm{PR}}) = 0.37464 + 1.54226 \omega_{\mathrm{PR}} - 0.26992 \omega_{\mathrm{PR}}^2. \tag{2.27}$$

ω_{PR} is known as the *acentric factor*, and is a substance-dependent scalar parameter. In the case of ethanol, its value is 0.644 [-]. The correlation is valid between $250 - 650$ [K] and for

pressures up to 280 [MPa]. The volume translation is computed so that density at $T_r = 0.7$ the Helmholtz equation of state for in [43].

This way, an analytical correlation between p, v and T is implemented. In this case, since p can be directly obtained when T and v are known, it is said that the relationship is *explicit in the pressure*. This is not true for the temperature nor the specific volume, since a nonlinear equation needs to be solved in order to obtain the corresponding magnitude from the other two. Another important property satisfied by this equation is that the partial derivatives of all three properties with respect to the other two may be expressed analytically as function of properties that are easy to measure, such as p, v and T. This is used in combination with several general thermodynamic identities resulting from the first and second laws of thermodynamics and from the theory of exact differentials to obtain more useful relationships between the partial derivatives and the measurable properties. Further, we introduce the specific *Helmholtz's free energy a*, and its dimensionless version α as

$$a \stackrel{\text{def}}{=} u - Ts, \qquad \alpha \stackrel{\text{def}}{=} a/RT. \tag{2.28}$$

As enthalpy and entropy, a and α are intensive properties, and need not have a physical meaning. They are introduced for notational convenience. Helmholtz's free energy has the important property of being a *fundamental function*, which means it can provide a complete description of the substance's thermodynamic state. Important identities exist that relate it and its partial derivatives to important properties, and their partial derivatives[2]. For this reason, it is desirable to count on analytical expressions for Helmholtz's free energy whose high accuracy is proven on a wide domain. The approach implemented in REFPROP used in this work utilizes the empirically obtained relationships from [43] and [150]. In the following, we (only) summarize those found in [43]. The corresponding empirical constants' values can be found there. The expression used for the dimensionless Helmholtz's free energy is

$$\alpha(\delta, \tau) = \alpha^0(\delta, \tau) + \overline{\alpha}(\delta, \tau), \tag{2.29}$$

where the functions' arguments are the reduced density $\delta = v_c/v$ and the reciprocal reduced temperature $\tau = T_c/T$. $\alpha^0(\delta, \tau)$ is the function that yields the dimensionless Helmholtz's free energy for an ideal gas. The function is corrected by means of $\overline{\alpha}(\delta, \tau)$, explained briefly. The expression for the dimensionless Helmholtz's free energy for the case of an ideal gas is

$$\alpha^0(\delta, \tau) = \frac{h_0^0 \tau}{RT_c} - \frac{s_0^0}{R} - 1 + \ln\left(\frac{\delta \tau_0}{\delta_0 \tau}\right) - \frac{\tau}{R}\int_{\tau_0}^{\tau} \frac{c_p^0(T)}{\tau^2}\mathrm{d}\tau + \frac{1}{R}\int_{\tau_0}^{\tau} \frac{c_p^0(T)}{\tau}\mathrm{d}\tau. \tag{2.30}$$

Arbitrary reference values $T_0 = 273.15$ [K], $p_0 = 0.001$ [MPa], $h_0^0 = 45800$ [J/mol] and $s_0^0 = 180$ [J/K mol] are considered[3]. Values $\delta_0 = v_c/v_0$ and $\tau_0 = T_c/T_0$, where v_0 is the ideal gas specific volume at (p_0, T_0). The ideal specific heat capacity $c_p^0(\tau)$ is assigned an empirical relationship, namely

$$c_p^0(T) = R\left(d_1 + \sum_{i=2}^{5} d_i \frac{(\theta_i/T)^2 \exp(\theta_i/T)}{(\exp(\theta_i/T) - 1)^2}\right). \tag{2.31}$$

In this expression, d_1 and d_i, θ_i for i in $\{2, \ldots, 5\}$ are empirical constants. With respect to the

---

[2]The reader is pointed to [24, 113] for an extensive list.

real-gas correction, the corresponding expression, again empirical, is

$$\overline{\alpha}(\delta, \tau) = \sum_{k=1}^{m} N_k \delta^{i_k} \tau^{j_k} \exp\left(-\gamma \delta^{\delta^{l_k}}\right). \tag{2.32}$$

Coefficients N_k and γ, and exponents i_k, j_k and l_k are fitted for ethanol using a specific set of data.

Having the analytic expressions for Helmholtz's free energy, many thermophysical properties can be evaluated including, but not limited to, the following[4]:

Pressure
$$\frac{p}{\varrho RT} = 1 + \delta \left(\frac{\partial \overline{\alpha}}{\partial \delta}\right)_\tau, \tag{2.33}$$

Internal energy
$$\frac{u}{RT} = \tau \left[\left(\frac{\partial \alpha^0}{\partial \tau}\right)_\delta + \left(\frac{\partial \overline{\alpha}}{\partial \tau}\right)_\delta\right], \tag{2.34}$$

Enthalpy
$$\frac{h}{RT} = \tau \left[\left(\frac{\partial \alpha^0}{\partial \tau}\right)_\delta + \left(\frac{\partial \overline{\alpha}}{\partial \tau}\right)_\delta\right] + \delta \left(\frac{\partial \overline{\alpha}}{\partial \delta}\right)_\tau + 1, \tag{2.35}$$

Entropy
$$\frac{s}{R} = \tau \left[\left(\frac{\partial \alpha^0}{\partial \tau}\right)_\delta + \left(\frac{\partial \overline{\alpha}}{\partial \tau}\right)_\delta\right] - \alpha^0 - \overline{\alpha}. \tag{2.36}$$

Notice that α is basically parametrized as a function of the temperature and the specific volume (or density). Together with the fact that analytical forms are available, the pressure, enthalpy, internal energy and entropy can be directly evaluated using Eqs. (2.33) to (2.36) when both properties are available. When this is not the case, additional algebra and/or the solution of nonlinear equations needs to be performed. For convenience, in this thesis we are interested in evaluating properties given knowledge of pressure-entropy and pressure-enthalpy pairs.

Properties as Functions of the Pressure and the Entropy. In case the pressure and the entropy are given, say $p = p^*$, $s = s^*$, the rest of the thermophysical properties can still be evaluated, but if the Helmholtz's free energy is used as the fundamental function, particular algorithmic steps need to be taken. Concretely, consider first Eqs. (2.33) and (2.36) as a system of nonlinear equations in (τ, δ) of the form $F_1(\tau, \delta; p^*, s^*) = 0$. Solving for those values yields the associated τ^*, δ^*. The temperature and the specific volume (or density) can be thus evaluated, along with the internal energy and the enthalpy using Eqs. (2.34) and (2.35). In this work we are mostly interested in the enthalpy in these circumstances.

Properties as Functions of the Pressure and the Enthalpy. In case the pressure and the entropy are given, say $p = p^*$, $h = h^*$, analogous to the previous case, consider first Eqs. (2.33) and (2.35) as a system of nonlinear equations in (τ, δ) of the form $F_2(\tau, \delta; p^*, h^*) = 0$. Solving for those values yields the associated τ^*, δ^*. The temperature and the specific volume (or density) can be thus evaluated, along with the internal energy and the entropy using Eqs. (2.34) and (2.36). In this work we are interested in evaluating the temperature, the entropy, the density, and the latter's partial derivatives with respect to enthalpy and pressure this way.

In summary, each time REFPROP receives a query for the evaluation of thermodynamic properties, the corresponding systems of nonlinear equations have to be solved, the corresponding

---

[3]The choice of the reference entropy and enthalpy does not have any impact on physically meaningful calculations, since on them the property values themselves are not relevant, but the *differences* between property values belonging to different thermodynamic states.

[4]The notation for the partial derivatives $(\partial \alpha / \partial x)_y$ is to be read "*the derivative of α with respect to x while keeping y constant*".

derivatives are evaluated and a set of identities needs to be applied. Since for our purposes these evaluations may have to be repeated on numerous ocasions, it is convenient to count on a fast way of accessing this important information. In Section 3.3 the above presented numerical approach will be complemented so as to allow for a faster computation of the different fluids' thermophysical properties.

Having introduced the different states of matter and the way the thermophysical properties can be evaluated at each thermodynamic state, we are in conditions of introducing a concrete thermodynamic cycle for power production: the Rankine cycle, which will be done in the next section. This cycle has the distinctive feature that an important component of it, the working fluid, undergoes a phase change from subcooled liquid to superheated vapor. In this work, we are interested in a particular version of this cycle, to be introduced in Chapter 3.

2.6 Thermodynamics on Power Cycles

Ways have been devised in which thermal energy may be transformed into work. One of those is the Rankine cycle, to be introduced in this section. The Rankine cycle is by far the established standard for vapor power systems. In particular, the heat recovery system for heavy duty trucks that is the object of study of this dissertation is a particular variant of this cycle. As any physical system, it is subject to the laws of thermodynamics described in previous sections of this chapter. We begin this section by exploring the corollaries that apply to the special case of power cycles like this. Afterwards, a basic variant of the cycle is introduced: the different thermodynamic processes are described, a thermodynamic analysis is performed for each one, and a brief description of the physical components carrying them on is supplied. Integrating the single processes, statements are made with respect to the cycle's efficiency and main design factors. We close the section by giving a brief overview of different variants of the cycle.

2.6.1 General Corollaries

A first thermodynamic analysis of power cycles can be made using Theorem 2.3.1 to evaluate the performance of a general thermodynamic power cycle, that is, a thermodynamic cycle whose goal is to deliver a positive net work to its surroundings while being thermally communicated with a hot and a cold body. We already know from Theorem 2.4.2 that this would impossible to achieve if the system was thermally communicated with a single thermal reservoir, but the presence of the second body makes this possible. On Fig. 2.3, the directions in which heat and work are considered positive are included.
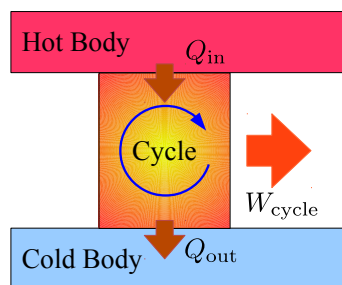
Figure 2.3: Energy transfer direction convection. When heat is transfer from the hot body to the cycle, or from the cycle to the cold body, its sign is possitive. Likewise, work performed by the cycle to its surroundings is assigned possitive sign.

With the conventions from Fig. 2.3 it follows from Theorem 2.3.1 for closed systems that

$$W_{\text{cycle}} = Q_{\text{in}} - Q_{\text{out}},$$

where W_{cycle} is the cycle's net work on its surroundings, Q_{in} represents the amount of heat transfered from the hot body to the system during the cycle and Q_{out} represents the amount of heat transfer from the system to the cold body during the cycle. In power plants, typically Q_{in} is obtained from the combustion of a fuel or from a controlled nuclear reaction. In the case of this thesis' system of interest, the source of Q_{in} is hot exhaust gas from a heavy duty truck. In power plants, Q_{out} is usually delivered to the environment by means of a near lake or a cooling tower. In the case of this thesis' system of interest, Q_{out} is delivered to the truck's coolant. Q_{in} may therefore be seen as an energy source, whereas Q_{out} as an energy waste. The cycle's *thermal efficiency* is thus defined as

$$\eta_{\text{TH}} \stackrel{\text{def}}{=} W_{\text{cycle}}/Q_{\text{in}} = 1 - Q_{\text{out}}/Q_{\text{in}}. \tag{2.37}$$

With the help of the second law of thermodynamics, more can be said about power cycles thermally communicated with two thermal reservoirs.

Corollary 2.6.1 *No thermodynamic cycle delivering a positive net work to its surroundings while being thermally communicated with a hot and a cold reservoir can reach a thermal efficiency of 100%.*

Proof. For such a cycle to reach a thermal efficiency of 100%, heat transfer Q_{out} should fade in (2.37), making the system actually in thermal contact with only one reservoir and thus violating Theorem 2.4.2. □

Further, from the same law, the following corollaries can be demonstrated (see e.g. [113] for a proof). As a previous concept, a *reversible power cycle* is a power cycle in which no irreversibilities within the system are found as it undergoes the cycle, and in which all heat transfers between the system and the thermal reservoirs occur reversibly.

Corollary 2.6.2 (Carnot Corollaries for Power Cycles) *The following two statements hold true:*

1. *The thermal efficiency of a reversible power cycle is greater than one of an irreversible power cycle when both are operating between the same two thermal reservoirs.*

2. *All reversible power cycles operating between the same two thermal reservoirs have the same thermal efficiency.*

Since neither the system characteristics nor the cycle details play a role in the derivation of the corollaries, and the actual factor that makes the heat transfers take place is the temperature difference between both reservoirs, it follows that the thermal efficiency of a reversible power cycle operating between two thermal reservoirs must be a function only of their temperatures. By choosing the Kelvin temperature scale, the ratio between the heat transfers between a system executing a reversible power cycle and two thermal reservoirs at temperatures θ_{H} and θ_{C}[56] each is given by

$$(Q_{\text{out}}/Q_{\text{in}})_{\text{rev. cycle}} = \theta_{\text{C}}/\theta_{\text{H}}.$$

As a consequence, the maximum thermal efficiency that any power cycle in thermal contact

---

[6]In this thesis, we use the symbol θ to denote the numerical value of a temperature in the Kelvin scale. In contrast, the letter T denotes the temperature as a property, independent of its scale.

[6]Subindex 'H' is associated to the hot reservoir, subindex 'C' is associated to the cold reservoir.

with two thermal reservoirs can obtain corresponds to that of the reversible cycle in thermal contact with the same thermal reservoirs, which is given by the expression

$$\eta_{\text{THmax}} = 1 - \theta_{\text{C}}/\theta_{\text{H}}. \tag{2.38}$$

It follows that both a low cool reservoir temperature and a high hot reservoir temperature improve the power cycle's maximum theoretical thermal efficiency.

2.6.2 Rankine Cycle

The Rankine cycle is an example of a thermodynamic power cycle thermally connected to two bodies at different temperatures. Since the idealization of these bodies corresponds to the thermal reservoirs used on Section 2.6.1, the associated deductions and definitions are valid for this case too. On its simplest form, the Rankine cycle consists of four processes applied to a fluid circulating through several components, also known as the *working fluid*. On Fig. 2.4, the components responsible of the realization of each process, their connections and the conventions of positive energy transfer directions (mass and energy flowing in the direction of the arrows are considered to be positive) are depicted. Additionally, in Fig. 2.5(a), the working fluid's intermediate thermodynamic states, denoted by (A)-(D), are represented on a p-v plane for a typical case. Since temperature and entropy are also thermodynamic properties, the values associated to states (A)-(D) can be also represented in a T-s diagram, which is extensively used to describe thermodynamic cycles. Fig. 2.5(b) shows a T-s diagram for a typical Rankine cycle. As explained briefly, it is important that states (A) and (C) correspond to subcooled liquid and superheated vapor, respectively.
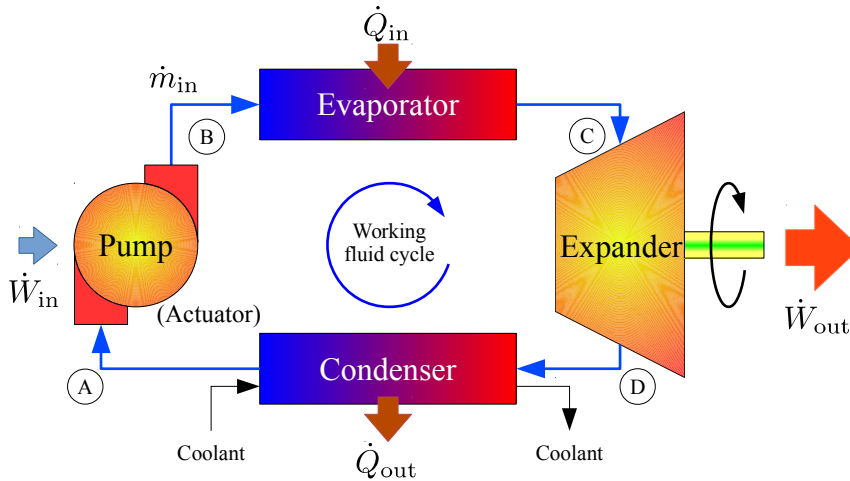
Figure 2.4: Rankine cycle: components, conexions and energy transfer direction conventions

The processes constituting the Rankine cycle correspond to:

- (A)-(B), **Pumping**: the working fluid is circulated by the pump. As a result, its pressure at (B) is higher than that at (A), and the working fluid enters the evaporator with massflow $\dot{m}_{\text{in}}$.

- (B)-(C), **Heating**: the working fluid enters the evaporator, where it is heated by an external heat source, so that it undergoes a phase change from a subcooled liquid to a superheated vapor state.

(a) p-v plane.
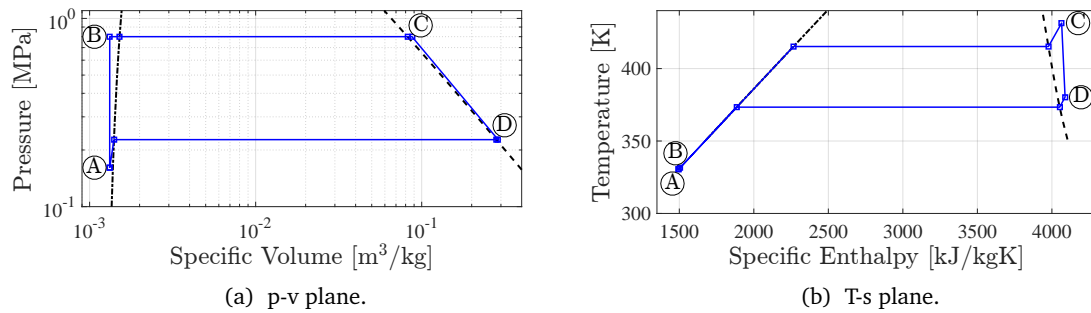
(b) T-s plane.

Figure 2.5: Rankine cycle: working fluid thermodynamic state representations on p-v and T-s planes

- Ⓒ-Ⓓ, **Expansion**: the working fluid vapor is expanded in a turbine (also called expander), delivering work as it flows through it. Consequently, the working fluid suffers a reduction on its pressure and temperature, and some condensation may take place.

- Ⓓ-Ⓐ, **Cooling**: so as to close the cycle and thus reinject the working fluid into the pump inlet, a condenser is included, through which the working fluid is cooled down until a subcooled liquid state is reached again.

It is important to keep the working fluid at a subcooled liquid state at Ⓐ. If bubbles are present at the pump's inlet (i.e. fluid is in a two-phase state), the phenomenon of *cavitation* takes place. This phenomenon takes place when the bubbles implode as a result of the high pressure found near the pump's outlet, thus generating a shock wave that impacts the face of the impeller, affecting performance and reducing its lifespan. Eventually, the succession of implosions may even destroy the impeller. Additionally, the working fluid at Ⓒ needs to be at a superheated vapor state since the mass of even small droplets is considerably higher than the same volume of vapor, causing a great impact in the expander blades. As with pumps, this is also cause of lower performance, lifespan reduction and eventually of device destruction.

Remark 2.6.3 *Unless stated otherwise, in this work we assume that the heat transfer from the hot body is big enough bring the working fluid from a subcooled liquid state Ⓑ to a superheated vapor state Ⓒ. On power plants the fuel injection can be controlled to fulfill such a requirement. However, as explained later in Chapter 3, it is not always possible control this in the system under study. When the heat transfer is not enough, a different operational mode is activated in which a bypass throttle parallel to the expander is opened, so that the working fluid traverses it instead of the expander. The system does not generate power during this period.*

We introduce the following nomenclature: an *adiabatic process* is one in which no heat transfer between the system and its surroundings takes place; an *isentropic process* as one in which the entropy change is zero; an *isobaric process* is one performed at constant system pressure; an *isothermal process* is one performed at constant system temperature.
Having defined the processes performed on a real Rankine cycle, we proceed to introduce the following idealizations, which ease its mathematical handling. Since they yield a reversible cycle, statements may be done on the real cycle's maximum theoretical efficiency.

- Ⓐ-Ⓑ: the pump has no friction and its machining tolerances are perfect. The working fluid does not exchange heat when inside the pump. Therewith, this process is considered isentropic.

- Ⓑ-Ⓒ: the heat transfer and fluid displacement take place at constant pressure through the evaporator.

- $\textcircled{C}$-$\textcircled{D}$: the working fluid's expansion is carried out reversibly, in a quasiequilibrium process. No heat exchange with the environment takes place during the expansion. This process is thus considered isentropic.

- $\textcircled{D}$-$\textcircled{A}$: the heat transfer and fluid displacement take place at constant pressure through the condenser.

Pumping and Expansion Processes

Applying Eqs. (2.3) and (2.9) to the pumping process, recognizing that the process is adiabatic ($\dot{Q}_{cv} = 0$), and considering the system as in steady state inside the pump ($dU_{cv}/dt = 0$, $dm/dt = 0$), the power input $\dot{W}_{A \to B}$ the pump needs to bring the system from state $\textcircled{A}$ to state $\textcircled{B}$ is

$$\dot{W}_{A \to B} = \dot{m}_{A \to B}(h_B - h_A), \tag{2.39}$$

where $\dot{m}_{A \to B}$ is the massflow imposed by the pump in steady state, and h_A and h_B represent the enthalpy associated to states $\textcircled{A}$ and $\textcircled{B}$, respectively.
The exact same reasoning applies for the ideal expander. Therefrom it follows that the amount of power delivered by it to its surroundings corresponds to

$$\dot{W}_{C \to D} = \dot{m}_{C \to D}(h_C - h_D), \tag{2.40}$$

where $\dot{m}_{C \to D}$ is the massflow flowing through the expander on steady state, and h_C and h_D represent the enthalpy associated to states $\textcircled{C}$ and $\textcircled{D}$, respectively.
Until now, only the first law of thermodynamics (Theorem 2.3.1) has been applied to these processes, under the hypothesis that they are adiabatic and operate in steady state[7]. From Eq. (2.39), for a given, fixed state $\textcircled{A}$, the work required by the pump per unit mass $\left(\dot{W}_{A \to B}/\dot{m}_{A \to B}\right)$ decreases with h_B. Considering the second law of thermodynamics through Eq. (2.16) for this process,

$$\dot{\sigma}_{A \to B} = \dot{m}_{A \to B}(s_B - s_A) \geqslant 0. \tag{2.41}$$

Since for pumps $\dot{m}_{A \to B} \geqslant 0$, this tells us that state $\textcircled{B}$ is only allowed to have specific entropies greater or equal to those of state $\textcircled{A}$. As a consequence of the first Carnot corollary, Corollary 2.6.2(1), the minimum allowed work required by the pump per unit mass is obtained in the limit case where no irreversibilities are found in the process ($\dot{\sigma}_{A \to B} = 0$), ergo, when the process is isentropic ($s_B = s_A$). Since in reality this is not the case, a new, theoretical state $\textcircled{B}_{is}$ (B isentropic) with the property that $s_{B,is} \overset{\text{def}}{=} s_A$ is introduced. A second property of $\textcircled{B}_{is}$, usually pressure, is assigned from $\textcircled{B}$, e.g. $p_{B,is} \overset{\text{def}}{=} p_B$, so that the enthalpy at state $\textcircled{B}_{is}$, $h_{B,is}$, may be evaluated following the procedures from Section 2.5.3 using $s_{B,is}$ and $p_{B,is}$, and the minimum allowed work required by the pump per unit mass to circulate the working fluid between pressures p_A and p_B corresponds to

$$\left(\dot{W}_{A \to B}/\dot{m}_{A \to B}\right)_{is} = h_{B,is} - h_A. \tag{2.42}$$

Since on real processes irreversibilities do appear, the *isentropic efficiency for the pump* is de-

---

[7]These assumptions are realistic, since the component's boundaries are too small to allow for big heat leaks, and the energy transfers by work due to the process are greatly superior to them.

fined as

$$\eta_{p,is} = \frac{\left(\dot{W}_{A\to B}/\dot{m}_{A\to B}\right)_{is}}{\left(\dot{W}_{A\to B}/\dot{m}_{A\to B}\right)} = \frac{h_{B,is} - h_A}{h_B - h_A}. \tag{2.43}$$

Experience shows that for actual pumps, $\eta_{p,is}$ reaches values between 0.75 and 0.85. In practice, this value is considered a given fixed parameter associated with the device. Given state Ⓐ and p_B, h_B is evaluated using $\eta_{p,is}$ as

$$h_B = h_A + \frac{1}{\eta_{p,is}}\left(h_{B,is} - h_A\right). \tag{2.44}$$

The previous reasoning can be applied to the expander as well, with the appropriate sign conventions. In that case, the given state corresponds to Ⓒ, and the pressure from Ⓓ, p_D, is given. A new theoretical state Ⓓ$_{is}$ is defined with the same entropy as Ⓒ and the pressure of Ⓓ, e.g. $s_{D,is} \overset{\text{def}}{=} s_C$ and $p_{D,is} \overset{\text{def}}{=} p_D$. The corresponding enthalpy $h_{D,is}$ is evaluated using $s_{D,is}$ and $p_{D,is}$ with the procedure of Section 2.5.3. Therewith, the maximum work delivered by the expander per unit mass is obtained for the isentropic process Ⓒ-Ⓓ$_{is}$, and corresponds to $\left(\dot{W}_{C\to D}/\dot{m}_{C\to D}\right)_{is}$, given by

$$\left(\dot{W}_{C\to D}/\dot{m}_{C\to D}\right)_{is} = h_C - h_{D,is}. \tag{2.45}$$

The *isentropic efficiency for the expander* $\eta_{ex,is}$ is introduced to account for irreversibilities as

$$\eta_{ex,is} = \frac{\left(\dot{W}_{C\to D}/\dot{m}_{C\to D}\right)}{\left(\dot{W}_{C\to D}/\dot{m}_{C\to D}\right)_{is}} = \frac{h_C - h_D}{h_C - h_{D,is}}. \tag{2.46}$$

Typical values for $\eta_{ex,is}$ are between 0.7 and 0.9. $\eta_{ex,is}$ is in practice used as a given fixed parameter associated with the device. Given state Ⓒ and p_D, h_D is evaluated using $\eta_{ex,is}$ as

$$h_D = h_C - \eta_{ex,is}\left(h_C - h_{D,is}\right). \tag{2.47}$$

Further, the *expander volumetric efficiency* $\eta_{ex,V}$ accounts for internal working fluid leakages. For an expander in which the expansion chamber volume is V_{ex}, if it operates at a rotational frequency f and a working fluid whose density at the inlet is ϱ flows through it with massflow $\dot{m}$, the volumetric efficiency is given by the expression

$$\eta_{ex,V} = \frac{\dot{m}}{\varrho f V_{ex}}. \tag{2.48}$$

Heating and Cooling Processes

Applying Eqs. (2.3) and (2.9) to the heating process on a steady state analysis ($\mathrm{d}U_{cv}/\mathrm{d}t = 0$, $\mathrm{d}m/\mathrm{d}t = 0$), since no work is performed on heat exchangers ($\dot{W}_{cv} = 0$), one obtains that the heat transfer from the surroundings to the working fluid between states Ⓑ and Ⓒ is given by

$$\dot{Q}_{B\to C} = \dot{m}_{B\to C}(h_C - h_B). \tag{2.49}$$

Since the process is considered isobaric, it holds that $p_C = p_B$. Additionally, for an internally reversible process, Eq. (2.16) ($dS_{cv}/dt = 0$, $\dot{\sigma}_{cv} = 0$)

$$\left(\dot{Q}_{B \to C}\right)_{\text{int. rev.}} = \dot{m}_{B \to C} \int_B^C T\,dS = \dot{m}_{B \to C} T_{B \to C}(s_C - s_B). \tag{2.50}$$

If the process is isothermal, $T_{B \to C}$ corresponds to the process' temperature. Otherwise, it corresponds to the process's mean temperature.

Considering the cooling process, the same analysis applies to conclude that the heat transfer from the working fluid to the surroundings between states Ⓓ and Ⓐ is given by

$$\dot{Q}_{D \to A} = \dot{m}_{D \to A}(h_D - h_A). \tag{2.51}$$

For isobaric processes it holds that $p_A = p_D$. If the process is considered internally reversible

$$\left(\dot{Q}_{D \to A}\right)_{\text{int. rev.}} = \dot{m}_{D \to A} \int_D^A T\,dS = \dot{m}_{D \to A} T_{D \to A}(s_A - s_D). \tag{2.52}$$

If the process is isothermal, $T_{D \to A}$ corresponds to the process' temperature. Otherwise, it corresponds to the process's mean temperature.

In practice, knowing h_B, $\dot{m}_{B \to C}$ and $\dot{Q}_{B \to C}$, the enthalpy h_C can be obtained using Eq. (2.49). Analogous for given h_D, $\dot{m}_{D \to A}$ and $\dot{Q}_{D \to A}$, using Eq. (2.51). The heat transfers $\dot{Q}_{D \to A}$ and $\dot{Q}_{B \to C}$ taking place inside the heat exchangers (the evaporator and the condenser) are treated with more detail in Section 2.7. They follow very complex relationships dependent on fluid thermophysical properties, massflow and heat exchanger geometry.

Thermal Efficiency

The Rankine cycle's thermal efficiency can be evaluated using Eq. (2.37) to obtain an expression involving the different state enthalpies

$$\eta_{\text{THRankine}} = 1 - \frac{Q_{\text{out}}}{Q_{\text{in}}} = 1 - \frac{h_D - h_A}{h_C - h_B}. \tag{2.53}$$

From the same equation, if the heat transfers are assumed to be internally reversible, and both the pumping and expansion processes are isentropic, the whole cycle is internally reversible, and the maximum allowed Rankine cycle thermal efficiency may also be expressed as a function of the mean heating and cooling temperatures as

$$\eta_{\text{THmax,Rankine}} = 1 - T_{D \to A}/T_{B \to C}. \tag{2.54}$$

This result is similar to Eq. (2.38). The temperatures T_C and T_H appearing there were the cool and hot reservoir temperatures of an idealized power cycle. On the contrary, temperatures $T_{D \to A}$ and $T_{B \to C}$ on Eq. (2.54) refer to the working fluid, and correspond to mean temperatures associated to a specific kind of process. Therefore, neither the external heat source nor the heat sink need to be thermal reservoirs. The conclusion is, in spite of this, similar to the case of a general power cycle connected to two thermal reservoirs: a high mean heating temperature and a low mean cooling temperature increment the cycle's maximum theoretical efficiency.

It is also interesting to observe the effect of the heating and cooling pressures p_B and p_D on the maximum theoretical efficiency. As seen on Section 2.5.1 (see Fig. 2.2), in two-phase liquid-vapor mixture states, the temperature and pressure on a simple compressible system are

related. It can be shown that the slope of the corresponding p-T curve is always positive, i.e. the saturation pressure increases with temperature. Additionally, on single-phase regions, for the same entropy, it can be shown that an increase in pressure implies an increase in temperature. With these arguments, incrementing pressures p_B and p_D has the same effect as increasing $T_{B \to C}$ and $T_{D \to A}$, respectively.

Thus far we have considered general thermodynamic principles and have applied them to the particular cases of simple compressible systems and power cycles. In particular, we have considered a simple topology of a Rankine cycle. In our analyses we have considered the heat transfers with the environment as given. In the following section, we give more insight on heat transfer modes, which will be useful when the evaporator model is extended in Section 3.2 to include transient operation modes.

2.7 Heat Transfer: Two-phase Flow

In this section, the heat transfer mode known as convection is introduced. In this work we are interested in the particular case of *internal forced convection boiling*, also known as *two-phase flow*. We proceed by firstly introducing the ruling equation for all convection processes: Newton's law of cooling. It turns out that one of its parameters depends heavily on the particular case the equation is applied to. Therefore, we continue by making an introductory explanation of the underlying physics and close with this work's main assumptions in this topic, which will be summoned in Chapter 3. The interested reader can find details in [11, 52].

The term *convection* is understood as that kind of heat transfer that takes place between a surface and a moving fluid when they are at different temperatures. The fluid's motion may be of a molecular, random nature; a macroscopic, bulk nature, or be constituted of the superposition of both. The fluid motion nature influences the internal local energy transfers, and therefore both mechanical and thermal aspects appear strongly coupled, so appropriate considerations need to be taken. All heat transfer processes by convection are described, regardless of their nature, by *Newton's law of cooling*: the convective heat flux from a surface at temperature $T_{\text{surf.}}$ to a fluid at temperature T_∞ far enough from it[8] $\dot{q}_{\text{conv.}}$, is given as

$$\dot{q}_{\text{conv.}} = \alpha(T_{\text{surf.}} - T_\infty), \tag{2.55}$$

where α is the *convection heat transfer coefficient*. This coefficient depends on the surface geometry, the nature of the fluid motion, and the fluid thermophysical and transport properties. In particular, in *forced convection* the flow is caused by external means, such as a pump. The term *internal flow* refers to one for which the surface confines the fluid. This influences the fluid's spatial velocity and temperature distributions. In this work we are interested on internal forced convection *boiling*, which is said to happen as the fluid experiences a phase change from liquid to vapor in its flow direction.

2.7.1 Internal Flow in Circular Tubes

In the following, we will consider only the case of two-phase flow along circular tubes. If that's the case, a configuration like that the one depicted in Fig. 2.6 is observed, where we focus on a *laminar flow regime* (that is, the fluid flows in laminae or layers, and no macroscopic mixing among layers is observed). Therein, the tube's internal radius is denoted as R, the radial coordinate from a cylindrical coordinate system is denoted by r and the longitudinal coordinate is denoted by z. The radial velocity and temperature distributions $V(r, z)$ and $T(r, z)$

---

[8]In the specialized literature this distance is known as the *thermal boundary layer*.

along the tube are depicted. Suppose that at $z = 0$, the fluid enters the tube with a uniform
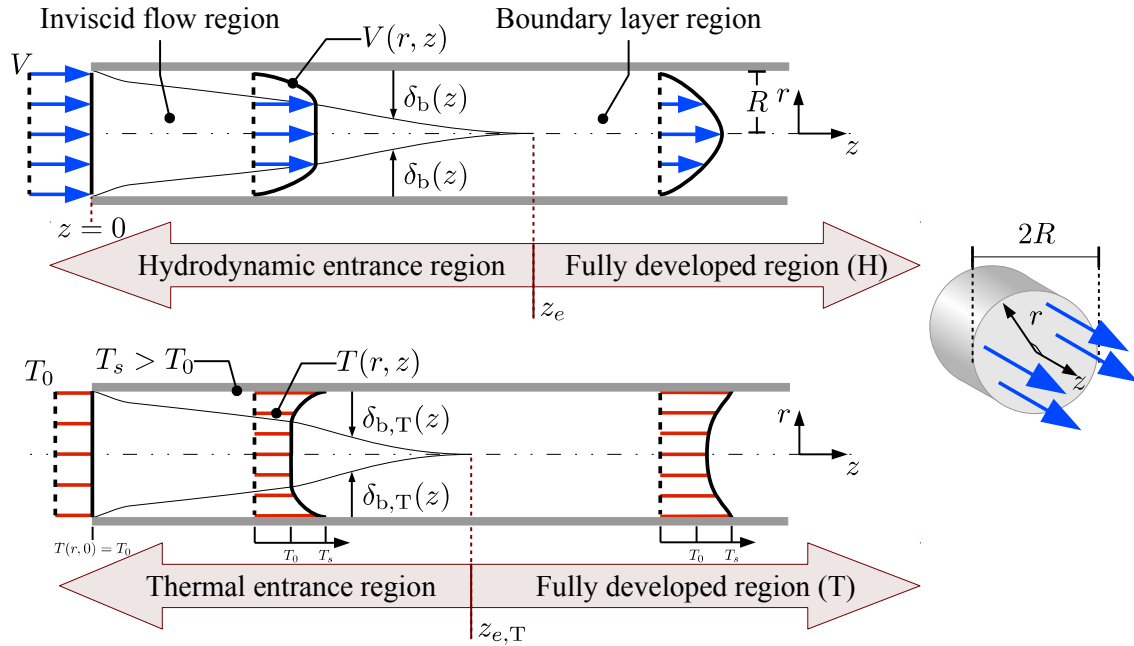
Figure 2.6: Hydrodynamic and thermal boundary layers in internal forced convection. Adapted from [11].

velocity distribution. At the contact with the tube's surface, effects associated with the fluid's viscosity cause the fluid velocity to become zero at the tube's surface (i.e. at $r = R$), and the velocity distribution suffers a distortion. Before the fluid traverses a distance z_e known as the *hydrodynamic entrance length*, its velocity increases as r decreases until eventually the original velocity is recovered at $r = r_b(z)$. The region of space in which the original velocity is not affected receives the name of *inviscid flow region*, whereas the one with the distorted velocity distribution is called the *hydrodynamic boundary layer region*. The latter's radial width, $\delta_b(z) = R - r_b(z)$, increases with z until the inviscid flow region disappears. The velocity distribution keeps changing with z until $z = z_e$, after which the flow is said to be *hydrodynamically fully developed*. The shape of the velocity distribution in the fully developed region is different depending on the flow's degree of turbulence.

Thermally, a similar phenomenon is observed. If the fluid enters the tube with a uniform temperature, i.e. $T(r, 0) = T_0$ for all $r \in [0, R]$, and the tube surface is at a temperature $T_{\text{surf.}} > T_0$, heat transfer by convection begins to take place and the fluid's temperature in regions close to the tube surface rises, creating a *thermal boundary layer*, whose inner boundary is defined by the radial distance $r_{b,T}(z)$ so that $T(r_{b,T}(z), z) = 0.99 T_{\text{surf.}}$. The thermal boundary layer's radial width, $\delta_{b,T}(z) = R - r_{b,T}(z)$, as δ_b, increases with z until eventually the whole radial temperature distribution is above T_0. The axial coordinate $z_{e,T}$ from which the relative shape of the radial temperature distribution stops changing with z is called the *thermal entrance length*, and the fluid is said to be *thermally fully developed* from that point on. The radial temperature distribution shape on the thermal fully developed region may be different according to if the surface is imposed to have constant temperature $T_{\text{surf.}}$ or a constant heat flux. In Fig. 2.6 only the first case is depicted.

Remark 2.7.1 *The thermal and hydrodynamic entrance lengths need not coincide.*

Remark 2.7.2 *As both temperature and velocity change in space, in practice, mass and energy conservation principles can be used to develop expressions linking mean values for temperature and massflow, which are easier to measure and manipulate mathematically and the aforementioned microscopic fluid velocity and temperature distributions. Our modeling in Chapter 3 uses these mean values as the basis for its calculations.*

2.7.2 Two-Phase Flow in Circular Tubes

If the fluid suffers a phase change from liquid to vapor as it traverses the tube, a configuration similar to the one depicted in Fig. 2.7 is observed. Therein it is assumed that tube is placed horizontally, which is relevant due to gravity's effect on the spatial distribution of the different phases. Along the first stretch, the fluid is found in a subcooled liquid state. Along the last stretch, the fluid is expected to be in a superheated vapor state. On these regions, the heat transfer takes place as explained in Section 2.7.1. Between both stretches, the fluid undergoes boiling. In the presence of forced convection boiling, the flow promoting convection not only
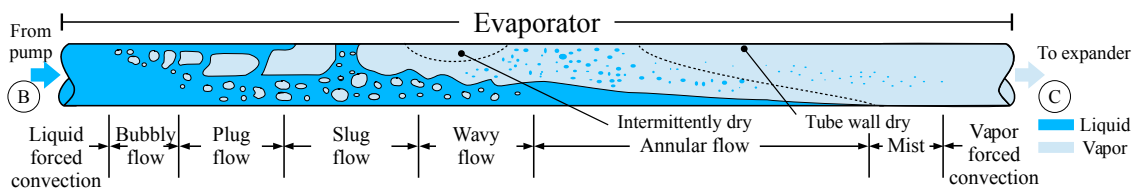
Figure 2.7: Two-phase flow in horizontal circular tubes. Adapted from [154].

is due to the fluid's bulk motion, but also due to the underlying buoyancy effects. In addition, the fluid's thermophysical properties such as its density suffer major changes during the phase change, which also presents different modes as explained briefly. The combination of all these factors is the reason why the fluid's heat transfer coefficient α_F can also vary dramatically as the fluid traverses the tube.

Initially the fluid is in a subcooled liquid state, and convection takes place under the forced convection mechanism explained in the previous section. This stage recieves therefore the name of *liquid forced convection*. Eventually, the saturation temperature is reached at the tube's surface, and first bubbles appear there: The stage known as *bubbly flow* begins. In horizontal tubes, the bubbles tend to distribute on the upper half of the tube. In the *plug flow* stage, these bubbles have increased their size, so that liquid plugs separated by elongated gas bubbles can be identified. Later, in the *slug flow* stage, the elongated bubbles have increased their diameters until they have become comparable to the tube's diameter, so that portions of the upper half of the tube are no longer in contact with the liquid. The bubbles are separated by liquid slugs similar to large amplitude waves. The *wavy flow* stage is characterized by the aparition of waves at the liquid-gas interface. They are noticeable, but do not reach the top of the tube. The *annular flow* stage is characterized by the aparition of a continuous liquid annular film around the perimeter of the tube. Small amplitude waves and vapor droplets that get dispersed into the gas core also appears. The upper part of the tube becomes dry before the lower part. In the *mist flow* stage, no more liquid is found next to the tube wall. Instead, small droplets appear in a continuous gas phase. With their eventual transformation into saturated vapor, the whole tube cross section is occupied by vapor, which starts the *vapor forced convection stage*. In this stage, the fluid is heated further for obtaining a superheated vapor at the exchanger outlet.

In order to give more insight into the different stages the fluid goes through as it undergoes two-phase flow, we notice that, since there is no mass accumulation inside the tube, except for

very short transients, for a given fluid massflow $\dot{m}$ entering the tube, if the latter's length is L, it must hold that

$$\dot{m} = \int_{r=0}^{r=R} \int_{\varphi=0}^{\varphi=2\pi} \varrho(r,z)\mathrm{V}(r,z)\, r\,\mathrm{d}\varphi\,\mathrm{d}r, \quad \forall z \in [0, L], \tag{2.56}$$

where $\varrho(r,z)$ corresponds to the fluid's density at coordinates (r,z). From Eq. (2.56) it can be easily seen that, as the fluid undergoes phase change, and in particular in the saturated flow boiling stage, the strong drop in density[9] causes an increase on the fluid's mean velocity by several orders of magnitude. This improves the conditions for heat transfer by convection.

In the saturated flow boiling stage, we define also the *mean quality*, dependent on the axial position z, as

$$\bar{x}(z) = \frac{1}{\dot{m}} \int_{r=0}^{r=R} \int_{\varphi=0}^{\varphi=2\pi} \varrho(r,z)\mathrm{V}(r,z)x(r,z)\, r\,\mathrm{d}\theta\,\mathrm{d}r. \tag{2.57}$$

where $x(r,z)$ can be defined for an infinitesimal control volume centered on coordinates (r,z) in a similar fashion as in Eq. (2.17). This magnitude increases through the saturated flow boiling stage. It has been observed that, as it approaches unity near the end of the stage, heat transfer by convection may be favored or disfavored, depending on the surface material and the fluid.

Summarizing the previous two paragraphs, the heat transfer coefficient α usually higher when the fluid is in subcooled liquid states as when it is found in saturated vapor states, varies along the saturated flow boiling stage, greatly increasing its value first (experience shows that it may become around one order of magnitude greated than in the liquid forced convection stage) to then, depending on the surface material and the fluid, increase or decrease to the value found in the vapor forced convection stage. In the case of interest in this work, experience shows that the heat transfer coefficient is lower in the vapor forced convection stage than in the liquid forced convection stage.

Chapter Summary

In this chapter we have introduced the basic nomenclature, concepts and laws concerning thermodynamics, the thermophysical properties of matter, power cycles and heat transfer by convection. After introducing the particular application we are interested in and its associated challenges, the next chapter builds upon these blocks to expand the evaporator model to tackle them more effectively, which results in a mathematically challenging dynamic model. In later chapters the formulated goals find their mathematical formulation, the numerical methodologies used to solve the underlying problems are introduced, and numerical results are presented. In this latter stage the concepts introduced in this chapter will play again a relevant role by allowing thermodynamic analyses to be performed on the computed results'.

---

[9]Since gases are several orders of magnitude less dense than liquids.

3 The Organic Rankine Cycle

The goal of this chapter is the mathematical formulation of the problems treated in this thesis, namely, the optimal control problem (OCP), the nonlinear model-predictive control strategy (NMPC) and the moving horizon estimation scheme (MHE). Firstly, we give an overview on modeling, control and estimation schemes that have been so far applied to the WHR in the literature. Next, our ORC model is formulated and our scheme of evaluation of thermophysical properties is described. Finally, using the model, the OCP, NMPC and MHE problems are formulated. Later, in Chapter 4, the numerical methods used to solve those problems are discussed.

3.1 Literature Review

In this section, for the reader's convenience, we give a brief overview on the approaches for modeling and control of ORC-based WHR and the distinctive features of our approach are indicated.

3.1.1 Models for the WHR

There exist several ways to represent the WHR. Typical approaches use those representations to build a model-based controller or tune a controller of a given structure. The system representations vary in accordance with the available actuators, the controlled variables and the data available as measurements.

One important family of model representations correspond to identified input-output models. These approaches have in common that little physical insight is used for their derivation. Their structure is often fix and their parameters are adjusted in a statistical way. An important branch of the modeling approaches are linear input/output structures. One simple scheme consist in identified two-input, two-output (TITO) transfer functions such as those found in [120, 121, 156] (the approach has been inspired by [3], who used it for vapor compression systems). TITO approaches model the relationship between the system inputs and outputs by means of a system of two linear ODEs, the parameters of which are determined by fitting techniques. Typical inputs correspond to combinations of pump massflow, turbine speed and the position of certain available bypass valves, and the outputs are often chosen as the turbine inlet temperature (TIT) and/or the turbine input pressure (TIP). First-order-plus-time-delay (FOPTD) transfer functions as used by [59, 119, 123] assume an uncoupled set of delayed linear ODEs to model the input/output dynamics, where the delay and the ODE coefficients are again identified through fitting techniques. In [59], several sets of parameters are obtained which correspond to several operating points and a switching model is proposed. Linear input-output blackbox models (see [98] for an introduction, [99] for a deep treatment) are also found in the literature [172, 174]. In those works, the Controller Auto-Regressive Integrated Moving-Average structure (CARIMA) has been considered. These discrete-time structures possess a great flexibility since they include terms for inputs, outputs, external inputs and colored noise. Moreover, nonlinear functions of one or several inputs or outputs can be included, although the model keeps being linear in the parameters.

State-space models are also found in the literature. In most papers, nonlinear ODE models arise from first principles formulations based on PDE formulations of the energy and mass conservation laws for fluids inside the evaporator. These models are attractive due to the intuitive phenomenological interpretation they offer to the experienced user. Depending on how the spatial dimension is discretized in order to obtain the ODE system, the model variant may belong to a *moving boundary* (MB) (see e.g. [20, 23, 31, 29, 57, 74, 78, 77, 109, 128]) or *finite-volume* (FV) (see e.g. [10, 21, 46, 47]) kind. For a comparison of both approaches, see [10, 35, 164]. Nonlinear models have been mainly used exclusively for the simulation of the real WHR behavior [59, 103, 104, 119, 120, 121, 122, 123, 174]. Only few publications, such as [30, 48], have used the full nonlinear models in the control formulation. Other works consider them only partially [59, 119, 120, 121, 122, 123]. Most works make use of linear ODE models. These models are usually obtained from the nonlinear models by means of linearization around some fixed operation point, typically a steady state [49, 50, 103, 104, 170]. See Chapter 3 for more details. To include nonlinearity, in [48, 49, 50, 51] several operating points are considered, giving rise to a switched linear model structure. One disadvantage of this approach is that extensive experimentation needs to be done before the best operational points for linearization can be obtained, including the statistical determination of the most frequent engine operational modes. Also, care should be taken in the definition of a switching algorithm to prevent chattering and keep fidelity in critical operational regions.

In this work, due to its better precision with a small number of state variables [164], we make use of a nonlinear, first-principles based model obtained through the MB approach. In contrast to most works, we make use of the full nonlinear dynamics. Since, as explained in Chapter 4, our methods impose differentiability requirements on the model, this aspect has been carefully investigated, and a tailored scheme for evaluating the model has been developed (see Section 3.3, cf. [62]). The scheme builds upon the one found in [58], adding an additional extrapolation feature.

3.1.2 Control of the WHR

In this thesis, we use the term *output* to refer to a quantity that is measured and whose behavior can be influenced follow a desired pattern. In ORC applications, typical outputs are superheating, evaporation temperature, evaporator pressure, and evaporator outlet vapor quality. On the other hand, the term *control* is used to describe a quantity influencing the output and that can be directly changed by a controller. In ORC applications, typical controls are the pump massflow, the expander speed and bypass valve positions for both the exhaust gas and the working fluid. Further, we use the term *external input* to denote a physical magnitudes affecting the output over which no influence can be exerted. In our case the external inputs are the exhaust gas characteristics at the evaporator inlet.

With regard to the control strategies used, the approaches found in the literature are varied. Most approaches can be clasified in two big groups, one consisting of approaches implementing a *feedback loop* only in which the computation of the controls results from comparing the outputs with a given reference[1], and the external inputs are *not* considered for those means; and one consisting of approaches implementing a *feedforward scheme* together on top of a feedback loop, which allows the exploitation of a known correlation between the external inputs and the outputs in the control computations and thus the consideration of external input measurements by the controller, which allows the controller to react in a more agile way. These schemes have been considered since feedback controllers alone have had difficulties due to delays associated with transport along the evaporator (see e.g. [119]).

---

[1]i.e. fed back, see Chapter 4 for a brief introduction

With respect to feedback loops, the most widespread alternative corresponds to the Proportional-integral-derivative (PID) controller family[2]. Since this method is well established, it can be found as a core part of the proposed solutions, as in [59, 74, 103, 104, 119, 120, 121, 122, 123, 131, 144, 156, 167], or as a counterpart for comparing a proposed scheme, as in [48, 49, 50]. Usually, the controller parameters are fixed, and several tuning methods are used. In contrast, in [59, 120, 121, 122, 123], several gain-scheduled PID strategies are proposed. In these approaches, the controller parameters vary as functions of certain measured quantities. This provides an improved adaptivity of the controller, which has a linear structure, to the strong ORC nonlinearities. Also, if equipped with an anti-windup strategy (see e.g. [96]), PID controllers are able to handle box constraints on the controls. PID controllers consider in general only the control/output dynamics. When there has been more than one control and/or output, decentralized controller structures have been used based in the pairwise strongest control/output couplings, which implies that the remaining coupling effects are neglected.

Another approach found corresponding to feedback loops corresponds to linear-quadratic controllers, mainly in the form of linear-quadratic-Gaussian controllers with integral action (LQGI). See Chapter 4 for an introduction, and [105, 169] for an advanced discussion. These state-space approaches have been applied in [103, 104, 170]. They superseed the decentralized PID schemes in their ability to handle multi-input, multi-output (MIMO) control tasks[3] directly. This can have a critical importance, since decentralized schemes may even become unstable if the system is put under the influence of large perturbations [171]. Moreover, the obtained control is optimal with respect to a performance index made up of an integral of quadratic forms in the state and the control under the assumption that the system is appropriately described by a linear ODE model; and has a known closed form as a function of the state. The integral action term helps in tracking a given set point. In comparison to PID controllers, a more sofisticated structure is required in this case, since an observer is needed to yield estimates of the state vector from sensor information. LQGI controllers make use of a Kalman filter for this task. One known limitation of these methods is their assumption of linear dynamics. As we have previously mentioned, this assumption does not hold for ORC-based systems. Another drawback of LQGI controllers for our application is their inability to directly consider constraints. This applies to the PID family as well.

Linear model-predictive control (LMPC) approaches (see e.g. [69, 107]) are also found in the literature. Similarities between these approaches and linear-quadratic approaches are the assumption of linear system dynamics, and the consideration of an underlying optimization problem with an objective function consisting of an integral or sum of quadratic forms in the controls and states. LMPC adds, in contrast, the posibility to consider linear constraints on those quantities. Additionally, since LMPC considers predictions of the system trajectories for its computations, it can be naturally extended to a feedforward scheme, as in [174].State-space MPC has been investigated for the ORC at the regulatory level. In [171] both unconstrained and constrained settings have been considered, and in [48, 49, 50, 51, 104], constraints have been included. In those works resorting to linear black-box models, the generalized predictive control (GPC) approach (see e.g. [27]) has been proposed with the inclusion of constraints in [174], and without them in [172]. In all these works, the squared deviation between the output predicted behavior and a reference set point is minimized. In all works considering LMPC with constraints, these have not been more complex than bounds on controls, control steps, and outputs. In spite the important improvement of including linear constraints, important constraints such as the maximum working fluid temperature are inevitably left out of the formulations. The dynamics keep being assumed linear. Using the switched linear models,

---

[2]See Chapter 4 for a brief introduction, see [6] for a deep discussion.
[3]i.e. a control taks in which several controls and outputs are considered simultaneously.

in [48, 49, 50, 51] a switched MPC formulation is implemented that improves the controller's performance. Nevertheless, in [48] it is shown that a nonlinear model-predictive control approach can still improve the results.

Nonlinear model-predictive control (NMPC) approaches (see e.g. [61, 107, 108]) superseed LMPC approaches in that they can easily deal with problems in which the system dynamics and/or constraints are not necessarily linear, and the cost function can be more general than an integral or sum of quadratic forms in states and the controls. This greater flexibility allows in general the use of more accurate models, the introduction of economic cost functions and the treatment of complex operational constraints. NMPC can be extended to a feedforward scheme the same way LMPC can. NMPC may thus be, in summary, more adequate for some applications, in particular for the control of the WHR. To our knowledge, in the literature of control of the WHR, NMPC has been used in [30, 48]. In a conventional NMPC approach, a sequence of nonlinear programming problems (NLPs) is posed and each is solved until a convergence criterion is satisfied. Therefore, suitable NMPC implementations must properly deal with the fact that the NLP algorithm used to compute a solution may take too long to converge to an optimum. In [48] the SQP solver used for the NMPC strategy is simply regarded as computationally too expensive and it is left for comparison only, even if it produces better results than the switched MPC strategy presented there. On the other hand, in [30] a meta-heuristic particle swarm optimization implementation is used to solve the raising NLPs. This approach is not suitable for real-time applications.

We can think of a theoretical limit case in which the truck's driving time between two positions and both the massflow and temperature of the exhaust gas entering the evaporator are completely known along the truck's trajectory. In that case it is interesting to know how should the WHR be operated (i.e. which values should the control function take on each time instant) so as to generate as much energy as possible while the operational constraints are being satisfied. Posed this way, the problem corresponds to an Optimal Control Problem (OCP). Pontryagin's Maximum Principle [125] (see also e.g. [22]) gives first order optimality conditions that help solving such problem in functional spaces. However, for complex engineering problems like the one under study in this thesis, an analytical solution to the problem may not be easy to obtain. In contrast, in this work we consider numerical solutions, as they can readily provide practical control values and performance estimations. To the knowledge of the author, the only references focusing on the optimal control of the WHR correspond to [122] and [62]. In [122], the use of an approach based on Dynamic Programming (DP) is proposed. The approach is able to consider nonlinear operational constraints in a DAE context. In [62], the numerical solution of the optimal control problem is achieved by means of the Direct Multiple Shooting (DMS) method (see e.g. [18, 92, 124]). In contrast to DP implementations, the DMS method does not suffer from the curse of dimensionality and is therefore well suited for models with higher number of states and finer time discretizations.

In contrast to the previously listed control approaches, in this thesis we propose one consisting of an NMPC scheme that explicitly takes nonlinear dynamics and constraints into consideration. The scheme's efficient numerical treatment, explained in detail in Chapter 4 makes it possible to carry out control updates within short times, making it applicable in the considered real-time environments. This is particularly advantageous considering the highly transient nature of the exhaust gas conditions. To illustrate this, in Chapter 5 a test scenario consisting of real-world data provided by Daimler AG is presented in which the scheme reaches computational times faster than 100 [ms] (a typical sampling time for an on-board controller) for different configuration settings. For this application, the proposed scheme makes use of exhaust gas measurements in order to produce accurate WHR behavior predictions and deals with the nonlinear optimization problem of maximizing the WHR net generated energy directly. With

the proposed scheme, the WHR is able to recover around 3% more exhaust gas energy than with standard control strategies. Additionally, an approximated local solution for the optimal control of the WHR is obtained for comparison under the same exhaust gas conditions by using different numerical instances of the DMS method.

3.1.3 State Estimation for the WHR

State-space control strategies determine the control values from knowledge of the corresponding model's state vector. Since the state vector cannot always be directly measured, a *state observer* is needed in order to produce an estimation of it from the available measurements which can be fed to the controller. When the models are linear, Luenberger observers [100] or the Kalman filter [79] can be used for these means. As explained before, Kalman filters are the method of choice in approaches like the LQGI, which can be found applied to WHR in [103, 104, 170]. The Kalman filter has been used in connection with other strategies in [48, 49]. The extended Kalman filter (EKF) [28] is an extension of the Kalman filter to the nonlinear case which has been applied to the WHR in [102, 104, 121, 123]. On the other hand, in [25] a structure resembling a Luenberger observer but considering a nonlinear model of the evaporator has been proposed. In most publications considering state-space control strategies applied to the WHR, the state is assumed known and no observers are considered.

In this thesis we consider a technique for estimating the state which to our knowledge has not been tested in the literature for WHR, namely the *moving horizon estimation* (MHE). In contrast to approaches based on the Kalman filter, in which the state vector at some instant is estimated using the previous estimate and the measurements corresponding to that same instant only, in MHE a time window is defined in which several past measurements can be considered in order to obtain the best possible state estimate according to some criterion, typically a least-squares objective function. As time passes, the latest measurements are included in the window and the oldest are discarded. In order to summarize the information previous to the last measurement entering the window, an additional term known as *arrival costs* is usually considered. In MHE, nonlinear dynamics and constraints can be fully taken into account, and model parameters can be naturally estimated if needed. Similar to NMPC, in MHE a sequence of NLPs is defined, and each member of the sequence can be solved until the satisfaction of some convergence criterion. MHE has been analyzed under this assumption in [110] for unconstrained nonlinear systems, in [135] for constrained linear systems and in [136, 138] for constrained nonlinear systems. In the case of MHE it is also desirable to obtain state estimates as fast as possible, but the computational burden of solving the complex NLPs makes that a nontrivial task. In this thesis we implement MHE by resorting to an adequate real-time iteration (RTI) algorithm as proposed in [42, 86]. In [86] the MHE scheme is shown to be more effective than an extended Kalman filter (EKF) implementation with comparable computational times. A stability proof for the scheme is given in [166].

To the author's knowledge, this is the first implementation that considers both the NMPC and the MHE approaches used simultaneously in the control of the WHR. The combination of NMPC and MHE produces a closed-loop, model-based implementation that receives realistic measurements as inputs and calculates the corresponding control functions as outputs. The proposed scheme's performance is evaluated considering MHE estimate accuracy. In Chapter 5, the proposed approach is compared with an NMPC strategy in which the state vector is perfectly known. The proposed scheme enables the WHR to generate around 2 [%] more energy than standard PI and LQGI controllers. These results have been accepted for publication in [63].

3.2 Model Formulation

The WHR in onboard applications is subject to a highly transient heat source, and therefore it is advantageous to take dynamic phenomena into account for the design of a control strategy. In this section, the WHR dynamic model used throughout this thesis is introduced and its main assumptions are indicated. The WHR components performing mainly mechanical work (pump, expander) are modeled in steady state using previously introduced equations, whereas a dynamic model based on the moving boundary approach is introduce to model the evaporator. Since the evaporation and condensing processes are highly decoupled, a simplified model for the condenser is used.

For details concerning the evaluation of thermophysical properties such as densities, entropies, enthalpies and their derivatives with respect to pressure and enthalpy, see Section 3.3.

3.2.1 Pump

For the pump we make use of the previously introduced Eqs. (2.39) and (2.44), since its dynamics are much faster than those of the heat exchangers. Moreover, under the assumption of a positive-displacement technology, the pump's outlet massflow is assumed to be the control, i.e $\boldsymbol{u}(t) \overset{\text{def}}{=} \dot{m}_{\text{in}}(t)$. The fixed parameters corresponding to the pump are $\boldsymbol{p}_{\text{p}} = \left(p_A, h_A, \eta_{\text{p,is}}, \eta_{\text{p,el}} \right)$. Notice that the first two correspond to the simplified condenser model to be introduced in Section 3.2.3. At the pump outlet, the pressure is denoted as p_B, which will be introduced in Section 3.2.4 as one of the model's dynamic states. Recapitulating, the following equations summarize the pump's model:

$$s_A = s_{\text{subc.liq.}}(p_A, h_A), \tag{3.1a}$$

$$h_{B,\text{is}} = h_{\text{subc.liq.}}(p_B, s_A), \tag{3.1b}$$

$$h_B = h_A + (h_{B,\text{is}} - h_A)/\eta_{\text{p,is}}, \tag{3.1c}$$

$$\dot{W}_{\text{in}} = \dot{m}_{\text{in}}(h_B - h_A)/\eta_{\text{p,el}}. \tag{3.1d}$$

In Eq. (3.1), the subscript 'subc.liq.' denotes the evaluation of a property at a subcooled liquid state. In normal operating conditions this is trivially satisfied since the values of the function arguments completely define the state and thus the phase. However, as will be explained in Section 3.3, this is not necessarily the case when the model is numerically evaluated, so that the notation can be used to relate the quantities to their corresponding fields according to the evaluation method to be introduced in Section 3.3.4.

3.2.2 Expander

As for the pump, the expander dynamics are much faster than those of the heat exchangers, therefore we make use of Eqs. (2.45), (2.47) and (2.48), to model the expander, which has been assumed of a positive-displacement type. The fixed parameters corresponding to the expander are $\boldsymbol{p}_{\text{ex}} = \left(\eta_{\text{ex,is}}, p_D, n_{\text{ex}}, \eta_{\text{ex,V}}, V_{\text{ex}}, \eta_{\text{ex,el}} \right)$. The expander inlet pressure p_C (the same as for the pump outlet) is to be introduced in Section 3.2.4 as one of the model's dynamic

states. The following equations summarize the expander's model:

$$\varrho_C = \varrho_{\text{suph.vap.}}(p_C, h_C), \tag{3.2a}$$

$$s_C = s_{\text{suph.vap.}}(p_C, h_C), \tag{3.2b}$$

$$\dot{m}_{\text{out}} = n_{\text{ex}} \eta_{\text{ex,V}} V_{\text{ex}} \varrho_C, \tag{3.2c}$$

$$h_{D,\text{is}} = h_{\text{suph.vap.}}(p_D, s_C), \tag{3.2d}$$

$$h_D = h_C - \eta_{\text{ex,is}}(h_C - h_{D,\text{is}}), \tag{3.2e}$$

$$\dot{W}_{\text{out}} = \eta_{\text{ex,el}} \dot{m}_{\text{out}}(h_C - h_D). \tag{3.2f}$$

As in Eq. (3.1), in Eq. (3.2) the subscript 'suph.vap.' denotes the evaluation of a property at a superheated vapor state. This notation can be used to relate the quantities to their fields according to the evaluation method to be introduced in Section 3.3.4.

3.2.3 Condenser

The condenser is assumed to be able to bring the working fluid from any inlet thermodynamic state specified by (p_D, h_D) to a fixed thermodynamic state specified by the fixed parameters (p_A, h_A). These assumptions are valid as a first approximation if the condenser includes an internal receiver.

3.2.4 Evaporator

As previously introduced, the system dynamics are modeled in the evaporator. In this section, the nonlinear dynamic model based on the Moving Boundary approach [77, 164] used to model it are introduced. Starting from the model presented on [23], modifications are introduced as in [62, 64] to match the requirements for successful application of the algorithms to be introduced in Chapter 4.

The evaporator is considered to be a cylindrical concentric counterflow heat exchanger of fixed length L, see Fig. 3.1. The outer tube is considered as perfectly isolating, so heat transfers to the surroundings are neglected. The exhaust gas flows along the space between both tubes, whereas the working fluid does it in the oposite direction along the inner tube's cavity. The inner tube is thus called wall. Its inner and outer diameters are d_{i} and d_{o}, respectively, which result in a transverse metal section area of

$$A_W = \pi(d_{\text{o}}^2 - d_{\text{i}}^2)/4,$$

and inner section area

$$A = \pi d_{\text{i}}^2/4.$$

With respect to the concepts introduced next, we have included Fig. 3.2 for the reader's convenience. Since it is expected that the working fluid undergoes a phase change along the evaporator, with which its thermophysical properties are prone to strong variations, the evaporator is therefore divided into three zones with variable lengths L_1, L_2 and $L_3 = L - L_1 - L_2$, inside which the fluid is assumed to be found in subcooled liquid, two-phase liquid-vapor mixture, and superheated vapor states, respectively. At the zone boundaries the working fluid is assumed to be found in the corresponding saturated states. The evaporating pressure p_{ev} ($\stackrel{\text{def}}{=} p_B \stackrel{\text{def}}{=} p_C$, see Eqs. (3.1) and (3.2)) and the output enthalpy h_C are used for the evaluation of the working fluid's properties inside the evaporator. Temperatures $\theta_{W,1}$, $\theta_{W,2}$ and $\theta_{W,3}$ account for each zone's mean wall temperatures. These variables form the state vector

(a) Perspective view.

(b) Longitudinal view.
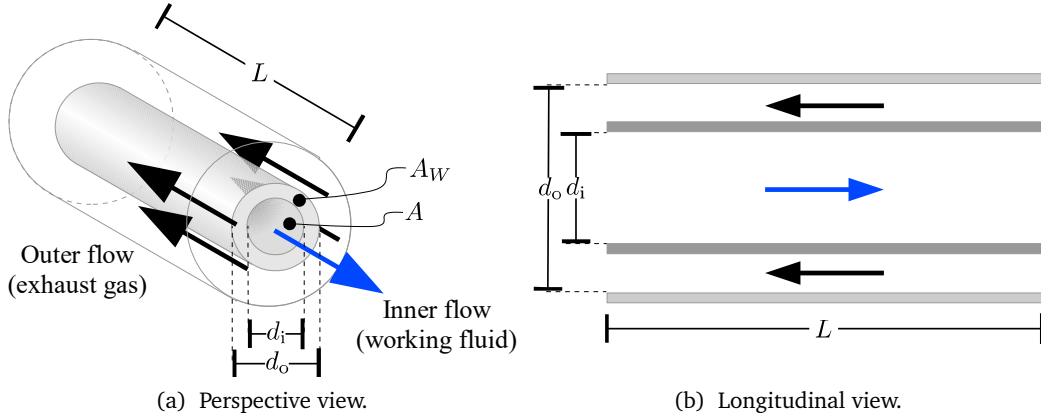
Figure 3.1: Concentric counterflow heat exchanger

$\boldsymbol{x}_{\mathrm{ev}} = \left(L_1, L_2, p_{\mathrm{ev}}, h_C, \theta_{W,1}, \theta_{W,2}, \theta_{W,3}\right)$, on which the following calculations will be based. The evaporator's working fluid inlet massflow corresponds to $\dot{m}_{\mathrm{in}}$, which is the control (see Section 3.2.1). The working fluid leaves the evaporator with massflow $\dot{m}_{\mathrm{out}}$ (see Section 3.2.2). On the other hand, the exhaust gas inlet massflow $\dot{m}_{G,\mathrm{in}}$ and temperature $\theta_{G,\mathrm{in}}$ constitute the external input vector, $\boldsymbol{w} = \left(\dot{m}_{G,\mathrm{in}}, \theta_{G,\mathrm{in}}\right)$. The evaporator's fixed parameter vector is $\boldsymbol{p}_{\mathrm{ev}} = (\, L, d_{\mathrm{i}}, d_{\mathrm{o}}, \varrho_W, c_W, \alpha_{F,1}, \alpha_{F,2}, \alpha_{F,3},\ \alpha_{G,1}, \alpha_{G,2}, \alpha_{G,3}, p_G\,)$, where ϱ_W and c_W are the wall's density and heat specific capacity, respectively, and $\alpha_{F,j}$, $\alpha_{G,j}$ are the working fluid and exhaust gas convection heat transfer coefficients corresponding to zone $j \in \{1, 2, 3\}$, respectively.
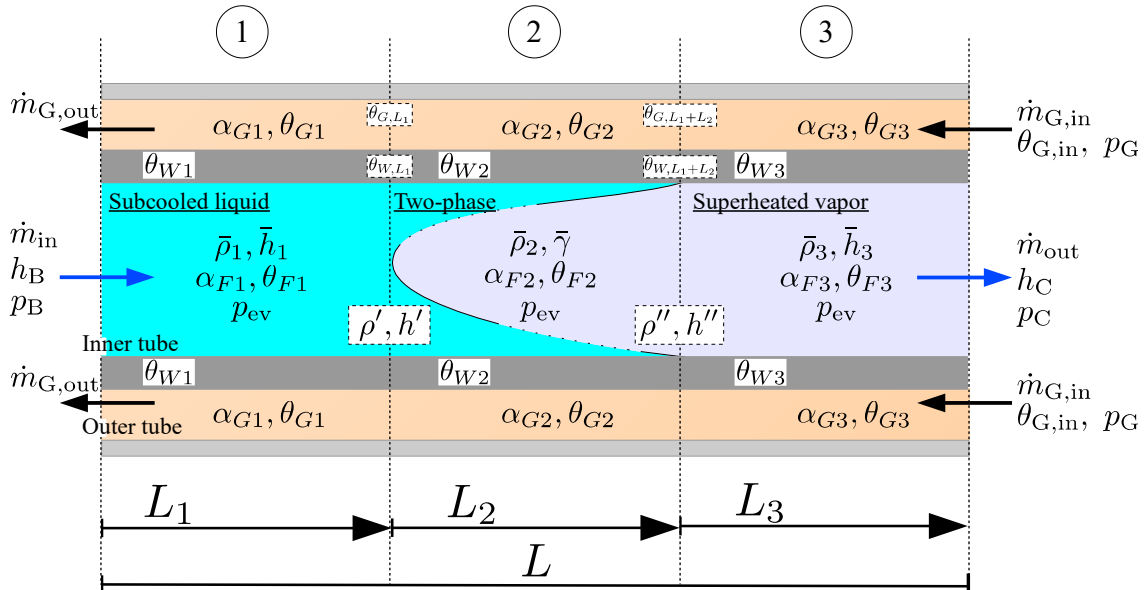
Figure 3.2: Volume control for the exhaust gas energy balance

For both the working fluid and the exhaust gas, the pressure drops along the evaporator, which are due to fluid viscosities and momentum changes are neglected. Therefore the pressure is considered equal to p_{ev} all along the evaporator, so that $p_B \overset{\text{def}}{=} p_C \overset{\text{def}}{=} p_{\mathrm{ev}}$. Hence, the mean zone pressures $\bar{p}_j$ also satisfy $\bar{p}_1 = \bar{p}_2 = \bar{p}_3 = p_{\mathrm{ev}}$. The associated saturated liquid and vapor enthalpies h' and h'', densities ϱ', ϱ'', their derivatives with respect to pressure $\mathrm{d}h'/\mathrm{d}p_{\mathrm{ev}}$, $\mathrm{d}h''/\mathrm{d}p_{\mathrm{ev}}$, $\mathrm{d}\varrho'/\mathrm{d}p_{\mathrm{ev}}$ and $\mathrm{d}\varrho''/\mathrm{d}p_{\mathrm{ev}}$, and $\theta_{F,2}$ are all evaluated at p_{ev}. The evaporator inlet working fluid enthalpy h_B is obtained as in (3.1c). Since h_A is a fixed parameter, it follows

that its time derivative is given by

$$\frac{dh_B}{dt} = \frac{1}{\eta_{p,is}} \frac{\partial h_{B,is}}{\partial p_B} \frac{dp_{ev}}{dt}. \tag{3.3}$$

$\partial h_{B,is}/\partial p_B$ has the same arguments as $h_{B,is}$. We calculate the zone mean enthalpies as $\bar{h}_1 := 0.5\left(h_B + h'\right)$, $\bar{h}_2 := 0.5\left(h' + h''\right)$ and $\bar{h}_3 := 0.5\left(h'' + h_C\right)$. For $j \in \{1,3\}$, the corresponding working fluid temperatures $\theta_{F,j}$, local densities $\bar{\varrho}_j$ and their derivatives with respect to pressure and enthalpy, $\partial \bar{\varrho}_j/\partial \bar{p}_j$ and $\partial \bar{\varrho}_j/\partial \bar{h}_j$, are evaluated at $(\bar{p}_j, \bar{h}_j)$. For the evaluations of quantities corresponding to $j = 1$ and $j = 3$, the subcooled liquid and superheated vapor surfaces are used as will be explained in Section 3.3, respectively.

For the two-phase zone, the density ratio, the mean void fraction $\bar{\gamma}(p_{ev})$, the local mean density $\bar{\varrho}_2$ and the mean enthalpy per unit volume $\overline{\varrho h}_2$ are calculated as follows:

$$\mu = \varrho''/\varrho', \tag{3.4a}$$

$$\bar{\gamma} = \frac{1 - \mu^{2/3}\left(1 + \log(\mu^{-2/3})\right)}{\left(1 - \mu^{2/3}\right)^2}, \tag{3.4b}$$

$$\bar{\varrho}_2 = \varrho' + \bar{\gamma}(\varrho'' - \varrho'), \tag{3.4c}$$

$$\overline{\varrho h}_2 = \varrho' h' + \bar{\gamma}(\varrho'' h'' - \varrho' h'). \tag{3.4d}$$

At the inner zone boundaries, the wall temperatures are defined as

$$\theta_{W,L_1} = (L_2 \theta_{W,1} + L_1 \theta_{W,2})/(L_1 + L_2), \tag{3.5a}$$

$$\theta_{W,L_1+L_2} = (L_3 \theta_{W,2} + L_2 \theta_{W,3})/(L_2 + L_3). \tag{3.5b}$$

Together with the exhaust gas zone mean temperatures $\theta_{G,j}$, which are derived briefly from the energy balance for the exhaust gas, the convection coefficients $\alpha_{F,j}$ and $\alpha_{G,j}$ can be used for calculating the heat transfers from the exhaust gas towards the wall $\dot{Q}_{GW,j}$ and from the wall towards the working fluid $\dot{Q}_{WF,j}$ as

$$\dot{Q}_{GW,j} = \pi d_o L_j \alpha_{G,j}\left(\theta_{G,j} - \theta_{W,j}\right), \tag{3.6a}$$

$$\dot{Q}_{WF,j} = \pi d_i L_j \alpha_{F,j}\left(\theta_{W,j} - \theta_{F,j}\right), \quad \forall j \in \{1,2,3\}. \tag{3.6b}$$

Remark 3.2.1 *In [11, 23, 157] expressions for the convection coefficients are given which involve the zone lengths, wall diameters, Nusselt, Reynolds and Prandtl numbers of each zone and consider appropriate corrections for the two-phase zone. The expressions depend in a very nonlinear fashion on the aforementioned physical quantities and on the fluid's physical state and flow regime in a discrete way. Although the direct inclusion of such expressions represents no obstacle for the purpose of simulation, special considerations have to be taken into account if derivative-based optimization is pursued. For instance, the model presented in this chapter can be carefully expanded by means of the inclusion of a proper switching function to include all the correct empirical correspondences.*

Exhaust Gas Energy and Mass Balances

In this model formulation it is assumed that, along the tube, the exhaust gas flow is *unsteady* and *uniform*, i.e., its velocity does not change with the position in the stream, but allowed to change in time [52], and that it is found in a thermodynamic steady state, i.e. control volumes

do not accumulate energy nor mass. A direct consequence of this is that

$$\dot{m}_{G,\text{out}} = \dot{m}_{G,\text{in}}.$$

As the exhaust gas enters evaporator zone j with temperature $\theta_{G,j}^+$ at $z = L_j^+$, it makes contact with the zone's wall, assumed at an homogeneous temperature $\theta_{W,j}$ and then, due to the corresponding heat transfer, exits the zone at $z = L_j^-$ at a temperature $\theta_{G,j}^-$. Under the assumptions above, a differential equation in the tube's longitudinal dimension can be formulated from which $\theta_{G,j}^-$ and an expression for the zone mean temperature $\theta_{G,j}$ can be obtained. To this end, consider a control volume of length $\mathrm{d}z$ placed at position z like the one in Fig. 3.3. The
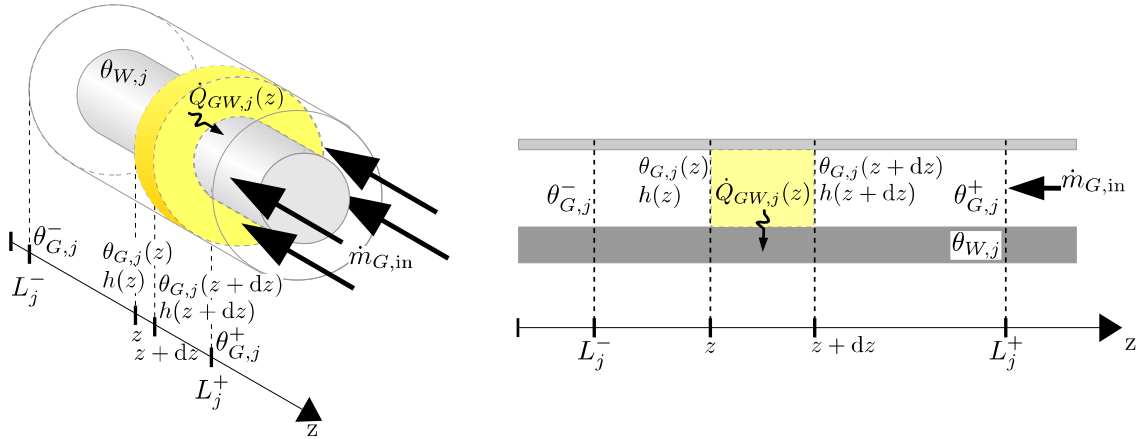
Figure 3.3: Volume control for the exhaust gas energy balance

exhaust gas enters the volume with a specific enthalpy $h_G(z + \mathrm{d}z)$ and leaves it with a specific enthalpy $h_G(z)$. From Eq. (2.9),

$$\dot{m}_{G,\text{in}} \left(h_G(z + \mathrm{d}z) - h_G(z) \right) = \dot{Q}_{GW,j}(z).$$

At constant pressure, it holds that

$$h_G(z + \mathrm{d}z) - h_G(z) = c_{G,j}(\theta_{G,j}(z + \mathrm{d}z) - \theta_{G,j}(z)).$$

Also, we incorporate Newton's law of cooling Eq. (2.55) to express $\dot{Q}_{GW,j}(z)$, so that

$$\dot{m}_{G,\text{in}} c_{G,j} \left(\theta_{G,j}(z + \mathrm{d}z) - \theta_{G,j}(z) \right) = \pi d_\mathrm{o} \mathrm{d}z \, \alpha_{G,j} \left(\theta_{G,j}(z) - \theta_{W,j} \right).$$

Reordering terms and taking limit for $\mathrm{d}z \to 0$ we obtain the initial value problem

$$\frac{\mathrm{d}\theta_{G,j}}{\mathrm{d}z}(z) = \frac{\pi d_\mathrm{o} \alpha_{G,j}}{\dot{m}_{G,\text{in}} c_{G,j}} \left(\theta_{G,j}(z) - \theta_{W,j} \right), \tag{3.7}$$

$$\theta_{G,j}(L_j^+) = \theta_{G,j}^+. \tag{3.8}$$

Equation (3.7) can be solved analytically to yield

$$\theta_{G,j}(z) = \theta_{W,j} \left(1 - \exp\left(\frac{\pi d_\mathrm{o} \alpha_{G,j}(z - L_j^+)}{\dot{m}_{G,\text{in}} c_{G,j}} \right) \right) + \theta_{G,j}^+ \exp\left(\frac{\pi d_\mathrm{o} \alpha_{G,j}(z - L_j^+)}{\dot{m}_{G,\text{in}} c_{G,j}} \right). \tag{3.9}$$

From Eq. (3.9) we calculate the exhaust gas zone mean temperature as

$$\begin{aligned}
\theta_{G,j} &= \frac{1}{L_j^+ - L_j^-} \int_{L_j^-}^{L_j^+} \theta_{G,j}(z)\mathrm{d}z \\
&= \theta_{W,j} + (\theta_{G,j}^+ - \theta_{W,j})\frac{\dot{m}_{G,\mathrm{in}}c_{G,j}}{\pi d_\mathrm{o}\alpha_{G,j}L_j}\left(1 - \exp\left(-\frac{\pi d_\mathrm{o}\alpha_{G,j}L_j}{\dot{m}_{G,\mathrm{in}}c_{G,j}}\right)\right).
\end{aligned} \tag{3.10}$$

Equation (3.9) can as well be used to obtain the downstream border temperature

$$\begin{aligned}
\theta_{G,j}^- &= \theta_{G,j}(z = L_j^-) \\
&= \theta_{W,j} + (\theta_{G,j}^+ - \theta_{W,j})\exp\left(-\frac{\pi d_\mathrm{o}\alpha_{G,j}L_j}{\dot{m}_{G,\mathrm{in}}c_{G,j}}\right).
\end{aligned} \tag{3.11}$$

Observing that $\theta_{G,3}^+ = \theta_{G,\mathrm{in}}$, that $\theta_{G,j}^+ = \theta_{G,j+1}^-$ for $j \in \{1,2\}$ and that $\theta_{G,1}^- = \theta_{G,\mathrm{out}}$, we can rename some of those quantities as $\theta_{G,L_1} \overset{\mathrm{def}}{=} \theta_{G,1}^+$ and $\theta_{G,L_1+L_2} \overset{\mathrm{def}}{=} \theta_{G,2}^+$. Defining $K_j := \frac{\pi d_\mathrm{o}\alpha_{G,j}L_j}{\dot{m}_{G,\mathrm{in}}c_{G,j}}$ we have

$$\theta_{G,L_1+L_2} = \theta_{W,3} + (\theta_{G,\mathrm{in}} - \theta_{W,3})\exp(-K_3), \tag{3.12a}$$

$$\theta_{G,L_1} = \theta_{W,2} + (\theta_{G,L_1+L_2} - \theta_{W,2})\exp(-K_2), \tag{3.12b}$$

$$\theta_{G,\mathrm{out}} = \theta_{W,1} + (\theta_{G,L_1} - \theta_{W,1})\exp(-K_1), \tag{3.12c}$$

and

$$0 = -\theta_{G,3} + \theta_{W,3} + (\theta_{G,\mathrm{in}} - \theta_{W,3})(1 - \exp(-K_3))/K_3, \tag{3.13a}$$

$$0 = -\theta_{G,2} + \theta_{W,2} + (\theta_{G,L_1+L_2} - \theta_{W,2})(1 - \exp(-K_2))/K_2, \tag{3.13b}$$

$$0 = -\theta_{G,1} + \theta_{W,1} + (\theta_{G,L_1} - \theta_{W,1})(1 - \exp(-K_1))/K_1. \tag{3.13c}$$

Equations (3.13a) to (3.13c) make up a nonlinear system of equations in the mean zone exhaust gas temperatures $\theta_{G,j}$ in which the fixed parameter vector $\boldsymbol{p} = (\boldsymbol{p}_\mathrm{ex}, \boldsymbol{p}_\mathrm{p}, \boldsymbol{p}_\mathrm{ev})$, the exhaust gas conditions $\boldsymbol{w}$ and the state vector $\boldsymbol{x}_\mathrm{ev}$ take part. From the latter, the components corresponding to the wall temperatures and the zone lengths are present. In turn, it will be seen later that $\dot{Q}_{GW,j}$ from Eq. (3.6a) also influences the wall temperature dynamics. Therefore, this general formulation gives rise to a DAE system [64]. However, the model can be evaluated in a computationally much less expensive way if the exhaust gas' specific heat capacities $c_{G,j}$, $j \in \{1,2,3\}$ are evaluated at each zone's upstream border, i.e. at $\theta_{G,j}^+$ [64]. instead of at $\theta_{G,j}$. Therewith, Eqs. (3.12) and (3.13) look like

$$\theta_{G,3} = \theta_{W,3} + (\theta_{G,\mathrm{in}} - \theta_{W,3})(1 - \exp(-K_3))/K_3, \tag{3.14a}$$

$$\theta_{G,L_1+L_2} = \theta_{W,3} + (\theta_{G,\mathrm{in}} - \theta_{W,3})\exp(-K_3), \tag{3.14b}$$

$$\theta_{G,2} = \theta_{W,2} + (\theta_{G,L_1+L_2} - \theta_{W,2})(1 - \exp(-K_2))/K_2, \tag{3.14c}$$

$$\theta_{G,L_1} = \theta_{W,2} + (\theta_{G,L_1+L_2} - \theta_{W,2})\exp(-K_2), \tag{3.14d}$$

$$\theta_{G,1} = \theta_{W,1} + (\theta_{G,L_1} - \theta_{W,1})(1 - \exp(-K_1))/K_1, \tag{3.14e}$$

and the exhaust gas temperatures $\theta_{G,j}$ can be sequentially evaluated as functions of $\boldsymbol{x}_\mathrm{ev}$, $\boldsymbol{p}$ and $\boldsymbol{w}$. Here $c_{G,j}$ is evaluated at $(p_G, \theta_{G,\mathrm{in}})$, $(p_G, \theta_{G,L_1+L_2})$ and (p_G, θ_{G,L_1}) for $j \in \{1,2,3\}$, respectively.

Wall Energy Balance

In the case of the wall, no mass transfer takes place, albeit its energy balance results of crucial importance at the same time. In the following it is assumed that the wall within each zone j, i.e. between $z = L_j^-$ and $z = L_j^+$, for $j \in \{1, 2, 3\}$, the wall possesses an infinite thermal conductivity. Thus, therein is temperature is homogeneous. We denote its value as $\theta_{W,j}$. Notwithstanding, the wall temperature is allowed to be discontinuous at the zone boundaries, although we neglect heat conduction between zones.

Similar to the exhaust gas energy balance, we consider a toroidal control volume over the wall in zone j of length $\mathrm{d}z$, internal diameter d_i and external diameter d_o at position z and write down Eq. (2.9). Both the geometry and the convention directions for positive heat transfer are depicted in Fig. 3.4. No work is done, and the only heat transfers with the surroundings are with the exhaust gas and the working fluid.
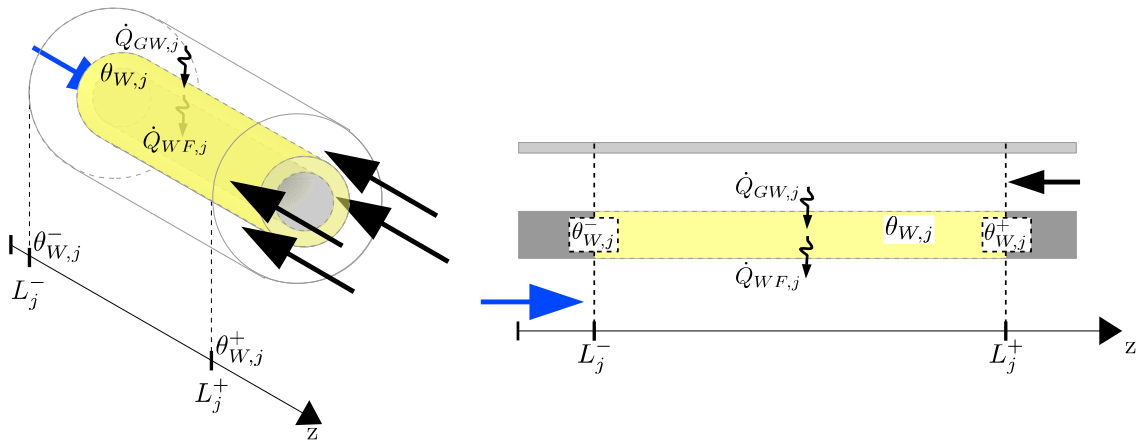
Figure 3.4: Volume control for the wall energy balance

Additionally, since the control volume corresponds to a solid, its internal energy $\mathrm{d}U_j$ can be expressed as a function of temperature as

$$\mathrm{d}U_j = \varrho_W c_W \theta_{W,j} \mathrm{d}V \tag{3.15}$$

Ergo, for the volume corresponding to zone j,

$$U_j = \int_{z=L_j^-}^{z=L_j^+} \int_{r=d_i/2}^{r=d_o/2} \int_{\varphi=0}^{\varphi=2\pi} \varrho_W c_W \theta_{W,j} r \,\mathrm{d}\varphi \,\mathrm{d}r \,\mathrm{d}z = \varrho_W c_W A_W \theta_{W,j} L_j. \tag{3.16}$$

Additionally, if the control volume boundaries change with time, a different amount of mass will be contained within them. Concretely, if the wall is found at a temperature $\theta_{W,j}^+$ at the boundary corresponding to L_j^+, the specific enthalpy associated to it corresponds to

$$h_j^+ = c_W \theta_{W,j}^+. \tag{3.17}$$

Additionally, if L_j^+ changes with rate $\frac{\mathrm{d}L_j^+}{\mathrm{d}t}$, the equivalent increment in the system's mass corresponds to

$$\dot{m}_j^+ = \varrho_W A_W \frac{\mathrm{d}L_j^+}{\mathrm{d}t}. \tag{3.18}$$

An analogous reasoning can be used for the other boundary position, L_j^-, associated to a temperature $\theta_{W,j}^-$. This leads to the wall energy balance from Eq. (2.9):

$$\varrho_W A_W c_W \frac{\mathrm{d}\theta_{W,j}}{\mathrm{d}t} = \dot{Q}_{GW,j} - \dot{Q}_{WF,j} + \varrho_W A_W c_W \theta_{W,j}^+ \frac{\mathrm{d}L_j^+}{\mathrm{d}t} - \varrho_W A_W c_W \theta_{W,j}^- \frac{\mathrm{d}L_j^-}{\mathrm{d}t}. \tag{3.19}$$

Equation (3.19) applies to all zones, recognizing that $\frac{\mathrm{d}L_1^-}{\mathrm{d}t} = 0$ and $\frac{\mathrm{d}L_3^+}{\mathrm{d}t} = 0$, with which $\theta_{W,1}^-$ and $\theta_{W,3}^+$ lose relevance, and that $\theta_{W,j}^+ = \theta_{W,j+1}^-$ for $j \in \{1,2\}$, so we can rebaptize $\theta_{W,L_1} \overset{\text{def}}{=} \theta_{W,1}^+$ and $\theta_{W,L_1+L_2} \overset{\text{def}}{=} \theta_{W,2}^+$.
Concretely, we have

$$\varrho_W A_W c_W \left(L_1 \frac{\mathrm{d}\theta_{W,1}}{\mathrm{d}t} + (\theta_{W,1} - \theta_{W,L_1})\frac{\mathrm{d}L_1}{\mathrm{d}t} \right) = \dot{Q}_{GW,1} - \dot{Q}_{WF,1}, \tag{3.20a}$$

$$\varrho_W A_W c_W \left(L_2 \frac{\mathrm{d}\theta_{W,2}}{\mathrm{d}t} + (\theta_{W,L_1} - \theta_{W,L_1+L_2})\frac{\mathrm{d}L_1}{\mathrm{d}t} + (\theta_{W,2} - \theta_{W,L_1+L_2})\frac{\mathrm{d}L_2}{\mathrm{d}t} \right) = \dot{Q}_{GW,2} - \dot{Q}_{WF,2}, \tag{3.20b}$$

$$\varrho_W A_W c_W \left(L_3 \frac{\mathrm{d}\theta_{W,3}}{\mathrm{d}t} + (\theta_{W,L_1+L_2} - \theta_{W,3})\frac{\mathrm{d}}{\mathrm{d}t}(L_1 + L_2) \right) = \dot{Q}_{GW,3} - \dot{Q}_{WF,3}, \tag{3.20c}$$

Remark 3.2.2 *Regarding the choice of the wall boundary temperatures θ_{W,L_1} and θ_{W,L_1+L_2}, a number of alternatives are available in the literature, and some of them are discussed in [77]. All alternatives have advantages and disadvantages regarding physical criteria such as energy conservation and numerical criteria such as dynamic chattering or undesired transients. The choice made by [77] is based on the fulfillment of energy conservation, in spite of the modelled behavior being against the measured trends. Moreover this choice, namely*

$$\theta_{W,L_1} = \begin{cases} \theta_{W,1} & \text{if} \quad \frac{\mathrm{d}}{\mathrm{d}t}L_1 < 0 \\ \theta_{W,2} & \text{if} \quad \frac{\mathrm{d}}{\mathrm{d}t}L_1 \geqslant 0 \end{cases} \quad \theta_{W,L_1+L_2} = \begin{cases} \theta_{W,2} & \text{if} \quad \frac{\mathrm{d}}{\mathrm{d}t}(L_1+L_2) < 0 \\ \theta_{W,3} & \text{if} \quad \frac{\mathrm{d}}{\mathrm{d}t}(L_1+L_2) \geqslant 0 \end{cases}, \tag{3.21}$$

has the structural drawbacks of introducing both an implicit nonlinear dependency on the state derivatives and a source of nondifferentiability in the model. Both drawbacks can be tackled by formulating the model structure as a fully-implicit DAE and introducing mixed-integer programming techniques, however [77] also shows that other alternatives such as Eq. (3.5) (this work's choice) yield similar results. In contrast to Eq. (3.21), our choice does not introduce nondifferentiabilities and does not involve the state derivatives in a nonlinear fashion. It has been observed that model evaluations are performed significantly faster using this variant.

Working Fluid Energy and Mass Balances

In the following analysis, we consider mass and energy balances for zone j. For these means, a cylindrical control volume is considered as in Fig. 3.5. We begin by the mass balance, considering Eq. (2.3).
The total working fluid mass contained in the control volume corresponds to

$$m_j = \int_{z=L_j^-}^{z=L_j^+} \int_{r=0}^{r=d_\text{i}/2} \int_{\varphi=0}^{\varphi=2\pi} \varrho(r,\varphi,z) r \,\mathrm{d}\varphi \,\mathrm{d}r \,\mathrm{d}z$$
$$= AL_j \bar{\varrho}_j, \tag{3.22}$$

On the other hand, the mass transfer to the control volume and viceversa has two sources. One, associated to advecting terms corresponding to mass transfer crossing the boundaries,
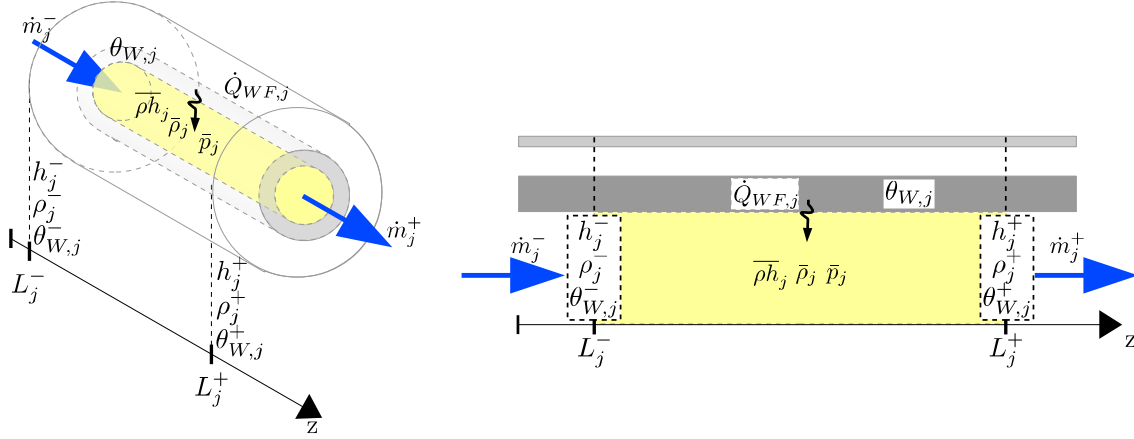
Figure 3.5: Control volume for the working fluid in zone j. The arrows indicate heat and mass transfer positive sign conventions.

described as $\dot{m}_j^-$ and $\dot{m}_j^+$, and another one due to the displacement of the boundaries itself. Similar to the analysis performed to obtain Eq. (3.18), if boundaries L_j^+ and L_j^- move with speed $\frac{\mathrm{d}L_j^+}{\mathrm{d}t}$ and $\frac{\mathrm{d}L_j^-}{\mathrm{d}t}$, and the fluid densities therein correspond to ϱ_j^+ and ϱ_j^-, respectively, the mass conservation principle applied to zone j reads

$$\frac{\mathrm{d}}{\mathrm{d}t}\left(AL_j\bar{\varrho}_j\right) = \dot{m}_j^- - A\varrho_j^-\frac{\mathrm{d}L_j^-}{\mathrm{d}t} - \dot{m}_j^+ + A\varrho_j^+\frac{\mathrm{d}L_j^+}{\mathrm{d}t}. \tag{3.23}$$

Likewise, from Eq. (2.8) we have that, the working fluid's internal energy per unit volume corresponds to

$$\varrho u = \varrho h - p.$$

Therefore, the internal energy contained inside the control volume is

$$U_j = \int_{z=L_j^-}^{z=L_j^+} \int_{r=0}^{r=d_\mathrm{i}/2} \int_{\varphi=0}^{\varphi=2\pi} (\varrho h(r,\varphi,z) - p)r\,\mathrm{d}\varphi\,\mathrm{d}r\,\mathrm{d}z$$
$$= AL_j(\overline{\varrho h}_j - \bar{p}_j). \tag{3.24}$$

Since the wall is considered rigid, the control volume performs no work on its surroundings. Besides, the heat transfer at the boundary corresponds to $\dot{Q}_{WF,j}$. The energy transfer terms by advection, if the fluid enters the control volume at L_j^- with enthalpy h_j^- and massflow $\dot{m}_j^-$, and leaves it at L_j^+ with enthalpy h_j^+ and massflow $\dot{m}_j^+$, are given by $\dot{m}_j^- h_j^-$ and $\dot{m}_j^+ h_j^+$. The boundaries' movement, which takes place at speeds $\frac{\mathrm{d}L_j^+}{\mathrm{d}t}$ and $\frac{\mathrm{d}L_j^-}{\mathrm{d}t}$, respectively, produces changes in the accumulated energy given by $A(\varrho_j^+ h_j^+ - p)\frac{\mathrm{d}L_j^+}{\mathrm{d}t}$ and $A(\varrho_j^- h_j^- - p)\frac{\mathrm{d}L_j^-}{\mathrm{d}t}$. Therewith, the energy conservation for the control volume reads

$$\frac{\mathrm{d}}{\mathrm{d}t}\left(AL_j(\overline{\varrho h}_j - \bar{p}_j)\right) = \dot{Q}_{WF,j} + \dot{m}_j^- h_j^- + A(\varrho_j^+ h_j^+ - \bar{p}_j)\frac{\mathrm{d}L_j^+}{\mathrm{d}t} - \dot{m}_j^+ h_j^+ - A(\varrho_j^- h_j^- - \bar{p}_j)\frac{\mathrm{d}L_j^-}{\mathrm{d}t}. \tag{3.25}$$

The next step in the formulation is to identify the terms in Eqs. (3.23) and (3.25) for each zone, which is done in Table 3.1. Notice that densities ϱ_1^- and ϱ_3^+ are not needed due to the fact that their respective borders are fixed, and thus are not evaluated. On the other hand, the following equalities hold, and the involved terms are assigned the quantities in parenthesis.

From those, the only ones not introduced thus far are $\dot{m}'$ and $\dot{m}''$. Expressions for them in terms of the other terms are given briefly.

$$\dot{m}_1^+ = \dot{m}_2^- \quad (\overset{\text{def}}{=} \dot{m}'), \qquad\qquad \dot{m}_2^+ = \dot{m}_3^- \quad (\overset{\text{def}}{=} \dot{m}''),$$

$$\varrho_1^+ = \varrho_2^- \quad (\overset{\text{def}}{=} \varrho'), \qquad\qquad \varrho_2^+ = \varrho_3^- \quad (\overset{\text{def}}{=} \varrho''),$$

$$h_1^+ = h_2^- \quad (\overset{\text{def}}{=} h'), \qquad\qquad h_2^+ = h_3^- \quad (\overset{\text{def}}{=} h''),$$

$$L_1^+ = L_2^-, \qquad\qquad\qquad L_2^+ = L_3^-.$$

Table 3.1: Term identification for the working fluid energy and mass balances for all three zones

Symbol	Zone 1	Zone 2	Zone 3
$\dot{m}_j^-$	$\dot{m}_{\text{in}}$	$\dot{m}'$	$\dot{m}''$
$\dot{m}_j^+$	$\dot{m}'$	$\dot{m}''$	$\dot{m}_{\text{out}}$
ϱ_j^-	——	ϱ'	ϱ''
ϱ_j^+	ϱ'	ϱ''	——
L_j^-	0	L_1	$L_1 + L_2$
L_j^+	L_1	$L_1 + L_2$	L
$\frac{\mathrm{d}}{\mathrm{d}t} L_j^-$	0	$\frac{\mathrm{d}}{\mathrm{d}t} L_1$	$\frac{\mathrm{d}}{\mathrm{d}t}(L_1 + L_2)$
$\frac{\mathrm{d}}{\mathrm{d}t} L_j^+$	$\frac{\mathrm{d}}{\mathrm{d}t} L_1$	$\frac{\mathrm{d}}{\mathrm{d}t}(L_1 + L_2)$	0
h_j^-	h_B	h'	h''
h_j^+	h'	h''	h_C
$\overline{\varrho h}_j$	$\bar{\varrho}_1 \bar{h}_1$	$\overline{\varrho h}_2$	$\bar{\varrho}_3 \bar{h}_3$

The working fluid mass balances for each zone individually thus read:

- Zone 1:

$$\frac{\mathrm{d}}{\mathrm{d}t}(AL_1\bar{\varrho}_1) = \dot{m}_{\text{in}} - \dot{m}' + A\varrho'\frac{\mathrm{d}L_1}{\mathrm{d}t}. \tag{3.26}$$

- Zone 2:

$$\frac{\mathrm{d}}{\mathrm{d}t}(AL_2\bar{\varrho}_2) = \dot{m}' - A\varrho'\frac{\mathrm{d}L_1}{\mathrm{d}t} - \dot{m}'' + A\varrho''\frac{\mathrm{d}}{\mathrm{d}t}(L_1 + L_2). \tag{3.27}$$

- Zone 3:

$$\frac{\mathrm{d}}{\mathrm{d}t}(AL_3\bar{\varrho}_3) = \dot{m}'' - A\varrho''\frac{\mathrm{d}}{\mathrm{d}t}(L_1 + L_2) - \dot{m}_{\text{out}}. \tag{3.28}$$

On the other hand, the working fluid energy balances for each zone individually read

- Zone 1:

$$\frac{\mathrm{d}}{\mathrm{d}t}\left(AL_1(\bar{\varrho}_1\bar{h}_1 - \bar{p}_1)\right) = \dot{Q}_{WF,1} + \dot{m}_{\text{in}}h_B + A(\varrho'h' - \bar{p}_1)\frac{\mathrm{d}L_1}{\mathrm{d}t} - \dot{m}'h'. \tag{3.29}$$

- Zone 2:

$$\frac{\mathrm{d}}{\mathrm{d}t}\left(AL_2(\overline{\varrho h}_2 - \bar{p}_2)\right) = \dot{Q}_{WF,2} + \dot{m}'h' + A(\varrho''h'' - \bar{p}_2)\frac{\mathrm{d}}{\mathrm{d}t}(L_1 + L_2) - \dot{m}''h'' - A(\varrho'h' - \bar{p}_2)\frac{\mathrm{d}L_1}{\mathrm{d}t}. \quad (3.30)$$

- Zone 3:

$$\frac{\mathrm{d}}{\mathrm{d}t}\left(AL_3(\bar{\varrho}_3\bar{h}_3 - \bar{p}_3)\right) = \dot{Q}_{WF,3} + \dot{m}''h'' - \dot{m}_{\mathrm{out}}h_C - A(\varrho''h'' - \bar{p}_3)\frac{\mathrm{d}}{\mathrm{d}t}(L_1 + L_2). \quad (3.31)$$

From Eqs. (3.26) and (3.28) expressions for both $\dot{m}'$ and $\dot{m}''$ in terms of already defined terms can be obtained:

$$\dot{m}' = \dot{m}_{\mathrm{in}} - \frac{\mathrm{d}}{\mathrm{d}t}(AL_1\bar{\varrho}_1) + A\varrho'\frac{\mathrm{d}L_1}{\mathrm{d}t}, \quad (3.32)$$

$$\dot{m}'' = \dot{m}_{\mathrm{out}} + \frac{\mathrm{d}}{\mathrm{d}t}(AL_3\bar{\varrho}_3) + A\varrho''\frac{\mathrm{d}}{\mathrm{d}t}(L_1 + L_2). \quad (3.33)$$

These expressions can be used in Eqs. (3.29) to (3.31) to eliminate these quantities. Additionally, Eqs. (3.26) to (3.28) can be summed up to produce the working fluid's global mass balance. After some algebra, the evaporator dynamics can be then summarized in the following equations:

From mass conservation of the working fluid along the tube, we have

$$\frac{\mathrm{d}}{\mathrm{d}t}\left(\sum_{j=1}^{3} AL_j\bar{\varrho}_j\right) = \dot{m}_{\mathrm{in}} - \dot{m}_{\mathrm{out}}. \quad (3.34)$$

Energy conservation for the working fluid for the subcooled liquid zone yields

$$\frac{\mathrm{d}}{\mathrm{d}t}\left(AL_1(\bar{\varrho}_1\bar{h}_1 - \bar{p}_1)\right) - h'\frac{\mathrm{d}}{\mathrm{d}t}(AL_1\bar{\varrho}_1) + A\bar{p}_1\frac{\mathrm{d}L_1}{\mathrm{d}t} = \dot{Q}_{WF,1} - \dot{m}_{\mathrm{in}}\left(h' - h_B\right). \quad (3.35)$$

Energy conservation for the working fluid for the mixed zone yields

$$\frac{\mathrm{d}}{\mathrm{d}t}\left(AL_2(\overline{\varrho h}_2 - \bar{p}_2)\right) + h'\frac{\mathrm{d}}{\mathrm{d}t}(AL_1\bar{\varrho}_1) + h''\frac{\mathrm{d}}{\mathrm{d}t}(AL_3\bar{\varrho}_3) + A\bar{p}_2\frac{\mathrm{d}L_2}{\mathrm{d}t} = \dot{Q}_{WF,2} - \left(\dot{m}_{\mathrm{out}}h'' - \dot{m}_{\mathrm{in}}h'\right). \quad (3.36)$$

For the superheated vapor zone, energy conservation leads to

$$\frac{\mathrm{d}}{\mathrm{d}t}\left(AL_3(\bar{\varrho}_3\bar{h}_3 - \bar{p}_3)\right) - h''\frac{\mathrm{d}}{\mathrm{d}t}(AL_3\bar{\varrho}_3) + A\bar{p}_3\frac{\mathrm{d}L_3}{\mathrm{d}t} = \dot{Q}_{WF,3} - \dot{m}_{\mathrm{out}}\left(h_C - h''\right). \quad (3.37)$$

Equations (3.34) to (3.37) can be further expanded to yield expressions depending only on the components of $\boldsymbol{x}_{\mathrm{ev}}$ and the fixed parameters. For those means, we require the following derivatives:

$$\frac{\mathrm{d}\bar{h}_1}{\mathrm{d}t}(p_{\mathrm{ev}}) = \frac{1}{2}\left[\left.\frac{\mathrm{d}h_B}{\mathrm{d}p_B}\right|_{p_{\mathrm{ev}}} + \left.\frac{\mathrm{d}h'}{\mathrm{d}p_{\mathrm{ev}}}\right|_{p_{\mathrm{ev}}}\right]\frac{\mathrm{d}p_{\mathrm{ev}}}{\mathrm{d}t}, \quad (3.38a)$$

$$\frac{\mathrm{d}\bar{h}_3}{\mathrm{d}t}(p_{\mathrm{ev}}) = \frac{1}{2}\left[\left.\frac{\mathrm{d}h''}{\mathrm{d}p_{\mathrm{ev}}}\right|_{p_{\mathrm{ev}}}\frac{\mathrm{d}p_{\mathrm{ev}}}{\mathrm{d}t} + \frac{\mathrm{d}h_C}{\mathrm{d}t}\right], \quad (3.38b)$$

$$\frac{\partial\bar{\gamma}}{\partial\mu}(p_{\mathrm{ev}}) = \frac{2}{3}\left[\frac{(1+\mu^{2/3})\log(\mu^{2/3}) + 2(1-\mu^{2/3})}{\mu^{1/3}(1-\mu^{2/3})^3}\right], \quad (3.38c)$$

$$\frac{\mathrm{d}\mu}{\mathrm{d}p}(p_{\mathrm{ev}}) = \frac{1}{\varrho'^2}\left[\varrho'\frac{\mathrm{d}\varrho''}{\mathrm{d}p_{\mathrm{ev}}}\Big|_{p_{\mathrm{ev}}} - \varrho''\frac{\mathrm{d}\varrho'}{\mathrm{d}p_{\mathrm{ev}}}\Big|_{p_{\mathrm{ev}}}\right], \quad (3.38d)$$

$$\frac{\mathrm{d}\bar{\varrho}_1}{\mathrm{d}t}(p_{\mathrm{ev}}, \bar{h}_1) = \left[\frac{\partial \varrho_{\mathrm{subc.liq.}}}{\partial p}\bigg|_{(p_{\mathrm{ev}}, \bar{h}_1)} \frac{\mathrm{d}p_{\mathrm{ev}}}{\mathrm{d}t} + \frac{\partial \varrho_{\mathrm{subc.liq.}}}{\partial h}\bigg|_{(p_{\mathrm{ev}}, \bar{h}_1)} \frac{\mathrm{d}\bar{h}_1}{\mathrm{d}t} \right], \tag{3.38e}$$

$$\frac{\mathrm{d}\bar{\varrho}_2}{\mathrm{d}t}(p_{\mathrm{ev}}) = \left[(1 - \bar{\gamma}) \frac{\mathrm{d}\varrho'}{\mathrm{d}p_{\mathrm{ev}}}\bigg|_{p_{\mathrm{ev}}} + \bar{\gamma} \frac{\mathrm{d}\varrho''}{\mathrm{d}p_{\mathrm{ev}}}\bigg|_{p_{\mathrm{ev}}} + (\varrho'' - \varrho') \frac{\partial \bar{\gamma}}{\partial \mu} \frac{\mathrm{d}\mu}{\mathrm{d}p}\bigg|_{p_{\mathrm{ev}}} \right] \frac{\mathrm{d}p_{\mathrm{ev}}}{\mathrm{d}t}, \tag{3.38f}$$

$$\frac{\mathrm{d}\bar{\varrho}_3}{\mathrm{d}t}(p_{\mathrm{ev}}, \bar{h}_3) = \left[\frac{\partial \varrho_{\mathrm{suph.vap.}}}{\partial p}\bigg|_{(p_{\mathrm{ev}}, \bar{h}_3)} \frac{\mathrm{d}p_{\mathrm{ev}}}{\mathrm{d}t} + \frac{\partial \varrho_{\mathrm{suph.vap.}}}{\partial h}\bigg|_{(p_{\mathrm{ev}}, \bar{h}_3)} \frac{\mathrm{d}\bar{h}_3}{\mathrm{d}t} \right], \tag{3.38g}$$

$$\frac{\mathrm{d}\varrho' h'}{\mathrm{d}p_{\mathrm{ev}}}(p_{\mathrm{ev}}) = h' \frac{\mathrm{d}\varrho'}{\mathrm{d}p_{\mathrm{ev}}}\bigg|_{p_{\mathrm{ev}}} + \varrho' \frac{\mathrm{d}h'}{\mathrm{d}p_{\mathrm{ev}}}\bigg|_{p_{\mathrm{ev}}}, \tag{3.38h}$$

$$\frac{\mathrm{d}\varrho'' h''}{\mathrm{d}p_{\mathrm{ev}}}(p_{\mathrm{ev}}) = h'' \frac{\mathrm{d}\varrho''}{\mathrm{d}p_{\mathrm{ev}}}\bigg|_{p_{\mathrm{ev}}} + \varrho'' \frac{\mathrm{d}h''}{\mathrm{d}p_{\mathrm{ev}}}\bigg|_{p_{\mathrm{ev}}}, \tag{3.38i}$$

$$\frac{\mathrm{d}(\overline{\varrho h_2})}{\mathrm{d}t}(p_{\mathrm{ev}}) = \left[(1 - \bar{\gamma}) \frac{\mathrm{d}\varrho' h'}{\mathrm{d}p_{\mathrm{ev}}}\bigg|_{p_{\mathrm{ev}}} + \bar{\gamma} \frac{\mathrm{d}\varrho'' h''}{\mathrm{d}p_{\mathrm{ev}}}\bigg|_{p_{\mathrm{ev}}} + (\varrho'' h'' - \varrho' h') \frac{\partial \bar{\gamma}}{\partial \mu} \frac{\mathrm{d}\mu}{\mathrm{d}p}\bigg|_{p_{\mathrm{ev}}} \right] \frac{\mathrm{d}p_{\mathrm{ev}}}{\mathrm{d}t}. \tag{3.38j}$$

It can be seen that both p_{ev} and h_C have a particular importance as the most relevant functions include them as arguments. Inserting Eq. (3.38) into Eqs. (3.34) to (3.37), performing the required algebra[4] and joining with Eqs. (3.20a) to (3.20c), we obtain a semi-implicit ODE system with the structure

$$M_{\mathrm{ev}}(x_{\mathrm{ev}}, p) \frac{\mathrm{d}x_{\mathrm{ev}}}{\mathrm{d}t} = b_{\mathrm{ev}}(x_{\mathrm{ev}}, u, p, w).$$

Matrix m_{ev} and vector b_{ev} have the following structure,

$$M_{\mathrm{ev}}(x_{\mathrm{ev}}, p) = \begin{bmatrix} M_{1,1} & M_{1,2} & M_{1,3} & M_{1,4} & 0 & 0 & 0 \\ M_{2,1} & 0 & M_{2,3} & 0 & 0 & 0 & 0 \\ M_{3,1} & M_{3,2} & M_{3,3} & 0 & 0 & 0 & 0 \\ M_{4,1} & M_{4,2} & M_{4,3} & M_{4,4} & 0 & 0 & 0 \\ M_{5,1} & 0 & 0 & 0 & M_{5,5} & 0 & 0 \\ M_{6,1} & M_{6,2} & 0 & 0 & 0 & M_{6,6} & 0 \\ M_{7,1} & M_{7,2} & 0 & 0 & 0 & 0 & M_{7,7} \end{bmatrix}, \tag{3.39a}$$

$$b_{\mathrm{ev}}(x_{\mathrm{ev}}, u, p, w) = \begin{bmatrix} b_1 & b_2 & b_3 & b_4 & b_5 & b_5 & b_7 \end{bmatrix}^T, \tag{3.39b}$$

where the entries correspond to the following expressions: From mass conservation of the working fluid along the inner tube, we have

$$M_{1,1} = A(\bar{\varrho}_1 - \bar{\varrho}_3) \tag{3.40a}$$

$$M_{1,2} = A(\varrho' + \bar{\gamma}(\varrho'' - \varrho') - \bar{\varrho}_3) \tag{3.40b}$$

$$M_{1,3} = A\left[L_1\left(\frac{\partial \bar{\varrho}_1}{\partial \bar{p}_1} + \frac{1}{2}\frac{\partial \bar{\varrho}_1}{\partial \bar{h}_1}\left(\frac{\mathrm{d}h'}{\mathrm{d}p_{\mathrm{ev}}} + \frac{\mathrm{d}h_B}{\mathrm{d}p_B} \right) \right) \right. \tag{3.40c}$$

$$\left. + L_2\left(\frac{\mathrm{d}\varrho'}{\mathrm{d}p_{\mathrm{ev}}} + \bar{\gamma}(\frac{\mathrm{d}\varrho''}{\mathrm{d}p_{\mathrm{ev}}} - \frac{\mathrm{d}\varrho'}{\mathrm{d}p_{\mathrm{ev}}}) + (\varrho'' - \varrho')\frac{\partial \bar{\gamma}}{\partial \mu}\frac{\mathrm{d}\mu}{\mathrm{d}p} \right) \right.$$

$$\left. + L_3\left(\frac{\partial \bar{\varrho}_3}{\partial \bar{p}_3} + \frac{1}{2}\frac{\partial \bar{\varrho}_3}{\partial \bar{h}_3}\frac{\mathrm{d}h''}{\mathrm{d}p_{\mathrm{ev}}} \right) \right]$$

$$M_{1,4} = \frac{1}{2}AL_3\frac{\partial \bar{\varrho}_3}{\partial \bar{h}_3} \tag{3.40d}$$

$$b_1 = \dot{m}_{\mathrm{in}} - \dot{m}_{\mathrm{out}}, \tag{3.40e}$$

Applying energy conservation to the working fluid for the subcooled liquid phase zone yields

$$M_{2,1} = \frac{1}{2} A \bar{\varrho}_1 \left(h_B - h' \right) \tag{3.41a}$$

$$M_{2,3} = A L_1 \left(\frac{1}{2}(h_B - h') \frac{\partial \bar{\varrho}_1}{\partial \bar{p}_1} + \frac{1}{2}(\bar{\varrho}_1 + \frac{1}{2}(h_B - h') \frac{\partial \bar{\varrho}_1}{\partial \bar{h}_1})(\frac{dh_B}{dp_B} + \frac{dh'}{dp_{ev}}) - 1 \right) \tag{3.41b}$$

$$M_{2,3} = A L_1 \left(\frac{1}{2}(h_B - h') \frac{\partial \bar{\varrho}_1}{\partial \bar{p}_1} + \frac{1}{2}(\bar{\varrho}_1 + (h_B - h') \frac{\partial \bar{\varrho}_1}{\partial \bar{h}_1})(\frac{dh_B}{dp_B} + \frac{dh'}{dp_{ev}}) - 1 \right) \tag{3.41c}$$

$$b_2 = \dot{Q}_{WF,1} + \dot{m}_{in} \left(h_B - h' \right). \tag{3.41d}$$

Energy conservation for the working fluid for the mixed phase yields

$$M_{3,1} = A(\bar{\varrho}_1 h' - \bar{\varrho}_3 h'') \tag{3.42a}$$

$$M_{3,2} = A \left(\varrho' h' + \bar{\gamma}(\varrho'' h'' - \varrho' h') - \bar{\varrho}_3 h'' \right) \tag{3.42b}$$

$$M_{3,3} = A \left[L_1 h' \left(\frac{\partial \bar{\varrho}_1}{\partial \bar{p}_1} + \frac{\partial \bar{\varrho}_1}{\partial \bar{h}_1} \frac{1}{2}(\frac{dh'}{dp_{ev}} + \frac{dh_B}{dp_B}) \right) \right. \tag{3.42c}$$

$$+ L_2 \left(\frac{d\varrho' h'}{dp_{ev}} + \bar{\gamma}(\frac{d\varrho'' h''}{dp_{ev}} - \frac{d\varrho' h'}{dp_{ev}}) + (\varrho'' h'' - \varrho' h') \frac{\partial \bar{\gamma}}{\partial \mu} \frac{d\mu}{dp} - 1 \right)$$

$$\left. + L_3 h'' \left(\frac{\partial \bar{\varrho}_3}{\partial \bar{p}_3} + \frac{1}{2} \frac{\partial \bar{\varrho}_3}{\partial \bar{h}_3} \frac{dh''}{dp_{ev}} \right) \right]$$

$$b_3 = \dot{m}_{in} h' - \dot{m}_{out} h'' + \dot{Q}_{WF,2}. \tag{3.42d}$$

For the gas phase, energy conservation leads to

$$M_{4,1} = \frac{1}{2} A \bar{\varrho}_3 (h'' - h_C) \tag{3.43a}$$

$$M_{4,2} = \frac{1}{2} A \bar{\varrho}_3 (h'' - h_C) \tag{3.43b}$$

$$M_{4,3} = A L_3 \left(\frac{1}{2}(h_C - h'') \frac{\partial \bar{\varrho}_3}{\partial \bar{p}_3} + \frac{1}{2} \frac{dh''}{dp_{ev}}(\bar{\varrho}_3 + \frac{1}{2}(h_C - h'') \frac{\partial \bar{\varrho}_3}{\partial \bar{h}_3}) - 1 \right) \tag{3.43c}$$

$$M_{4,4} = \frac{1}{2} A L_3 \left(\bar{\varrho}_3 + \frac{1}{2}(h_C - h'') \frac{\partial \bar{\varrho}_3}{\partial \bar{h}_3} \right) \tag{3.43d}$$

$$b_4 = \dot{m}_{out} \left(h'' - h_C \right) + \dot{Q}_{WF,3}. \tag{3.43e}$$

For the energy balance in the inner tube itself holds, for the first region,

$$M_{5,1} = \varrho_W A_W c_W (\theta_{W,1} - \theta_{W,L_1}) \tag{3.44a}$$

$$M_{5,5} = \varrho_W A_W c_W L_1 \tag{3.44b}$$

$$b_5 = \dot{Q}_{GW,1} - \dot{Q}_{WF,1}. \tag{3.44c}$$

The second region yields

$$M_{6,1} = \varrho_W A_W c_W (\theta_{W,L_1} - \theta_{W,L_1+L_2}) \tag{3.45a}$$

$$M_{6,2} = \varrho_W A_W c_W (\theta_{W,2} - \theta_{W,L_1+L_2}) \tag{3.45b}$$

$$M_{6,6} = \varrho_W A_W c_W L_2 \tag{3.45c}$$

$$b_6 = \dot{Q}_{GW,2} - \dot{Q}_{WF,2}. \tag{3.45d}$$

In the third region, the energy balance leads to the terms

$$M_{7,1} = \varrho_W A_W c_W (\theta_{W,L_1+L_2} - \theta_{W,3}) \tag{3.46a}$$

$$M_{7,2} = \varrho_W A_W c_W (\theta_{W,L_1+L_2} - \theta_{W,3}) \tag{3.46b}$$

$$M_{7,7} = \varrho_W A_W c_W L_3 \tag{3.46c}$$

$$b_7 = \dot{Q}_{GW,3} - \dot{Q}_{WF,3}. \tag{3.46d}$$

3.2.5 Model Reduction

As discussed in [168], for high molecular weight organic fluids the ORC's maximum efficiency is obtained when the working fluid is in a saturated vapor state at the expander inlet. In particular, this means it is desired that the third zone fades out ($L_3 = 0$, $h_C = h''$) and only the first two-zones become active in the model. From Eqs. (3.40d), (3.43d) and (4.39) it is possible to see that matrix m_{ev} becomes singular when this takes place. On the other hand, in practice, the working fluid is still superheated by a small amount in order to give the system a security margin in case unexpected disturbances push the working fluid thermodynamic state at the expander inlet towards the vapor dome. On the one hand, it is possible to model this security margin as a hard constraint on L_3, to be introduced in Section 3.5.1. In spite of that, external disturbances or the trial of some control function values during computations may still cause L_3 to fade out with the consequent numerical difficuties implied by m_{ev}'s rank loss. The model can be thus further robustified by introducing the following model reduction: assume that the working fluid at zone 3 is found in a thermodynamic steady state. Concretely, time derivatives are eliminated from Eqs. (3.28) and (3.31) to produce

- Zone 3's steady state mass balance:

$$0 = \dot{m}'' - \dot{m}_{out}, \tag{3.47}$$

- Zone 3's steady state energy balance:

$$0 = \dot{Q}_{WF,3} + \dot{m}'' h'' - \dot{m}_{out} h_C. \tag{3.48}$$

With these changes, performing similar algebraic steps, Eqs. (3.34) to (3.37) become

$$\frac{d}{dt}\left(\sum_{j=1}^{2} AL_j \bar{\varrho}_j\right) - A\varrho'' \frac{d}{dt}(L_1 + L_2) = \dot{m}_{in} - \dot{m}_{out} \tag{3.49}$$

$$\frac{d}{dt}\left(AL_1(\bar{\varrho}_1 \bar{h}_1 - \bar{p}_1)\right) - h' \frac{d}{dt}(AL_1 \bar{\varrho}_1) + A\bar{p}_1 \frac{dL_1}{dt} = \dot{Q}_{WF,1} - \dot{m}_{in}(h' - h_B) \tag{3.50}$$

$$\frac{d}{dt}\left(AL_2(\overline{\varrho h}_2 - \bar{p}_2)\right) + h' \frac{d}{dt}(AL_1 \bar{\varrho}_1) + A\varrho'' h'' \frac{dL_3}{dt} + A\bar{p}_2 \frac{dL_2}{dt} = \dot{Q}_{WF,2} - (\dot{m}_{out} h'' - \dot{m}_{in} h') \tag{3.51}$$

$$0 = \dot{Q}_{WF,3} - \dot{m}_{out}(h_C - h''). \tag{3.52}$$

Eqs. (3.20a) to (3.20c) and (3.49) to (3.52) form a nonlinear semi-implicit DAE system with differential state vector $x = (L_1, L_2, p_{ev}, \theta_{W,1}, \theta_{W,2}, \theta_{W,3})$, algebraic state vector $z = (h_C)$, control vector u and external input vector w. The system's only algebraic equation corresponds

to (3.52), whose left-hand side is denoted as $g(x, z, p)$. The system structure is

$$M(x(t), z(t), p) \frac{\mathrm{d}x}{\mathrm{d}t}(t) = b(x(t), z(t), u(t), p, w(t)), \tag{3.53a}$$

$$0 = g(x(t), z(t), p), \tag{3.53b}$$

$$x(t_0) = x_0. \tag{3.53c}$$

This formulation is advantageous since no terms multiplied by L_3 are present in M and hence it doesn't undergo rank loss, even if L_3 approaches zero. The output enthalpy h_C remains on the superheated vapor zone as long as $L_3 > 0$ and the corresponding wall temperature remains higher than the mean working fluid temperature.

This DAE system is of index 1, highly nonlinear, and stiff. Concrete model parameter values used in this thesis are given in Chapter 5.

3.2.6 Model Outputs

Besides the model's dynamic equations, we are interested on two kind of output functions. On the one hand, the *model measurements* are defined as

$$y(x, z, w, p) = \begin{bmatrix} p_{\mathrm{ev}}, & \theta_C, & \theta_{G,\mathrm{out}} \end{bmatrix}^T, \tag{3.54}$$

with $\theta_{G,\mathrm{out}}$ from Eq. (3.12c), and $\theta_C = \theta_C(p_{\mathrm{ev}}, h_C)$ is evaluated as explained in Section 3.3. This measurement vector will be used for the state estimator defined in Section 3.5.3. On the other hand, the *superheating* has been used by several authors (see e.g. [131, 167, 46]). It is defined as

$$y^{\mathrm{SH}}(x, z) = \theta_C(p_{\mathrm{ev}}, h_C) - \theta_{F,2}(p_{\mathrm{ev}}), \tag{3.55}$$

and will be retaken in Section 4.3, when alternative controllers are introduced. and is particularly useful for

3.3 Evaluation of Thermophysical Properties and External Inputs

In order to evaluate functions M, b and g in (3.53), it is necessary to evaluate the thermophysical properties corresponding to the exhaust gas and the working fluid. For the latter, properties may correspond to single-phase or saturated states (see Chapter 2). In this thesis, properties corresponding to single-phase states are evaluated using pressure-enthalpy (p, h) and pressure-entropy (p, s) pairs, whereas properties corresponding to saturated states, and the two-phase state temperature, are evaluated using the pressure p. The working fluid corresponds to ethanol. Additionally, the external inputs are considered as functions of time. Table 3.2 summarizes all quantities to evaluate, their nature and dependencies. For the exhaust gas a mixture of 74% nitrogen, 13% CO_2 and 13% water vapor is considered. Since it is a single-phase fluid, the pressure-temperature pair (p, θ) is used for evaluations.

As explained in Section 2.5.3, it is possible to evaluate the required thermophysical properties using the software REFPROP [93]. One option would be to resort to this software every time functions M, b and g are evaluated. In order to achieve evaluation speed gains, our course of action is as follows: REFPROP is used only once, offline, to calculate the properties' values for selected fixed values of pressure, temperature, entropy and enthalpy as appropriate. Afterwards, suitable functions are obtained that represent the data. The model implementation makes use of those functions to evaluate the thermophysical properties as required. Important

Table 3.2: Thermophysical properties and their evaluation arguments

Working fluid: Single-phase states		Working fluid: Saturated and two-phase states	
Property	Evaluated at	Property	Evaluated at
$\theta_{F,1}, \bar{\varrho}_1, \partial \bar{\varrho}_1/\partial \bar{p}_1, \partial \bar{\varrho}_1/\partial \bar{h}_1$	$(\bar{p}_1, \bar{h}_1)$	$h', h'', \varrho', \varrho''$	(p_{ev})
$\theta_{F,3}, \bar{\varrho}_3, \partial \bar{\varrho}_3/\partial \bar{p}_3, \partial \bar{\varrho}_3/\partial \bar{h}_3$	$(\bar{p}_3, \bar{h}_3)$	$\text{d}h'/\text{d}p_{\text{ev}}, \; \text{d}h''/\text{d}p_{\text{ev}},$	(p_{ev})
		$\text{d}\varrho'/\text{d}p_{\text{ev}}, \text{d}\varrho''/\text{d}p_{\text{ev}}$	
θ_C, ϱ_C, s_C	(p_C, h_C)	$\theta_{F,2}$	(p_{ev})
s_A	(p_A, h_A)	Exhaust gas properties	
$h_{D,\text{is}}$	(p_D, s_C)	Property	Evaluated at
$h_{B,\text{is}}, \partial h_{B,\text{is}}/\partial p_B$	(p_B, s_A)	$c_{G,1}$	$\left(p_G, \theta_{G,L_1}\right)$
External inputs		$c_{G,2}$	$\left(p_G, \theta_{G,L_1+L_2}\right)$
Property	Evaluated at	$c_{G,3}$	$\left(p_G, \theta_{G,\text{in}}\right)$
$\dot{m}_{G,\text{in}}$	(t)		
$\theta_{G,\text{in}}$	(t)		

speed gains can be obtained by proceeding this way if the representing functions are cheap to evaluate. Since piecewise linear and bilinear interpolation techniques have yielded poor results when combined with the algorithms to be presented in Section 4.1, an approach is proposed that uses cubic and bicubic splines to construct the representing functions. The approach builds upon [58], adding a new extrapolation feature.

3.3.1 Cubic and Bicubic Splines

Following the lines of [13, 33, 143], let the values of a function $f : [\tau_0, \tau_n] \subset \mathbb{R} \to \mathbb{R}^n$ at the mesh points $\pi \overset{\text{def}}{=} \{\tau_0 < \tau_1 < \ldots < \tau_n\}$ (also known as joints), be denoted as $y_i = f(\tau_i)$, and the values of its first derivatives at the borders $\text{d}f/\text{d}\tau(\tau_0)$ and $\text{d}f/\text{d}\tau(\tau_n)$, be known (the latter can be approximated by finite differences on the first and last intervals, respectively). The cubic spline $s(\tau; \pi, f) : [\tau_0, \tau_n] \subset \mathbb{R} \to \mathbb{R}^n$ interpolating such values (i.e. $s(\tau_i) = y_i \; \forall i \in \{0, \ldots, n\}$) is a piecewise cubic polynomial of class $\mathcal{C}^2[\tau_0, \tau_n]$ of the form

$$s(\tau; \pi, f) = \sum_{j=0}^{3} a_j^i (\tau - \tau_i)^j \quad \text{if } \tau \in [\tau_i, \tau_{i+1}], \text{ for some } i \in \{0, \ldots, n-1\}, \qquad (3.56)$$

with coefficients $a_j^i \in \mathbb{R}^n \; \forall j \in \{0, \ldots, 3\}$. In [33] it has been shown that there is exactly one cubic spline satisfying the aforementioned properties. Moreover, the set $S(\tau; \pi)$ of functions of class $\mathcal{C}^2$ on $[\tau_0, \tau_n]$ that are equal to cubic polynomials on each interval $[\tau_i, \tau_{i+1}]$ forms a linear space of dimension $n + 3$. Additionally, the spline $s(\tau; \pi, f)$ is the solution to the variational problem

$$\min_{u \in \mathcal{C}^2[\tau_0, \tau_n]} \int_{\tau_0}^{\tau_n} \left(\text{d}^2 u/\text{d}\tau^2(\tau)\right)^2 \text{d}\tau \qquad (3.57)$$
$$\text{s.t.} \quad u(\tau_i) = y_i, \quad \forall i \in \{1, \ldots, n\}.$$

This is an attractive property of the spline interpolation, since it is also related with the curvature of the interpolating function. The integral in Eq. (3.57) can be considered as a linearized

approximation to the strain energy of a thin beam,

$$\int_{\tau_0}^{\tau_n} \left(\frac{d^2u/d\tau^2}{(1+(du/d\tau)^2)^{3/2}}(\tau) \right)^2.$$

This result was proven by [70] for the case where the second derivatives at the borders $d^2f/d\tau^2(\tau_0)$ and $d^2f/d\tau^2(\tau_n)$ both fade. In [159] the proof was extended for periodic functions, and in [34] this fact has been extended for splines of arbitrary odd degree and prescribed first derivatives at the borders. The result can be interpreted as the spline "trying to keep the shape of a beam" subject to the interpolation constraints.

Further, regarding its approximation properties, in [34] it is proved that, if $f \in \mathcal{C}^2[\tau_0, \tau_n]$, the spline $s(\cdot; \pi, f)$ minimizes

$$\int_{\tau_0}^{\tau_n} \left(\frac{d^2}{d\tau^2}(f(\tau) - s(\tau)) \right)^2 d\tau \tag{3.58}$$

among all the piecewise functions of degree at most three and class $\mathcal{C}^2$ on $[\tau_0, \tau_n]$. This solution is not unique, since s plus a polynomial of degree at most one will also satisfy it.

Another interesting property of the cubic splines is their convergence: defining

$$I = \{0, \dots, n-1\}, \quad \Delta\tau_i = \tau_{i+1} - \tau_i \; i \in I, \quad |\pi| \overset{\text{def}}{=} \max_{i \in I} \Delta\tau_i, \text{ and } \quad M_\pi = |\pi| / \min_{i \in I} \Delta\tau_i, \tag{3.59}$$

in [12] it is shown that if $f \in \mathcal{C}^4[\tau_0, \tau_n]$, then there exist constants $K_r(M_\pi)$ depending on the mesh-ratio bound M_π alone such that

$$\left\| \frac{d^{(r)}}{d\tau^{(r)}}(f - s(\cdot; \pi, f)) \right\| \leqslant K_r \left\| \frac{d^{(4)}f}{d\tau^{(4)}} \right\| |\pi|^{4-r}, \quad \forall r \in \{0, \dots, 3\}, \tag{3.60}$$

where $\|f\| \overset{\text{def}}{=} \max_{\tau \in [\tau_0, \tau_n]} f(\tau)$. A similar bound can be found in [67].

The aforementioned properties make cubic spline interpolation very attractive for applications. This has motivated the introduction of the bicubic splines for the bivariate case. An original approach was proposed in [14] and improved later in [33]. Consider the function $u : [x_0, x_I] \times [y_0, y_J] \subset \mathbb{R}^2 \to \mathbb{R}$, defined on a rectangular region. Consider the mesh points $\pi_x \overset{\text{def}}{=} \{x_0 < x_1 < \dots < x_I\}$ and $\pi_y \overset{\text{def}}{=} \{y_0 < y_1 < \dots < y_J\}$, and let the following characteristics of u be known:

- The function values at the meshpoints, i.e.
  $u_{ij} \overset{\text{def}}{=} u(x_i, y_j) \; \forall i \in \{0, \dots, I\}, \; j \in \{0, \dots, J\}$

- The function's first order derivatives at the mesh's boundary points, i.e.
  $p_{ij} \overset{\text{def}}{=} \partial u/\partial x(x_i, y_j) \; \forall i \in \{0, I\}, \; j \in \{0, \dots, J\}$, and
  $q_{ij} \overset{\text{def}}{=} \partial u/\partial y(x_i, y_j) \; \forall i \in \{0, \dots, I\}, \; j \in \{0, J\}$

- The function's crossed derivatives at the four corners of the mesh, i.e.
  $s_{ij} \overset{\text{def}}{=} \partial^2 u/\partial x \partial y(x_i, y_j) \; \forall i \in \{0, I\}, \; j \in \{0, J\}$

The bicubic spline $c(x, y; \pi_x, \pi_y, u) : [x_0, x_I] \times [y_0, y_J] \subset \mathbb{R}^2 \to \mathbb{R}$ satisfying

$$
\begin{aligned}
c(x_i, y_j) &= u_{ij} \ \forall i \in \{0, \dots, I\}, \ j \in \{0, \dots, J\}, \\
\partial c / \partial x(x_i, y_j) &= p_{ij} \ \forall i \in \{0, I\}, \ j \in \{0, \dots, J\}, \\
\partial c / \partial y(x_i, y_j) &= q_{ij} \ \forall i \in \{0, \dots, I\}, \ j \in \{0, J\}, \ \text{and} \\
\partial^2 c / \partial x \partial y(x_i, y_j) &= s_{ij} \ \forall i \in \{0, I\}, \ j \in \{0, J\},
\end{aligned}
\tag{3.61}
$$

is a piecewise bicubic polynomial of the form

$$
c(x, y) = \sum_{m=0}^{3} \sum_{n=0}^{3} a_{mn}^{ij} (x - x_i)^m (y - y_j)^n \quad \text{if } (x, y) \in R_{ij} = [x_i, x_{i+1}] \times [y_j, y_{j+1}],
\tag{3.62}
$$
$$
\text{for some } i \in \{0, \dots, I-1\} \text{ and some } j \in \{0, \dots, J-1\}.
$$

The information concerning derivatives can be approximated by finite differences. In [33] it is shown that the bicubic spline satisfying these conditions exists and is unique, and that it actually belongs to the tensor product of the spline spaces associated to each dimension, i.e. $c(x, y; \pi_x, \pi_y, u) \in S(x; \pi_x) \otimes S(y; \pi_y)$. As such, they inherit the property of being of class $\mathcal{C}^2$ on the rectangular region $[x_0, x_I] \times [y_0, y_J]$. As stated in [13], the bicubic splines satisfy the variational property of minimizing

$$
\iint_{[x_0, x_I] \times [y_0, y_J]} \left(\frac{\partial^4 u}{\partial x^2 \partial y^2} \right)^2 \mathrm{d}x \mathrm{d}y + \int_{\partial([x_0, x_I] \times [y_0, y_J])} \left(\frac{\partial^2 u}{\partial s^2} \right) \mathrm{d}s,
\tag{3.63}
$$

where $\partial([x_0, x_I] \times [y_0, y_J])$ denotes the rectangle edge and $\partial / \partial s$ denotes the tangential derivative. In the same reference, a property analogous to Eq. (3.60) has been given:

$$
\| u(x, y) - c(x, y) \| = o(|\pi_x|^4 + |\pi_y|^4),
\tag{3.64}
$$

using analogous definitions as Eq. (3.59).

In summary, the aforementioned properties of the splines make them a very suitable option to represent the data obtained by REFPROP. In the univariate case, in contrast to the usual Lagrange interpolation for equidistant meshes, splines minimize the oscillations. Moreover, since the degree of each piecewise polynomial remains three, the number of floating point operations required on each evaluation is smaller. These properties are also inherited in the bivariate case. On the other hand, the good spline convergence qualities makes it possible to reduce the $|\pi|$, $|\pi_x|$ and/or $|\pi_y|$ if more precision is desired. This is supported by the smooth functional forms of Eqs. (2.33) to (2.36).

3.3.2 Saturated and Two-phase Properties

Based on the previous section, we represent the properties corresponding to saturated and two-phase states in Table 3.2 as follows: the vector function

$$
\begin{aligned}
d : [p_{\min}, p_{\max}] &\to \mathbb{R}^4 \\
p \to d(p) &:= \begin{bmatrix} h'(p) & h''(p) & \varrho'(p) & \varrho''(p) & \theta_{F,2}(p) \end{bmatrix}^T
\end{aligned}
\tag{3.65}
$$

depends only on the process pressure p. We apply thus a univariate cubic spline approach to represent the data. For these means, a pressure mesh $\pi_p = \{p_{\min} = p_0 < p_1 < \dots < p_{N_p} = p_{\max}\}$ is defined on which vectors $y_i = d(p_i)$, $i \in \{0, \dots, N_p\}$ are evaluated using REFPROP.

Next, the cubic spline $s(p; \pi_p, d)$ interpolating the pairs $\{p_i, y_i\}_{i=0}^{N_p}$ is obtained using the approach described in [33] (cf. [146]). Once its coefficients are known, the spline can be evaluated in $[p_{\min}, p_{\max}]$ using Horner's method (cf. [117]), whenever model functions $\boldsymbol{M}$, $\boldsymbol{b}$ and $\boldsymbol{g}$ of Eq. (3.53) are evaluated, to obtain the components of d. Whenever the derivatives w.r.t. pressure, dh'/dp_{ev}, dh''/dp_{ev}, $d\varrho'/dp_{\mathrm{ev}}$ and $d\varrho''/dp_{\mathrm{ev}}$ are needed on $[p_{\min}, p_{\max}]$, they are obtained directly from the spline, using its analytic expression.

Extrapolation.   In Chapter 4 the iterative dynamic optimization algorithms model Eq. (3.53) is subject to are explained. As they converge, the thermophysical properties may be evaluated at points laying outside the domain of definition of the corresponding splines. It is, therefore, appropriate to consider an extrapolation scheme for those cases. The extrapolation scheme should yield values of the corresponding properties that deviate from those at the domain of definition's borders with a suitably bounded change rate, so that evaluations can be safely performed far from away the border. In addition, changes of signs are not desired, and the monotonicity of the extrapolation with respect to its arguments should resemble the one of the data close to the border. For the properties corresponding to saturated and two-phase states, the corresponding spline is expanded by means of linear affine functions defined on each side that match the splines' slope and value at the corresponding border. Concretely, if $s(\cdot; \pi_p, d)$ is the spline interpolating the values of d on π_p, we consider the function

$$f(p) = \begin{cases} s(p_{\min}; \pi_p, d) + (p - p_{\min})ds/dp(p_{\min}; \pi_p, d) & \text{, if } p < p_{\min} \\ s(p; \pi_p, d) & \text{, if } p \in [p_{\min}, p_{\max}] \\ s(p_{\max}; \pi_p, d) + (p - p_{\max})ds/dp(p_{\max}; \pi_p, d) & \text{, if } p > p_{\max}. \end{cases} \quad (3.66)$$

to represent the data for all $p \in \mathbb{R}$.

3.3.3 External Inputs

The continuous-time model Eq. (3.53) requires a continuous-time representation of the external input vector $\boldsymbol{w}(t)$, i.e for all t in the simulation interval, the value of $\boldsymbol{w}(t)$ should be defined. This can be done in several ways, and even real-world data can be represented. In scenarios based on real-world data, which have been provided by our industry cooperation partner Daimler AG and correspond to exhaust gas temperature and massflow data recorded during several test drives of a real heavy duty truck, we proceed similarly as in Section 3.3.2 in order to represent them, but since the amount of data under consideration is large, a mesh much coarser than the data sampling time is used and the external inputs are not interpolated but approximated by a cubic spline. The spline knots are fixed, and uniformly spaced on a predetermined time interval. For these scenarios, the model is not evaluated at times outside the aforementioned time interval, so the extrapolation feature is not used.

3.3.4 Single-Phase and Exhaust Gas Properties

As shown in Table 3.2, the working fluid single-phase properties are parametrized with respect to pressure-enthalpy (p, h) and pressure-entropy (p, s) pairs. Depending on this, the treatment of the data varies, as explained in the following paragraphs. For a better understanding of the choices made in this subsection, it is important to have in mind the discussion about states of matter, phase changes and thermophysical properties on Section 2.5.

Functions Depending on Pressure-Enthalpy Pairs. We begin by defining $p_{\min}$, $p_{\max}$, $h_{\min}$ and $h_{\max}$ so that $p_{\min} < p_{\max}$ and $h_{\min} < h_{\max}$. The latter are chosen so that a portion of the projection of the vapor dome on the p-h plane is contained in $[p_{\min}, p_{\max}] \times [h_{\min}, h_{\max}]$. We proceed to obtain the required thermophysical data from REFPROP on set of coordinates contained in $[p_{\min}, p_{\max}] \times [h_{\min}, h_{\max}]$. In principle, we could directly define a rectangular mesh on the region and proceed to construct the corresponding bicubic splines. However, the physical nature of the functions to represent poses difficulties for the achievement of satisfactory results: both the temperature and the density derivatives with respect to the enthalpy are discontinuous at the saturation curves. Also, in the two-phase region, the density decreases violently as h increases. To make things worse, the saturation curves are not parallel to any of the axes of the p-h plane. As pointed out in [13], cubic and bicubic splines of class C^2 are not local, which means that the values of the resulting representing function at some specific coordinates in the domain of definition depend on all the input data. A direct implementation of the bicubic spline approach described in Section 3.3.1 would result in unexpected oscillations even far away from the saturated states, and, furthermore, in inconsistent values close to the saturated states themselves, which is particularly critical since terms involving saturated and non-saturated states interact heavily in our model. The problem persists even if the mesh is refined.

On the other hand, if pressure $p_{\max}$ is bounded below the critical pressure p_c, it holds that $h'(p) < h''(p)$ for all $p \in [p_{\min}, p_{\max}]$. We can thus partition the rectangle $[p_{\min}, p_{\max}] \times [h_{\min}, h_{\max}]$ into three non-rectangular regions

$$SL = \{(p,h)\,/\,p \in [p_{\min}, p_{\max}], h_{\min} \leqslant h \leqslant h'(p)\}$$
$$VD = \{(p,h)\,/\,p \in [p_{\min}, p_{\max}], h'(p) < h < h''(p)\}$$
$$SV = \{(p,h)\,/\,p \in [p_{\min}, p_{\max}], h''(p) \leqslant h \leqslant h_{\max}\}$$

associated with the subcooled liquid region (SL), the vapor dome (VD) and the superheated vapor region (SV). The regions are depicted in Fig. 3.6. These regions are each homeomorph to a square $S = [0,1] \times [0,1]$. We introduce the transformations

$$x(p^L) = (p^L - p_{\min})/(p_{\max} - p_{\min}), \quad y(p^L, h^L) = (h^L - h_{\min})/(h'(p^L) - h_{\min}), \qquad (3.67)$$

mapping the coordinates $(p^L, h^L) \in SL$ onto $(x, y) \in S$, and

$$x(p^V) = (p^V - p_{\min})/(p_{\max} - p_{\min}), \quad y(p^V, h^V) = (h^V - h''(p^V))/(h_{\max} - h''(p^V)) \quad (3.68)$$

mapping the coordinates $(p^V, h^V) \in SV$ onto $(x, y) \in S$.

The inverse transformations are also available. Namely,

$$p^L = p_{\min} + x(p_{\max} - p_{\min}), \quad h^L = h_{\min} + y(h'(p^L) - h_{\min}), \qquad (3.69)$$

mapping the coordinates $(x, y) \in S$ onto $(p^L, h^L) \in SL$, and

$$p^V = p_{\min} + x(p_{\max} - p_{\min}), \quad h^V = h''(p^V) + y(h_{\max} - h''(p^V)), \qquad (3.70)$$

mapping the coordinates $(x, y) \in S$ onto $(p^V, h^V) \in SV$.

We proceed therefore as follows: consider an equidistant rectangular mesh of $N_p \times N_h$ points on the square $S = [0,1] \times [0,1]$, and the index sets $I_I = \{1, \ldots, N_p\}$ and $I_J = \{1, \ldots, N_h\}$. Each point (x_i, y_j) on this mesh can be mapped onto SL using Eq. (3.69), and onto SV using

Eq. (3.70). This way, the meshes

$$SL_m = \left\{(p_i^L, h_j^L), i \in I_I, j \in I_J\right\} \subset SL \text{ and } SV_m = \left\{(p_i^V, h_j^V), i \in I_I, j \in I_J\right\} \subset SV, \quad (3.71)$$

are formed. We use REFPROP to evaluate temperature, density and entropy at all meshpoints in SL_m and SV_m. Let us denote for each property the obtained values by $X_{i,j}^L$ for SL_m and $X_{i,j}^V$ for SV_m, for all $i \in I_I, j \in I_J$. For each property $X \in \{\varrho, \theta, s\}$ and triplet set $\{(x_i, y_j, X_{i,j}^L)/(i,j) \in I_I \times I_J\}$ and $\{(x_i, y_j, X_{i,j}^V)/(i,j) \in I_I \times I_J\}$, the coefficients a_{mn}^{ij} of the interpolating bicubic spline are obtained using the method proposed by [33] (see also [145]). Let us denote them by *subcooled spline* and *superheated spline*, respectively. These splines are the ones used in the model for the evaluation of each property on the corresponding region. For evaluating s_A, $\theta_{F,1}$ and $\bar{\varrho}_1$, the (p,h) pair where the property is to be evaluated is firstly mapped onto $(x,y) \in S$ using Eq. (3.67). The subcooled spline is evaluated at (x,y) then. The density derivatives $\partial \bar{\varrho}_1 / \partial \bar{p}_1$ and $\partial \bar{\varrho}_1 / \partial \bar{h}_1$ at (p,h) are obtained from the spline directly and applying the chain rule. The evaluation process is analogous for $\theta_{F,3}$, $\bar{\varrho}_3$, $\partial \bar{\varrho}_3 / \partial \bar{p}_3$, $\partial \bar{\varrho}_3 / \partial \bar{h}_3$, ϱ_C and s_C, using Eq. (3.68) to transform the coordinates and evaluating the superheated spline instead.

On each case, since the meshes are equidistant, the indices i and j corresponding to each cell in the transformed square can be readily computed. At this point the evaluation takes thus no longer than six sums and multiplications per function.
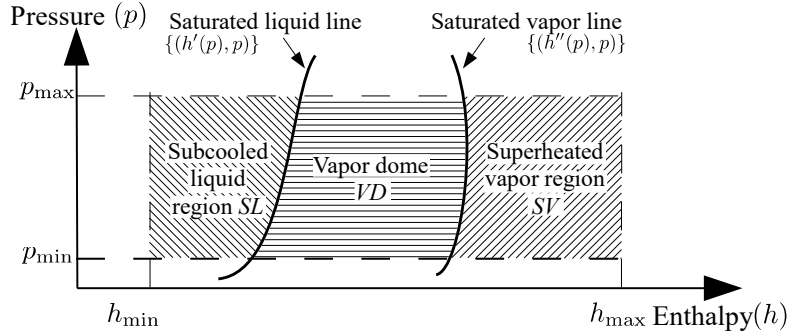
Figure 3.6: Representation of a typical p-h diagram for a working fluid. Definition of interpolation regions SL, VD and SV

Functions Depending on Pressure-Entropy Pairs. The enthalpies $h_{B,is}$ and $h_{D,is}$, which are parametrized on (p,s) pairs, do not suffer from the irregular behavior described previously, so we can proceed directly proceed by defining s_{min} and s_{max} and a rectangular mesh PS_m of $N_p \times N_s$ points on $PS = [p_{min}, p_{max}] \times [s_{min}, s_{max}]$. REFPROP is used to evaluate the enthalpy on each meshpoint. With the resulting (p,s,h) triplets, an interpolating bicubic spline is obtained and used for evaluation inside PS The derivative $\partial h_{B,is} / \partial p_B$ is obtained directly from the spline, as above.

Extrapolation. Since the actual range of values the input pairs (p,h), (p,s) can take during simulation and optimization is not necessarily known in advance, it is necessary to define an adequate extrapolation strategy, as discussed previously. We propose the following approach: Let us denote the spline evaluation pair as $P = (P_1, P_2)$. If one or both spline arguments fall outside regions S or PS, as the case may be, evaluate the spline at the closest point at the border (in a norm-1 sense), called $\tilde{P}$, obtaining $\tilde{X}$; then, calculate the spline gradient at $\tilde{P}$, denoted by $\nabla \tilde{X} = (\partial X / \partial P_1, \ \partial X / \partial P_2)$, and then add a correction term equal to $\nabla \tilde{X}^T (P - \tilde{P})$

to $\tilde{X}$. The spline derivatives are given by $\nabla \tilde{X}$. This extrapolation approach shows advantages over directly evaluating the spline outside its domain of definition, since the obtained values do not suffer from oscillations and their change rate is moderate, allowing for evaluations also far away from the border. This approach is illustrated in Fig. 3.7. Notice that in the case of pressure-enthalpy pairs, we refer to the borders the square S.
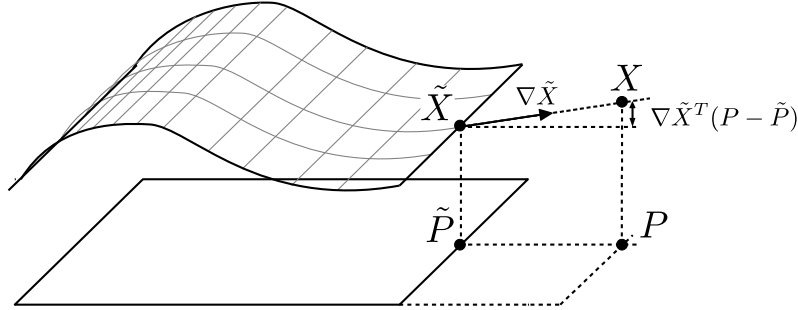
Figure 3.7: Extrapolation approach

Exhaust Gas Properties.   For the exhaust gas properties we proceed as in the case of the working fluid properties depending on (p, s) pairs, but parametrize with respect to (p, θ) pairs. On the $[p_{G,\min}, p_{G,\max}] \times [\theta_{G,\min}, \theta_{G,\max}]$ region a $N_{pG} \times N_{\theta G}$ rectangular mesh is defined upon which the properties are evaluated and the splines are obtained.

3.3.5 Summary

The substance used as the working fluid in the ORC is the responsible for the energy transfer taking place inside it. Therefore, the numerical values of its thermophysical properties, given each thermodynamic state it is found at should be known with accuracy and become available as computations take place. Specialized software exists for these means, upon which we have relied for our implementation. In order to obtain computational speed gains, however, we have implemented a scheme based on both uni- and bivariate splines that interpolate the data obtained from the specialized software. Adequate transformations have been found that overcome oscillatory phenomena and inconsistencies that would otherwise rise is splines were constructed directly from available data. Moreover, we have implemented an extrapolation scheme that expands the evaluability region of model Eq. (3.53) in its state and parameter space. This proves valuable for the convergence of the optimal control algorithms to be introduced in Chapter 4.

3.4 Model Properties

In this subsection a set of properties of the model described by Eq. (3.53) will be studied. This will be useful to establish whether or not the current formulation satisfies the assumptions required by the numerical algorithms to be introduced in Chapter 4. The properties considered are also of interest for alternative control algorithms used for comparison. Some properties are explored numerically in Chapter 5.

Mass Matrix Invertibility and Condition.   The structure of matrices M_{ev} and M in Eq. (4.39) permits the derivation of sufficient conditions for its invertibility.
A careful of scaling of M_{ev} and M should be considered so as to avoid numerical difficulties during the integration process. In this thesis we express the mass balance in $[\mathrm{g}]$ and the energy

balances in [kW]. This influences $\boldsymbol{b}_{ev}$ and $\boldsymbol{g}$ as well. The state variables are also internally scaled to have units of [m] (L_1, L_2), [MPa] (p_{ev}), [MJ/kg] (h_C) and [hK][5] ($\theta_{W,1}$, $\theta_{W,2}$, $\theta_{W,3}$). The columns of $\boldsymbol{M}_{ev}$ and $\boldsymbol{M}$ are scaled accordingly.

DAE Index. The algebraic expansion of $\partial \boldsymbol{g}/\partial \boldsymbol{z}$ leads to the condition

$$\frac{\partial \boldsymbol{g}}{\partial \boldsymbol{z}} = -\underbrace{\frac{1}{2}\pi d_i L_3 \alpha_{F,3}}_{(+)} \underbrace{\left.\frac{\partial \theta_{F,3}}{\partial \bar{h}_3}\right|_{(\bar{h}_3, p_{ev})}}_{(+)} - \underbrace{n_{ex}\eta_{ex,V}V_{ex}}_{(+)} \underbrace{\left.\frac{\partial \varrho_C}{\partial h_C}\right|_{(\bar{h}_3, p_{ev})}}_{(-)} \underbrace{\left(h_C - h''(p_{ev})\right)}_{(+)}$$

$$- \underbrace{n_{ex}\eta_{ex,V}V_{ex}\varrho_C(\bar{h}_3, p_{ev})}_{(+)} \quad \neq \quad 0 \tag{3.72}$$

to ensure the DAE Eq. (3.53) is of index 1. On normal operating conditions, the different summands in Eq. (3.72) have the signs indicated on the same equation. The highly nonlinear dependence of the involved partial derivatives makes it difficult to characterize the region where the condition holds analytically. However, given the characteristics of most substances, in particular the one we use, it can be claimed that this condition is unlikely to be violated on a normal operating trajectory. In this thesis we assume that the DAE index is 1.

Equilibrium States. Assuming that matrix $\boldsymbol{M}(\boldsymbol{x}, \boldsymbol{z})$ is invertible, $\boldsymbol{x}$ and $\boldsymbol{z}$ are equilibrium states (i.e. $d\boldsymbol{x}/dt = 0$) if and only if the following equalities are satisfied:

$$0 = \dot{m}_{in} - \dot{m}_{out} \tag{3.73a}$$

$$0 = \pi d_i L_1 \alpha_{F,1} \left(\theta_{W,1} - \theta_{F,1}\right) - \dot{m}_{in}\left(h' - h_B\right), \tag{3.73b}$$

$$0 = \pi d_i L_2 \alpha_{F,2} \left(\theta_{W,2} - \theta_{F,2}\right) - \left(\dot{m}_{out}h'' - \dot{m}_{in}h'\right), \tag{3.73c}$$

$$0 = \pi d_i L_3 \alpha_{F,3} \left(\theta_{W,3} - \theta_{F,3}\right) - \dot{m}_{out}\left(h_C - h''\right). \tag{3.73d}$$

$$0 = d_o \alpha_{G,1} \left(\theta_{G,1} - \theta_{W,1}\right) - d_i \alpha_{F,1} \left(\theta_{W,1} - \theta_{F,1}\right), \tag{3.73e}$$

$$0 = d_o \alpha_{G,2} \left(\theta_{G,2} - \theta_{W,2}\right) - d_i \alpha_{F,2} \left(\theta_{W,2} - \theta_{F,2}\right), \tag{3.73f}$$

$$0 = d_o \alpha_{G,3} \left(\theta_{G,3} - \theta_{W,3}\right) - d_i \alpha_{F,3} \left(\theta_{W,3} - \theta_{F,3}\right). \tag{3.73g}$$

These equalities have been formed by imposing the components of Eq. (3.39b) to be zero, while incorporating Eqs. (3.12) and (3.13). The latter set of equations impose a challenging nonlinear coupling between state variables, parameters, control and external disturbances. For this reason, in this thesis Eq. (3.73) are treated numerically. For the same reason, it may not be true that any given combination of controls and external disturbances inside usual operational margins has an associated equilibrium state laying on a feasible region. Knowing that the working fluid at the evaporator output is likely to be found in regions close to the saturated vapor line if a nearly optimal control strategy is to be considered [131], we let the equilibrium control vector $\bar{\boldsymbol{u}}$ to be a degree of freedom and solve

$$\min_{\boldsymbol{x},\boldsymbol{z},\boldsymbol{u}} h_C; \quad \text{s.t.} \ \boldsymbol{b}(\boldsymbol{x},\boldsymbol{z},\boldsymbol{u},\boldsymbol{p},\boldsymbol{w}) = 0; \quad \boldsymbol{g}(\boldsymbol{x},\boldsymbol{z},\boldsymbol{p}) = 0; \quad \boldsymbol{c}(\boldsymbol{x},\boldsymbol{z},\boldsymbol{u},\boldsymbol{p}) \geqslant 0. \tag{3.74}$$

In the following, the symbols $\bar{x} = \bar{x}(\bar{w}, \boldsymbol{p})$, $\bar{z} = \bar{z}(\bar{w}, \boldsymbol{p})$, $\bar{u} = \bar{u}(\bar{w}, \boldsymbol{p})$ denote the equilibrium states and control solving Eq. (3.74), depending on the given external disturbance $\bar{w}$ and

---

[5] $1\,[hK] = 100\,[K]$.

parameter vector p.

Linearization around equilibrium points. Consider function $f(\cdot) = \left[M(\cdot)^{-1} b(\cdot); \quad g(\cdot) \right]$. At the equilibrium state $[\bar{x}, \bar{z}]$ and control $\bar{u}$ and external disturbances $\bar{w}$ it holds that $f(\bar{x}, \bar{z}, \bar{u}, \bar{w}, p) = 0$. If all functions are of class $\mathcal{C}^1$ in a neighborhood around the equilibrium state and control, the remainder term of a first-order Taylor expansion around an equilibrium state

$$\epsilon = f(\bar{x} + \delta x, \bar{z} + \delta z, \bar{u} + \delta u, \bar{w}, p) - \left(\bar{A}_x \delta x + \bar{A}_z \delta z + \bar{B} \delta u \right) = o\left(\| [\delta x; \ \delta z; \ \delta u] \| \right), \quad (3.75)$$

with

$$\bar{A}_x = \frac{\partial f}{\partial x} \bigg|_{(\bar{x}, \bar{z}, \bar{u}, \bar{w}, p)}, \quad \bar{A}_z = \frac{\partial f}{\partial z} \bigg|_{(\bar{x}, \bar{z}, \bar{u}, \bar{w}, p)}, \quad \text{and} \quad \bar{B} = \frac{\partial f}{\partial u} \bigg|_{(\bar{x}, \bar{z}, \bar{u}, \bar{w}, p)} \quad (3.76)$$

can be neglected. Defining additionally

$$\bar{A} = \left[\ \bar{A}_x \ \middle| \ \bar{A}_z \ \right], \quad \text{and} \quad \bar{C} = \left[\ \frac{\partial y}{\partial x} \bigg|_{(\bar{x}, \bar{z}, \bar{u}, \bar{w}, p)} \ \middle| \ \frac{\partial y}{\partial z} \bigg|_{(\bar{x}, \bar{z}, \bar{u}, \bar{w}, p)} \ \right] \quad (3.77)$$

the following new linear ODE system can be thus defined:

$$\frac{d\tilde{x}}{dt}(t) = \bar{A} \tilde{x}(t) + \bar{B} \tilde{u}(t), \quad (3.78a)$$

$$\tilde{y}(t) = \bar{C} \tilde{x}(t), \qquad \forall t \in [t_0, t_f] \quad (3.78b)$$

$$\tilde{x}(t_0) = 0. \quad (3.78c)$$

In which $\tilde{x}$, $\tilde{u}$ and $\tilde{y}$ represent the deviations from the equilibrium states and control, and the deviation in the measurement function due to $\tilde{x}$, respectively. In this formulation we consider $\tilde{x}$ to contain both the deviations of x and z. Notice that the origin is an equilibrium state for Eq. (3.78) when $\tilde{u} = 0$.

In digital control, a difference equation relating the states $\tilde{x}_k$ and $\tilde{x}_{k+1}$ at the contiguous sample times t_k and $t_{k+1} = t_k + T_s$ is preferable [101, 114]. Integrating Eq. (3.78) between both time instants yields

$$\tilde{x}_{k+1} = e^{\bar{A} T_s} \tilde{x}_k + \left(e^{\bar{A} t_{k+1}} \int_{t_k}^{t_{k+1}} e^{-\bar{A} \tau} \bar{B} \, d\tau \right) \tilde{u}_k, \quad (3.79)$$

where the control $\tilde{u}(\tau) = \tilde{u}_k$ has been taken out of the integral since in a digital controller, it will be constant for $\tau \in [t_k, t_{k+1}]$. Here the matrix exponential is

$$e^{\bar{A} t} = \sum_{i=0}^{\infty} \frac{1}{i!} \bar{A}^i, \quad \bar{A}^0 \stackrel{\text{def}}{=} \mathbb{I}. \quad (3.80)$$

The exact discretization of Eq. (3.78) corresponds therefore to

$$\tilde{x}_{k+1} = A \tilde{x}_k + B \tilde{u}_k, \quad (3.81a)$$

$$\tilde{y}_k = C \tilde{x}_k, \qquad \forall k \in \mathcal{K} \quad (3.81b)$$

$$\tilde{x}_0 = 0, \quad (3.81c)$$

with

$$A = e^{\bar{A}T_s}, \quad B = \bar{A}^{-1}\left(e^{\bar{A}T_s} - \mathbb{I}\right)\bar{B}, \text{ and } \quad C = \bar{C}. \tag{3.82}$$

In Eq. (3.81), $\mathcal{K} \subset \mathbb{N}_0$ is the index set of all the samples k considered on a given time horizon.

3.5 Problem Statement

In this section we give a mathematical formulation to the optimization problems dealt with in this thesis. First, based on model Eq. (3.53), we proceed to formulate a fixed time horizon *optimal control problem* (OCP) for a given external input vector $w(t)$ and initial state x_0. This problem is interesting because its solution would allow us to know best how to operate the WHR in order to recover as much energy as possible from the exhaust gas. This approach would be perfectly applicable if some sort of truck driving strategy programming was available, so that both the exhaust gas inputs and the drive duration could be precisely predicted. The advent of autonomous driving gives good reasons that this will be possible in the near future, and the relations existing between mechanical and thermal variables (torque-speed and exhaust gas massflow-temperature) is faily well understood. On the other hand, full knowledge of the state vector could be obtained with appropriate estimation methods. As long as the aforementioned techniques are not available, the solution of the optimal control problem can still be used to bring insight and evaluate the performance of other control strategies under the same scenario, at least in simulation environments.

Closely related to the optimal control problem recently discussed is the technique of *nonlinear model-predictive control* (NMPC). Therein, a discrete sequence of optimal control subproblems is considered, each with similar objective function and path constraints as in the previous case. In each subproblem, a sorter time horizon, also called the *prediction horizon* is considered, and the initial state is allowed to differ between subproblems. This formulation is established to provide state feedback, which becomes necessary as disturbances, model-plant mismatches or unpredicted changes in the exhaust gas conditions may cause the solution of the OCP, open-loop in its nature, to become invalid. At the same time, this formulation enables the controller to pursue the optimization of the objective function while satisfying the constraints.

In NMPC, for each optimal control subproblem, the knowledge of the initial state is required. In our particular case, not all states in model Eq. (3.53) are directly measurable, so a state observer is required. The technique of choice for this thesis corresponds to *moving horizon estimation* (MHE). Similar to NMPC, in MHE a sequence of estimation subproblems, generally in the form of a least-squares problem is considered. Each problem's goal is the estimation of the differential state vector x using the information contained in the last M measurements.

3.5.1 Optimal Control Problem (OCP)

As previously stated, we are interested in controlling the WHR in an optimal fashion with respect to an objective function, satisfying the operational constraints, also known as *path constraints*. For the formulation, we consider the WHR operation along the fixed time interval $[t_0, t_\mathrm{f}]$. The initial state vector x_0 in Eq. (3.53) is considered given.

Objective Function. The goal is to maximize the net energy recovery for the WHR on a fixed time interval. Using Eqs. (3.1d) and (3.2f), we define the net output power as

$$L(x, z, u, p) = \dot{W}_{\text{out}}(x, z, p) - \dot{W}_{\text{in}}(x, u, p), \tag{3.83}$$

so that the objective function to be maximized, the net output energy, is

$$\Phi(t_{\mathrm{f}}) \stackrel{\text{def}}{=} \int_{t_0}^{t_{\mathrm{f}}} L(\boldsymbol{x}(t), \boldsymbol{z}(t), \boldsymbol{u}(t), \boldsymbol{p}) \, \mathrm{d}t. \tag{3.84}$$

Path Constraints. Path constraints must be satisfied along the whole operational timespan. They are summarized in a vector function $\boldsymbol{c}(t) : \mathbb{R}^{n_{\mathrm{x}}} \times \mathbb{R}^{n_{\mathrm{z}}} \times \mathbb{R}^{n_{\mathrm{u}}} \times \mathbb{R}^{n_{\mathrm{p}}} \longrightarrow \mathbb{R}^{n_{\mathrm{c}}}$; $\boldsymbol{c}(\boldsymbol{x}(t), \boldsymbol{z}(t), \boldsymbol{u}(t), \boldsymbol{p}) \geqslant 0$, $\forall t \in [t_0, t_{\mathrm{f}}]$, where n_{x}, n_{z}, n_{u} and n_{p} are the differential state, algebraic state and control dimensions, respectively. Its components are defined as follows:

- Limitation of pump capacity,

$$\boldsymbol{c}_1(\boldsymbol{u}) = \dot{m}_{\mathrm{in,max}} - \dot{m}_{\mathrm{in}}; \quad \boldsymbol{c}_2(\boldsymbol{u}) = \dot{m}_{\mathrm{in}} - \dot{m}_{\mathrm{in,min}}. \tag{3.85}$$

- Prevention of droplets entering the expander,

$$\boldsymbol{c}_3(\boldsymbol{x}, \boldsymbol{z}) = h_C - h''(p_{\mathrm{ev}}). \tag{3.86}$$

- Limitation of third zone length to lower bound $L_{3,\mathrm{min}} \geqslant 0$ to prevent numerical difficulties,

$$\boldsymbol{c}_4(\boldsymbol{x}, \boldsymbol{p}) = L - L_1 - L_2 - L_{3,\mathrm{min}}. \tag{3.87}$$

- Prevention of working fluid thermal decomposition,

$$\boldsymbol{c}_{4+j}(\boldsymbol{x}, \boldsymbol{z}) = \theta_{F,\mathrm{max}} - \theta_{F,j}(\bar{p}_j, \bar{h}_j), \ \forall j \in \{1, 2, 3\} \quad \text{and} \quad \boldsymbol{c}_8(\boldsymbol{x}, \boldsymbol{z}) = \theta_{F,\mathrm{max}} - \theta_C(p_C, h_C). \tag{3.88}$$

- Box constraints for the rest of the state vector,

$$\boldsymbol{c}_{7+2j}(\boldsymbol{x}) = L_{\mathrm{max}} - L_j \text{ and } \boldsymbol{c}_{8+2j}(\boldsymbol{x}) = L_j - L_{\mathrm{min}}, \ \forall j \in \{1, 2\};$$
$$\boldsymbol{c}_{13}(\boldsymbol{x}) = p_{\mathrm{max}} - p_{\mathrm{ev}}; \quad \boldsymbol{c}_{14}(\boldsymbol{x}) = p_{\mathrm{ev}} - p_{\mathrm{min}}; \tag{3.89}$$
$$\boldsymbol{c}_{13+2j}(\boldsymbol{x}) = \theta_{W,\mathrm{max}} - \theta_{W,j} \text{ and } \boldsymbol{c}_{14+2j}(\boldsymbol{x}) = \theta_{W,j} - \theta_{W,\mathrm{min}} \ \forall j \in \{1, 2, 3\}$$

Remark 3.5.1 (Minimum third zone length) *In our practical experience it has been observed that, in accordance to the results of [168], on the optimum state trajectories the thermodynamic state of the working fluid at the expander inlet approaches the saturated vapor curves. This implies the vanishing of the third zone (i.e. $L_3 = 0$) at the instants where this takes place, which in turn can cause numerical difficulties in e.g. Eq. (3.14) ($K_3 = 0$) and Eq. (4.39) ($M_{7,7} = 0$, see Eq. (3.46)). To handle this, we have introduced Eq. (3.87) and the minimum length $L_{3,min}$ to ensure a minimum robustness margin against this phenomenon. Our numerical experience indicates that the energy recovery for a typical heavy duty truck drive is practically independent of $L_{3,min}$ when this value is small.*

Remark 3.5.2 (Convexity of the OCP Constraints) *Most components of $\boldsymbol{c}(t)$ are linear and thus convex. On the other hand, Equations (3.86) and (3.88) are not. Both depend highly on the working fluids being used in the WHR. For dry working fluids, Eq. (3.86) will be convex if pressure p_{ev} is not too close to the critical pressure. Otherwise it will be nonconvex. Equation (3.88) can be convex depending on the working fluid. For the case of ethanol, both Eqs. (3.86) and (3.88) are nonconvex.*

Optimal Control Problem. Putting the DAE model Eq. (3.53), the path constraints and the objective function together, the optimal control problem

$$P_{\text{OCP}} : \min_{\boldsymbol{x}(\cdot),\boldsymbol{z}(\cdot),\boldsymbol{u}(\cdot)} \quad -\int_{t_0}^{t_{\text{f}}} L(\boldsymbol{x}(t),\boldsymbol{z}(t),\boldsymbol{u}(t),\boldsymbol{p})\,\mathrm{d}t$$

$$\text{s.t.} \quad M(\boldsymbol{x}(t),\boldsymbol{z}(t),\boldsymbol{p})\frac{\mathrm{d}\boldsymbol{x}}{\mathrm{d}t}(t) = \boldsymbol{b}(\boldsymbol{x}(t),\boldsymbol{z}(t),\boldsymbol{u}(t),\boldsymbol{p},\boldsymbol{w}(t)), \tag{OCP}$$

$$0 = \boldsymbol{g}(\boldsymbol{x}(t),\boldsymbol{z}(t),\boldsymbol{p}) \quad \forall t \in [t_0,t_{\text{f}}],$$

$$0 \leqslant \boldsymbol{c}(\boldsymbol{x}(t),\boldsymbol{z}(t),\boldsymbol{u}(t),\boldsymbol{p}) \quad \forall t \in [t_0,t_{\text{f}}],$$

$$0 = \boldsymbol{x}(t_0) - \boldsymbol{x}_0,$$

is posed.

3.5.2 Nonlinear Model-Predictive Control (NMPC)

In this case we consider the same objective function, path constraints and model as for Eq. (OCP). In contrast to Eq. (OCP), in this formulation not a single optimal control problem, but a sequence of them, indexed with a superindex $k \in \mathcal{K} = \{0,1,\ldots,K\}$ is considered. In each member of the sequence, if the sampling time is T_s, a prediction horizon starting at $t_0^{(k)} = t_0 + kT_s$ and ending at $t_{\text{f}}^{(k)} = t_0^{(k)} + \Delta t_{\text{NMPC}}$ is introduced. Δt_{NMPC} is the prediction horizon length. At $t_0^{(k)}$, the initial differential state is $\hat{\boldsymbol{x}}^{(k)}$. With these considerations we define the k-th optimal control subproblem of NMPC as

$$P_{\text{NMPC}}^{(k)} : \min_{\boldsymbol{x}(\cdot),\boldsymbol{z}(\cdot),\boldsymbol{u}(\cdot)} \quad -\int_{t_0^{(k)}}^{t_{\text{f}}^{(k)}} L(\boldsymbol{x}(t),\boldsymbol{z}(t),\boldsymbol{u}(t),\boldsymbol{p})\,\mathrm{d}t$$

$$\text{s.t.} \quad M(\boldsymbol{x}(t),\boldsymbol{z}(t),\boldsymbol{p})\frac{\mathrm{d}\boldsymbol{x}}{\mathrm{d}t}(t) = \boldsymbol{b}(\boldsymbol{x}(t),\boldsymbol{z}(t),\boldsymbol{u}(t),\boldsymbol{p},\boldsymbol{w}(t)), \tag{NMPC$_k$}$$

$$0 = \boldsymbol{g}(\boldsymbol{x}(t),\boldsymbol{z}(t),\boldsymbol{p}) \quad \forall t \in [t_0^{(k)},t_{\text{f}}^{(k)}],$$

$$0 \leqslant \boldsymbol{c}(\boldsymbol{x}(t),\boldsymbol{z}(t),\boldsymbol{u}(t),\boldsymbol{p}) \quad \forall t \in [t_0^{(k)},t_{\text{f}}^{(k)}],$$

$$0 = \boldsymbol{x}(t_0^{(k)}) - \hat{\boldsymbol{x}}^{(k)}.$$

3.5.3 Moving Horizon Estimation (MHE)

Similar to Eq. (NMPC$_k$), to estimate $\hat{\boldsymbol{x}}^{(k)}$, a sequence of least-squares problems $P_{\text{MHE}}^{(k)}$, $k \in \mathcal{K}$ on a moving estimation window starting at $t_{0,\text{MHE}}^{(k)} = t_0^{(k)} - \Delta t_{\text{MHE}}$ and ending at $t_{\text{f,MHE}}^{(k)} = t_0^{(k)}$ is defined in which measurements

$$\Xi_k = \left[\xi_{k-M},\xi_{k-M+1},\ldots,\xi_k\right], \tag{3.90}$$

are available at times $t_{k-M+j}^{(k)} = t_0^{(k)} + (j-M)T_s$ for $j \in \{0,\ldots,M\}$. Notice that $\Delta t_{\text{MHE}} = MT_s$. Each measurement ξ_j consists of a vector $\left[p_B,\theta_C,\theta_{G,\text{out}}\right]^T$ with associated standard deviations $\left[\sigma_p,\sigma_{\theta_F},\sigma_{\theta_G}\right]^T$. The past controls $\boldsymbol{u}(\cdot)$ and external inputs $\boldsymbol{w}(\cdot)$ are also available along $[t_{0,\text{MHE}}^{(k)},t_{\text{f,MHE}}^{(k)}]$.

Objective Function. For the MHE we consider the objective function

$$\sum_{j=k-M}^{k} \|\xi_j - y(\hat{x}^{(j)}, \hat{z}^{(j)}, w(t_j), p)\|_W^2 + \|L_3(\hat{x}^{(k)}, p) - \overline{L_3}\|_{\sigma_L}^2, \tag{3.91}$$

where $\|e\|_W^2 = e^T W^T W e$ and $W = \text{diag}\left(\left[\sigma_p^{-1}, \sigma_{\theta_F}^{-1}, \sigma_{\theta_G}^{-1}\right]\right)$. The third-zone length at (x, p) is $L_3(x, p) = L - x_1 - x_2$. $\overline{L_3}$ and σ_L constitute a terminal cost term. Since the superheating at a near-optimal operating point should be as low as possible [131], we choose $\overline{L_3} > 0$ small. This term is added in order to obtain a well-posed problem.

Path Constraints. A constraint function $c_{\text{MHE}}(t) : \mathbb{R}^{n_x} \times \mathbb{R}^{n_p} \longrightarrow \mathbb{R}^{n_{c,\text{MHE}}}$; $c_{\text{MHE}}(x(t), p) \geqslant 0$, $\forall t \in [t_{0,\text{MHE}}^{(k)}, t_{f,\text{MHE}}^{(k)}]$ is introduced whose first component is (3.87) and the rest come from a wall temperature arrangement,

$$c_{\text{MHE},2}(x, p) = \theta_{W,2} - \theta_{W,1}, \quad c_{\text{MHE},3}(x, p) = \theta_{W,3} - \theta_{W,2}. \tag{3.92}$$

Equations (3.87) and (3.92) are introduced to avoid unphysical model behavior. Notice that, other than in Eqs. (NMPC_k) and (OCP), there is no initial value constraint in the MHE formulation.

Remark 3.5.3 (Convexity of the MHE Constraints) *All components of $c_{MHE}(t)$ are linear and thus convex.*

State Estimation Problem. With the previous considerations, the state estimation problem is formulated as

$$P_{\text{MHE}}^{(k)}: \min_{\substack{\hat{x}^{(j)}, \hat{z}^{(j)} \\ j \in \{k-M,\dots,k\}}} \sum_{j=k-M}^{k} \|\xi_j - y(\hat{x}^{(j)}, \hat{z}^{(j)}, w(t_j), p)\|_W^2 + \|L_3(\hat{x}^{(k)}, p) - \overline{L_3}\|_{\sigma_L}^2.$$

$$\text{s.t.} \quad 0 = \hat{x}^{(j+1)} - f(\hat{x}^{(j)}, u(\cdot), p, w(\cdot)) \quad \forall j \in \{k-M,\dots,k-1\} \tag{MHE$_k$}$$

$$0 = g(\hat{x}^{(j)}, \hat{z}^{(j)}, p) \quad \forall j \in \{k-M,\dots,k\},$$

$$0 \leqslant c_{\text{MHE}}(\hat{x}^{(j)}, p) \quad \forall j \in \{k-M,\dots,k\},$$

where $f(\hat{x}^{(j)}, u(\cdot), p, w(\cdot))$ maps the differential state from $\hat{x}^{(j)}$ at t_j to the one at t_{j+1} resulting from integrating Eqs. (3.53a) and (3.53b) using $u(\cdot)$, $w(\cdot)$ and p.

Overview

In Sections 3.5.1 to 3.5.3 several optimization problems have been defined. The use of the first-principles nonlinear model Eq. (3.53) is common to each of them. Additionally, in the case of Problems Eqs. (OCP) and (NMPC_k), their formulations include the state and control trajectories in function spaces as decision variables. This makes them optimization problems on an infinite-dimensional space.

To treat Problems Eqs. (OCP) and (NMPC_k) numerically, in Section 4.1 we will introduce the *Direct Multiple Shooting method* (DMS), firstly proposed by Plitt [124]. As a result of applying the method on each case, related, highly structured Nonlinear Programming Problems (NLP) are obtained which can be solved with nonlinear programming techniques to obtain approximate solutions. In this thesis, we use a newer version of the method, implemented in the optimal control package MUSCOD [92].

Notice, on the other hand, that the fact that the measurements in Eq. (MHE_k) are sampled, and the fixed amount of measurements entering the estimation window make the problem have a natural formulation in discrete time. The DMS method can also be used to solve this kind of problems.

4 Numerical Methods

Having stated the problems we are dealing with throughout this thesis in Section 3.5, we proceed to review the algorithmic blocks implementing the functionalities required for their solution. We begin describing the direct multiple shooting for optimal control, which reparametrizes Eq. (OCP) (or Eq. (NMPC$_k$) accordingly) and gives rise to a finite-dimensional, highly structured nonlinear programming problem (NLP). An algorithm for the solution of such problems is reviewed next, which in turn requires means to solve systems of differential-algebraic equations, which are reviewed lastly.

4.1 Direct Multiple Shooting for Optimal Control

The DMS method has been introduced for the numerical solution of optimal control problems by [18, 124]. The idea is to first produce a discrete-time version of Eq. (OCP). Since this corresponds to a finite dimensional NLP, the next step is to solve this problem using nonlinear programming techniques on a digital computer. In this section, we proceed to briefly explain particular variants of the method, but there are many more. For a detailed general overview, see e.g. [92].

In general, the DMS method is adequate to solve optimization problems under ODE/DAE constraints on closed, bounded time intervals $[t_0, t_f]$. If the initial state is known, let it be x_0. The first algorithmic step of the direct multiple shooting method consists in dividing the time horizon into N intervals, given by introducing $N + 1$ nodes with $t_0 < t_1 < \ldots < t_N = t_f$. In this thesis, we choose an equidistant node distribution, i.e. $t_i = t_0 + \left(\frac{i}{N}\right)(t_f - t_0)$, $\forall i \in \{0, \ldots, N\}$, although other distributions are also possible. The next step is the approximation of the control on each interval by a finite-dimensional representation with local support, i.e. $u(t) \approx \tilde{u}_i(t; q_i) \in n_u$ $\forall t \in [t_i, t_{i+1}]$, $\forall i \in \{0, \ldots, N-1\}$. Typical choices for $\tilde{u}_i(t; q_i)$ are families of piecewise polynomials. In particular, in this thesis we make use of a piecewise constant representation on each interval, i.e. $\tilde{u}_i(t; q_i) = q_i \in n_u$ $\forall t \in [t_i, t_{i+1}]$, $\forall i \in \{0, \ldots, N-1\}$. Further, we introduce vectors $s_0^x, s_1^x, \ldots, s_N^x$ and $s_0^z, s_1^z, \ldots, s_N^z$ of dimensions n_x and n_z respectively, called the *node differential* and *algebraic state vectors*, respectively. For each $i \in \{0, \ldots, N-1\}$, we denote by $x(t; t_i, s_i^x, s_i^z, q_i, p)$ the differential part of the solution, evaluated at time t, of the *relaxed initial value problem*

$$
\begin{aligned}
M(x(t), z(t), p)\frac{\mathrm{d}x}{\mathrm{d}t}(t) &= b(x(t), z(t), \tilde{u}(t; q_i), p, w(t)); \\
0 &= g(x(t), z(t), p) - g(s_i^x, s_i^z, p)\zeta_i(t), \ t \in [t_i, t_{i+1}] \\
x(t_i) &= s_i^x, \ z(t_i) = s_i^z.
\end{aligned}
\tag{4.1}
$$

The algebraic part of the DAE has been modified. In Eq. (4.1), any combination of initial values s_i^x, s_i^z is consistent, even if they would be not consistent in Eq. (3.53b). This reduces the computational load, since no consistency iterations have to be carried out to solve Eq. (4.1), and gives additional flexibility to the NLP solver later on, allowing intermediate steps in which consistency of the original DAE system is not exactly satisfied. A typical choice for functions ζ_i

is

$$\zeta_i(t) = \exp(-\beta(t - t_i)/(t_{i+1} - t_i)), \ \forall t \in [t_i, t_{i+1}]. \tag{4.2}$$

The factor $\beta > 0$ is suitably chosen so as to damp the initial inconsistency. On each interval the contributions to the objective function,

$$L_i(\boldsymbol{s}_i^x, \boldsymbol{s}_i^z, \boldsymbol{q}_i, \boldsymbol{p}) = \int_{t_i}^{t_{i+1}} L(\boldsymbol{x}_i(t), \boldsymbol{z}_i(t), \tilde{\boldsymbol{u}}(t; \boldsymbol{q}_i), \boldsymbol{p}) \, \mathrm{d}t, \tag{4.3}$$

can be obtained simultaneously if the ODE satisfied by the additional fictitious scalar differential state $\boldsymbol{x}_L$,

$$\begin{aligned}
\frac{\mathrm{d}}{\mathrm{d}t} \boldsymbol{x}_L(t) &= L(\boldsymbol{x}_i(t), \boldsymbol{z}_i(t), \tilde{\boldsymbol{u}}(t; \boldsymbol{q}_i), \boldsymbol{p}), & \forall t \in [t_i, t_{i+1}] \\
\boldsymbol{x}_L(t_i) &= 0 & \forall i \in \{0, \ldots, N-1\},
\end{aligned} \tag{4.4}$$

is integrated together with Eq. (4.1) [91].

In spite of having relaxed the algebraic constraints in Eq. (4.1), it is indeed desired that the node algebraic states corresponding to the solution of the NLP be consistent. Moreover, the differential state trajectories should be continuous at the nodes. We introduce thus the algebraic and the continuity constraints both at the nodes. In addition, at the first node, the node differential state vector $\boldsymbol{s}_0^x$ is chosen to correspond to the fixed initial state $\boldsymbol{x}_0$:

$$\begin{aligned}
\boldsymbol{x}(t_{i+1}; t_i, \boldsymbol{s}_i^x, \boldsymbol{s}_i^z, \boldsymbol{q}_i, \boldsymbol{p}) - \boldsymbol{s}_{i+1}^x &= 0, & \forall i \in \{0, \ldots, N-1\} & \tag{4.5a} \\
\boldsymbol{g}(\boldsymbol{s}_i^x, \boldsymbol{s}_i^z, \boldsymbol{p}) &= 0, & \forall i \in \{0, \ldots, N\} & \tag{4.5b} \\
\boldsymbol{s}_0^x - \boldsymbol{x}_0 &= 0. & & \tag{4.5c}
\end{aligned}$$

Concerning the path constraints, one option (see e.g. [92, 126] for other possibilities) is to evaluate them at the shooting nodes as

$$\boldsymbol{c}(\boldsymbol{s}_i^x, \boldsymbol{s}_i^z, \tilde{\boldsymbol{u}}(t_i; \boldsymbol{q}_i), \boldsymbol{p}) \geqslant 0 \qquad \forall i \in \{0, \ldots, N\}. \tag{4.6}$$

At this point, we have introduced an additional, auxiliary control vector $\boldsymbol{q}_N$, associated to the last multiple shooting node. This variable is imposed to satisfy the constraint

$$\boldsymbol{q}_N - \boldsymbol{q}_{N-1} = 0. \tag{4.7}$$

The resulting nonlinear programming problem (NLP) is

$$\begin{aligned}
\min_{\{\boldsymbol{s}_i^x, \boldsymbol{s}_i^z, \boldsymbol{q}_i\}_{i=0}^N} \quad & -\sum_{i=0}^{N-1} L_i(\boldsymbol{s}_i^x, \boldsymbol{s}_i^z, \boldsymbol{q}_i, \boldsymbol{p}) & & \tag{4.8a} \\
\text{s.t.} \quad & \boldsymbol{x}(t_{i+1}; t_i, \boldsymbol{s}_i^x, \boldsymbol{s}_i^z, \boldsymbol{q}_i, \boldsymbol{p}) - \boldsymbol{s}_{i+1}^x = 0, & i \in \{0, \ldots, N-1\}, & \tag{4.8b} \\
& \boldsymbol{g}(\boldsymbol{s}_i^x, \boldsymbol{s}_i^z, \boldsymbol{p}) = 0, & i \in \{0, \ldots, N\}, & \tag{4.8c} \\
& \boldsymbol{s}_0^x - \boldsymbol{x}_0 = 0, & & \tag{4.8d} \\
& \boldsymbol{q}_N - \boldsymbol{q}_{N-1} = 0 & & \tag{4.8e} \\
& \boldsymbol{c}(\boldsymbol{s}_i^x, \boldsymbol{s}_i^z, \boldsymbol{q}_i, \boldsymbol{p}) \geqslant 0, & i \in \{0, \ldots, N\}, & \tag{4.8f}
\end{aligned}$$

Defining $\boldsymbol{v} = \left[\boldsymbol{s}_0^x; \boldsymbol{s}_0^z; \boldsymbol{q}_0; \boldsymbol{s}_1^x; \boldsymbol{s}_1^z; \boldsymbol{q}_1; \ldots; \boldsymbol{q}_{N-1}; \boldsymbol{s}_N^x; \boldsymbol{s}_N^z; \boldsymbol{q}_N \right]$ as the decision variable vector, Prob-

lem (4.8) is

$$\min_{\mathbf{v}} \ \mathbf{F}(\mathbf{v}) \ \text{s.t.} \ \mathbf{G}(\mathbf{v}) = 0, \ \mathbf{H}(\mathbf{v}) \geqslant 0. \tag{4.9}$$

The dimension of $\mathbf{v}$ is $n_{\mathrm{v}} = (N+1)(n_{\mathrm{x}}+n_{\mathrm{z}}+n_{\mathrm{u}})$. Functions $\mathbf{G}$ and $\mathbf{H}$ have their images in spaces of dimension $n_{\mathrm{G}} = (N+1)(n_{\mathrm{x}}+n_{\mathrm{z}}) + n_{\mathrm{u}}$ and $n_{\mathrm{H}} = (N+1)n_{\mathrm{c}}$, respectively. Problem (4.9) is solved by means of a tailored partially reduced SQP method.

Remark 4.1.1 (Direct Multiple Shooting for NMPC) *In the NMPC case, for each $k \in \mathcal{K}$, consider $\hat{\mathbf{x}}_0^{(k)}$ instead of $\mathbf{x}_0$ in Eq. (4.5c). For all $i \in \{0, \dots, N\}$, the nodes are placed at $t_i^{(k)} = t_0^{(k)} + (i/N) \Delta t_{NMPC}$. The time limits in Eqs. (4.1) to (4.3) and (4.5) are thus $[t_i^{(k)}, t_{i+1}^{(k)}] \ \forall i \in \{0, \dots, N-1\}$. Proceeding as before, from each subproblem (NMPC$_k$) an NLP with the same structure as Eq. (4.8) is obtained, and thus the constraint vectors and decision variable components and dimensions remain the same. It is still possible to emphasize the dependency of each subproblem on the initial state $\hat{\mathbf{x}}_0^{(k)}$ and the current time $t_0^{(k)}$, and denote that the decision variable vector belongs to subproblem (NMPC$_k$) by writing the NLP*

$$\min_{\mathbf{v}_k} \ \mathbf{F}(\mathbf{v}_k) \ \text{s.t.} \ \mathbf{G}(\mathbf{v}_k; \hat{\mathbf{x}}_0^{(k)}, t_0^{(k)}) = 0, \ \mathbf{H}(\mathbf{v}_k) \geqslant 0, \tag{4.10}$$

with

$$\mathbf{v}_k = \left[\mathbf{s}_{0,k}^x; \mathbf{s}_{0,k}^z; \mathbf{q}_{0,k}; \mathbf{s}_{1,k}^x; \mathbf{s}_{1,k}^z; \mathbf{q}_{1,k}; \dots; \mathbf{q}_{N-1,k}; \mathbf{s}_{N,k}^x; \mathbf{s}_{N,k}^z; \mathbf{q}_{N,k} \right]. \tag{4.11}$$

Remark 4.1.2 (Direct Multiple Shooting for MHE) *In the MHE case, for each $k \in \mathcal{K}$, the k-th MHE subproblem (MHE$_k$) of Section 3.5.3 can be treated by means of the direct multiple shooting method by placing the nodes at times $t_{k-M+j}^{(k)}$ for $j \in \{k-M, \dots, k\}$. In this case, we denote the node differential and algebraic states as $\hat{\mathbf{x}}^{(j)}$ and $\hat{\mathbf{z}}^{(j)}$. This way, the node states can directly be interpreted as the state estimate iterates of subproblem (MHE$_k$). If we replace the function mapping $\mathbf{f}(\cdot)$ of subproblem (MHE$_k$) by the continuity constraints Eq. (4.5a), we obtain an NLP with the same structure as subproblem (MHE$_k$). To this end, we consider a zero-order hold sampling of the control, i.e. $\mathbf{u}(t) = \mathbf{u}(t_j) \ \forall t \in [t_j, t_{j+1}]$ and denote as $\mathbf{x}(t_{j+1}; t_j, \hat{\mathbf{x}}^{(j)}, \hat{\mathbf{z}}^{(j)}, \mathbf{u}(t_j), \mathbf{p})$ the result of integrating Eq. (4.1) along $[t_j, t_{j+1}]$ starting from $\hat{\mathbf{x}}^{(j)}$ and $\hat{\mathbf{z}}^{(j)}$ in place of $\mathbf{s}_i^x$ and $\mathbf{s}_i^z$ and using the control $\mathbf{u}(t)$ and the external inputs $\mathbf{w}(t)$. Therewith, the resulting k-th NLP subproblem is*

$$\min_{\substack{\hat{\mathbf{x}}^{(j)}, \hat{\mathbf{z}}^{(j)} \\ j \in \{k-M, \dots, k\}}} \ \sum_{j=k-M}^{k} \| \boldsymbol{\xi}_j - \mathbf{y}(\hat{\mathbf{x}}^{(j)}, \hat{\mathbf{z}}^{(j)}, \mathbf{w}(t_j), \mathbf{p}) \|_W^2 + \| L_3(\hat{\mathbf{x}}^{(k)}, \mathbf{p}) - \overline{L_3} \|_{\sigma_L}^2. \tag{4.12a}$$

$$\text{s.t.} \quad 0 = \mathbf{x}(t_{j+1}; t_j, \hat{\mathbf{x}}^{(j)}, \hat{\mathbf{z}}^{(j)}, \mathbf{u}(t_j), \mathbf{p}) - \hat{\mathbf{x}}^{(j+1)} \quad \forall j \in \{k-M, \dots, k-1\}, \tag{4.12b}$$

$$0 = \mathbf{g}(\hat{\mathbf{x}}^{(j)}, \hat{\mathbf{z}}^{(j)}, \mathbf{p}) \quad \forall j \in \{k-M, \dots, k\}, \tag{4.12c}$$

$$0 \leqslant \mathbf{c}_{MHE}(\hat{\mathbf{x}}^{(j)}, \hat{\mathbf{z}}^{(j)}, \mathbf{u}(t_j), \mathbf{p}) \quad \forall j \in \{k-M, \dots, k\}, \tag{4.12d}$$

which can be summarized as

$$\min_{\mathbf{v}_k} \ \| \mathbf{F}_{MHE}(\mathbf{v}_k, \boldsymbol{\Xi}_k) \|_2^2 \ \text{s.t.} \ \mathbf{G}_{MHE}(\mathbf{v}_k, \boldsymbol{\Xi}_k) = 0, \ \mathbf{H}_{MHE}(\mathbf{v}_k) \geqslant 0. \tag{4.13}$$

Therein, the decision variable vector $\mathbf{v}_k$ corresponds to

$$\mathbf{v}_k = \left[\hat{\mathbf{x}}^{(k-M)}; \hat{\mathbf{z}}^{(k-M)}; \hat{\mathbf{x}}^{(k-M+1)}; \hat{\mathbf{z}}^{(k-M+1)}; \dots; \hat{\mathbf{x}}^{(k)}; \hat{\mathbf{z}}^{(k)} \right]. \tag{4.14}$$

Therewith, the dimension of $\mathbf{v}_k$ is $n_{\mathrm{v,MHE}} = (M+1)(n_{\mathrm{x}}+n_{\mathrm{z}})$. Functions $\mathbf{G}_{MHE}$ and $\mathbf{H}_{MHE}$ have

their images in spaces of dimension $n_{G,MHE} = (M+1)(n_x + n_z)$ and $n_{H,MHE} = (M+1)n_{c,MHE}$, respectively.

4.1.1 A Tailored Sequential Quadratic Programming Method

Without loss of generality, in this section we focus on Eq. (4.9). In principle, its solution could be performed by means of any NLP software. However, great gains in computational efficiency can be obtained if the problem's special structure is leveraged. Introducing the Lagrangian multiplier vectors $\boldsymbol{\lambda} \in \mathbb{R}^{n_G}$ and $\boldsymbol{\mu} \in \mathbb{R}^{n_H}$ and the Lagrangian function

$$
\begin{aligned}
\mathcal{L} : \mathbb{R}^{n_v} \times \mathbb{R}^{n_G} \times \mathbb{R}^{n_H} &\longrightarrow \mathbb{R} \\
\mathcal{L}(\boldsymbol{v}, \boldsymbol{\lambda}, \boldsymbol{\mu}) &= \mathbf{F}(\boldsymbol{v}) - \boldsymbol{\lambda}^T \mathbf{G}(\boldsymbol{v}) - \boldsymbol{\mu}^T \mathbf{H}(\boldsymbol{v});
\end{aligned}
\tag{4.15}
$$

if we consider the k-th iteration of a general QP subproblem arising in a standard full-Hessian SQP implementation, where the current solution iterate is $\boldsymbol{v}_k$, and the current Lagrange multiplier estimates are $\boldsymbol{\lambda}_k$ and $\boldsymbol{\mu}_k$,

$$
\begin{aligned}
\min_{\Delta \boldsymbol{v}} \nabla_{\boldsymbol{v}} \mathbf{F}(\boldsymbol{v}_k)^T \Delta \boldsymbol{v} &+ \frac{1}{2} \Delta \boldsymbol{v}^T \nabla_{\boldsymbol{v}}^2 \mathcal{L}(\boldsymbol{v}_k, \boldsymbol{\lambda}_k, \boldsymbol{\mu}_k) \Delta \boldsymbol{v} \\
\text{s.t.} \quad \mathbf{G}(\boldsymbol{v}_k) &+ \nabla_{\boldsymbol{v}} \mathbf{G}(\boldsymbol{v}_k)^T \Delta \boldsymbol{v} = 0 \quad , \\
\mathbf{H}(\boldsymbol{v}_k) &+ \nabla_{\boldsymbol{v}} \mathbf{H}(\boldsymbol{v}_k)^T \Delta \boldsymbol{v} \geqslant 0
\end{aligned}
\tag{4.16}
$$

an efficient tailored SQP method can be devised by observing the structure of the involved matrices.

Since in the next paragraphs we will be discussed the properties of Eq. (4.16) and algorithmic steps taking all place within a single iteration k, we will temporarily drop this index in order to keep notation simple.

Structure of the QP. The first property of Eq. (4.16) that becomes evident is that the constraint Jacobian and the Lagrangian Hessian possess a sparse structure. This is due to the partial separability property of each function, which is a direct consequence of having introduced independent node variables, and having parametrized the control trajectories in a space of piecewise functions whose support is exactly each multiple shooting interval: we have that the corresponding functions $\mathbf{F}$, $\mathbf{G}$ and $\mathbf{H}$ can be written as a sum of functions depending on disjoint sets of variables. Defining the Jacobian matrices

$$
X_i^x \stackrel{\text{def}}{=} \frac{\partial \boldsymbol{x}}{\partial \boldsymbol{s}^x} \bigg|_{(t_{i+1}; t_i, s_i^x, s_i^z, q_i, p)} , \ X_i^z \stackrel{\text{def}}{=} \frac{\partial \boldsymbol{x}}{\partial \boldsymbol{s}^z} \bigg|_{(t_{i+1}; t_i, s_i^x, s_i^z, q_i, p)} , \ \text{and } X_i^q \stackrel{\text{def}}{=} \frac{\partial \boldsymbol{x}}{\partial \boldsymbol{q}} \bigg|_{(t_{i+1}; t_i, s_i^x, s_i^z, q_i, p)} ; \tag{4.17a}
$$

$$
G_i^x \stackrel{\text{def}}{=} \frac{\partial \boldsymbol{g}}{\partial \boldsymbol{x}}(s_i^x, s_i^z, q_i, p), \quad G_i^z \stackrel{\text{def}}{=} \frac{\partial \boldsymbol{g}}{\partial \boldsymbol{z}}(s_i^x, s_i^z, q_i, p), \quad \text{and } G_i^q \stackrel{\text{def}}{=} \frac{\partial \boldsymbol{g}}{\partial \boldsymbol{u}}(s_i^x, s_i^z, q_i, p); \tag{4.17b}
$$

$$
C_i^x \stackrel{\text{def}}{=} \frac{\partial \boldsymbol{c}}{\partial \boldsymbol{x}}(s_i^x, s_i^z, q_i, p), \quad C_i^z \stackrel{\text{def}}{=} \frac{\partial \boldsymbol{c}}{\partial \boldsymbol{z}}(s_i^x, s_i^z, q_i, p), \quad \text{and } C_i^q \stackrel{\text{def}}{=} \frac{\partial \boldsymbol{c}}{\partial \boldsymbol{u}}(s_i^x, s_i^z, q_i, p), \tag{4.17c}
$$

and the subvectors $\Delta \boldsymbol{v}_i \stackrel{\text{def}}{=} [\Delta s_i^x; \Delta s_i^z; \Delta q_i]$, we realize that the Lagrangian function (4.15) has a partially separable structure,

$$
\begin{aligned}
\mathcal{L}(\boldsymbol{v}, \boldsymbol{\lambda}, \boldsymbol{\mu}) = \sum_{i=0}^{N-1} \Big\{ &L_i(s_i^x, s_i^z, q_i, p) - \lambda_i^{x T} \big(\boldsymbol{x}(t_{i+1}; t_i, s_i^x, s_i^z, q_i, p) - s_{i+1}^x \big) \\
&- \lambda_i^{z T} \boldsymbol{g}(s_i^x, s_i^z, p) - \mu_i^T \boldsymbol{c}(s_i^x, s_i^z, q_i, p) \Big\} \\
&- \lambda_0^{0 T} \big(s_0^x - \boldsymbol{x}^{(k)} \big) - \lambda_N^{z T} \boldsymbol{g}(s_N^x, s_N^z, p) - \mu_N^T \boldsymbol{c}(s_N^x, s_N^z, q_N, p),
\end{aligned}
\tag{4.18}
$$

so we can write Eq. (4.16) as

$$\min_{\Delta \boldsymbol{v}_0,\dots,\Delta \boldsymbol{v}_N} \sum_{i=0}^{N} \left\{ \frac{1}{2} \Delta \boldsymbol{v}_i^T \nabla_{\boldsymbol{v}_i}^2 \mathcal{L}_i(\boldsymbol{v}_k, \boldsymbol{\lambda}_k, \boldsymbol{\mu}_k) \Delta \boldsymbol{v}_i + \nabla_{\boldsymbol{v}_i} L_i(\boldsymbol{s}_i^x, \boldsymbol{s}_i^z, \boldsymbol{q}_i, \boldsymbol{p})^T \Delta \boldsymbol{v}_i \right\} \tag{4.19a}$$

$$\text{s.t.} \quad \boldsymbol{X}_i^x \Delta \boldsymbol{s}_i^x + \boldsymbol{X}_i^z \Delta \boldsymbol{s}_i^z + \boldsymbol{X}_i^q \Delta \boldsymbol{q}_i - \Delta \boldsymbol{s}_{i+1}^x = \boldsymbol{s}_{i+1}^x - \boldsymbol{x}_{i+1} \quad \forall i \in \{0,\dots,N-1\}, \tag{4.19b}$$

$$\boldsymbol{G}_i^x \Delta \boldsymbol{s}_i^x + \boldsymbol{G}_i^z \Delta \boldsymbol{s}_i^z + \boldsymbol{G}_i^q \Delta \boldsymbol{q}_i = -\boldsymbol{g}_i \quad \forall i \in \{0,\dots,N\}, \tag{4.19c}$$

$$\Delta \boldsymbol{s}_0^x = \boldsymbol{x}^{(k)} - \boldsymbol{s}_0^x, \tag{4.19d}$$

$$\Delta \boldsymbol{q}_N - \Delta \boldsymbol{q}_{N-1} = 0, \tag{4.19e}$$

$$\boldsymbol{C}_i^x \Delta \boldsymbol{s}_i^x + \boldsymbol{C}_i^z \Delta \boldsymbol{s}_i^z + \boldsymbol{C}_i^q \Delta \boldsymbol{q}_i \geqslant -\boldsymbol{c}_i \quad \forall i \in \{0,\dots,N\}, \tag{4.19f}$$

where we have simplified the notation by introducing $\boldsymbol{g}_i = \boldsymbol{g}(\boldsymbol{s}_i^x, \boldsymbol{s}_i^z, \boldsymbol{p})$, $\boldsymbol{c}_i = \boldsymbol{c}(\boldsymbol{s}_i^x, \boldsymbol{s}_i^z, \boldsymbol{q}_i, \boldsymbol{p})$ and $\boldsymbol{x}_{i+1} = \boldsymbol{x}(t_{i+1}; t_i, \boldsymbol{s}_i^x, \boldsymbol{s}_i^z, \boldsymbol{q}_i, \boldsymbol{p})$. Further,

$$\mathcal{L}_i = \begin{cases} L_i(\boldsymbol{s}_i^x, \boldsymbol{s}_i^z, \boldsymbol{q}_i, \boldsymbol{p}) - \boldsymbol{\lambda}_0^{0^T} \left(\boldsymbol{s}_0^x - \boldsymbol{x}^{(k)} \right) - \boldsymbol{\lambda}_i^{x^T} \left(\boldsymbol{x}_{i+1} - \boldsymbol{s}_{i+1}^x \right) - \boldsymbol{\lambda}_i^{z^T} \boldsymbol{g}_i - \boldsymbol{\mu}_i^T \boldsymbol{c}_i & \text{if } i = 0 \\ L_i(\boldsymbol{s}_i^x, \boldsymbol{s}_i^z, \boldsymbol{q}_i, \boldsymbol{p}) - \boldsymbol{\lambda}_i^{x^T} \left(\boldsymbol{x}_{i+1} - \boldsymbol{s}_{i+1}^x \right) - \boldsymbol{\lambda}_i^{z^T} \boldsymbol{g}_i - \boldsymbol{\mu}_i^T \boldsymbol{c}_i & \text{if } 1 \leqslant i \leqslant N-1 \\ -\boldsymbol{\lambda}_i^{z^T} \boldsymbol{g}_i - \boldsymbol{\mu}_i^T \boldsymbol{c}_i & \text{if } i = N \end{cases}$$

$$\forall i \in \{0,\dots,N\}. \tag{4.20}$$

Partial Reduction. Since the DAE Eq. (3.53) is of index 1, $\boldsymbol{G}_i^z$ is invertible for all $i \in \{0,\dots,N\}$. Thus, for given steps $\Delta \boldsymbol{s}_i^x$ and $\Delta \boldsymbol{q}_i$, a value of $\Delta \boldsymbol{s}_i^z$ can be found that satisfies Eq. (4.19c), i.e. so that $\Delta \boldsymbol{v}_i$ lies in the null space of the linearized consistency constraints (4.19c). The step can be obtained as

$$\Delta \boldsymbol{s}_i^z = -\left(\boldsymbol{G}_i^z \right)^{-1} (\boldsymbol{G}_i^x \Delta \boldsymbol{s}_i^x + \boldsymbol{G}_i^q \Delta \boldsymbol{q}_i + \boldsymbol{g}_i)$$
$$= \boldsymbol{D}_i^x \Delta \boldsymbol{s}_i^x + \boldsymbol{D}_i^q \Delta \boldsymbol{q}_i + \boldsymbol{d}_i^g \quad \forall i \in \{0,\dots,N\}, \tag{4.21}$$

where matrices $\boldsymbol{D}_i^x$ and $\boldsymbol{D}_i^q$, and vector $\boldsymbol{d}_i^g$ are obtained by solving the linear system of equations

$$\boldsymbol{G}_i^z \left[\boldsymbol{D}_i^x \mid \boldsymbol{D}_i^q \mid \boldsymbol{d}_i^g \right] = -\left[\boldsymbol{G}_i^x \mid \boldsymbol{G}_i^q \mid \boldsymbol{g}_i \right], \tag{4.22}$$

which is usually sparse. In our implementation we use the Harwell subroutine MA48 [44, 137] to solve Eq. (4.22). This way, the steps corresponding to the algebraic node states $\Delta \boldsymbol{s}_i^z$, and the linearized consistency constraints can be completely eliminated from the QP subproblem (4.19). The expression for $\Delta \boldsymbol{v}_i$ is

$$\Delta \boldsymbol{v}_i = \underbrace{\begin{bmatrix} \mathbb{I}_{n_x} & 0 \\ \boldsymbol{D}_i^x & \boldsymbol{D}_i^q \\ 0 & \mathbb{I}_{n_u} \end{bmatrix}}_{\boldsymbol{D}_i} \underbrace{\begin{bmatrix} \Delta \boldsymbol{s}_i^x \\ \Delta \boldsymbol{q}_i \end{bmatrix}}_{\Delta \boldsymbol{v}_i^{\mathcal{N}}} + \underbrace{\begin{bmatrix} 0 \\ \boldsymbol{d}_i^g \\ 0 \end{bmatrix}}_{\boldsymbol{d}_i} = \boldsymbol{D}_i \Delta \boldsymbol{v}_i^{\mathcal{N}} + \boldsymbol{d}_i. \tag{4.23}$$

The remaining constraints take the form

$$(\boldsymbol{X}_i^x + \boldsymbol{X}_i^z \boldsymbol{D}_i^x) \Delta \boldsymbol{s}_i^x + (\boldsymbol{X}_i^q + \boldsymbol{X}_i^z \boldsymbol{D}_i^q) \Delta \boldsymbol{q}_i - \Delta \boldsymbol{s}_{i+1}^x = \boldsymbol{s}_{i+1}^x - \boldsymbol{x}_{i+1} - \boldsymbol{X}_i^z \boldsymbol{d}_i^g \quad \forall i \in \{0,\dots,N-1\}, \tag{4.24a}$$

$$\Delta \boldsymbol{s}_0^x = \boldsymbol{x}^{(k)} - \boldsymbol{s}_0^x \tag{4.24b}$$

$$(\boldsymbol{C}_i^x + \boldsymbol{C}_i^z \boldsymbol{D}_i^x) \Delta \boldsymbol{s}_i^x + (\boldsymbol{C}_i^q + \boldsymbol{C}_i^z \boldsymbol{D}_i^q) \Delta \boldsymbol{q}_i \geqslant -\left(\boldsymbol{c}_i + \boldsymbol{C}_i^z \boldsymbol{d}_i^g \right) \quad \forall i \in \{0,\dots,N\}, \tag{4.24c}$$

and, dropping arguments, the objective function takes the form (see Eq. (4.23))

$$\sum_{i=0}^{N}\left\{\frac{1}{2}\begin{bmatrix}\Delta s_i^x\\\Delta q_i\end{bmatrix}^T \boldsymbol{D}_i^T\nabla_{\boldsymbol{v}_i}^2\mathcal{L}_i\boldsymbol{D}_i\begin{bmatrix}\Delta s_i^x\\\Delta q_i\end{bmatrix}+(\boldsymbol{D}_i^T\nabla_{\boldsymbol{v}_i}^2\mathcal{L}_i\boldsymbol{d}_i+\boldsymbol{D}_i^T\nabla_{\boldsymbol{v}_i}L_i)^T\begin{bmatrix}\Delta s_i^x\\\Delta q_i\end{bmatrix}\right.$$
$$\left.+\frac{1}{2}\boldsymbol{d}_i^T\nabla_{\boldsymbol{v}_i}^2\mathcal{L}_i\boldsymbol{d}_i+\nabla_{\boldsymbol{v}_i}L_i^T\boldsymbol{d}_i\right\}. \tag{4.25}$$

Hessian approximation. In most partially reduced SQP implementations, the gradient cross term $\boldsymbol{D}_i^T\nabla_{\boldsymbol{v}_i}^2\mathcal{L}_i\boldsymbol{d}_i$ is neglected, and we proceed the same way. This is justified close to the solution, where $\boldsymbol{d}_i$ approaches zero, since $\boldsymbol{g}_i$ also does. Additionally, the terms $\frac{1}{2}\boldsymbol{d}_i^T\nabla_{\boldsymbol{v}_i}^2\mathcal{L}_i\boldsymbol{d}_i$ and $\nabla_{\boldsymbol{v}_i}L_i^T\boldsymbol{d}_i$ are constant, so they can be taken out of the objective function. The remaining partially reduced Hessian matrix block $\boldsymbol{D}_i^T\nabla_{\boldsymbol{v}_i}^2\mathcal{L}_i\boldsymbol{D}_i$ can be approximated by a symmetric and positive definite matrix

$$\boldsymbol{B}_k^{(i)}=\begin{bmatrix}\boldsymbol{B}_{ss}^{(i)} & \boldsymbol{B}_{sq}^{(i)}\\\boldsymbol{B}_{sq}^{(i)T} & \boldsymbol{B}_{qq}^{(i)}\end{bmatrix}, \tag{4.26}$$

so that the *partially reduced* QP with approximated Hessian can be written as

$$\min_{\substack{\Delta s_0^x,\ldots,\Delta s_N^x\\\Delta q_0,\ldots,\Delta q_N}}\sum_{i=0}^{N}\left\{\frac{1}{2}\Delta s_i^{x\,T}\boldsymbol{B}_{ss}^{(i)}\Delta s_i^x+\Delta s_i^{x\,T}\boldsymbol{B}_{sq}^{(i)}\Delta q_i+\frac{1}{2}\Delta q_i^{\,T}\boldsymbol{B}_{qq}^{(i)}\Delta q_i+\boldsymbol{U}_i^x\Delta s_i^x+\boldsymbol{U}_i^q\Delta q_i\right\} \tag{4.27a}$$

$$\text{s.t.}\qquad \boldsymbol{V}_i^x\Delta s_i^x+\boldsymbol{V}_i^q\Delta q_i-\Delta s_{i+1}^x=s_{i+1}^x-x_{i+1}-\boldsymbol{V}_i^g \qquad \forall i\in\{0,\ldots,N-1\}, \tag{4.27b}$$

$$\Delta s_0^x=x^{(k)}-s_0^x, \tag{4.27c}$$

$$\Delta q_N-\Delta q_{N-1}=0, \tag{4.27d}$$

$$\boldsymbol{W}_i^x\Delta s_i^x+\boldsymbol{W}_i^q\Delta q_i\geqslant-\boldsymbol{c}_i-\boldsymbol{W}_i^g \qquad \forall i\in\{0,\ldots,N\}, \tag{4.27e}$$

where we have introduced the matrices

$$\boldsymbol{U}_i^x\overset{\text{def}}{=}(\nabla_{s_i^x}L_i)^T+(\nabla_{s_i^z}L_i)^T\boldsymbol{D}_i^x \qquad \boldsymbol{U}_i^q\overset{\text{def}}{=}(\nabla_{q_i}L_i)^T+(\nabla_{s_i^z}L_i)^T\boldsymbol{D}_i^q \qquad \boldsymbol{U}_i^g\overset{\text{def}}{=}\nabla_{s_i^z}L_i^T\boldsymbol{d}_i^g \quad (4.28a)$$

$$\boldsymbol{V}_i^x\overset{\text{def}}{=}\boldsymbol{X}_i^x+\boldsymbol{X}_i^z\boldsymbol{D}_i^x \qquad\qquad \boldsymbol{V}_i^q\overset{\text{def}}{=}\boldsymbol{X}_i^q+\boldsymbol{X}_i^z\boldsymbol{D}_i^q \qquad\qquad \boldsymbol{V}_i^g\overset{\text{def}}{=}\boldsymbol{X}_i^z\boldsymbol{d}_i^g \quad (4.28b)$$

$$\boldsymbol{W}_i^x\overset{\text{def}}{=}\boldsymbol{C}_i^x+\boldsymbol{C}_i^z\boldsymbol{D}_i^x \qquad\qquad \boldsymbol{W}_i^q\overset{\text{def}}{=}\boldsymbol{C}_i^q+\boldsymbol{C}_i^z\boldsymbol{D}_i^q \qquad\qquad \boldsymbol{W}_i^g\overset{\text{def}}{=}\boldsymbol{C}_i^z\boldsymbol{d}_i^g, \quad (4.28c)$$

which can be efficiently generated as will be discussed in Section 4.1.2.

Condensing. At this point the *condensing* technique [124] can be applied: we leverage the fact that the partially reduced continuity constraints (4.27b) are equivalent to a *forward recursion*

$$\Delta s_{i+1}^x=\boldsymbol{V}_i^x\Delta s_i^x+\boldsymbol{V}_i^q\Delta q_i-s_{i+1}^x+x_{i+1}+\boldsymbol{V}_i^g \qquad \forall i\in\{0,\ldots,N-1\} \tag{4.29}$$

to obtain an affine linear relationship between two sets of variables $\Delta\boldsymbol{v}_1^c$ and $\Delta\boldsymbol{v}_2^c$. To this end, we reorder the variables by means of a permutation matrix $\boldsymbol{P}$ such that

$$\Delta\boldsymbol{v}^{\mathcal{N}}=\boldsymbol{P}\begin{bmatrix}\Delta\boldsymbol{v}_1^c\\\Delta\boldsymbol{v}_2^c\end{bmatrix},\text{ with}$$

$$\Delta\boldsymbol{v}_1^c=\begin{bmatrix}\Delta s_1^x;\Delta s_2^x;\ldots;\Delta s_N^x;\Delta q_N\end{bmatrix},\text{ and }\Delta\boldsymbol{v}_2^c=\begin{bmatrix}\Delta s_0^x;\Delta q_0;\ldots;\Delta q_{N-1}\end{bmatrix}. \tag{4.30}$$

If we define the matrices

$$
V_x^c = \begin{bmatrix}
\mathbb{I}_{n_x} & 0 & 0 & 0 & 0 \\
-V_1^x & \mathbb{I}_{n_x} & 0 & 0 & 0 \\
0 & \ddots & \ddots & 0 & 0 \\
0 & 0 & -V_{N-1}^x & \mathbb{I}_{n_x} & 0 \\
0 & 0 & 0 & 0 & \mathbb{I}_{n_q}
\end{bmatrix}
\quad \text{and} \quad
V_q^c = \begin{bmatrix}
V_0^x & V_0^q & 0 & 0 & 0 \\
0 & 0 & V_1^q & 0 & 0 \\
0 & 0 & 0 & \ddots & 0 \\
0 & 0 & 0 & 0 & V_{N-1}^q \\
0 & 0 & 0 & 0 & \mathbb{I}_{n_q}
\end{bmatrix},
\tag{4.31}
$$

and the vector $V_g^c = [V_{g\,0}^c ; \ldots ; V_{g\,N}^c]$ component-wise as

$$
\left(V_g^c\right)_i = \begin{cases} V_i^g + x_{i+1} - s_{i+1}^x & \text{if } 0 \leqslant i \leqslant N-1 \\ 0 & \text{otherwise} \end{cases} \quad \text{for } i \in \{0, \ldots, N\},
\tag{4.32}
$$

we can write the partially reduced continuity constraints (4.27b) and the control equality (4.19e) in matrix form as

$$
V_x^c \Delta v_1^c = V_q^c \Delta v_2^c + V_g^c.
\tag{4.33}
$$

This way, matrix V_x^c is invertible, and it holds that

$$
\Delta v_1^c = T \Delta v_2^c + t
\tag{4.34}
$$

for the matrix $T \stackrel{\text{def}}{=} (V_x^c)^{-1} V_q^c$ and vector $t \stackrel{\text{def}}{=} (V_x^c)^{-1} V_g^c$, which possess the structures

$$
T = \begin{bmatrix}
X_{1|0} & Q_{1|0} & 0 & 0 & 0 & 0 \\
X_{2|0} & Q_{2|0} & Q_{2|1} & 0 & 0 & 0 \\
X_{3|0} & Q_{3|0} & Q_{3|1} & Q_{3|2} & 0 & 0 \\
\vdots & \vdots & \vdots & \vdots & \ddots & 0 \\
X_{N|0} & Q_{N|0} & Q_{N|1} & Q_{N|2} & \cdots & Q_{N|N-1} \\
0 & 0 & 0 & 0 & 0 & \mathbb{I}_{n_q}
\end{bmatrix}
\quad \text{and} \quad
t = \begin{bmatrix}
t_1 \\
t_2 \\
t_3 \\
\vdots \\
t_N \\
0
\end{bmatrix}.
\tag{4.35}
$$

In (4.35), matrices $X_{i|0}$ can be interpreted as *propagation matrices* of the effect of a step Δs_0^x in the rest of the steps Δs_i^x. Likewise, matrices $Q_{j|i}$ give an account for the effect of a step Δq_i in the future steps Δs_j^x. This explains the structure of matrix T, and the recursive formulae

$$
X_{i+1|0} = V_i^x X_{i|0}, \qquad\qquad \forall i \in \{0, \ldots, N-1\}, \quad X_{0|0} = \mathbb{I}_{n_x}
\tag{4.36a}
$$

$$
Q_{j+1|j} = V_j^q, \quad Q_{i+1|j} = V_i^q Q_{i|j}, \quad \forall j \in \{0, \ldots, N-1\}, \; i \in \{j+1, \ldots, N-1\}
\tag{4.36b}
$$

$$
t_{i+1} = V_i^x t_i + x_{i+1} - s_{i+1}^x + V_i^g \quad \forall i \in \{0, \ldots, N-1\}, \; t_0 = 0,
\tag{4.36c}
$$

with which

$$
\Delta s_i^x = X_{i|0} \Delta s_0^x + \sum_{j=0}^{i-1} Q_{i|j} \Delta q_j + t_i, \qquad \forall i \in \{1, \ldots, N\}.
\tag{4.37}
$$

The introduction of the permutation matrix P of (4.30), allows to write the QP subproblem (4.27) as

$$\min_{\Delta v_1^c, \Delta v_2^c} \quad \frac{1}{2} \Delta v_1^{cT} B_k^{(1,1)} \Delta v_1^c + \Delta v_1^{cT} B_k^{(1,2)} \Delta v_2^c + \frac{1}{2} \Delta v_2^{cT} B_k^{(2,2)} \Delta v_2^c + g_1^{cT} \Delta v_1^c + g_2^{cT} \Delta v_2^c \tag{4.38a}$$

$$\text{s.t.} \quad A_{11}^c \Delta v_1^c + A_{12}^c \Delta v_2^c = b_1^c \tag{4.38b}$$

$$A_{21}^c \Delta v_1^c + A_{22}^c \Delta v_2^c = b_2^c \tag{4.38c}$$

$$C_1^c \Delta v_1^c + C_2^c \Delta v_2^c \geqslant c^c, \tag{4.38d}$$

where matrices $B_k^{(m,n)}$, A_{mn}^c and C_m^c and vectors g_m^c, b_m^c and c^c, with the appropriate indices m and n, result from permuting the columns and/or rows of the matrices in Eq. (4.27) in accordance to Eq. (4.30). The rows of (4.38b) correspond to the continuity constraints (4.27b) and the constraint on the last control (4.19e). The rows of (4.38c) correspond to the initial state constraint Eq. (4.27c). Finally, the block matrices of Eq. (4.38a) are defined as

$$B_k^{(1,1)} = \begin{bmatrix} B_{ss}^{(1)} & 0 & 0 & 0 & 0 \\ 0 & B_{ss}^{(2)} & 0 & 0 & 0 \\ 0 & 0 & \ddots & 0 & 0 \\ 0 & 0 & 0 & B_{ss}^{(N)} & B_{sq}^{(N)} \\ 0 & 0 & 0 & B_{sq}^{(N)T} & B_{qq}^{(N)} \end{bmatrix}, \quad B_k^{(1,2)} = \begin{bmatrix} 0 & 0 & B_{sq}^{(1)} & 0 & 0 \\ 0 & 0 & 0 & \ddots & 0 \\ 0 & 0 & 0 & 0 & B_{sq}^{(N-1)} \\ 0 & 0 & 0 & 0 & 0 \\ 0 & 0 & 0 & 0 & 0 \end{bmatrix} \tag{4.39a}$$

$$\text{and } B_k^{(2,2)} = \begin{bmatrix} B_{ss}^{(0)} & B_{sq}^{(0)} & 0 & 0 & 0 \\ B_{sq}^{(0)T} & B_{qq}^{(0)} & 0 & 0 & 0 \\ 0 & 0 & B_{qq}^{(1)} & 0 & 0 \\ 0 & 0 & 0 & \ddots & 0 \\ 0 & 0 & 0 & 0 & B_{qq}^{(N-1)} \end{bmatrix}. \tag{4.39b}$$

After applying Eq. (4.34), the *condensed* QP subproblem is obtained. It takes the form

$$\min_{\Delta v_2^c = \left[\Delta s_0^x; \Delta q_0; \dots; \Delta q_{N-1}\right]} \quad \frac{1}{2} \Delta v_2^{cT} B_k^c \Delta v_2^c + \overline{g}^{cT} \Delta v_2^c \tag{4.40a}$$

$$\text{s.t.} \quad \Delta s_0^x = x^{(k)} - s_0^x, \tag{4.40b}$$

$$\bar{C}^c \Delta v_2^c \geqslant \bar{c}^c, \tag{4.40c}$$

where the matrices

$$B_k^c = T^T B_k^{(1,1)} T + T^T B_k^{(1,2)} + B_k^{(1,2)T} T + B_k^{(2,2)}$$

$$= \begin{bmatrix} \bar{B}_{s,s} & \bar{B}_{s,0} & \cdots & \bar{B}_{s,N-1} \\ \hline \bar{B}_{s,0}^T & \bar{B}_{0,0} & \cdots & \bar{B}_{0,N-1} \\ \vdots & \vdots & \ddots & \vdots \\ \bar{B}_{s,N-1}^T & \bar{B}_{0,N-1}^T & \cdots & \bar{B}_{N-1,N-1} \end{bmatrix}, \tag{4.41a}$$

$$\bar{C}^c = C_2^c + C_1^c T = \begin{bmatrix} \bar{C}_{0,s} & \bar{C}_{0,0} & 0 & 0 \\ \vdots & \vdots & \ddots & 0 \\ \bar{C}_{N-1,s} & \bar{C}_{N-1,0} & \cdots & \bar{C}_{N-1,N-1} \\ \bar{C}_{N,s} & \bar{C}_{N,0} & \cdots & \bar{C}_{N,N-1} \end{bmatrix}, \tag{4.41b}$$

and the vectors

$$\bar{g}^{c} = T^{T}B_{k}^{(1,1)}t + B_{k}^{(1,2)}t + T^{T}g_{1}^{c} + g_{2}^{c} = [\bar{g}_{s} \mid \bar{g}_{0} \mid \cdots \mid \bar{g}_{N-1}]^{T}, \tag{4.41c}$$

$$\bar{c}^{c} = c^{c} - C_{1}^{c}t \qquad\qquad\qquad = [\bar{c}_{0}; \cdots; \bar{c}_{N}], \tag{4.41d}$$

can be calculated by means of the formulas

$$\bar{B}_{s,s} = B_{ss}^{(0)} + \sum_{i=1}^{N} X_{i|0}^{T}B_{ss}^{(i)}X_{i|0} \tag{4.42a}$$

$$\bar{B}_{s,i} = X_{i|0}^{T}B_{sq}^{(i)} + \sum_{j=i+1}^{N} X_{j|0}^{T}B_{ss}^{(j)}Q_{j|i} \qquad \forall i \in \{0,\ldots,N-1\} \tag{4.42b}$$

$$\bar{B}_{i,j} = Q_{j|i}^{T}B_{sq}^{(i)} + \sum_{k=i+1}^{N} Q_{k|i}^{T}B_{ss}^{(k)}Q_{k|j} \qquad \forall j \in \{0,\ldots,N-1\},\ i \in \{j+1,\ldots,N-1\} \tag{4.42c}$$

$$\bar{B}_{i,i} = B_{qq}^{(i)} + \sum_{k=i+1}^{N} Q_{k|i}^{T}B_{ss}^{(k)}Q_{k|i} \qquad \forall i \in \{0,\ldots,N-1\} \tag{4.42d}$$

$$\bar{C}_{i,s} = W_{i}^{x}X_{i|0} \qquad\qquad \forall i \in \{0,\ldots,N\} \tag{4.42e}$$

$$\bar{C}_{i,i} = W_{i}^{q} \qquad\qquad \forall i \in \{0,\ldots,N-1\}, \tag{4.42f}$$

$$\bar{C}_{i,j} = W_{i}^{x}Q_{i|j} \qquad\qquad \forall i \in \{1,\ldots,N\},\ j \in \{0,\ldots,i-1\},$$
$$(i,j) \neq (N,N-1)$$

$$\bar{C}_{N,N-1} = W_{N}^{x}Q_{N|N-1} + W_{N}^{q} \tag{4.42g}$$

$$\bar{g}_{s} = U_{0}^{x} + \sum_{i=1}^{N}(U_{i}^{x} + t_{i}^{T}B_{ss}^{(i)})X_{i|0} \tag{4.42h}$$

$$\bar{g}_{j} = U_{0}^{q} + \sum_{i=1}^{N}(U_{i}^{x} + t_{i}^{T}B_{ss}^{(i)})Q_{i|j} \qquad \forall j \in \{0,\ldots,N-1\} \tag{4.42i}$$

$$\bar{c}_{0} = -(c_{0} + W_{0}^{g}) \tag{4.42j}$$

$$\bar{c}_{i} = -(c_{i} + W_{i}^{g} - W_{i}^{x}t_{i}) \qquad \forall i \in \{1,\ldots,N\}. \tag{4.42k}$$

For further details on the condensing step, see [18, 36, 91, 92, 124].

Efficient condensing strategies. A direct implementation of Eqs. (4.36) to (4.42) leads to an algorithm with a complexity which is cubic on the number of multiple shooting intervals N. The most expensive steps, which correspond to Eq. (4.42c), are associated with the formation of the lower-right part of the partially reduced Hessian B_{k}^{c}, see Eq. (4.41a). Fortunately, it is also possible to implement a condensing algorithm with a complexity of $\mathcal{O}(N^{2})$, as suggested in [5], cf. [53]. To that end, the special structure of matrix B_{k}^{c} is exploited together with the fact that, for each i in $\{0,\ldots,N\}$, the matrix $B_{k}^{(i)}$ is symmetric and positive definite. Observing that

$$B_{k}^{c} = V_{q}^{c\,T}(V_{x}^{c})^{-T}B_{k}^{(1,1)}T + T^{T}B_{k}^{(1,2)} + B_{k}^{(1,2)\,T}T + B_{k}^{(2,2)}, \tag{4.43}$$

the auxiliary matrix $Z^{c} \overset{\text{def}}{=} (V_{x}^{c})^{-T}B_{k}^{(1,1)}T$ can be defined. The matrix T can be formed in $\mathcal{O}(N^{2})$ steps according to Eq. (4.36) and then be used to build Z^{c} with the help of the following

identities:

$$Z_{N+1,1}^{c} = B_{sq}^{(N)^{T}} X_{N,0}, \qquad Z_{N+1,i}^{c} = B_{sq}^{(N)^{T}} Q_{N,i-2}, \ \forall i \in \{2,\ldots,N+1\} \qquad (4.44a)$$

$$Z_{N,1}^{c} = B_{ss}^{(N)} X_{N,0}, \qquad Z_{N,i}^{c} = B_{ss}^{(N)} Q_{N,i-2}, \quad \forall i \in \{2,\ldots,N+1\} \qquad (4.44b)$$

$$Z_{i,1}^{c} = B_{ss}^{(i)} X_{i,0} + V_{i}^{x\,T} Z_{i+1,1}^{c} \qquad\qquad \forall i \in \{N-1,\ldots,1\} \qquad (4.44c)$$

$$Z_{i,j}^{c} = B_{ss}^{(i)} Q_{i,j-2} + V_{i}^{x\,T} Z_{i+1,j}^{c} \qquad\quad \forall i \in \{N-1,\ldots,1\}, j \in \{1,\ldots,N+1\} \qquad (4.44d)$$

Using Z^{c}, the block matrices constituting B_{k}^{c} can be obtained. Starting with the blocks corresponding to the diagonal, the following identities can be used:

$$\bar{B}_{s,s} = B_{ss}^{(0)} + (V_{0}^{x})^{T} Z_{1,1}^{c} \qquad (4.45a)$$

$$\bar{B}_{i,i} = B_{qq}^{(i)} + (V_{i}^{q})^{T} Z_{i+1,i+2}^{c} \qquad\qquad \forall i \in \{0,\ldots,N-2\} \quad (4.45b)$$

$$\bar{B}_{N-1,N-1} = B_{qq}^{(N-1)} + (V_{N-1}^{q})^{T} Z_{N,N+1}^{c} + Z_{N+1,N+1}^{c}, \qquad (4.45c)$$

whereas the blocks located below the diagonal can be computed by means of

$$\bar{B}_{s,i}^{T} = B_{sq}^{(i)^{T}} X_{i,0} + (V_{i}^{q})^{T} Z_{i+1,1}^{c} \qquad\qquad \forall i \in \{0,\ldots,N-2\} \quad (4.45d)$$

$$\bar{B}_{s,N-1}^{T} = B_{sq}^{(N-1)^{T}} X_{N-1,0} + (V_{N-1}^{q})^{T} Z_{N,1}^{c} + Z_{N+1,1}^{c} \qquad (4.45e)$$

$$\bar{B}_{i,j}^{T} = B_{sq}^{(i)^{T}} Q_{i,j} + (V_{i}^{q})^{T} Z_{i+1,j+2}^{c} \quad \forall i \in \{1,\ldots,N-2\}, j \in \{0,\ldots,i-1\} \qquad (4.45f)$$

$$\bar{B}_{N-1,j}^{T} = B_{sq}^{(N-1)^{T}} Q_{N-1,j} + (V_{N-1}^{q})^{T} Z_{N,j+2}^{c} + Z_{N+1,j+2}^{c} \quad \forall j \in \{0,\ldots,N-2\} \qquad (4.45g)$$

Notice that due to symmetry, only the computation of the lower triangular portion of B_{k}^{c} is needed to obtain the whole matrix.

Solution of the condensed QP. The condensed QP subproblem (4.40) can be solved by means of a standard QP solver. In this work we have resorted to a C-converted version of QPOPT 1.0-10 [56]. As a result, a solution vector $\Delta v_{2}^{c\diamond}$ and the respective Lagrange multiplier vectors $\lambda_{2}^{\diamond}$ corresponding to (4.40b) and $\mu^{\diamond}$ corresponding to (4.40c) are obtained. Afterwards, Eq. (4.34) can be used to obtain the remaining part of the solution vector for Eq. (4.38), $\Delta v_{1}^{c\diamond}$. The Lagrange multiplier vector corresponding to the consistency constraints (4.38b) can be reconstructed by means of the identity[1]

$$\lambda_{1}^{\diamond} = A_{11}^{c\,-T}(B_{k}^{(1,1)} \Delta v_{1}^{c\diamond} + B_{k}^{(1,2)} \Delta v_{2}^{c\diamond} + g_{1}^{c} - C_{1}^{c\,T} \mu^{\diamond}). \qquad (4.46)$$

Termination criterion and step length selection. With the solution vectors $\Delta v_{1}^{c\diamond}$, $\Delta v_{2}^{c\diamond}$, Eq. (4.30) can be applied to obtain $\Delta v^{\mathcal{N}\diamond}$. Then, Eq. (4.23) can be applied blockwise to obtain the full step Δv_{i}. Afterwards, with the multipliers $\lambda_{k}^{\diamond} = (\lambda_{1}^{\diamond}, \lambda_{2}^{\diamond})$ and $\mu_{k}^{\diamond}$ (here we have reintroduced the index k corresponding to each SQP iteration), the termination criterion can

---

[1]Cf. [36]. In our formulation, no constraints other than the continuity and the initial state are included in (4.38). Therefore $A_{21}^{c} = 0$, and $\lambda_{1}^{\diamond}$ is independent of $\lambda_{2}^{\diamond}$.

be checked. For those means we define the quantity

$$K(\boldsymbol{v}_k, \Delta \boldsymbol{v}^{c\diamond}, \boldsymbol{\lambda}^\diamond, \boldsymbol{\mu}^\diamond) \overset{\text{def}}{=} \max_{i \in \{0, \dots, N\}} \|\boldsymbol{g}(\boldsymbol{s}_i^x, \boldsymbol{s}_i^z, \boldsymbol{p})\|_\infty + \sum_{i=0}^{N} \left| \boldsymbol{U}_i^x \Delta \boldsymbol{s}_i^{x\diamond} + \boldsymbol{U}_i^q \Delta \boldsymbol{q}_i^\diamond + \boldsymbol{U}_i^g \right|$$

$$+ \sum_{i=0}^{N-1} \sum_{j=1}^{n_x} \left| \boldsymbol{\lambda}_{i,j}^{x\diamond} \left(\boldsymbol{s}_{i+1,j}^x - \boldsymbol{x}_{i+1,j} - \boldsymbol{V}_{i,j}^g \right) \right| + \sum_{i=0}^{N} \sum_{j=1}^{n_c} \left| \boldsymbol{\mu}_{i,j}^\diamond \left(-\boldsymbol{c}_{i,j} - \boldsymbol{W}_{i,j}^g \right) \right| \quad (4.47)$$

and check whether $K(\boldsymbol{v}_k, \Delta \boldsymbol{v}^{c\diamond}, \boldsymbol{\lambda}^\diamond, \boldsymbol{\mu}^\diamond)$ is less or equal than a predefined NLP accuracy ACC. If this is the case the routine is stopped, and $[\boldsymbol{v}^\star; \boldsymbol{\lambda}^\star; \boldsymbol{\mu}^\star] := [\boldsymbol{v}_k; \boldsymbol{\lambda}_k; \boldsymbol{\mu}_k]$ is returned as the solution. Otherwise, a line search strategy like the partially multiplier-free strategy of [92] can be used in order to obtain a step length α_k with which the current iterate $\boldsymbol{v}_k$ and Lagrange multiplier estimates $\boldsymbol{\lambda}_k$ and $\boldsymbol{\mu}_k$ can be updated:

$$\begin{bmatrix} \boldsymbol{\lambda}_{k+1} \\ \boldsymbol{\mu}_{k+1} \end{bmatrix} = \begin{bmatrix} \boldsymbol{\lambda}_k \\ \boldsymbol{\mu}_k \end{bmatrix} + \alpha_k \begin{bmatrix} \boldsymbol{\lambda}_k^\diamond - \boldsymbol{\lambda}_k \\ \boldsymbol{\mu}_k^\diamond - \boldsymbol{\mu}_k \end{bmatrix}, \quad \text{and} \quad \boldsymbol{v}_{k+1} = \boldsymbol{v}_k + \alpha_k \Delta \boldsymbol{v}_k. \quad (4.48)$$

Partially reduced approximated Hessian update. Before updating $\Delta \boldsymbol{v}_k$, the "old" partially reduced Lagrangian gradient is computed blockwise using the new multiplier estimates $\boldsymbol{\lambda}_{k+1}$ and $\boldsymbol{\mu}_{k+1}$, and the current iterate's solution estimate $\boldsymbol{v}_k$, as

$$\boldsymbol{D}_{i,k}^T \nabla_{\boldsymbol{v}_{i,k}} \mathcal{L}_i(\boldsymbol{v}_{i,k}, \boldsymbol{\lambda}_{k+1}, \boldsymbol{\mu}_{k+1}) =$$

$$\begin{bmatrix} \boldsymbol{U}_{i,k}^x & \boldsymbol{U}_{i,k}^q \end{bmatrix}^T - \begin{bmatrix} \boldsymbol{V}_{i,k}^x & \boldsymbol{V}_{i,k}^q \\ \boldsymbol{W}_{i,k}^x & \boldsymbol{W}_{i,k}^q \end{bmatrix}^T \begin{bmatrix} \boldsymbol{\lambda}_{i,k+1}^x \\ \boldsymbol{\mu}_{i,k+1} \end{bmatrix} - \begin{bmatrix} (\boldsymbol{\lambda}_{0,k+1}^0 - \boldsymbol{\lambda}_{i-1,k+1}^x)\delta_{i,0} + \boldsymbol{\lambda}_{i-1,k+1}^x \\ 0 \end{bmatrix},$$

$$\forall i \in \{0, \dots, N\}, \quad (4.49)$$

where $\delta_{i,0} = 1$ if $i = 0$, and zero otherwise. After updating $\boldsymbol{v}_k$, the new matrices of Eq. (4.23) can be computed, and both the right-hand sides of Eqs. (4.19b) to (4.19f) and the new directional derivatives of Eq. (4.28) can be computed. With the latter, the "new" partially reduced Lagrangian gradient is computed blockwise as in Eq. (4.49), with $\boldsymbol{v}_{k+1}$, $\boldsymbol{\lambda}_{k+1}$ and $\boldsymbol{\mu}_{k+1}$ as arguments. These partially reduced Lagrangian gradients are used for implementing a high-rank updating scheme for the partially reduced Hessian approximation $\boldsymbol{B}_{k+1}$ [18, 92, 124]. Concretely, the well-known modified BFGS scheme by Powell [127] is applied to each block $\boldsymbol{B}_{k+1}^{(i)}$ of Eq. (4.26): for $i \in \{0, \dots, N\}$,

$$\boldsymbol{\delta}_{i,k} = \alpha_k \begin{bmatrix} \Delta \boldsymbol{s}_i^x; & \Delta \boldsymbol{q}_i \end{bmatrix} \quad (4.50a)$$

$$\boldsymbol{\gamma}_{i,k} = \boldsymbol{D}_{i,k+1}^T \nabla_{\boldsymbol{v}_{i,k+1}} \mathcal{L}_i(\boldsymbol{v}_{i,k+1}, \boldsymbol{\lambda}_{k+1}, \boldsymbol{\mu}_{k+1}) - \boldsymbol{D}_{i,k}^T \nabla_{\boldsymbol{v}_{i,k}} \mathcal{L}_i(\boldsymbol{v}_{i,k}, \boldsymbol{\lambda}_k, \boldsymbol{\mu}_k), \quad (4.50b)$$

$$\Theta_{i,k} = \begin{cases} 1 & \text{if } \boldsymbol{\delta}_{i,k} \geqslant \epsilon_\Theta \boldsymbol{\delta}_{i,k}^T \boldsymbol{B}_k^{(i)} \boldsymbol{\delta}_{i,k} \\ \left((1 - \epsilon_\Theta) \boldsymbol{\delta}_{i,k}^T \boldsymbol{B}_k^{(i)} \boldsymbol{\delta}_{i,k} \right) / \left(\boldsymbol{\delta}_{i,k}^T \boldsymbol{B}_k^{(i)} \boldsymbol{\delta}_{i,k} - \boldsymbol{\delta}_{i,k}^T \boldsymbol{\gamma}_{i,k} \right) & \text{otherwise,} \end{cases} \quad (4.50c)$$

$$\boldsymbol{\eta}_{i,k} = \Theta_{i,k} (\boldsymbol{\gamma}_{i,k} - \boldsymbol{B}_k^{(i)} \boldsymbol{\delta}_{i,k}) + \boldsymbol{B}_k^{(i)} \boldsymbol{\delta}_{i,k}, \quad \text{and} \quad (4.50d)$$

$$\boldsymbol{B}_{k+1}^{(i)} = \boldsymbol{B}_k^{(i)} + \frac{\boldsymbol{\eta}_{i,k} \boldsymbol{\eta}_{i,k}^T}{\boldsymbol{\eta}_{i,k}^T \boldsymbol{\delta}_{i,k}} - \frac{\boldsymbol{B}_k^{(i)} \boldsymbol{\delta}_{i,k} \boldsymbol{\delta}_{i,k}^T \boldsymbol{B}_k^{(i)}}{\boldsymbol{\delta}_{i,k}^T \boldsymbol{B}_k^{(i)} \boldsymbol{\delta}_{i,k}}. \quad (4.50e)$$

The initial block matrices $\boldsymbol{B}_0^{(i)}$ are all calculated using a procedure described in [92, 124], in which a scalar κ_R is chosen so that $\boldsymbol{B}_0^{(i)} = (1/\kappa_R)\mathbb{I}_{n_x + n_u}$.

Limited memory updates. In our computations we have also used a *limited memory* version of this implementation: storing the last 2ℓ vectors $\boldsymbol{\delta}_{i,k-\ell+1}\ldots\boldsymbol{\delta}_{i,k}$, and $\boldsymbol{\gamma}_{i,k-\ell+1},\ldots,\boldsymbol{\gamma}_{i,k}$, the vectors $\boldsymbol{\zeta}_{i,l}$, $\boldsymbol{\eta}_{i,l}$ and the scalars $\vartheta_{i,l}$, and $\varpi_{i,l}$ can be generated using the formulas

$$\boldsymbol{\zeta}_{i,l} = \frac{1}{\kappa_R}\boldsymbol{\delta}_{i,l} + \sum_{j=k-\ell+1}^{l-1}\frac{\boldsymbol{\eta}_{i,j}^T\boldsymbol{\delta}_{i,j}}{\vartheta_{i,j}}\boldsymbol{\eta}_{i,j} - \frac{\boldsymbol{\zeta}_{i,j}^T\boldsymbol{\delta}_{i,j}}{\varpi_{i,j}}\boldsymbol{\zeta}_{i,j}, \tag{4.51a}$$

$$\boldsymbol{\eta}_{i,l} = \Theta_{i,l}(\boldsymbol{\gamma}_{i,l} - \boldsymbol{\zeta}_{i,l}) + \boldsymbol{\zeta}_{i,l}, \tag{4.51b}$$

$$\vartheta_{i,l} = \boldsymbol{\eta}_{i,l}^T\boldsymbol{\delta}_{i,l}, \text{ and} \tag{4.51c}$$

$$\varpi_{i,l} = \boldsymbol{\delta}_{i,l}^T\boldsymbol{\zeta}_{i,l}, \tag{4.51d}$$

for $l \in \{k-\ell+1,\ldots,k\}$. Using these vectors and scalars the blocks for the next iteration can be obtained as

$$\boldsymbol{B}_{k+1}^{(i)} = \frac{1}{\kappa_R}\mathbb{I}_{n_x+n_u} + \sum_{j=k-\ell+1}^{k}\left(\frac{\boldsymbol{\eta}_{i,j}\boldsymbol{\eta}_{i,j}^T}{\vartheta_{i,j}} - \frac{\boldsymbol{\zeta}_{i,j}\boldsymbol{\zeta}_{i,j}^T}{\varpi_{i,j}}\right). \tag{4.52}$$

During the first ℓ iterations, we consider initial Hessian approximation $\boldsymbol{B}_0^{(i)}$ described above, and apply Eqs. (4.51) and (4.52) starting the corresponding sums from $j = 0$ instead of $j = k-\ell+1$.

Once $\boldsymbol{v}_{k+1}$, $\boldsymbol{\lambda}_{k+1}$, $\boldsymbol{\mu}_{k+1}$ and $\boldsymbol{B}_{k+1}$ are known, we are ready to lay out the next QP subproblem, and the previously described steps can be repeated from Eq. (4.30) on. In the following, we sketch with some more precision the way, the evaluation of the right-hand sides of Eqs. (4.19b) to (4.19f) and of the directional derivatives of Eq. (4.23) takes place. The following section is based on [8, 9, 15, 17].

4.1.2 Integration and Differentiation

As explained in the previous section, on each SQP iteration the determination of the range and the null spaces of the linearized consistency constraints (4.19c) must take place. For these means, function $\boldsymbol{g}(\boldsymbol{s}_i^x,\boldsymbol{s}_i^z,\boldsymbol{q}_i,\boldsymbol{p})$ can be directly evaluated, and its Jacobian matrices $\boldsymbol{G}_i^x$, $\boldsymbol{G}_i^z$ and $\boldsymbol{G}_i^q$ can be approximated via finite differences. In particular, the sparsity pattern of $\boldsymbol{g}(\cdot)$ can be exploited so as to save computational effort. The same strategy can also be applied to evaluate function $\boldsymbol{c}(\boldsymbol{s}_i^x,\boldsymbol{s}_i^z,\boldsymbol{q}_i,\boldsymbol{p})$ and obtain its Jacobian matrices $\boldsymbol{C}_i^x$, $\boldsymbol{C}_i^z$ and $\boldsymbol{C}_i^q$. Resorting to $\boldsymbol{D}_i^x$, $\boldsymbol{D}_i^q$ and $\boldsymbol{d}_i^g$ from Eq. (4.22), we can obtain matrices $\boldsymbol{W}_i^x$, $\boldsymbol{W}_i^q$ and vector $\boldsymbol{W}_i^g$ by means of matrix and vector multiplications. The partial separability of the NLP problem (4.9) results very advantageous at this point, since a small number of perturbations are required for the approximation of each Jacobian matrix.

A much more computationally expensive task is that of evaluating the partially reduced linearized continuity constraints (4.27b) and the partially reduced objective function gradients of Eq. (4.27a). In order to compute $\boldsymbol{x}_{i+1}$, Eq. (4.1) needs to be solved on each interval. The Jacobian matrices $\boldsymbol{V}_i^x$, $\boldsymbol{V}_i^z$ and $\boldsymbol{V}_i^q$ correspond thus to directional derivatives of this *solution* in the directions given by the columns of matrix $\boldsymbol{D}_i$ of Eq. (4.23). The same applies for the partially reduced objective function gradients $\boldsymbol{U}_i^x$, $\boldsymbol{U}_i^q$ and $\boldsymbol{U}_i^g$. Similar to what is done for $\boldsymbol{c}_i$ or $\boldsymbol{g}_i$ as explained the previous paragraph, these directional derivatives could be computed by means of finite differences, an approach that we call *external numerical differentiation (END)*: integrate Eq. (4.1) with perturbed initial states and controls as adequate, say $(\boldsymbol{s}_i^x,\boldsymbol{s}_i^z,\boldsymbol{q}_i)+\epsilon\boldsymbol{D}_{i,j}$ for $\boldsymbol{D}_{i,j}$ the j-th column of matrix $\boldsymbol{D}_i$, obtaining the perturbed differential state at the end of the interval $\boldsymbol{x}_{i+1}^\epsilon$, and then approximate the corresponding derivative by means of the finite

difference $(\boldsymbol{x}_{i+1}^{\epsilon} - \boldsymbol{x}_{i+1})/\epsilon$.

For all our future arguments, let us assume that the DAE integrations take place with some predefined relative integration tolerance TOL. A well-known fact is that, due to the discrete nature of the stepsize and order selection mechanisms of modern DAE integrators, their output is in general a discontinuous function of the initial values and parameters (recall that $\boldsymbol{q}_i$ is seen by the integrator as a DAE parameter): if they are changed, jumps in the order of TOL are to be expected in the output (see e.g. [55]). This makes it necessary to have a very small integration tolerance TOL for END to produce derivative approximations that are accurate enough to work with the NLP accuracy ACC: both $\boldsymbol{x}_{i+1}^{\epsilon}$ and $\boldsymbol{x}_{i+1}$ are at a distance of $o(\mathrm{TOL})$ from their real values, and the difference $\boldsymbol{x}_{i+1}^{\epsilon} - \boldsymbol{x}_{i+1}$, assuming the Hessian matrices of the components of $\boldsymbol{x}_{i+1}$ are bounded in the region of interest, is at a distance of $o(\epsilon^2)$ from the $\epsilon \boldsymbol{D}_{i,j}$-directed derivative. The result is that END can approximate the derivative with a precision of $o(\sqrt{\mathrm{TOL}})$ at best, which occurs at $\epsilon^2 = o(\mathrm{TOL})$ (cf. [17]). Another disadvantage of END is that the similarity between the nominal and the perturbed trajectories is not exploited, leading to inefficiencies for the case when the underlying DAE system is stiff, which is our case. For example, the integrator may have to repeat the same adaption steps on the same integration instants many times.

An alternative introduced in [15], called *internal numerical differentiation (IND)*, consists on differentiating the trajectory generated by the adaptive stepsize and order scheme itself. There exist many variants of the method, that has been as well adapted to deal with a variety of integration routines for both ODEs and DAEs, see e.g. [15, 124, 16, 45, 158, 8, 1, 2]. In [16], the *analytical limit of IND* has been introduced: for linear multistep integration methods, the numerical integration of the *directional variational DAE*,

$$\boldsymbol{M}|_{(\cdot)} \frac{\mathrm{d}}{\mathrm{d}t} \big[\, \boldsymbol{V}^x \big| \boldsymbol{V}^q \big| \boldsymbol{V}^g \,\big] = \Delta_x|_{(\cdot)} \big[\, \boldsymbol{V}^x \big| \boldsymbol{V}^q \big| \boldsymbol{V}^g \,\big] + \Delta_z|_{(\cdot)} \big[\, \boldsymbol{Z}^x \big| \boldsymbol{Z}^q \big| \boldsymbol{Z}^g \,\big] + \big[\, 0 \big| \tfrac{\partial \boldsymbol{b}}{\partial \boldsymbol{q}} \big| 0 \,\big] \tag{4.53a}$$

$$\frac{\mathrm{d}}{\mathrm{d}t} \big[\, \boldsymbol{U}^x \big| \boldsymbol{U}^q \big| \boldsymbol{U}^g \,\big] = \frac{\partial L}{\partial \boldsymbol{x}} \bigg|_{(\cdot)}^T \big[\, \boldsymbol{V}^x \big| \boldsymbol{V}^q \big| \boldsymbol{V}^g \,\big] + \frac{\partial L}{\partial \boldsymbol{z}} \bigg|_{(\cdot)}^T \big[\, \boldsymbol{Z}^x \big| \boldsymbol{Z}^q \big| \boldsymbol{Z}^g \,\big] \tag{4.53b}$$

$$0 = \frac{\partial \boldsymbol{g}}{\partial \boldsymbol{x}} \bigg|_{(\cdot)} \big[\, \boldsymbol{V}^x \big| \boldsymbol{V}^q \big| \boldsymbol{V}^g \,\big] + \frac{\partial \boldsymbol{g}}{\partial \boldsymbol{z}} \bigg|_{(\cdot)} \big[\, \boldsymbol{Z}^x \big| \boldsymbol{Z}^q \big| \boldsymbol{Z}^g \,\big] + \big[\, 0 \big| 0 \big| \zeta_i|_{(\cdot)} \boldsymbol{g}_i \,\big] \tag{4.53c}$$

$$\big[\, \boldsymbol{V}^x \big| \boldsymbol{V}^q \big| \boldsymbol{V}^g \,\big](t_i) = \big[\, \mathbb{I}_{n_x} \big| 0_{n_x \times n_u} \big| 0_{n_x \times 1} \,\big], \quad \big[\, \boldsymbol{Z}^x \big| \boldsymbol{Z}^q \big| \boldsymbol{Z}^g \,\big](t_i) = \big[\, \boldsymbol{D}_i^x \big| \boldsymbol{D}_i^q \big| \boldsymbol{d}_i^g \,\big], \tag{4.53d}$$

$$\big[\, \boldsymbol{U}^x \big| \boldsymbol{U}^q \big| \boldsymbol{U}^g \,\big](t_i) = \big[\, 0_{1 \times n_x} \big| 0_{1 \times n_u} \big| 0 \,\big], \tag{4.53e}$$

in which $(\cdot)$ is expanded to the arguments of each function as defined in Eq. (4.1); and Δ_x, Δ_z and $\big[\, \boldsymbol{Z}^x \big| \boldsymbol{Z}^q \big| \boldsymbol{Z}^g \,\big]$ are given briefly; converges towards the actual directional derivative matrices $\boldsymbol{U}_i^x = \boldsymbol{U}^x(t_{i+1})$, $\boldsymbol{U}_i^q = \boldsymbol{U}^q(t_{i+1})$, $\boldsymbol{U}_i^g = \boldsymbol{U}^g(t_{i+1})$, $\boldsymbol{V}_i^x = \boldsymbol{V}^x(t_{i+1})$, $\boldsymbol{V}_i^q = \boldsymbol{V}^q(t_{i+1})$ and $\boldsymbol{V}_i^g = \boldsymbol{V}^g(t_{i+1})$ as the integration step and the approximation error of the corresponding partial derivatives converge to zero [17]. The expressions for Δ_x and Δ_z are

$$\Delta_x = \frac{\partial \boldsymbol{b}}{\partial \boldsymbol{x}}(\boldsymbol{x}(t), \boldsymbol{z}(t), \tilde{\boldsymbol{u}}(t; \boldsymbol{q}_i), \boldsymbol{p}, \boldsymbol{w}(t)) - \sum_{j=1}^{n_x} \frac{\mathrm{d}x_j}{\mathrm{d}t}(t) \frac{\partial \boldsymbol{M}_{\cdot,j}}{\partial \boldsymbol{x}}(\boldsymbol{x}(t), \boldsymbol{z}(t), \boldsymbol{p}) \text{ and} \tag{4.54a}$$

$$\Delta_z = \frac{\partial \boldsymbol{b}}{\partial \boldsymbol{z}}(\boldsymbol{x}(t), \boldsymbol{z}(t), \tilde{\boldsymbol{u}}(t; \boldsymbol{q}_i), \boldsymbol{p}, \boldsymbol{w}(t)) - \sum_{j=1}^{n_x} \frac{\mathrm{d}x_j}{\mathrm{d}t}(t) \frac{\partial \boldsymbol{M}_{\cdot,j}}{\partial \boldsymbol{z}}(\boldsymbol{x}(t), \boldsymbol{z}(t), \boldsymbol{p}), \tag{4.54b}$$

where $\boldsymbol{M}_{\cdot,j}$ represents the j-th column of matrix $\boldsymbol{M}$. In Eq. (4.53a), we have also introduced

the directional derivatives

$$Z_i^x \stackrel{\text{def}}{=} \frac{\partial z}{\partial s_i^x}\bigg|_{(t_{i+1};t_i,s_i^x,s_i^z,q_i,p)} + \frac{\partial z}{\partial s_i^z}\bigg|_{(t_{i+1};t_i,s_i^x,s_i^z,q_i,p)} D_i^x, \tag{4.55a}$$

$$Z_i^q \stackrel{\text{def}}{=} \frac{\partial z}{\partial s_i^x}\bigg|_{(t_{i+1};t_i,s_i^x,s_i^z,q_i,p)} + \frac{\partial z}{\partial s_i^z}\bigg|_{(t_{i+1};t_i,s_i^x,s_i^z,q_i,p)} D_i^q, \text{ and} \tag{4.55b}$$

$$Z_i^g \stackrel{\text{def}}{=} \frac{\partial z}{\partial s_i^x}\bigg|_{(t_{i+1};t_i,s_i^x,s_i^z,q_i,p)} + \frac{\partial z}{\partial s_i^z}\bigg|_{(t_{i+1};t_i,s_i^x,s_i^z,q_i,p)} d_i^g, \tag{4.55c}$$

which have to be computed to solve Eq. (4.53a), even if they are not used by the optimization level.

In this thesis, we approximate the partial derivatives by means of finite differences, with which our approximation error for the partial derivatives is of $o(\sqrt{\epsilon_{\text{mach}}})$, where ϵ_{mach} is the machine precision. Numerical experience shows that this approach performs satisfactorily. Other possibilities, e.g. symbolic or automatic differentiation, have been considered as possible future extensions.

In summary, for each interval we integrate simultaneously Eqs. (4.1), (4.4) and (4.53a) and the results are used for building Eqs. (4.27b) to (4.27e) and Eq. (4.26) through Eq. (4.50) or Eq. (4.51). These integrations are performed in this thesis by means of the software package DAESOL [8] (cf. [9, 45]), which implements *backward difference formulae (BDF)* method. BDF methods have been introduced in [32] for the DAE case and extended to the DAE case in [54]. For an introduction to BDF methods for the solution of ODEs, see e.g. [66]. For the numerical solution of stiff ODEs and DAEs, see e.g. [65]. BDF methods belong to the family of *linear multistep methods*, so the aforementioned convergence result holds. They have also proved effective for stiff ODEs and DAEs, which corresponds to our case. The efficient implementation of [8] features a step and order selection method based on a local error estimate specially tailored for the variable-step case, and a monitoring strategy that reduces the number of times the BDF Jacobian matrices are computed and factorized. Additionally, the starting values required for a BDF method of order k are provided by starte phase based on an adequate Runge-Kutta method. For our purposes, DAESOL's feature of automatically delivering the desired directional derivatives in an IND context (that is, applying the step and order selection methods only to the nominal trajectories, which correspond to Eqs. (4.1) and (4.4)) is of critical importance.

4.1.3 Summary

In order to solve Problem (4.9) we proceed as follows: first, define the relative integration tolerance TOL and the NLP accuracy ACC, a maximum number of iterations ITMAX, and a maximum number of QP iterations QPMAX.

Initialization Phase

I.1 Set $k = 0$, define an initial guess v_0.

I.2 Evaluate functions $F(v_0)$, $H(v_0)$ and $G(v_0)$, and specific directional derivatives of these functions, proceeding as described in Section 4.1.2.

I.3 Choose a suitable, positive definite matrix B_0 as initial estimate for the partially reduced Hessian. We proceed as in [92, 124]. Go to step O.1.

Optimization Phase for $k = 0, 1, \ldots, \text{ITMAX}$ do:

O.1 Form the partially reduced quadratic optimization subproblem (4.27).

O.2 Condense subproblem (4.27) using Eqs. (4.30) to (4.42), obtaining subproblem (4.40).

O.3 Within a maximum number of iterations QPMAX, solve (4.40) using a standard QP solver, obtaining the KKT point $\left[\Delta\boldsymbol{\nu}_2^{c\diamond}; \boldsymbol{\lambda}_2^{\diamond}; \boldsymbol{\mu}^{\diamond}\right]$.

O.4 Use Eqs. (4.34) and (4.46) to reconstruct $\Delta\boldsymbol{\nu}_1^{c\diamond}$ and $\boldsymbol{\lambda}_1^{\diamond}$. Use Eqs. (4.23) and (4.30) to reconstruct $\Delta\boldsymbol{\nu}^{\mathcal{N}}$ and then $\Delta\boldsymbol{\nu}_i$.

O.5 Check the termination criterion: compute $K(\boldsymbol{\nu}_k, \Delta\boldsymbol{\nu}^{c\diamond}, \boldsymbol{\lambda}^{\diamond}, \boldsymbol{\mu}^{\diamond})$ from Eq. (4.47), and if $K(\boldsymbol{\nu}_k, \Delta\boldsymbol{\nu}^{c\diamond}, \boldsymbol{\lambda}^{\diamond}, \boldsymbol{\mu}^{\diamond}) \leqslant$ ACC, finish returning $[\boldsymbol{\nu}^{\star}; \boldsymbol{\lambda}^{\star}; \boldsymbol{\mu}^{\star}] := [\boldsymbol{\nu}_k; \boldsymbol{\lambda}_k; \boldsymbol{\mu}_k]$ as the solution. Otherwise proceed.

O.6 Use a line search strategy to obtain a steplength α_k (see e.g. [92]).

O.7 Apply Eq. (4.48) for the Lagrange multipliers first. Obtain the old Lagrangian gradient using Eq. (4.49). To this end, obtain the directional derviatives as described in Section 4.1.2.

O.8 Then, apply Eq. (4.48) for the solution estimate and obtain the new Lagrangian gradient by means of Eq. (4.49), also using the techniques of Section 4.1.2.

O.9 Update the Hessian approximation, obtaining $\boldsymbol{B}_{k+1}$. Proceed using the high-rank updates of Eq. (4.50) or the limited-memory updates of Eqs. (4.51) and (4.52).

O.10 Set $k \rightarrow k+1$ and return to step O.1.

4.2 Real-Time Iteration Schemes

After having introduced the procedure with which the optimal control problem solution can be approximated, we carry forward by briefly describing the Real-Time Iteration Schemes for NMPC and MHE in Sections 4.2.1 and 4.2.2, respectively. These schemes can perform much faster than conventional schemes in which the Nonlinear Programming Problems (NLPs) solvers iterate until the termination criterion is satisfied and thus are more adequate for applications such as ours, in which fast feedback is desired.

4.2.1 Real-Time Iteration Scheme for NMPC

In Section 4.1, the course of action with which we solve Eq. (OCP) has been described. Clearly, it may take several iterations before a KKT point for Problem (4.9) is achieved when the procedure is initialized with a remote initial guess $\boldsymbol{\nu}_0$. In a real-time context, where *state feedback* controls $\boldsymbol{u}(t^{(k)}) = \boldsymbol{u}(\hat{\boldsymbol{x}}^{(k)}(t^{(k)}))$ are desired to ensure a quick reaction to arising disturbances, a sequence of optimization problems of the same kind of Problem (4.8) is posed, which should be solved as quickly as possible in order to minimize the delays between the state measurement and the control updates, and thus keep producing near-optimal trajectories. Moreover, if these delays are too large, the scheme's stability and the feasiblity of the trajectories are at risk. In principle, we could make use of the same strategies of Section 4.1 to solve each member of the optimization problem sequence until the satisfaction of the termination criterion described there, which we will refer to as *conventional NMPC approach*. In [19, 36, 37], however, some key observations are done about the sequence of optimization problems: Firstly, the whole family of optimization problems is continuously parametrized by the initial state $\hat{\boldsymbol{x}}^{(k)}$ of (NMPC$_k$). As a consequence, the solution to each problem can be related to that of the consecutive ones through of this parameter. In particular, if $\hat{\boldsymbol{x}}^{(k)}$ suffers only small perturbations, which is most likely to happen if the computational times are kept short for each problem, the corresponding solutions of consecutive problems will lay close to each other, and the active

sets will be almost the same. In this context, it has been shown that, starting from a solution $\boldsymbol{v}^\star(\hat{\boldsymbol{x}}^{(k)})$ of the k-th problem, the solution $\boldsymbol{v}^\star(\hat{\boldsymbol{x}}^{(k+1)})$ of the $k+1$-th problem is approximated to first order by $\boldsymbol{v}^\star(\hat{\boldsymbol{x}}^{(k)}) + \Delta\boldsymbol{v}_{\mathcal{L}}$, where $\Delta\boldsymbol{v}_{\mathcal{L}}$ is a step computed by solving Eq. (4.40) using an exact Hessian matrix instead of $\boldsymbol{B}_k$. Mathematically,

$$\left\| \boldsymbol{v}^\star(\hat{\boldsymbol{x}}^{(k+1)}) - \left(\boldsymbol{v}^\star(\hat{\boldsymbol{x}}^{(k)}) + \Delta\boldsymbol{v}_{\mathcal{L}} \right) \right\| = o\left(\left\| \hat{\boldsymbol{x}}^{(k+1)} - \hat{\boldsymbol{x}}^{(k)} \right\|^2 \right), \tag{4.56}$$

which holds even if both problems have different active sets.

Secondly, within each problem, the most computationally demanding steps in each SQP iteration correspond to the computation of the DAE system solution and its associated directional derivatives (see steps O.7 and O.8 of Section 4.1.3), together with the manipulation of the required block matrices in the condensing context (steps O.2 and O.9 of Section 4.1.3). None of these steps, except the initial state constraints require knowledge on $\hat{\boldsymbol{x}}^{(k)}$, so they can be performed anticipatively, based on the knowledge provided by the last iteration. Then, once $\hat{\boldsymbol{x}}^{(k)}$ has been determined (directly measured, or estimated from measurements), the step computation (namely, step O.3 of Section 4.1.3) requires a computational time several orders of magnitude smaller than the others. Proceeding this way can drastically reduce the delay between the state measurement and the control updates, achieving values of only a few milliseconds.

Finally, close to the a KKT point of a given NLP, line-search strategies usually accept step lengths of unity length, i.e. $\alpha_k = 1$, so this choice can be assumed close to the optimum and thus step O.6 of Section 4.1.3 can be skipped.

With the previous observations in mind, in [36, 37] the Real-Time Iteration scheme (RTI) has been proposed: the idea is to treat the whole family of optimization problems with one algorithm, which iterates in an endless loop and assigns *only one SQP iteration* to each problem. The solution estimates $\boldsymbol{v}_k$, the Lagrange multipliers $\boldsymbol{\lambda}_k$ and $\boldsymbol{\mu}_k$, and the plant (or process) state $\hat{\boldsymbol{x}}^{(k)}$ evolve thus simultaneously. Convergence of each optimization subproblem is not pursued, but a quick adaption to the new plant conditions instead.

Starting from $[\boldsymbol{v}_k; \boldsymbol{\lambda}_k; \boldsymbol{\mu}_k]$, associated to the step performed right after knowing $\hat{\boldsymbol{x}}^{(k)}$, the algorithm can be summarized in the following steps:

Preparation Phase

R.1 Initialize Problem $k+1$ with $[\boldsymbol{v}_k; \boldsymbol{\lambda}_k; \boldsymbol{\mu}_k]$ as initial guess for solution estimate and Lagrange multipliers, and the same working set (i.e. active set guess) as in Problem k.

R.2 From $\boldsymbol{v}_k$, perform steps O.1, O.2, O.8 and O.9 of Section 4.1.3, without forming Eq. (4.27c) yet.

Feedback Phase

(In the meantime, the plant has evolved under the influence of the previous control to a new state whose estimation $\hat{\boldsymbol{x}}^{(k+1)}$ has become available)

R.3 Once $\hat{\boldsymbol{x}}^{(k+1)}$ is known, consider Eq. (4.40) and remove Eq. (4.40b), as well as all those components from $\boldsymbol{B}_k^c$ and $\overline{\boldsymbol{g}}^c$ that are related with $\hat{\boldsymbol{x}}^{(k+1)}$, from it. Set $\Delta\boldsymbol{s}_{0,k+1}^x := \hat{\boldsymbol{x}}^{(k+1)} - \boldsymbol{s}_{0,k}^x$ and solve the QP with the remaining blocks only.

R.4 Once the solution $\Delta\boldsymbol{q}_{0,k+1}, \dots \Delta\boldsymbol{q}_{N,k+1}$ is known, pass the control value $\boldsymbol{q}_{0,k} + \Delta\boldsymbol{q}_{0,k+1}$ immediately to the plant.

Transition Phase

R.5 Reverse the condensing and reduction steps as in step O.4. Update the Lagrange multipliers with $\alpha_{k+1} = 1$ and compute the old Lagrangian gradient as in step O.7.

R.6 Set $\boldsymbol{v}_{k+1} = \boldsymbol{v}_k + \Delta\boldsymbol{v}_k$.

To these steps, which are essentially a rearrangement of what is done in the offline context of Section 4.1.3, we can add the following optional step which can improve the algorithm's performance in some cases:

Shift Phase

R.7 Discard subvector $\left[\boldsymbol{s}^x_{0,k+1}; \boldsymbol{s}^z_{0,k+1}; \boldsymbol{q}_{0,k+1} \right]$ from $\boldsymbol{v}_{k+1}$, and the Lagrange multipliers associated to constraints on the first node.

R.8 Copy the rest of the subvectors and their associated directional derivatives, Hessian blocks and Lagrange multipliers towards the left, e.g. $\left[\boldsymbol{s}^x_{j,k+1}; \boldsymbol{s}^z_{j,k+1}; \boldsymbol{q}_{j,k+1} \right] :=$ $\left[\boldsymbol{s}^x_{j+1,k+1}; \boldsymbol{s}^z_{j+1,k+1}; \boldsymbol{q}_{j+1,k+1} \right]$, for all $j \in \{0, \dots, N-1\}$.

(As a remark, at the end of step R.8, all subvectors and matrices corresponding to the last and the next-to-last nodes coincide)

After this, set $k := k + 1$, wait for $\hat{\boldsymbol{x}}^{(k+2)}$ and return to step R.1.

It is important to notice that, due to the close dovetailing of system and optimizer dynamics, stability of the closed-loop system is not implied by standard nonlinear model predictive control results [40]. In [36, 37], an NMPC implementation using the real-time iterations for a tracking problem (that is, one in which the objective function is the squared norm of the deviation of a system output vector with respect to an output reference trajectory) is discussed and implemented for the case in which the prediction horizon shrinks. For that case, contractivity and loss of optimality results are given in [38]. In [39], contractivity, loss of optimality and *nominal stability* for the case in which the prediction horizon keeps constant and the shift phase is applied, are shown under certain assumptions. For the nominal stability, a terminal constraint is used which forces the state to arrive at the origin, assumed to be an equilibrium state, at the end of each prediction horizon. For the case when no shift phase is used and there are no terminal constraints, but a terminal cost function, the nominal stability is proved in [41].

In [61] it is stressed out that nominal stability (in that reference also known as *attractivity*) is a weaker property than the property known as *asymptotic stability* in nonlinear system theory: the former guarantees the state to converge to an equilibrium state as time tends to infinity, without giving any description of the behavior in the meantime, whereas the latter states the existence of a *bound on the error that decreases strictly with time*. It is also argued that in case of applying non-optimal NMPC strategies, as it is our case, the control should be particularly close to optimal in order to both assure attractivity and the existance of a (time-independent) bound on the error. Under certain regularity assumptions, these conditions may imply asymptotic stability (see e.g. [81]). The conditions under which RTI can yield asymptotic stability have still not been investigated rigorously.

Regarding the computational time, on top of the algorithmic improvements presented above, the number of multiple shooting intervals N also plays an important role, since the linear algebra required for the preparation phase has a total computational cost of $\mathcal{O}(N^3)$. It is thus recommended to keep this number low. This might also imply an adjustment to the prediction horizon length Δt_{NMPC} so as to improve optimality, feasiblity and model evaluability. See e.g. [17] for mesh selection criteria for multiple-shooting.

4.2.2 Real-Time Iteration Scheme for MHE

In [41, 85, 86] the RTI scheme has been also extended to MHE. Therein, the sequence of optimization problemes are continuously parametrized by the data vectors ξ_j in the estimation window, and the initial state constraint is not present. For the specific least-squares objective function of Problem (MHE$_k$) it is adequate to use a *Generalized Gauss-Newton Method* (see e.g. [15, 17]) for solving Eq. (4.13): an initial solution estimate $\boldsymbol{v}_k$, is updated as $\boldsymbol{v}_k + \Delta\boldsymbol{v}_k$, where $\Delta\boldsymbol{v}_k$ is the result of solving the quadratic subproblem

$$
\begin{aligned}
\min_{\Delta\boldsymbol{v}} \quad & (\nabla_{\boldsymbol{v}}\mathbf{F}_{\text{MHE}}(\boldsymbol{v}_k,\Xi_k)^T\mathbf{F}_{\text{MHE}}(\boldsymbol{v}_k,\Xi_k))^T\Delta\boldsymbol{v} + \frac{1}{2}\Delta\boldsymbol{v}^T\nabla_{\boldsymbol{v}}\mathbf{F}_{\text{MHE}}(\boldsymbol{v}_k,\Xi_k)^T\nabla_{\boldsymbol{v}}\mathbf{F}_{\text{MHE}}(\boldsymbol{v}_k,\Xi_k)\Delta\boldsymbol{v} \\
\text{s.t.} \quad & \mathbf{G}_{\text{MHE}}(\boldsymbol{v}_k,\Xi_k) + \nabla_{\boldsymbol{v}}\mathbf{G}_{\text{MHE}}(\boldsymbol{v}_k,\Xi_k)^T\Delta\boldsymbol{v} = 0 \\
& \mathbf{H}_{\text{MHE}}(\boldsymbol{v}_k) + \nabla_{\boldsymbol{v}}\mathbf{H}_{\text{MHE}}(\boldsymbol{v}_k)^T\Delta\boldsymbol{v} \geqslant 0.
\end{aligned}
\tag{4.57}
$$

Therein, the Lagrangian Hessian approximation $\nabla_{\boldsymbol{v}}\mathbf{F}_{\text{MHE}}(\boldsymbol{v}_k,\Xi_k)^T\nabla_{\boldsymbol{v}}\mathbf{F}_{\text{MHE}}(\boldsymbol{v}_k,\Xi_k)$ requires only first derivatives, is independent on the Lagrange multipliers, and has a sparse block structure. The partial reduction and the condensing steps can be performed as in Section 4.1.1, so that the partially reduced Lagrangian Hessian approximation blocks

$$
\boldsymbol{D}_i^T\nabla_{\boldsymbol{v}}\mathbf{F}_{\text{MHE}}(\boldsymbol{v}_k,\Xi_k)_i^T\nabla_{\boldsymbol{v}}\mathbf{F}_{\text{MHE}}(\boldsymbol{v}_k,\Xi_k)_i\boldsymbol{D}_i
$$

can be readily computed from the directional derivatives $\nabla_{\boldsymbol{v}}\mathbf{F}_{\text{MHE}}(\boldsymbol{v}_k,\Xi_k)_i\boldsymbol{D}_i$. The same applies to the partially reduced objective function gradient blocks

$$
(\nabla_{\boldsymbol{v}}\mathbf{F}_{\text{MHE}}(\boldsymbol{v}_k,\Xi_k)_i\boldsymbol{D}_i)^T(\mathbf{F}_{\text{MHE}}(\boldsymbol{v}_k,\Xi_k)_i + \nabla_{\boldsymbol{v}}\mathbf{F}_{\text{MHE}}(\boldsymbol{v}_k,\Xi_k)_i\boldsymbol{d}_i),
$$

and the partially reduced constraint residuals and Jacobians. (cf. Eqs. (4.23), (4.27b) and (4.27e)).

Similar to NMPC, a larger number of intervals M increases the computational complexity of the linear algebra steps at this point as $\mathcal{O}(M^3)$. On the other hand, a larger M can improve the estimation quality, since more past information is entering the optimization problem in an explicit way. Thus, the choice of M needs to be performed carefully for each application.

Starting from $[\boldsymbol{v}_k;\boldsymbol{\lambda}_k;\boldsymbol{\mu}_k]$, associated to the step performed right after having computed $[\hat{\boldsymbol{x}}^{(k)};\hat{\boldsymbol{z}}^{(k)}]$, the algorithm can be summarized in the following steps:

Preparation Phase

    M.1 From the right-most subvector $[\hat{\boldsymbol{x}}^{(k)};\hat{\boldsymbol{z}}^{(k)}]$, predict the values of $[\hat{\boldsymbol{x}}^{(k+1)};\hat{\boldsymbol{z}}^{(k+1)}]$ using the difference equation, the control $\boldsymbol{u}(t_k)$ for the whole interval $[t_k,t_{k+1}]$, and no state noise. Obtain as well the corresponding directional derivatives.

    M.2 Discard subvector $[\hat{\boldsymbol{x}}^{(k-M)};\hat{\boldsymbol{z}}^{(k-M)}]$ from $\boldsymbol{v}_{k+1}$, and the Lagrange multipliers associated to constraints on the first node.

    M.3 Copy the rest of the subvectors and their associated directional derivatives, Hessian blocks and Lagrange multipliers towards the left, e.g. $[\hat{\boldsymbol{x}}^{(j)};\hat{\boldsymbol{z}}^{(j)}] := [\hat{\boldsymbol{x}}^{(j+1)};\hat{\boldsymbol{z}}^{(j+1)}]$, for all $j \in \{0,\dots,N-1\}$. Replace the last node's subvectors, directional derivatives and Hessian blocks with the ones obtained in step M.1, e.g. $[\hat{\boldsymbol{x}}^{(k)};\hat{\boldsymbol{z}}^{(k)}] := [\hat{\boldsymbol{x}}^{(k+1)};\hat{\boldsymbol{z}}^{(k+1)}]$.

    M.4 With the directional derivatives, perform the necessary linear algebra to condense the system and build the partially reduced Hessian blocks as in Section 4.1.1.

Estimation Phase

(In the meantime, the plant has evolved, and a new measurement vector ξ_{k+1}, with associated covariance matrix W is now available.)

M.5 Once ξ_{k+1} is known, solve the condensed QP of step M.4, obtaining Δv_{k+1}.

M.6 Pass the state estimates $\hat{x}^{(k+1)} + \Delta\hat{x}^{(k+1)}$ and $\hat{z}^{(k+1)} + \Delta\hat{z}^{(k+1)}$ immediately to the controller.

Transition Phase

M.7 Reverse the condensing and reduction steps as in step R.5.

M.8 Set $v_{k+1} = v_k + \Delta v_k$, $k = k + 1$ and return to step M.1.

4.2.3 Initialization

As previously mentioned, the RTI scheme has very good convergence properties for both NMPC and MHE if the solution estimates keep close to the optima for each problem. For this reason, in this thesis we perform an initialization phase that makes use of the offline optimization of Section 4.1.3. Our computations are based on the availability of recorded controls, measurements and external inputs (exhaust gas conditions) of an operational scenario at least for an interval $[t_0, t_0 + \Delta t_{\mathrm{MHE}} + \Delta t_{\mathrm{NMPC}}]$. Concretely, in this thesis the NMPC and MHE are initialized as follows:

Initialize the MHE

I.1 Using an initial differential state estimate $\hat{x}^{(0)}$, and the controls and external inputs corresponding to the scenario under consideration on the interval $[t_{0,\mathrm{MHE}}^{(M)}, t_{\mathrm{f,MHE}}^{(M)}]$ (recall that $t_{\mathrm{f,MHE}}^{(M)} = t_0^{(M)}$), initialize the node state vectors by integrating Eq. (4.1) along $[t_{0,\mathrm{MHE}}^{(M)}, t_{\mathrm{f,MHE}}^{(M)}]$. The initial algebraic state estimate $\hat{z}^{(0)}$ can be chosen to be consistent with $\hat{x}^{(0)}$, but that need not be the case.

I.2 Considering the measurements $\Xi^{(M)}$ that correspond to the current scenario, and using the initial node state vectors and controls of the previous step as initial guesses of the solution, solve Problem (4.13) until the satisfaction of the termination criterion of Eq. (4.47) as described in Chapter 4. Denote the primal solution as $v_{\mathrm{MHE},0}^{\star}$.

I.3 From $v_{\mathrm{MHE},0}^{\star}$, obtain the estimate $\hat{x}^{(M)}$ and send it to the NMPC. Initialize the RTI scheme for MHE described in Section 4.2.2 using the Jacobians and Hessian approximations of the last SQP iteration of step I.2.

I.4 Wait for the new measurements ξ_{M+1} from the WHR. Once available, continue by performing the steps described in Section 4.2.2.

Initialize the NMPC

I.5 Receive the estimate $\hat{x}^{(M)}$ from the MHE. Using it as initial differential state and the controls and the exhaust gas conditions of the current scenario, integrate Eq. (4.1) between $t_0^{(M)}$ and $t_{\mathrm{f}}^{(M)} = t_0^{(M)} + \Delta t_{\mathrm{NMPC}}$ to generate the initial guesses of the node state vectors and their associated Jacobians and Hessian approximations. To this end, an initial algebraic state that is consistent with $\hat{x}^{(M)}$ can be used, but that need not be the case .

I.6 Solve the M-th optimal control subproblem (4.10) until the satisfaction of the termination criterion of Eq. (4.47) as described in Chapter 4. Denote the primal solution as $\boldsymbol{v}^\star_{\text{NMPC},M}$.

I.7 Use $\boldsymbol{v}^\star_{\text{NMPC},M}$ and its corresponding Jacobians and Hessian approximations to initialize the RTI scheme for NMPC described in Section 4.2.1. Additionally, obtain the control $\boldsymbol{q}_{0,M}$ from $\boldsymbol{v}_{\text{NMPC},M}{}^\star$ and apply it to the WHR during $[t_\text{f}^{(M)}, t_\text{f}^{(M)} + T_s]$.

I.8 Wait for the new estimate $\hat{\boldsymbol{x}}^{(M+1)}$ from the MHE. Once available, continue by performing the steps described in Section 4.2.1.

Whenever the MHE scheme is absent, the NMPC scheme can be directly initialized by following steps I.5 to I.8; considering a given initial differential state $\hat{\boldsymbol{x}}^{(0)}$, an initial algebraic state $\hat{\boldsymbol{z}}^{(0)}$ that need not be consistent, recorded controls and exhaust gas inputs on the interval $[t_0^{(0)}, t_\text{f}^{(0)}]$, and $M = 0$.

4.2.4 NMPC-MHE Closed Loop

Having already introduced the algorithms behind our online control and estimation implementations, we sketch a block diagram describing the information processing paths, given in Fig. 4.1(a). Since the NMPC and the MHE modules perform their computation in parallel, and the plant evolves at the same time, a time diagram describing the step sequences is given in Fig. 4.1(b).

In this thesis we make the assumption that both the NMPC and the MHE modules have been properly initialized at the moment the plant begins to operate, i.e. the WHR is operational. This way, the very first control applied $\boldsymbol{q}_{0,0}$, is feasible and close to optimal. The sampling time T_s is assumed constant, and each measurement ξ_k is made available with this period. In Fig. 4.1(a), the delays between the sampling and estimation $\delta_{\text{MHE}}^{(k)}$, and between the estimation and the control updates $\delta_{\text{NMPC}}^{(k)}$ have been explicitly depicted. In our implementation, however, these delays are orders of magnitude smaller than the sampling time, approaching the ideal case where $\delta_{\text{MHE}}^{(k)} = \delta_{\text{NMPC}}^{(k)} = 0$. Notice that these times can be actually considered as random variables, since the QPs to be solved during the corresponding estimation and feedback phases depend on the external inputs $\boldsymbol{w}(t)$, which cannot be known a priori. In spite of the fact that the complexity of active-set QP solution stategies grows exponentially in the number of variables (see e.g. [84]), the computational times remain bounded in practice if the state perturbations are small. As previously stated, the most expensive algorithmic steps are the respective preparation phases, where DAEs must be solved. Again, these times correspond in a strict sense to random variables, since different exhaust gas predictions (NMPC) and/or histories (MHE) will require different choices for the orders and step sizes in the DAE solvers. For this case, keeping prediction horizons (NMPC) and estimation windows (MHE) short will reduce the computational costs in this phase, as a general rule. On the other hand, the linear algebra costs are reduced by choosing a lesser number of nodes. In this thesis, the choice of the aforementioned parameters is performed empirically, considering typical, real operational scenarios[2].

4.3 Linear Control Strategies

After having introduced the proposed control and estimation schemes, in this section we briefly review formulate instances of the PI and LQGI control strategies, which are undoubtedly the

---

[2]This choice can, in some sense, be interpreted as an application-dependent design task for this kind of controllers.
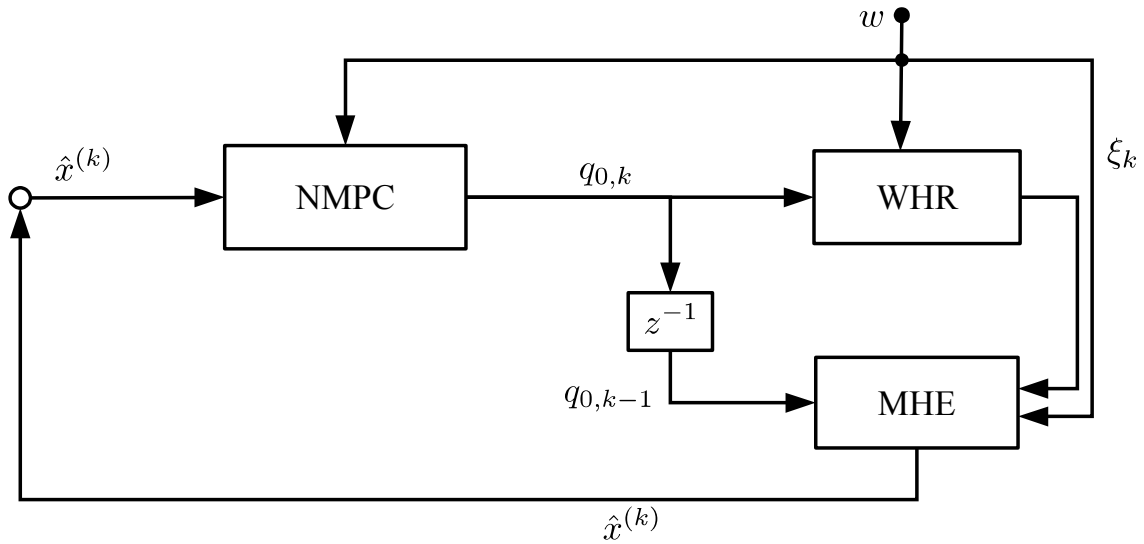
(a) Block diagram.
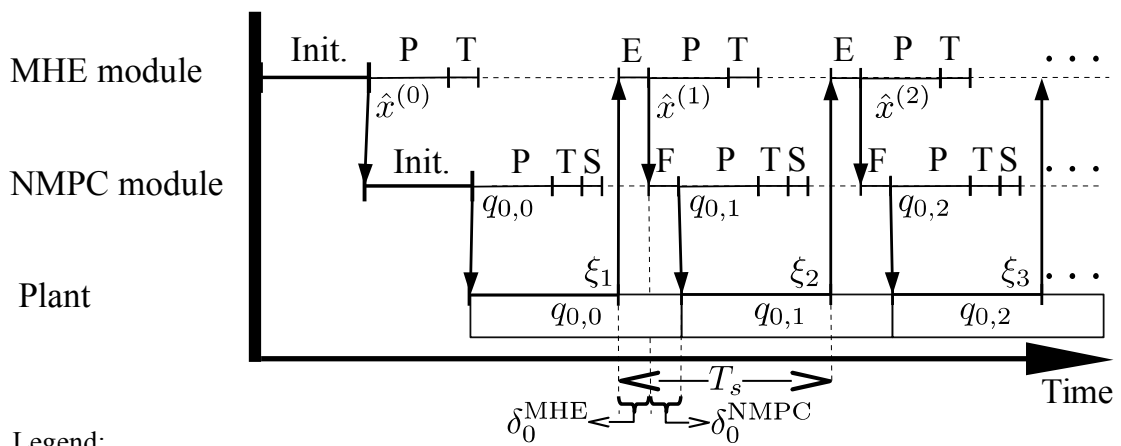
Legend:
  P: Preparation phase   F: Feedback phase $\boxed{q_{0,k}}$ Control applied to plant
  T: Transition phase   S: Shift phase (optional) $q, \hat{x}, \xi \downarrow$ Signal path
  E: Estimation phase   - - - - - Idle process

(b) Time diagram.

Figure 4.1: Block and time diagrams for the NMPC-MHE closed loop

most used in real-world industrial applications. These strategies will be considered in Chapter 5 as benchmarks for the schemes proposed in Section 3.5. With digital applications in mind, we devote ourselves to the discrete-time cases only. Additionally, due to our system's characteristics, we restric ourselves to single-input, single-output (SISO) instances.

We begin by defining the superheating (see Section 3.2.6) as the controlled variable. Let $y_k^{\text{SH}} \overset{\text{def}}{=} y^{\text{SH}}(x^{(k)}, z^{(k)})$. For a given *target superheating* $y^{\text{SH}*}$, the *superheating error* at time t_k is defined as $e_k = y^{\text{SH}*} - y_k^{\text{SH}}$.

4.3.1 The Proportional-Integral (PI) Controller

On each time instant t_k, the discrete-time PI controller uses the current superheating error e_k and its accumulation over time to obtain the current control $\tilde{u}_{k,\text{pre}}^{\text{PI}}$ as follows

$$\tilde{u}_{k,\text{pre}}^{\text{PI}} = K_p e_k + K_i I_{k-1}, \tag{4.58}$$

where the *error integral* I_k satisfies the following difference equation

$$I_k = I_{k-1} + T_s \xi_k e_k, \quad \forall k \in \mathcal{K}; \quad I_{-1} = 0. \tag{4.59}$$

In Eq. (4.58), ξ_k forms the *anti-windup* mechanism: if $\tilde{u}_{k,\text{pre}}^{\text{PI}}$ causes the control to fall outside its bounds, the current error e_k is not incorporated in the sum for the next time step, i.e.

$$\xi_k = \begin{cases} 0 & \text{if } \tilde{u}_{k,\text{pre}}^{\text{PI}} \notin [\dot{m}_{\text{in,min}} - \bar{u}, \dot{m}_{\text{in,max}} - \bar{u}], \\ 1 & \text{otherwise} \end{cases}, \quad \forall k \in \mathcal{K}. \tag{4.60}$$

The upper and lower bounds on the control are defined as in Eq. (3.85). The control is truncated before it is applied to the system.

$$u_k^{\text{PI}} = \max(\dot{m}_{\text{in,min}}, \min(\dot{m}_{\text{in,max}}, \tilde{u}_{k,\text{pre}}^{\text{PI}} + \bar{u})). \tag{4.61}$$

There are several ways to obtain the values for constants K_p and K_i. In this thesis we apply frequency-domain techniques to the small-signal system Eq. (3.81). Design parameters are the minimum phase margin PM and the open-loop gain crossover frequency ω_c (see e.g. [6, 115] for an introduction to several PID controller tuning techniques).

The PI controller can be represented by means of the block diagram shown in Fig. 4.2. Therein we have considered the noise terms Ψ_k^y and Ψ_k^x to affect the superheating measurements and the state of the plant on each instant k.

4.3.2 Linear-Quadratic-Gaussian Controller with Integral Action (LQGI)

The LQGI controller results from a tandem conection between a classical Kalman filter [79] (the observer) and a linear-quadratic regulator (LQR, the controller) featuring an integral action explained briefly. In this thesis we make use of the discrete-time version of both.

We begin considering system Eq. (3.81), where the output is y^{SH} as defined in Eq. (3.55). The state and the output are perturbed by Gaussian white noise terms[3] $\Psi_k = \begin{bmatrix} \Psi_k^x; & \Psi_k^y \end{bmatrix}$ for all $k \in \mathcal{K}$, with symmetric, each associated to a positive definite covariance matrix

$$Q_\Psi = \mathbb{E}\left\{\Psi_k \Psi_k^T\right\}. \tag{4.62}$$

---

[3]A sequence of independent, identically normally distributed random variables with zero mean
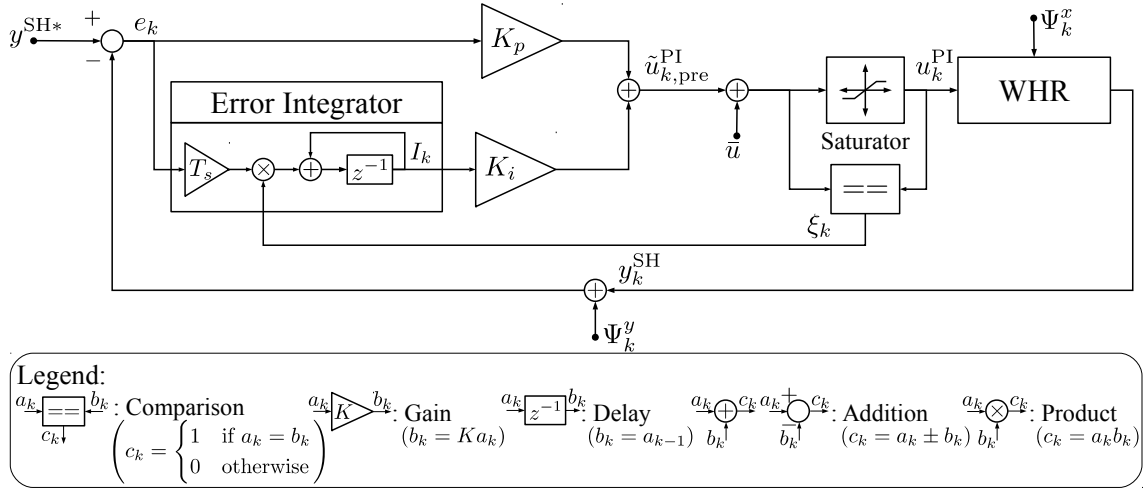
Figure 4.2: PI controller block diagram

The system's dynamics can be therewith written as

$$\tilde{x}_{k+1} = A\tilde{x}_k + B\tilde{u}_k + \Psi_k^x, \qquad \tilde{y}_k = C\tilde{x}_k + \Psi_k^y, \quad \forall k \in \mathcal{K} \qquad \tilde{x}_0 = 0. \qquad (4.63)$$

In our implementation of the LQGI controller, following the *separation principle*, an estimate $\check{x}$ of state $\tilde{x}$ is firstly obtained by means of a delayed Kalman filter. The estimate is later on used on an linear-quadratic regulator instance as if it was the true state. The delayed Kalman filter's state difference equation corresponds to

$$\check{x}_{k+1|k} = A\check{x}_{k|k-1} + B\tilde{u}_k + L(-e_k - C\check{x}_{k|k-1}), \qquad (4.64)$$

In Eq. (4.64), $\check{x}_{k|k-1}$ denotes a one-step prediction of $\tilde{x}_k$, i.e. one obtained using information up to instant t_{k-1}. Notice that in instant k, the filter's state is $\check{x}_{k|k-1}$. This state is augmented with the accumulated superheating error I_k satisfying the difference equation

$$I_{k+1} = I_k + T_s e_k, \quad I_0 = 0. \qquad (4.65)$$

The linear-quadratic regulator is found for the augmented state vector by solving

$$\min_{\tilde{u}_0, \tilde{u}_1, \dots} \quad J_{\mathrm{LQGI}} = \mathbb{E}\left\{ \sum_{k=0}^{\infty} \begin{bmatrix} \check{x}_{k|k-1} \\ \tilde{u}_k \end{bmatrix}^T \Lambda_{xu} \begin{bmatrix} \check{x}_{k|k-1} \\ \tilde{u}_k \end{bmatrix} + \Lambda_I I_k^2 \right\} \qquad (4.66a)$$

$$\text{s.t} \quad \check{x}_{k+1|k} = (A - LC)\check{x}_{k|k-1} + B\tilde{u}_k - Le_k \qquad (4.66b)$$

$$I_{k+1} = I_k + T_s e_k, \qquad (4.66c)$$

$$\check{y}_{k|k-1} = C\check{x}_{k|k-1}, \qquad (4.66d)$$

$$\check{x}_{0|-1} = \check{x}_{-1}, \quad I_0 = 0 \qquad (4.66e)$$

As a result, the LQR feedback gain $\begin{bmatrix} K_x & K_I \end{bmatrix}$ is obtained, with which the control takes the form

$$\tilde{u}_k = \tilde{u}_{k,\mathrm{pre}}^{\mathrm{LQGI}} = -(K_x \check{x}_{k|k-1} + K_I I_k). \qquad (4.67)$$

Defining $\tilde{x}_k^{\mathrm{LQGI}} \stackrel{\text{def}}{=} \begin{bmatrix} \check{x}_{k|k-1}; & I_k \end{bmatrix}$, the LQGI is a dynamic system with the form

$$\tilde{x}_{k+1|k}^{\mathrm{LQGI}} = A_{\mathrm{LQGI}}\tilde{x}_{k|k-1}^{\mathrm{LQGI}} + B_{\mathrm{LQGI}}e_k, \quad \tilde{u}_{k,\mathrm{pre}}^{\mathrm{LQGI}} = C_{\mathrm{LQGI}}\tilde{x}_{k|k-1}^{\mathrm{LQGI}}, \quad \tilde{x}_{0|-1}^{\mathrm{LQGI}} = \begin{bmatrix} \check{x}_{0|-1}; & I_0 \end{bmatrix}, \quad (4.68)$$

Where matrices $\boldsymbol{A}_{\mathrm{LQGI}}$, $\boldsymbol{B}_{\mathrm{LQGI}}$ and $\boldsymbol{C}_{\mathrm{LQGI}}$ are obtained by means of the formulas

$$\boldsymbol{A}_{\mathrm{LQGI}} = \begin{bmatrix} \boldsymbol{A} - \boldsymbol{LC} - \boldsymbol{BK}_x & -\boldsymbol{BK}_I \\ 0 & 1 \end{bmatrix}, \quad \boldsymbol{B}_{\mathrm{LQGI}} = \begin{bmatrix} -\boldsymbol{L} \\ T_s \end{bmatrix}, \quad \boldsymbol{C}_{\mathrm{LQGI}} = \begin{bmatrix} -\boldsymbol{K}_x & -\boldsymbol{K}_I \end{bmatrix}. \quad (4.69)$$

The LQGI controller can be represented by the block diagram in Fig. 4.3.
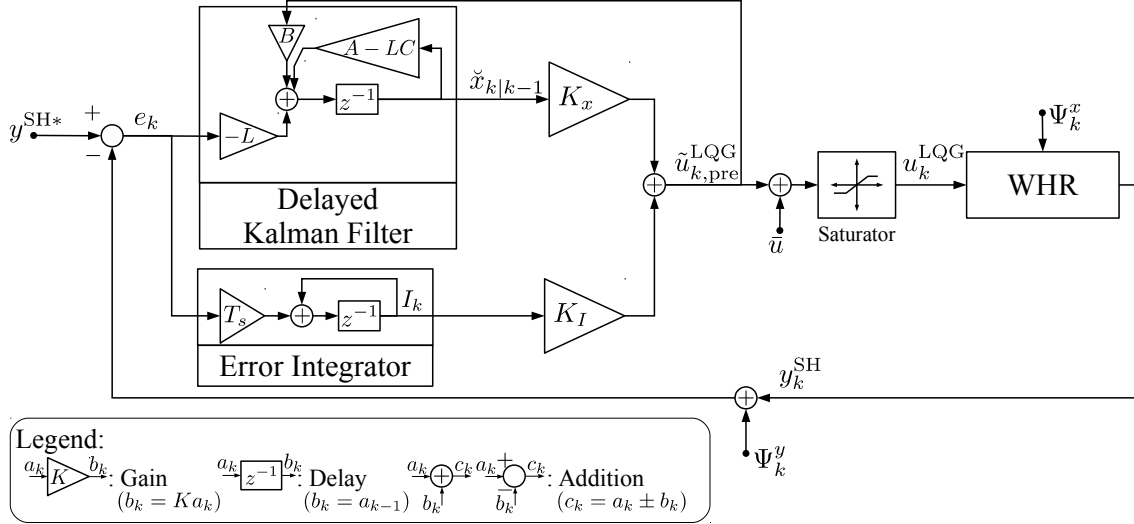
Figure 4.3: LQGI controller block diagram

To keep the controller within its bounds, the LQGI controller output $\tilde{u}_{k,\mathrm{pre}}^{\mathrm{LQGI}}$ is truncated as

$$u_k^{\mathrm{LQGI}} = \max(\dot{m}_{\mathrm{in,min}}, \min(\dot{m}_{\mathrm{in,max}}, \tilde{u}_{k,\mathrm{pre}}^{\mathrm{LQGI}} + \bar{u})). \quad (4.70)$$

Overview

In this chapter we have given brief descriptions of the main control and estimation methods considered in this thesis. In particular, we have proposed the use of the direct multiple shooting method to tackle the infinite-dimensional optimization problems stated in Chapter 3. The method originates related finite-dimensional optimization problems whose solutions can be obtained efficiently with the help of the numerical techniques described in this chapter. These methods stand out for their ability to handle the full nonlinear dynamics and the operational constraints formulated in Chapter 3 while pursuing the minimization of the considered objective functions. In this chapter we have also given an overview on the real-time iteration scheme for NMPC and MHE.

In Chapter 5 we consider numerical instances of the formulated models and control strategies and proceed to compare the performance the WHR is able to achieve under each of them.

5 Numerical Results

In this chapter, the results obtained from several numerical tests on the proposed methodologies for a scenario proposed by our industry cooperation partner are shown and analyzed. We first proceed in Section 5.1 by assigning numerical values to a series of magnitudes, defined in previous chapters, that are needed for evaluating the model and solving the DAEs corresponding to the model. Next, our scenario, consisting of real-world measurements carried out by our industry cooperation partner Daimler AG during a heavy duty truck trip in Baden-Württemberg, Germany, in 2015, is introduced and, based on it, the results of the model linearizations and the tunings required for the PI and LQGI controllers introduced in Chapter 4 are shown. Finally, we show and analyze the numerical results obtained for several experiments that have been performed in order to assess our solution scheme for the OCP and the schemes for NMPC and MHE. In Section 5.2, several numerical instances of the DMS method for the solution of the OCP are tested. Next, in Section 5.3, the performance of the NMPC scheme is analyzed for different prediction horizons and numbers of nodes. The effect of counting on accurate predictions of the exhaust gas conditions along the prediction horizon is also studied. Further, the NMPC scheme is compared with the LQGI and PI strategies defined in Chapter 4. Finally, in Section 5.4, the MHE scheme performance is tested, and the results emanating from the simultaneous operation of both the MHE and the NMPC schemes are compared with those of Section 5.3.

All tests have been performed using a single core of a desktop computer with an Intel(R) Core(TM) i7-6700 CPU @ 3.40GHz with 16GB RAM running Ubuntu Linux 14.04.

5.1 Preliminaries

In this subsection we proceed to assign numerical values to quantities that are not considered as decision variables in our optimization problems, but are required to evaluate the model. Namely, we specify the meshes for the evaluation of the thermophysical properties and the constraint bounds.

5.1.1 Thermophysical Properties

For the evaluation of the thermophysical properties and the external inputs, the values of the parameters defined in Section 3.3 are listed in Table 5.1. These values are used for defining the meshes and regions for the set of cubic and bicubic splines described in the same Section.

Validation: In order to assess the quality of these interpolations, REFPROP is used to generate validation data sets for each curve and surface. The data sets are generated over domains that correspond to the interval $[p_{\min}, p_{\max}]$ for the the saturated and two-phase properties; the regions SL and SV for the single-phase properties depending on pressure-enthalpy pairs; the PS square for the single-phase properties depending on pressure-entropy pairs; and the $[p_{G,\min}, p_{G,\max}] \times [\theta_{G,\min}, \theta_{G,\max}]$ square for the exhaust gas properties; see Sections 3.3.2 and 3.3.4. On each domain, an equally distributed point mesh is defined that is much more dense than those used for obtaining the splines (i.e. those defined by Table 5.1). The mean

Table 5.1: Values of parameters used for the evaluation of thermophysical properties and external inputs. The data corresponding to the external inputs span a time horizon of $2600[s]$. The number of intervals used for their spline approximation corresponds to $N_t = 390$.

Parameter	Value	Units	Parameter	Value	Units	Parameter	Value
$p_{\min}$	100	[kPa]	$p_{\max}$	6.15	[MPa]	N_p	95
$h_{\min}$	0.22	[MJ/kg]	$h_{\max}$	2.5	[MJ/kg]	N_h	18
$s_{\min}$	0.82	[kJ/kgK]	$s_{\max}$	4.527	[kJ/kgK]	N_s	20
$p_{G,\min}$	100	[kPa]	$p_{G,\max}$	200	[kPa]	N_{pG}	2
$\theta_{G,\min}$	350	[K]	$\theta_{G,\max}$	1700	[K]	$N_{\theta G}$	46

and standard deviations of the relative errors resulting of estimating the data obtained through REFPROP by means of the corresponding splines are summarized in Table 5.2, where it can be seen that the deviations are in all cases tightly concentrated around very small values.

Table 5.2: Mean and standard deviation of the percentage relative error of the spline interpolation

Saturated and two-phase state properties			Single-phase state properties		
Variable [%]	Mean [%]	Std.Dev. [%]	Variable [%]	Mean [%]	Std.Dev. [%]
h'	$2.1480 \cdot 10^{-2}$	$8.1939 \cdot 10^{-2}$	Depending on $p-h$ pairs, on domain SL		
h''	$5.4653 \cdot 10^{-3}$	$1.6990 \cdot 10^{-2}$	θ_F	$5.9852 \cdot 10^{-3}$	$1.8654 \cdot 10^{-2}$
ϱ'	$1.4935 \cdot 10^{-2}$	$5.4249 \cdot 10^{-2}$	ϱ	$5.1352 \cdot 10^{-3}$	$1.4971 \cdot 10^{-2}$
ϱ''	$1.6358 \cdot 10^{-2}$	$4.1670 \cdot 10^{-2}$	s	$1.1453 \cdot 10^{-2}$	$3.5532 \cdot 10^{-2}$
$\theta_{F,2}$	$1.2092 \cdot 10^{-3}$	$1.0384 \cdot 10^{-2}$	Depending on $p-h$ pairs, on domain SV		
Exhaust gas properties			θ_F	$3.0096 \cdot 10^{-3}$	$1.0487 \cdot 10^{-2}$
c_G	$4.0780 \cdot 10^{-6}$	$1.9796 \cdot 10^{-5}$	ϱ	$2.1365 \cdot 10^{-2}$	$4.1902 \cdot 10^{-2}$
			s	$1.9796 \cdot 10^{-3}$	$8.2992 \cdot 10^{-3}$
			Depending on $p-s$ pairs		
			h	$1.5072 \cdot 10^{-2}$	$3.6038 \cdot 10^{-2}$

5.1.2 Constraints

For the constraints (3.85) to (3.89), the following values are chosen,

- Pump massflows: $\dot{m}_{\text{in,min}} = 1.8$ [kg/h] and $\dot{m}_{\text{in,max}} = 386.8$ [kg/h]

- Tube lengths: $L_{\min} = 0.1$ [m], $L_{3,\min} = 0.033$ [m] and $L_{\max} = 140.69$ [m]

- Pressures: $p_{\min} = 100$ [kPa] and $p_{\max} = 6.0$ [MPa]

- Wall temperatures: $\theta_{W,\min} = 200$ [K] and $\theta_{W,\max} = 1000$ [K]

- Ethanol decomposition temperature: $\theta_{F,\max} = 523.15$ [K]

The pump minimum and maximum massflows have been decided jointly with our industry cooperation partner. On the other hand, $L_{3,\min}$ is obtained from numerical tests as a magnitude small enough for its influence in the energy recovery to be negligible but big enough to provide robustness to our computations (see Remark 3.5.1). The ethanol decomposition temperature

is chosen based on known facts about ethanol (see e.g. [95]), which is assumed as our working fluid. The rest of the upper and lower bounds are chosen so that they do not play a major role in the final results but help in the convergence towards the solution. The pressure upper and lower bounds are selected taking Table 5.1 into account as well.

5.1.3 Model Parameters and Initial State

In all our experiments, the WHR dynamics are assumed to be perfectly represented by the DAE system (3.53). The values of its parameters used throughout this thesis are listed in Table 5.3. Further, the WHR model is started at $t = t_0$ with the initial state $x(t_0) \stackrel{\text{def}}{=} x_0$ of Table 5.4.

Table 5.3: WHR model parameter values

Param.	Value	Units	Param.	Value	Units	Param.	Value	Units
L	$2.00 \cdot 10^{+1}$	[m]	d_i	$1.19 \cdot 10^{-2}$	[m]	d_o	$9.00 \cdot 10^{-2}$	[m]
ϱ_W	$8.92 \cdot 10^{+3}$	[kg/m^3]	c_W	$3.85 \cdot 10^{+2}$	[J/kgK]	$\alpha_{F,1}$	$9.06 \cdot 10^{+3}$	[W/m^{2}K]
$\alpha_{F,2}$	$1.89 \cdot 10^{+4}$	[W/m^{2}K]	$\alpha_{F,3}$	$8.00 \cdot 10^{+2}$	[W/m^{2}K]	$\alpha_{G,1}$	$1.82 \cdot 10^{+3}$	[W/m^{2}K]
$\alpha_{G,2}$	$5.00 \cdot 10^{+3}$	[W/m^{2}K]	$\alpha_{G,3}$	$8.00 \cdot 10^{+2}$	[W/m^{2}K]	p_G	$1.02 \cdot 10^{+2}$	[kPa]
$\eta_{\text{ex,is}}$	$9.00 \cdot 10^{-1}$	[-]	p_D	$2.26 \cdot 10^{+2}$	[kPa]	n_{ex}	$1.08 \cdot 10^{+2}$	[Hz]
$\eta_{\text{ex,V}}$	$5.30 \cdot 10^{-2}$	[-]	V_{ex}	$1.53 \cdot 10^{-3}$	[m^3]	$\eta_{\text{ex,el}}$	$8.20 \cdot 10^{-1}$	[-]
p_A	$1.61 \cdot 10^{+2}$	[kPa]	h_A	$3.49 \cdot 10^{-1}$	[MJ/kg]	$\eta_{\text{p,is}}$	$3.34 \cdot 10^{-1}$	[-]
$\eta_{\text{p,el}}$	$9.20 \cdot 10^{-1}$	[-]						

Table 5.4: Initial differential state x_0 for the WHR

$L_{1,0}$ [m]	$L_{2,0}$ [m]	$p_{\text{ev}0}$ [MPa]	$\theta_{W,1,0}$ [K]	$\theta_{W,2,0}$ [K]	$\theta_{W,3,0}$ [K]
16.11	2.51	0.56	371.60	429.39	591.92

A consistent initial algebraic state corresponds to $h_{C,0} = 1.44$ [MJ/kg].

With regard to the model parameters, the evaporator dimensions L, d_i and d_o are obtained from manual tuning. Further, the tube's density ϱ_W and specific heat capacity c_W come from assuming it as made of copper and evaluating the corresponding properties using REFPROP. Also, the heat transfer coefficients have been obtained from manual tuning, starting from guesses provided by the model of [23]. On the other hand, the exhaust gas pressure p_G corresponds to the atmospheric pressure at sea level, and the working fluid pressure and enthalpy at the pump inlet p_A and h_A, and the working fluid pressure at the expander outlet p_D have been handed over by our cooperation partner. They correspond to least-squares estimates of those quantities obtained using data corresponding to the scenario specified in Section 5.1.4. The expander and pump efficiencies $\eta_{\text{ex,is}}$, $\eta_{\text{ex,V}}$, $\eta_{\text{ex,el}}$, $\eta_{\text{p,is}}$ and $\eta_{\text{p,el}}$ have been obtained from manual tuning, starting from typical values. Finally, the expander volume V_{ex} is typical for devices of its kind.

5.1.4 Scenario

In this section, we introduce the scenario used to test the proposed control and estimation strategies. It consists of exhaust gas temperature measurements and exhaust gas massflow estimations recorded during a real heavy duty truck drive performed by Daimler AG. The data

are approximated by splines as explained in Section 3.3.3. The resulting curves constitute function $w(t)$ of Eq. (3.53) and are plotted in Fig. 5.1.

(a) Exhaust gas inlet massflow.

(b) Exhaust gas inlet temperature.
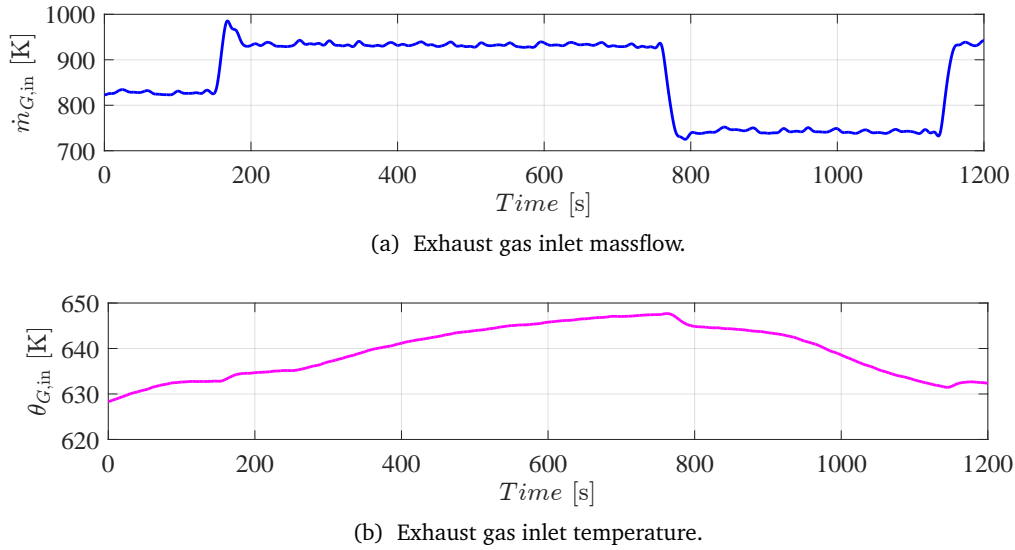
Figure 5.1: Scenario considered for all tests in this thesis

In addition to the exhaust gas conditions plotted in Fig. 5.1, our industry cooperation partner had also handed over data corresponding to further important quantities recorded during the same drive the curves in Fig. 5.1 were. These data include the working fluid massflow and the measurements ξ of Section 3.5.3, and have been used to determine adequate values for some of the model's parameters and for initializing the controls and/or differential states in implementations using the DMS method. For the sake of brevity, those data are not plotted.

5.1.5 Model Linearization and Linear Controllers

Given the parameter set from Section 5.1.3, we obtain the values $\bar{w} = (822.81\,[\text{kg/h}], 628.37\,[\text{K}])$, which correspond to $w(t_0)$. The solution of Eq. (3.74) yields the equilibrium state and control in Table 5.5.

Table 5.5: Equilibrium state and control for $\bar{w} = (822.81\,[\text{kg/h}], 628.37\,[\text{K}])$.

$\bar{L}_1\,[\text{m}]$	$\bar{L}_2\,[\text{m}]$	$\bar{p}_{\text{ev}}\,[\text{MPa}]$	$\bar{\theta}_{W,1}\,[\text{K}]$	$\bar{\theta}_{W,2}\,[\text{K}]$	$\bar{\theta}_{W,3}\,[\text{K}]$	$\bar{m}_{\text{in}}\,[\text{kg/h}]$
17.12	2.38	0.55	371.06	432.02	598.21	247.11

From this operating point we obtain the discrete-time linearized model Eq. (3.81) using a sampling time of $T_s = 100\,[\text{ms}]$.

Remark 5.1.1 (Linear Model Properties) *It can be verified that the discrete-time linearized model is stable, observable and controllable by analyzing its poles and the associated Gram matrices, see e.g. [101, 112]. The discrete-time linearized model exhibits a zero at the origin, i.e. a time-delay and is thus of nonminimum phase.*

Tuning of alternative controllers

PI Controller. For the PI controller defined in Section 4.3.1, a phase margin PM of at least $90\,[°]$ and an open-loop gain crossover frequency of $\omega_c = 0.1\,[\text{rad/s}]$. This in accordance to the nonminimum-phase nature of the discrete-time linearized model and the sampling time T_s. The results are the constants $K_p = -3.9336\cdot10^0\,[\text{kg/Kh}]$ and $K_i = -5.3213\cdot10^{-1}\,[\text{kg/Khs}]$.

LQGI Controller. For the LQGI controller defined in Section 4.3.2, the noise covariance matrix is chosen as $\boldsymbol{Q}_\Psi = 10^{-3}\mathbb{I}_{n_x+n_z+1}$. Additionally, the cost function of Eq. (4.66a) is defined using matrices $\boldsymbol{\Lambda}_{xu} = \mathbb{I}_{n_x+n_z+n_u}$, and $\boldsymbol{\Lambda}_I = 1$. The gains constituting the Kalman filter gain and the LQR are given by

$$
\boldsymbol{K}_x = \big[2.55\cdot10^{+2}, 2.14\cdot10^{+2}, -3.21\cdot10^{+1}, -4.41\cdot10^{+1},\dots \tag{5.1a}
$$
$$
5.69\cdot10^{+2}, -2.95\cdot10^{+2}, -6.78\cdot10^{+1}, -1.45\cdot10^{-3}\big]
$$
$$
\boldsymbol{K}_I = \big[9.90\cdot10^{-1}\big] \tag{5.1b}
$$
$$
\boldsymbol{L} = \big[-6.75\cdot10^{-2}, 5.70\cdot10^{-2}, 1.54\cdot10^{-4}, 7.26\cdot10^{-4},\dots \tag{5.1c}
$$
$$
-4.78\cdot10^{-4}, -7.74\cdot10^{-3}, -5.24\cdot10^{-3}, 4.73\cdot10^{-1}\big]
$$

Remark 5.1.2 (Stability of the PI and LQGI controllers) *With the aforementioned settings, the frequency responses of each closed-loop system incorporating respectively the PI and the LQGI controllers can be analyzed to conclude that both controllers are stable.*

5.1.6 Moving Horizon Estimation

For those experiments considering the MHE scheme of Section 3.5.3, we consider the measurements' standard deviations to be The measurements' standard deviations are $\sigma_p = 10$ [kPa], $\sigma_{\theta_F} = 1$ [K] and $\sigma_{\theta_G} = 1$ [K]. These are based on the error bands of typical industrial pressure and temperature sensors, see e.g. [72, 73]. For the terminal cost we use the values, $\sigma_L = 1.0$ [m] and $\overline{L}_3 = 0.5$ [m]. These values have been chosen from numerical experience. Additionally, unless other specified the number of shooting intervals is chosen as $M = 10$. The estimation window is defined as $\Delta t_{\text{MHE}} = 1$ [s].
Whenever the NMPC and the MHE are used together, the MHE keeps the aforementioned values and, for the NMPC, the number of shooting intervals is chosen as $N = 3$ and the prediction horizon corresponds to $\Delta t_{\text{NMPC}} = 5$ [s]. Both the NMPC and the MHE assume the exhaust gas conditions are known.

5.1.7 Time, Tolerances and Constraint Violations

Sampling time: In this thesis, unless otherwise indicated we consider a time interval $\mathcal{T} = [t_0, t_f]$ with $t_0 = 0$, $t_f = 1200$ [s]. In real-time implementations (i.e. NMPC, MHE, PI, LQGI), the sampling time is $T_s = 100$ [ms], and we divide the time interval in thus $K = \lfloor(t_f-t_0)/T_s\rfloor = 12000$ subintervals. The sample times $t_k = t_0+kT_s$, $\forall k \in \mathcal{K} = \{0, 1, \dots, K\}$ constitute the *sampling mesh*. We remark that $t_0^{(k)} = t_k$, i.e. the current time in NMPC and MHE implementations coincides with the sample times.

Computational time vectors: For NMPC, we introduce the real *computational time vector* $\boldsymbol{t}_c$ of dimension $K + 1$. We define its k-th component as the sum of the computational times of both the preparation and feedback phases associated to the k-th NMPC subproblem $P_{\text{NMPC}}^{(k)}$. We

denote as $\max(\mathbf{t}_c)$ the maximum computational time achieved. In this thesis we are interested in instances of our NMPC scheme in which $\max(\mathbf{t}_c) < T_s$.

Tolerances: In the schemes that make use of the DMS method, i.e. the optimal control solution scheme, the NMPC and the MHE, the NLP accuracy is chosen as $\text{ACC} = 1 \cdot 10^{-3}$ (see Section 4.1.1), whereas integration tolerance corresponds to $\text{TOL} = 1 \cdot 10^{-5}$ (see Section 4.1.2).

Constraint Violation: To assess the constraint violation in each experiment along $[t_0, t_\mathrm{f}]$, the *constraint violation vector* $\mathbf{\Gamma} \in \mathbb{R}^{20}$ is defined using the components of $\mathbf{c}(t)$ from (3.85) - (3.89) as

$$\Gamma_i = -\frac{1}{t_\mathrm{f} - t_0} \int_{t_0}^{t_\mathrm{f}} \min(0, \mathbf{c}_i(\mathbf{x}(t), \mathbf{z}(t), \mathbf{u}(t), \mathbf{p}))\mathrm{d}t, \quad i \in \{1, \dots, 20\}, \tag{5.2}$$

The integrals are approximated by a trapezoidal sum over the sampling mesh. These computations are done a posteriori using the actual state and control trajectories generated by the application of each control strategy.

5.2 Optimal Control

In this section we proceed to analyze the numerical solutions of the optimal control problem as stated in Section 3.5.1, considering the full nonlinear dynamics of Eq. (3.53). In all our tests we use the initial state in Table 5.4, the parameter values of Table 5.3, and assume the exhaust gas conditions (i.e. the external inputs), given in Section 5.1.4, as perfectly known.

In Section 5.2.1, the results of considering different numbers of multiple shooting intervals N to solve the associated OCP are summarized. In Section 5.2.2 the transient behavior of a selected obtained solution is analyzed.

In all experiments in this section, the iterations of the tailored SQP algorithm of Section 4.1.1 are performed until the convergence criterion is satisfied, i.e. the quantity $K(\mathbf{v}_k, \Delta \mathbf{v}^{c\diamond}, \mathbf{\lambda}^\diamond, \mathbf{\mu}^\diamond)$ defined in Eq. (4.47) is less than ACC.

5.2.1 Optimal Control for Different Numbers of Intervals

In this section we consider the numerical solution of the OCP of Section 3.5 by means of the DMS and the tailored SQP methods of Section 4.1. We analyze the effect of choosing different different numbers of multiple shooting intervals N.

In each experiment, the finite-dimensional control vectors $\mathbf{q}_0, \mathbf{q}_1, \dots, \mathbf{q}_N$ are initialized by interpolating working fluid massflow measurement data corresponding to the scenario defined in Section 5.1.4. Further, the node differential and algebraic state vectors are initialized by integrating Eq. (3.53); using the initial finite-dimensional control vectors, the external inputs of Section 5.1.4 and the initial differential states in Table 5.4. The algebraic state for the first multiple shooting node is chosen to be consistent with the corresponding differential state through the consistency conditions Eq. (3.53b).

The solutions are summarized in Table 5.6, where the net generated energy $\Phi(t_\mathrm{f})$ of Eq. (3.84), the computation time until the satisfaction of the termination criterion and the constraint violation vector $\mathbf{\Gamma}$ are given[1]. In order to evaluate $\mathbf{\Gamma}$, for each value of N, the state vectors at the sampling mesh are obtained by integration of the DAE system (3.53) using the obtained controls.

---

[1]In all tables, components of $\mathbf{\Gamma}$ that were null for all experiments are omitted

In Table 5.6, a clear convergent behavior can be seen. The objective function value changes only in the second decimal between the solutions for $N = 150$ and $N = 1000$, only in the third decimal between the solutions for $N = 600$ and $N = 1000$. These changes in the number of intervals correspond to factors of 6.67 and 1.67, respectively. Additionally, the constraint satisfaction improves in general as the number of nodes is incremented.

The entries where $\Gamma_3 > 0$ or $\Gamma_8 > 0$ are associated to small violations in the prevention of droplets entering the expander and in the prevention of working fluid thermal decomposition at expander inlet, respectively. They represent very small magnitude oscillations around $c_3(x, z) = 0$ and $c_8(x, z) = 0$ that can be tolerated, and are a consequence of the use of time meshes that are relatively coarse in comparison to the fast WHR dynamics. In any case, tiny security margins can be added in the constraint formulation as done for $c_4(x)$ (limitation of the evaporator's third zone to a lower bound). In this case column Γ_4 in Table 5.6 shows that the violations are much smaller than the value chosen for $L_{3,\text{min}}$,

The table also evinces the high computational times that are reached as the time mesh is refined. This gives a solid motivation for our NMPC scheme, which is tested on the following section, for applications where a quick response is needed. Notwithstanding, the values and trajectories obtained for $N = 1000$ can be considered as a tight upper bound of the actual optimal controls and trajectories.

Table 5.6: Results for the optimal control with different number of intervals

N	$\Phi(t_f)$ [MJ]	Comp. Time [s]	Constraint Violation				
			Γ_1 [kg/h]	Γ_2 [kg/h]	Γ_3 [MJ/kg]	Γ_4 [m]	Γ_8 [K]
5	4.6557	11.65	$0.00 \cdot 10^0$	$0.00 \cdot 10^0$	$0.00 \cdot 10^0$	$5.24 \cdot 10^{-4}$	$4.03 \cdot 10^{-4}$
10	4.7120	7.93	$0.00 \cdot 10^0$	$0.00 \cdot 10^0$	$2.83 \cdot 10^{-6}$	$1.27 \cdot 10^{-3}$	$8.22 \cdot 10^{-4}$
20	4.7351	17.39	$1.53 \cdot 10^{-6}$	$0.00 \cdot 10^0$	$0.00 \cdot 10^0$	$9.25 \cdot 10^{-4}$	$1.87 \cdot 10^{-3}$
40	4.7346	49.95	$0.00 \cdot 10^0$	$0.00 \cdot 10^0$	$0.00 \cdot 10^0$	$4.29 \cdot 10^{-4}$	$1.49 \cdot 10^{-2}$
75	4.7595	149.95	$0.00 \cdot 10^0$	$0.00 \cdot 10^0$	$0.00 \cdot 10^0$	$1.28 \cdot 10^{-4}$	$6.80 \cdot 10^{-2}$
150	4.8234	215.61	$0.00 \cdot 10^0$	$0.00 \cdot 10^0$	$0.00 \cdot 10^0$	$8.40 \cdot 10^{-6}$	$4.88 \cdot 10^{-2}$
300	4.8452	1225.34	$0.00 \cdot 10^0$	$3.99 \cdot 10^{-5}$	$0.00 \cdot 10^0$	$3.70 \cdot 10^{-5}$	$5.00 \cdot 10^{-2}$
600	4.8843	10750.99	$0.00 \cdot 10^0$	$0.00 \cdot 10^0$	$5.23 \cdot 10^{-7}$	$1.56 \cdot 10^{-4}$	$1.15 \cdot 10^{-1}$
1000	4.8764	40309.74	$0.00 \cdot 10^0$	$0.00 \cdot 10^0$	$4.06 \cdot 10^{-8}$	$7.81 \cdot 10^{-5}$	$2.00 \cdot 10^{-2}$

5.2.2 Transient Analysis

For the reader's convenience, in this section we include an analysis concerning the transient evolution of selected magnitudes as the approximated optimal control is applied to the WHR. In Figs. 5.2 to 5.6 the results for $N = 5$, $N = 20$, $N = 75$, $N = 300$ and $N = 1000$ are included in that order. It can be seen how the increment in the degrees of freedom of the control allows it to leverage the dynamics of the WHR to reach higher net generated powers as some constraints become active as explained below. The following analyses are done on the curves of Fig. 5.6. In this case, the solution is characterized by the application of the minimum massflow during the first instants. When the maximum working fluid temperature is achieved shortly afterwards, the control adapts, so that the constraint keeps active at the multiple shooting nodes as the state evolves. During this process, the pressure increases and so do the power generation and the third zone length. As this takes place, the control exhibits oscillations which are briefly explained.
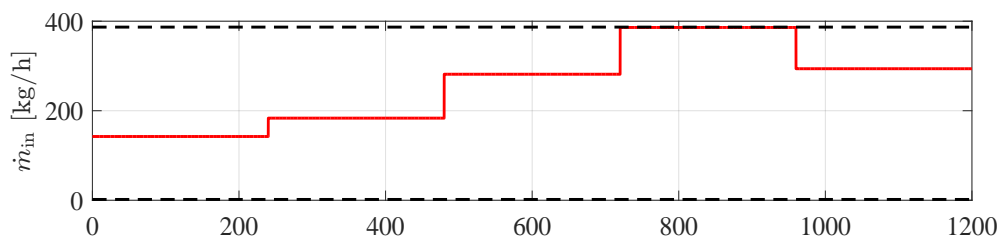
(a) Working fluid massflow (control). Dashed: upper and lower bounds.
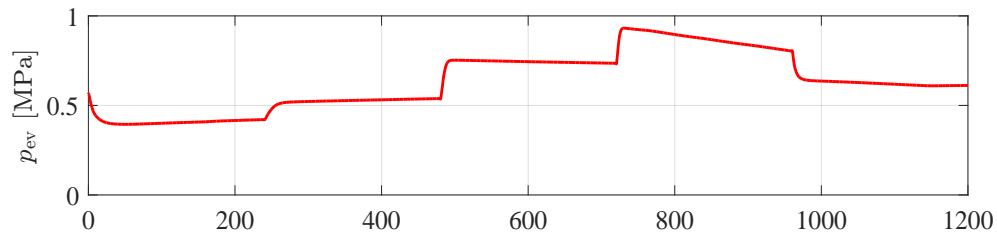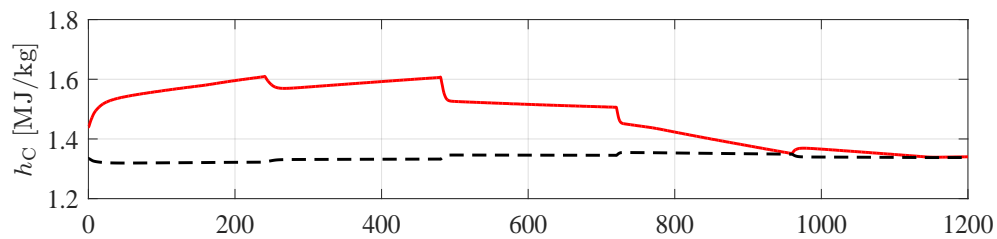
(b) Evaporator pressure.

(c) Working fluid enthalpy at the evaporator outlet. Dashed: saturated vapor enthalpy.
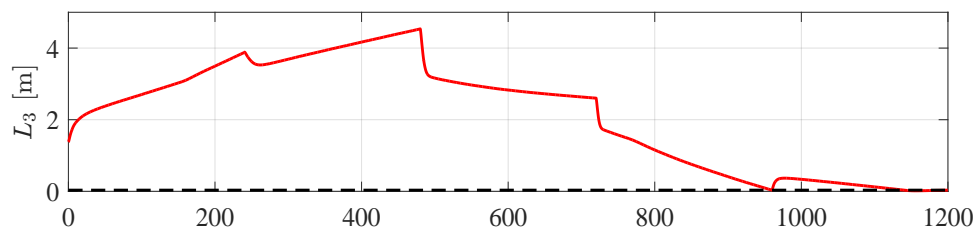
(d) Evaporator vapor zone length. Dashed: minimum zone length.
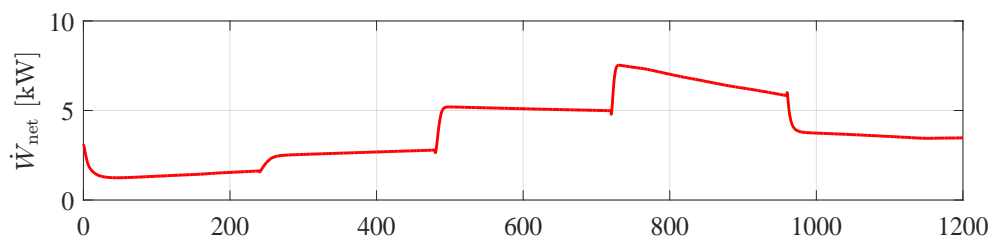
(e) Net generated power.
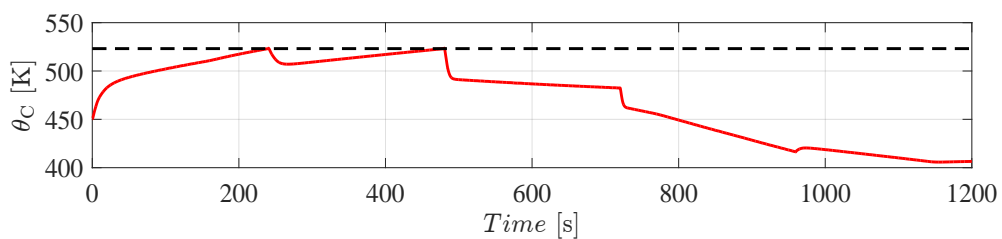
(f) Working fluid temperature at the evaporator outlet. Dashed: maximum allowable temperature.

Figure 5.2: Transient behavior of selected quantities obtained with the DMS method for $t_{\mathrm{f}} = 1200$ [s] and $N = 5$.
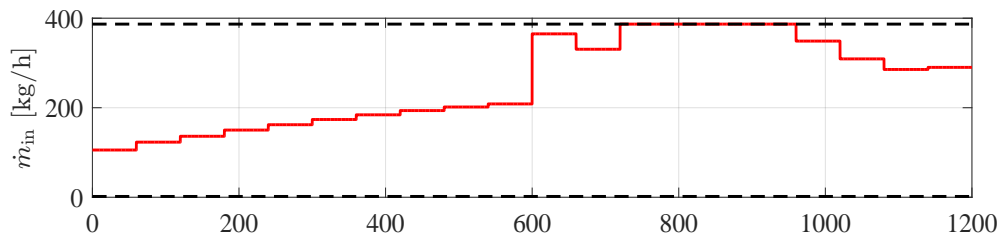
(a) Working fluid massflow (control). Dashed: upper and lower bounds.
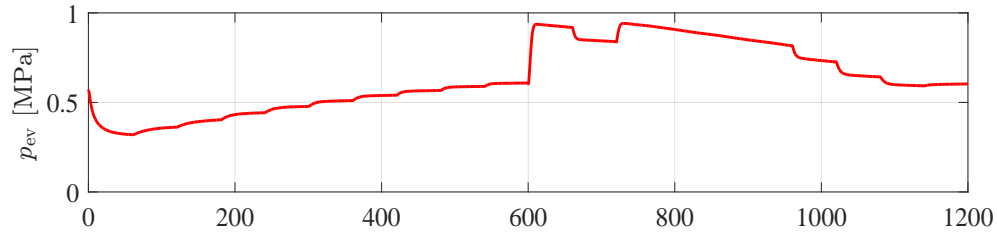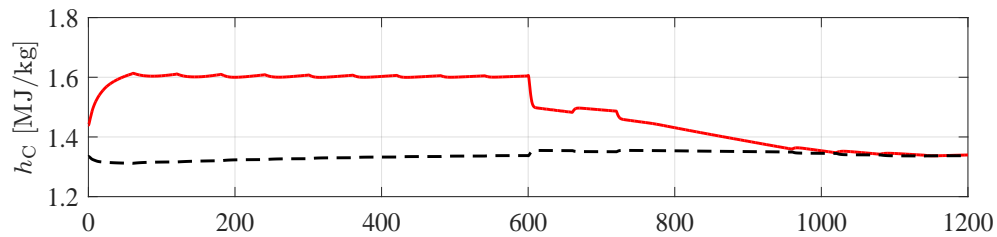
(b) Evaporator pressure.

(c) Working fluid enthalpy at the evaporator outlet. Dashed: saturated vapor enthalpy.
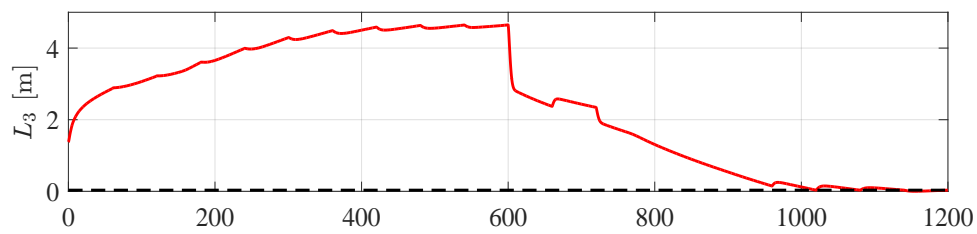
(d) Evaporator vapor zone length. Dashed: minimum zone length.
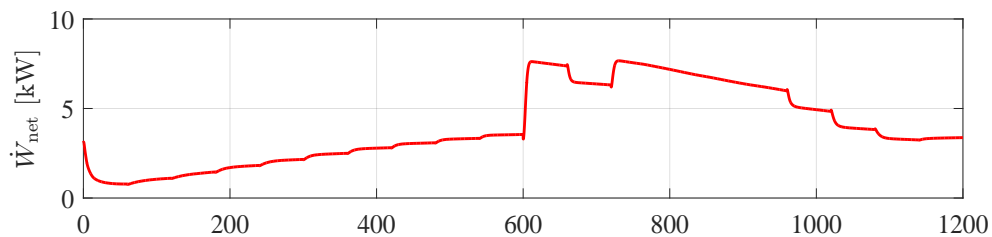
(e) Net generated power.
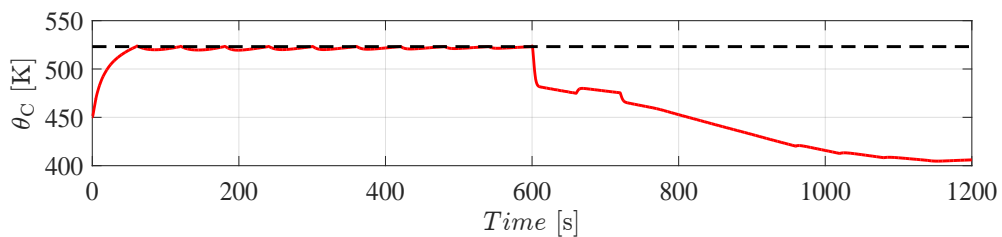
(f) Working fluid temperature at the evaporator outlet. Dashed: maximum allowable temperature.

Figure 5.3: Transient behavior of selected quantities obtained with the DMS method for $t_\mathrm{f} = 1200$ [s] and $N = 20$.
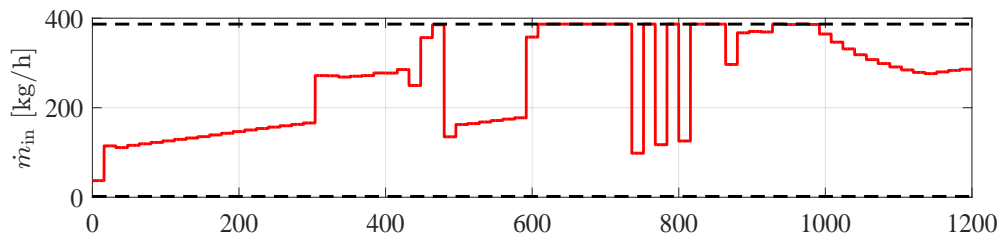
(a) Working fluid massflow (control). Dashed: upper and lower bounds.
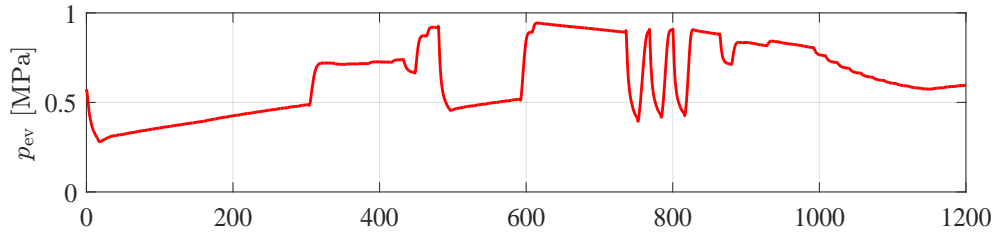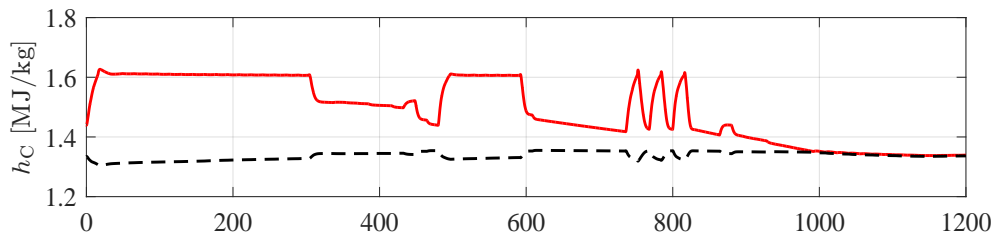
(b) Evaporator pressure.

(c) Working fluid enthalpy at the evaporator outlet. Dashed: saturated vapor enthalpy.
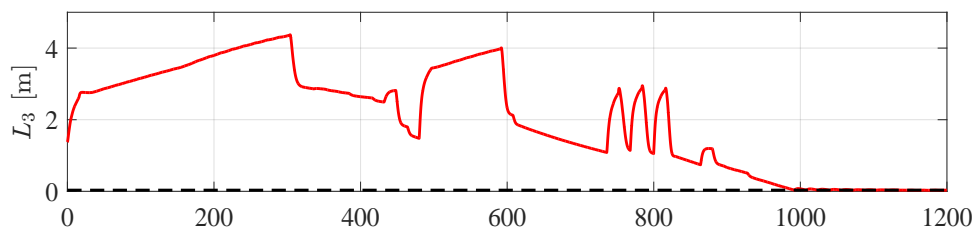
(d) Evaporator vapor zone length. Dashed: minimum zone length.
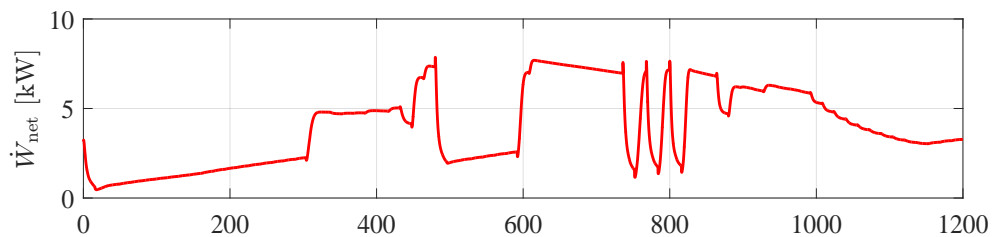
(e) Net generated power.
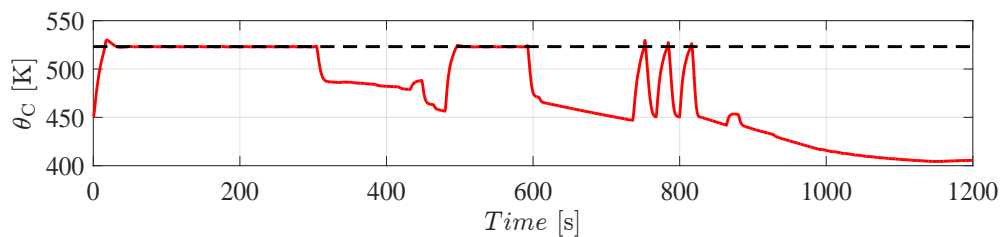
(f) Working fluid temperature at the evaporator outlet. Dashed: maximum allowable temperature.

Figure 5.4: Transient behavior of selected quantities obtained with the DMS method for $t_{\mathrm{f}} = 1200$ $[\mathrm{s}]$ and $N = 75$.
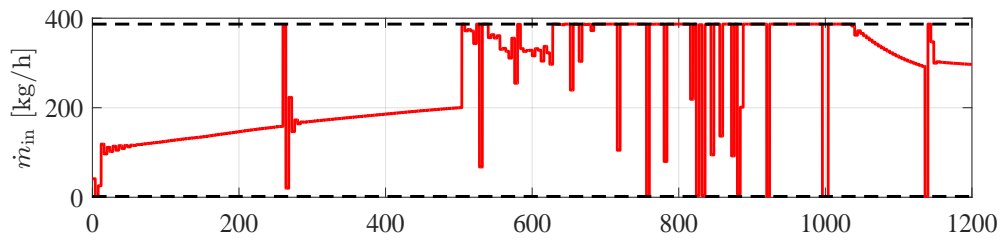
(a) Working fluid massflow (control). Dashed: upper and lower bounds.
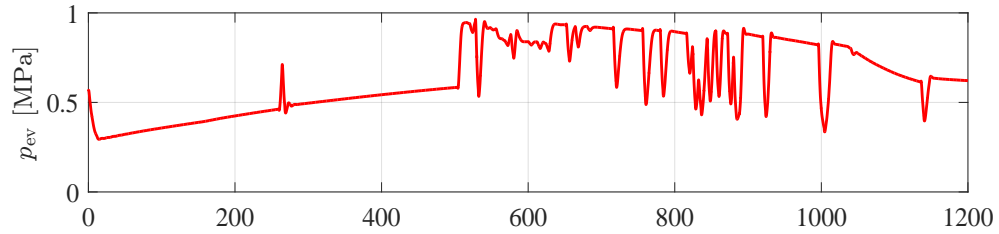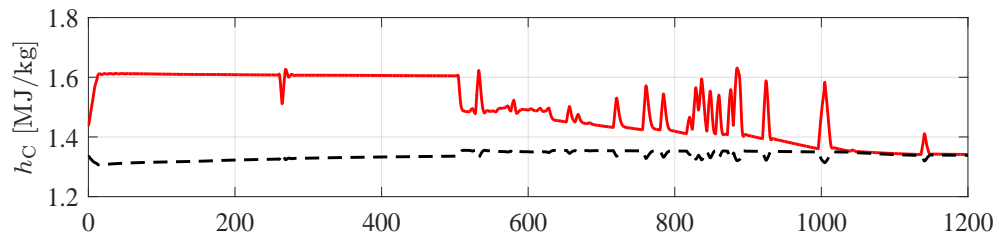
(b) Evaporator pressure.

(c) Working fluid enthalpy at the evaporator outlet. Dashed: saturated vapor enthalpy.
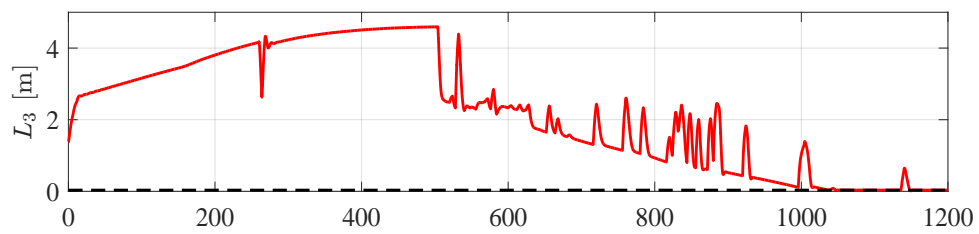
(d) Evaporator vapor zone length. Dashed: minimum zone length.
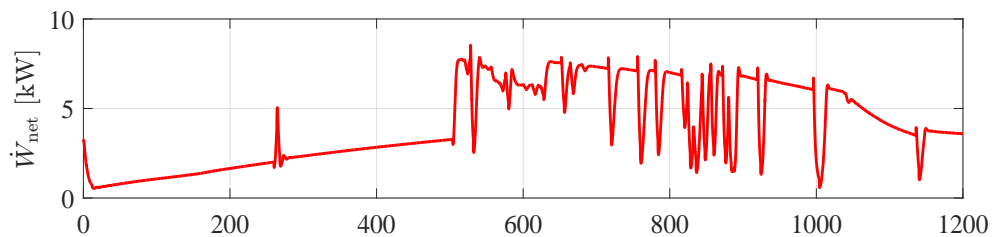
(e) Net generated power.
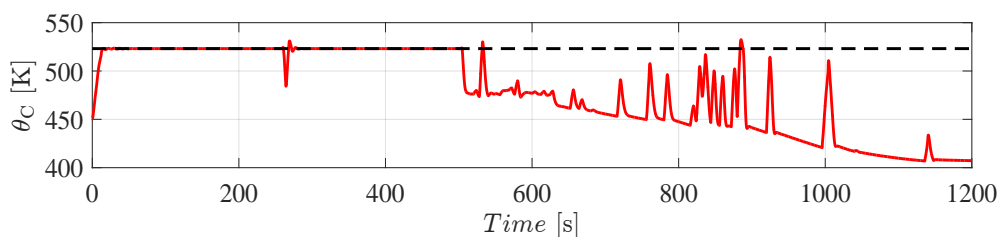
(f) Working fluid temperature at the evaporator outlet. Dashed: maximum allowable temperature.

Figure 5.5: Transient behavior of selected quantities obtained with the DMS method for $t_f = 1200$ [s] and $N = 300$.
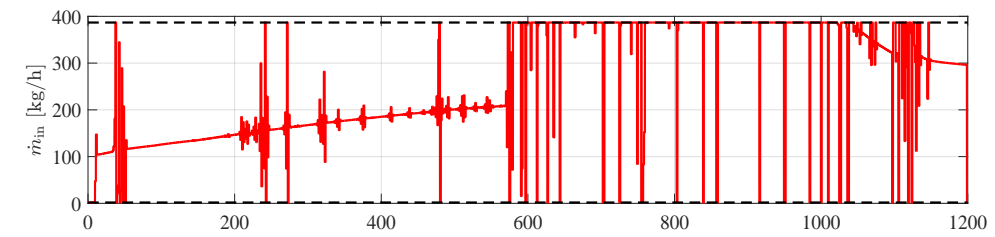
(a) Working fluid massflow (control). Dashed: upper and lower bounds.
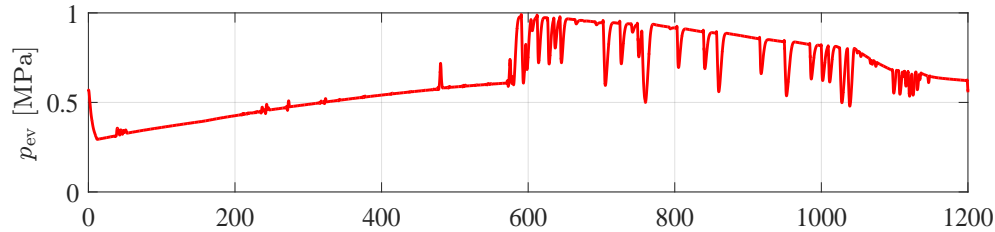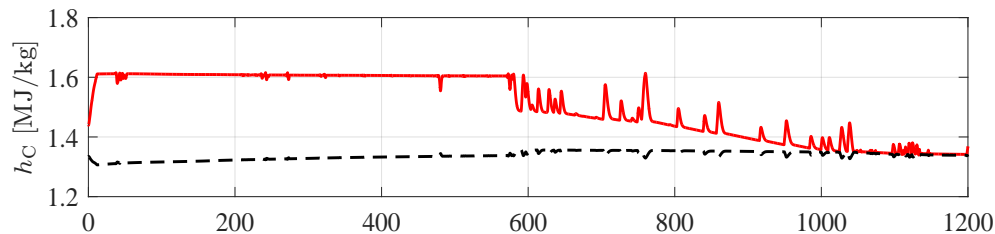
(b) Evaporator pressure.

(c) Working fluid enthalpy at the evaporator outlet. Dashed: saturated vapor enthalpy.
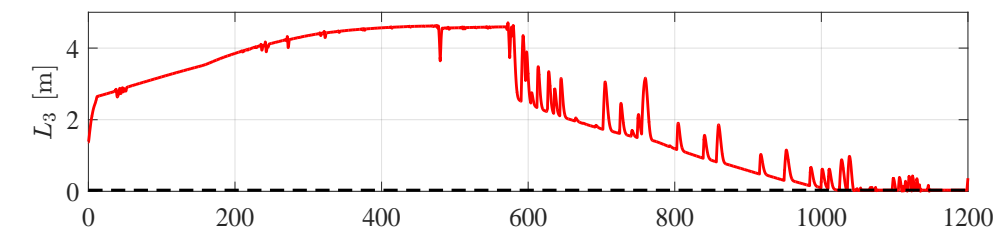
(d) Evaporator vapor zone length. Dashed: minimum zone length.
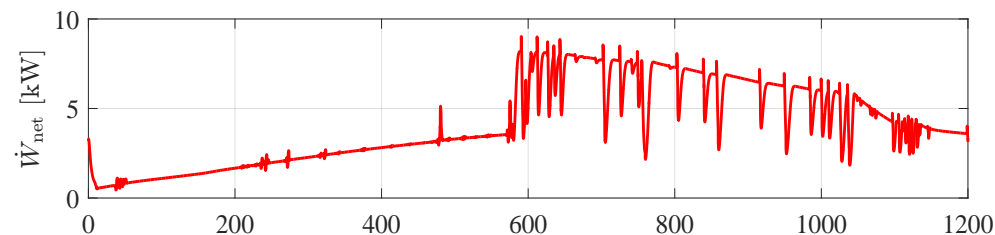
(e) Net generated power.
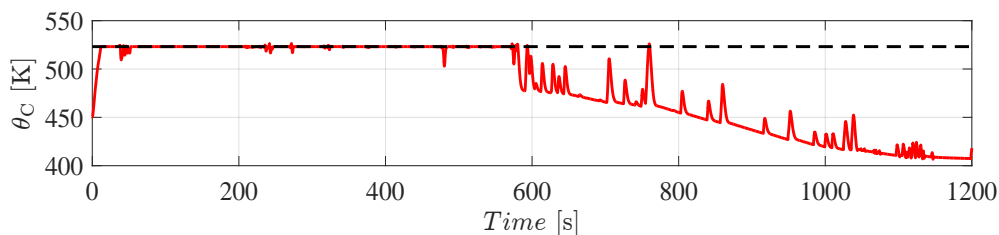
(f) Working fluid temperature at the evaporator outlet. Dashed: maximum allowable temperature.

Figure 5.6: Transient behavior of selected quantities obtained with the DMS method for $t_f = 1200$ [s] and $N = 1000$.
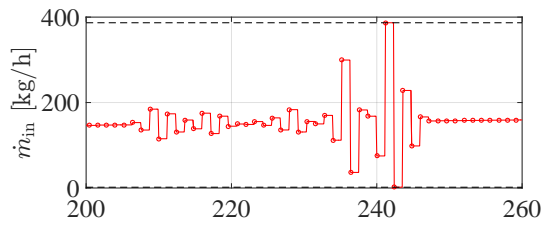
(a) Working fluid massflow (control). Dashed: upper and lower bounds.
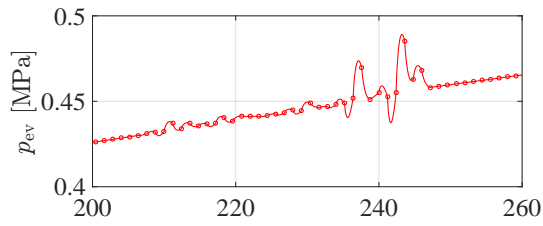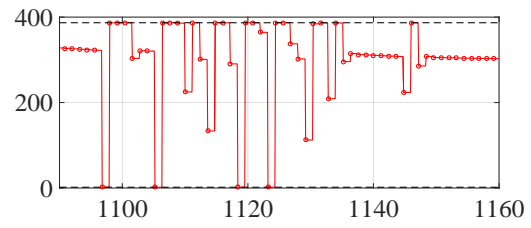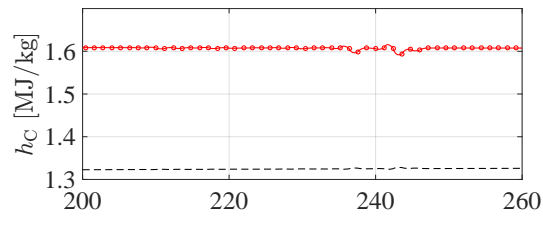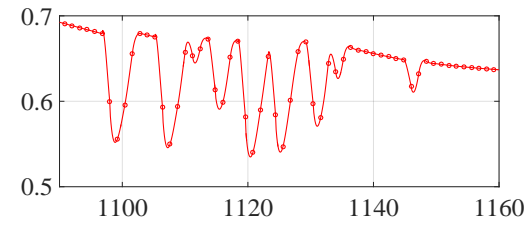
(b) Evaporator pressure.

(c) Working fluid enthalpy at the evaporator outlet. Dashed: saturated vapor enthalpy.
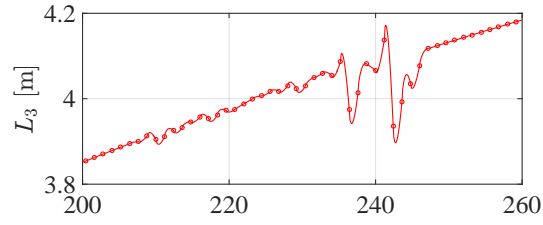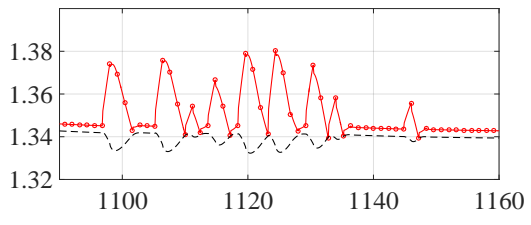
(d) Evaporator vapor zone length. Dashed: minimum zone length.
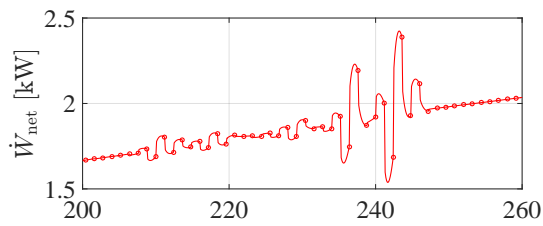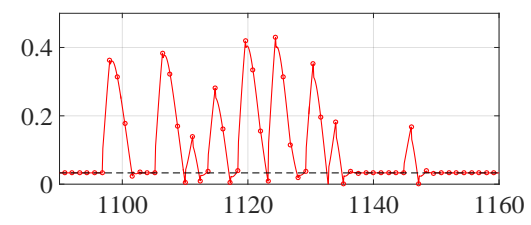
(e) Net generated power.
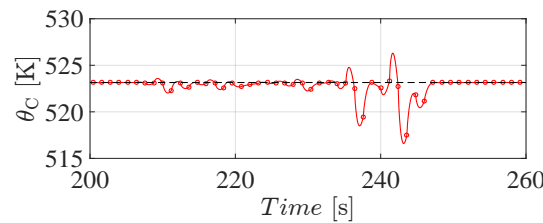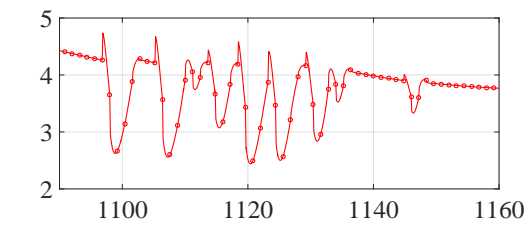
(f) Working fluid temperature at the evaporator outlet. Dashed: maximum allowable temperature.
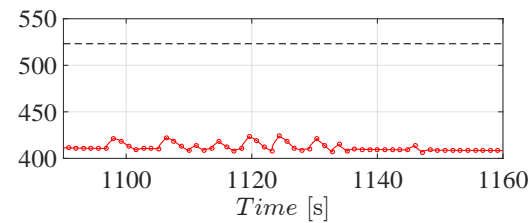
Legend: o   Quantity value at the multiple shooting nodes

Figure 5.7: Zoom for the quantities shown in Fig. 5.6 on selected time intervals where noticeable oscillations are present.

At a certain instant near $t = 600$ [s], the operating mode is changed: The pump starts delivering maximum massflow, with which the evaporating pressure reaches high levels as the evaporator outlet enthalpy approaches the corresponding saturated vapor enthalpy. These changes importantly increase the power generation. By contrast, the enthalpy (and thus the temperature) at the evaporator outlet, and the vapor zone length decrease. As time evolves, almost all plotted variables exhibit a tendency to decrease, with the exception of the control, which stays at its maximum except for very short time instants in which it reduces its value, often to its minimum. These oscillations reduce the power generation, but increase the vapor reserves inside the evaporator (which are directly proportional to L_3). At around $t = 1050$ [s], a new operating mode begins. This mode is characterized by the vapor zone length becoming minimum i.e. the entrance of constraint (3.87) into the active set. This coincides with the outlet enthalpy being extremely close to the saturated vapor enthalpy. Thus, the control reduces its value from its maximum in a gradual manner so as to keep the vapor zone length at its minimum. Several oscillations appear as before.

Comment on the optimal trajectories' transient behavior: It is remarkable that the optimal strategy does not aim to recover the maximum net power possible at the first instants of the time interval under consideration, cf. Section 5.3.2, but performs a drastic increment of its power generation only after a considerable amount of time. It can be seen that the strategy first aims at the accumulation of an important amount of vapor inside the evaporator and then increments the massflow in order to increase the power generation (see Eq. (3.2f)). This incremented massflow must in turn be warmed up through longer distances within the evaporator before it reaches the saturated liquid and vapor states, so that the lengths of both the subcooled and two-phase regions increase. As a consequence, the third zone length decreases. Further, since this implies a decrease in the heat transfer area between the wall and the working fluid in that zone, the working fluid temperature at the evaporator outlet also does. A similar argument can be used to explain the system's dynamics when the control decreases.

Keeping these arguments in mind, we proceed to comment on the oscillations experienced by the control and the plotted quantities as the system evolves. At this point we remark that these oscillations depend on the control representation and on the path constraints' discretization, see Eq. (4.6). In the following analyses we will focus on Figs. 5.6 and 5.7. In Fig. 5.7, the results corresponding to $N = 1000$ are zoomed at the time intervals [200, 260] [s] and [1090, 1160] [s]. These intervals are associated to strong control oscillations at instants where (3.88) and (3.87) belong to the active set, respectively.

At each multiple shooting node located between shortly after $t = 0$ [s] and shortly before $t = 600$ [s], the working fluid temperature at the evaporator output equals its maximum allowed value. Nevertheless, since between consecutive multiple shooting nodes no path constraint is imposed, the control leverages the fast dynamic modes of the WHR in order to produce short-duration peaks on the net generated power and return the temperature to its maximum allowed value. We notice that this is possible due to the fact that the evaporator dynamics delay the effect of the control, which is applied at the evaporator inlet, on the working fluid temperature at the evaporator outlet, as explained before.

The oscillations exhibited by the control between shortly before $t = 600$ [s] and shortly after $t = 1000$ [s] improve the objective function value by reducing the mean rate at which the third zone length shrinks. This allows to extend the time the power generation is kept high, compare the peaks in Figs. 5.6(d) and 5.6(e). After the third zone length reaches its minimum, shortly after $t = 1000$ [s], the strategy aims to keep it on that value. As a result, it can be observed that the power generation decreases much faster.

Between shortly after $t = 1000$ [s] and $t = 1200$ [s], the third zone length is reaches its

minimum value, which means the minimum admissible vapor amount is contained inside the evaporator. If in this conditions the control is reduced, this length increases, which makes it possible to continue by increasing the control to its maximum until the third zone length is minimum again. Such an oscillation in the control causes that, when the third zone length is minimum again, the pressure reaches a higher value than the one it would have reached had the oscillation not taken place. Therefore, the pressure decreases at a slower mean rate, which in turn keeps the net generated power high. This is how the observed oscillations contribute to optimality.

In summary, along the trajectories, the active set on each instant always included one of these main constraints: the limitation of pump capacity (3.85) (both upper and lower bounds), the limitation of the third zone length (3.87) and the prevention of the working fluid thermal decomposition at the evaporator outlet (3.88). The optimal strategy clearly leverages the fact that we have specified a fixed time horizon for the WHR operation. Further, the third zone length plays a major role in the determination of the optimal control. The thermal and mechanical dynamics of the system are leveraged by the control so as to maximize the objective function and satisfy the constraints.

5.3 Nonlinear Model-Predictive Control

In this section we present the results corresponding to different numerical instances of the NMPC scheme presented in Chapter 4. In each experiment, the controller model is Eq. (3.53), its parameter set is the one in Table 5.3 and its initial state $\hat{\boldsymbol{x}}_0^{(0)}$ is equal to Table 5.4, i.e. the controller model and its initial state are assumed to coincide with the dynamics and the initial state of the real WHR.

With regard to the exhaust gas conditions, i.e. the external inputs $\boldsymbol{w}(t)$, we perform two kinds of experiments with the goal to assess the potential benefit of counting on accurate predictions of their values: in the experiments of the first kind, we consider the external inputs as fully known for the prediction horizon $[t_0^{(k)}, t_f^{(k)}]$; in the experiments of the second kind, in each subproblem only the external inputs' values at $t = t_0^{(k)}$ are assumed to be known, and their prediction is assumed to correspond to a constant extrapolation of those values along the prediction horizon.

In Section 5.3.1, we proceed to summarize and analize the results obtained with our NMPC scheme by using different values of the prediction horizon Δt_{NMPC} and the number of intervals N. In our analyses we take computational times, objective function values and feasibility into account. Finally, on Section 5.3.2 the NMPC strategy is compared with the optimal trajectories of Section 5.2, and the PI and LQGI control strategies of Section 4.3.

5.3.1 NMPC for Different Numbers of Intervals and Prediction Horizon Lengths

As stated in Section 4.2, the choice of the number of multiple shooting nodes N and the prediction horizon Δt_{NMPC} can impact the algorithm's performance with respect to optimality, feasibility, computational time and even model evaluability. In order to evaluate the concrete impact of these configuration parameters, a set of 84 experiments has been performed to test the practical performance of the NMPC scheme. The independent variables of our experiment set correspond to the knowledge level of the future exhaust gas conditions (fully known or not, as previously explained), and the number of intervals and the prediction horizon chosen as a pair $(N, \Delta t_{\mathrm{NMPC}} \, [\mathrm{s}]) \in \{1, 3, 7, 15, 30, 60\} \times \{2, 10, 25, 50, 200, 350, 500\}$. The dependent variables of the experiment set correspond to the net generated energy $\Phi(t_f)$, the maximum computation time $\max(\boldsymbol{t}_c)$ and the constraint violation vector $\boldsymbol{\Gamma}$. The goals of this study are

the determination of the best $(N, \Delta t_{\text{NMPC}} \ [\text{s}])$ pair for the NMPC scheme in this concrete application; the acquisition of knowledge regarding the influence of these choices in the NMPC scheme's performance in this application; and the assessment of the potential benefit of counting on accurate exhaust gas predictions on the NMPC scheme's performance.

From the whole set of results, those experiments in which the NMPC routine successfully swept the whole horizon $[t_0^{(k)}, t_{\text{f}}^{(k)}]$ and $\max(t_c)$ is not greater than T_s are called *real-time feasible results*.

Among those, the ones for which the prevention of droplets entering the expander (3.86) and the prevention of the working fluid thermal decomposition (3.88) were never violated (i.e. $\Gamma_i = 0$, $i \in \{3, 5, 6, 7, 8\}$) are called *acceptable results*. Notice that not all real-time feasible results are acceptable.

The upper part of Table 5.7 lists the acceptable results. These results are summarized by the ranges for $\Phi(t_f)$, $\max(t_c)$ and Γ in the lower part of the same table. Additionally, column 'FK' indicates if the experiments considered $w(t)$ as fully known along each prediction horizon.

Table 5.7: Acceptable results for the NMPC with different number of intervals and prediction horizon

FK	N	Δt_{NMPC} [s]	$\Phi(t_f)$ [MJ]	$\max(t_c)$ [s]	Γ_1 [kg/h]	Γ_2 [kg/h]	Γ_3 [MJ/kg]	Γ_4 [m]	Γ_8 [K]
No	1	10	4.2659	0.029	$0.00 \cdot 10^0$	$0.00 \cdot 10^0$	$0.00 \cdot 10^0$	$5.34 \cdot 10^{-4}$	$0.00 \cdot 10^0$
No	1	25	4.2686	0.033	$0.00 \cdot 10^0$	$0.00 \cdot 10^0$	$0.00 \cdot 10^0$	$1.59 \cdot 10^{-3}$	$0.00 \cdot 10^0$
No	3	2	4.2651	0.061	$0.00 \cdot 10^0$	$0.00 \cdot 10^0$	$0.00 \cdot 10^0$	$1.71 \cdot 10^{-6}$	$0.00 \cdot 10^0$
No	3	25	4.2656	0.058	$0.00 \cdot 10^0$	$0.00 \cdot 10^0$	$0.00 \cdot 10^0$	$4.08 \cdot 10^{-4}$	$0.00 \cdot 10^0$
No	3	50	4.2671	0.073	$0.00 \cdot 10^0$	$0.00 \cdot 10^0$	$0.00 \cdot 10^0$	$1.04 \cdot 10^{-3}$	$0.00 \cdot 10^0$
No	7	25	4.2651	0.076	$0.00 \cdot 10^0$	$0.00 \cdot 10^0$	$0.00 \cdot 10^0$	$1.23 \cdot 10^{-4}$	$0.00 \cdot 10^0$
No	7	50	4.2655	0.084	$0.00 \cdot 10^0$	$0.00 \cdot 10^0$	$0.00 \cdot 10^0$	$3.20 \cdot 10^{-4}$	$0.00 \cdot 10^0$
Yes	1	10	4.2662	0.043	$0.00 \cdot 10^0$	$0.00 \cdot 10^0$	$0.00 \cdot 10^0$	$6.95 \cdot 10^{-4}$	$0.00 \cdot 10^0$
Yes	3	2	4.2651	0.060	$0.00 \cdot 10^0$	$0.00 \cdot 10^0$	$0.00 \cdot 10^0$	$1.11 \cdot 10^{-6}$	$0.00 \cdot 10^0$
Yes	3	10	4.2653	0.078	$0.00 \cdot 10^0$	$0.00 \cdot 10^0$	$0.00 \cdot 10^0$	$1.38 \cdot 10^{-4}$	$0.00 \cdot 10^0$
Yes	3	25	4.2658	0.042	$0.00 \cdot 10^0$	$0.00 \cdot 10^0$	$0.00 \cdot 10^0$	$5.26 \cdot 10^{-4}$	$0.00 \cdot 10^0$
Yes	3	50	4.2677	0.065	$0.00 \cdot 10^0$	$0.00 \cdot 10^0$	$0.00 \cdot 10^0$	$1.41 \cdot 10^{-3}$	$0.00 \cdot 10^0$
Yes	7	50	4.2656	0.085	$0.00 \cdot 10^0$	$0.00 \cdot 10^0$	$0.00 \cdot 10^0$	$4.10 \cdot 10^{-4}$	$0.00 \cdot 10^0$

For all acceptable results: ($w(t)$ constant)	$\Phi(t_f)$	$\in [4.2651, 4.2686]$ [MJ]
	$\max(t_c)$	$\in [0.0288, 0.0843]$ [s]
	Γ_4	$\in \left[1.7090 \cdot 10^{-6},\ 1.5854 \cdot 10^{-3}\right]$ [m], $\quad \Gamma_i \in \{0\} \forall i \neq 4$

For all acceptable results: ($w(t)$ fully known)	$\Phi(t_f)$	$\in [4.2651, 4.2677]$ [MJ]
	$\max(t_c)$	$\in [0.0420, 0.0849]$ [s]
	Γ_4	$\in \left[1.1129 \cdot 10^{-6},\ 1.4114 \cdot 10^{-3}\right]$ [m], $\quad \Gamma_i \in \{0\} \forall i \neq 4$

It can be seen in Table 5.7 that, as in Section 5.2.1, the violations on c_4, are much smaller than the security margin $L_{3,\text{min}}$ and thus acceptable. These violations are due to the external inputs' influence on the state trajectory. Our NMPC scheme succeeds in keeping the evaporator's superheated vapor zone volume close to its minimum allowed value (i.e. $c_4(x, p) = 0$) in spite of the disturbances leading the state into regions where it becomes slightly lesser (i.e. $c_4(x, p) < 0$).

Additionally, from the realization of the whole set of experiments, the following observations can be made:

1. Only values of $N \in \{1, 3, 7\}$ and $\Delta t_{\text{NMPC}} \in \{2, 10, 25, 50\}$ [s] yielded real-time feasible results, independent of the knowledge of the external inputs.

2. For a fixed Δt_{NMPC}, increasing N leads, independent on the knowledge of the external inputs, to lesser constraint violations, a lesser $\Phi(t_f)$, and a greater $\max(t_c)$.

3. In general, the consideration of full external input knowledge allows the WHR to reach a greater value of $\Phi(t_f)$. The increment is more substantial for greater values of Δt_{NMPC}. However, for those experiments that yielded acceptable results with and without full external input knowledge, energy recovery gains are only between 0.00% and 0.02%. This indicates that the extrapolation of $w(t)$ as constant for prediction purposes is an approximation that is accurate enough for the considered value of T_s and the corresponding prediction horizons.

For the sake of completeness, a subset of results that could not be classified as acceptable is included in Table 5.8.

Table 5.8: Selection of results that are not acceptable for the NMPC with different number of intervals and prediction horizon

FK	N	Δt_{NMPC} [s]	$\Phi(t_f)$ [MJ]	$\max(t_c)$ [s]	Constraint Violation				
					Γ_1 [kg/h]	Γ_2 [kg/h]	Γ_3 [MJ/kg]	Γ_4 [m]	Γ_8 [K]
No	1	50	4.2745	0.048	$0.00 \cdot 10^0$	$0.00 \cdot 10^0$	$9.75 \cdot 10^{-5}$	$2.97 \cdot 10^{-3}$	$0.00 \cdot 10^0$
No	7	200	4.2695	0.153	$0.00 \cdot 10^0$	$0.00 \cdot 10^0$	$3.77 \cdot 10^{-6}$	$1.79 \cdot 10^{-3}$	$0.00 \cdot 10^0$
No	15	25	4.2649	0.131	$0.00 \cdot 10^0$	$0.00 \cdot 10^0$	$0.00 \cdot 10^0$	$1.92 \cdot 10^{-5}$	$0.00 \cdot 10^0$
No	15	200	4.2665	0.244	$0.00 \cdot 10^0$	$0.00 \cdot 10^0$	$0.00 \cdot 10^0$	$7.82 \cdot 10^{-4}$	$0.00 \cdot 10^0$
No	30	25	4.2649	0.223	$0.00 \cdot 10^0$	$0.00 \cdot 10^0$	$0.00 \cdot 10^0$	$3.49 \cdot 10^{-6}$	$0.00 \cdot 10^0$
No	30	50	4.2649	0.279	$0.00 \cdot 10^0$	$0.00 \cdot 10^0$	$0.00 \cdot 10^0$	$3.18 \cdot 10^{-5}$	$0.00 \cdot 10^0$
No	60	25	4.2649	0.395	$0.00 \cdot 10^0$	$0.00 \cdot 10^0$	$0.00 \cdot 10^0$	$1.80 \cdot 10^{-6}$	$0.00 \cdot 10^0$
No	60	50	4.2649	0.443	$0.00 \cdot 10^0$	$0.00 \cdot 10^0$	$0.00 \cdot 10^0$	$3.51 \cdot 10^{-6}$	$0.00 \cdot 10^0$
No	60	200	4.2010	0.727	$0.00 \cdot 10^0$	$0.00 \cdot 10^0$	$0.00 \cdot 10^0$	$0.00 \cdot 10^0$	$0.00 \cdot 10^0$
Yes	1	50	4.2816	0.046	$0.00 \cdot 10^0$	$0.00 \cdot 10^0$	$2.59 \cdot 10^{-4}$	$6.12 \cdot 10^{-3}$	$0.00 \cdot 10^0$
Yes	7	200	4.2718	0.127	$0.00 \cdot 10^0$	$0.00 \cdot 10^0$	$3.90 \cdot 10^{-5}$	$3.00 \cdot 10^{-3}$	$0.00 \cdot 10^0$
Yes	15	25	4.2649	0.132	$0.00 \cdot 10^0$	$0.00 \cdot 10^0$	$0.00 \cdot 10^0$	$3.13 \cdot 10^{-5}$	$0.00 \cdot 10^0$
Yes	15	200	4.2669	0.233	$0.00 \cdot 10^0$	$0.00 \cdot 10^0$	$0.00 \cdot 10^0$	$1.05 \cdot 10^{-3}$	$0.00 \cdot 10^0$
Yes	30	25	4.2649	0.223	$0.00 \cdot 10^0$	$0.00 \cdot 10^0$	$0.00 \cdot 10^0$	$2.35 \cdot 10^{-6}$	$0.00 \cdot 10^0$
Yes	30	50	2.5436	1.851	$0.00 \cdot 10^0$	$0.00 \cdot 10^0$	$0.00 \cdot 10^0$	$8.08 \cdot 10^{-6}$	$0.00 \cdot 10^0$
Yes	60	25	4.2649	0.395	$0.00 \cdot 10^0$	$0.00 \cdot 10^0$	$0.00 \cdot 10^0$	$1.37 \cdot 10^{-6}$	$0.00 \cdot 10^0$
Yes	60	50	4.2649	0.476	$0.00 \cdot 10^0$	$0.00 \cdot 10^0$	$0.00 \cdot 10^0$	$2.47 \cdot 10^{-6}$	$0.00 \cdot 10^0$
Yes	60	200	4.2011	0.670	$0.00 \cdot 10^0$	$0.00 \cdot 10^0$	$0.00 \cdot 10^0$	$0.00 \cdot 10^0$	$0.00 \cdot 10^0$

5.3.2 Comparison Between the NMPC, the LQGI and the PI Strategies

To test the proposed NMPC strategy against standard methods, the LQGI and PI controllers of Section 4.3 with the tuned parameters of Section 5.1.5 are considered. We proceed firstly by performing tests using a target superheating of $y^{\text{SH}*} = 10$ [K]. Since it turns out that the NMPC strategy makes the system operate around a superheating of 1.2 [K], an additional set of tests was considered, this time using a reference of $y^{\text{SH}*} = 1.2$ [K]. Table 5.9 summarizes the results.

In Table 5.9 it is possible to see that the results produced by both the LQGI and PI strategies are acceptable, except for the case in which the LQGI controller is given a reference $y^{\text{SH}*} = 1.2$ [K]. In that case the prevention of droplets entering the expander Eq. (3.86) and the minimum third zone length Eq. (3.87) are being importantly violated. This is due to the discrepance between

Table 5.9: Results for different control strategies

Control strategy	$y^{\text{SH}*}$ [K]	$\Phi(t_f)$ [MJ]	$\max(t_c)$ [s]	Constraint Violation				
				Γ_1 [kg/h]	Γ_2 [kg/h]	Γ_3 [MJ/kg]	Γ_4 [m]	Γ_8 [K]
LQGI	10.0	4.1306	0.011	$0.00 \cdot 10^0$	$0.00 \cdot 10^0$	$0.00 \cdot 10^0$	$0.00 \cdot 10^0$	$0.00 \cdot 10^0$
	1.2	4.1444	0.007	$0.00 \cdot 10^0$	$0.00 \cdot 10^0$	$1.27 \cdot 10^{-3}$	$2.16 \cdot 10^{-2}$	$0.00 \cdot 10^0$
PI	10.0	4.1413	0.003	$0.00 \cdot 10^0$	$0.00 \cdot 10^0$	$0.00 \cdot 10^0$	$0.00 \cdot 10^0$	$0.00 \cdot 10^0$
	1.2	4.1403	<0.001	$0.00 \cdot 10^0$	$0.00 \cdot 10^0$	$0.00 \cdot 10^0$	$1.49 \cdot 10^{-3}$	$0.00 \cdot 10^0$

the nonlinear nature of the WHR and the linear model assumed by the LQGI controller. The PI controller satisfied all constraints, except the minimum third-zone length Eq. (3.87). This violation can be tolerated, since its magnitude is much smaller than the security margin $L_{3,\text{min}}$, and a small volume of vapor is still contained within the evaporator. This is supported by the fact that it satisfies the prevention of droplets entering the expander.

By comparing Tables 5.6, 5.7 and 5.9, it is possible to see that

1. The net energy generation can be sorted according to the type of control used[2] i.e, $\Phi(t_f)_{\text{Optimal Control}} > \Phi(t_f)_{\text{NMPC+FK}} > \Phi(t_f)_{\text{NMPC}} > \Phi(t_f)_{\text{LQGI}} > \Phi(t_f)_{\text{PI}}$. We stress in particular that the proposed NMPC scheme is able to generate around 2.9 [%] more energy than the LQGI and PI controllers.

2. The proposed NMPC scheme has a bigger computational time than the LQGI and PI controllers. Nevertheless, we stress that it achieves computational times that are suitable for real-time environments.

3. The proposed NMPC scheme is able to yield constraint violations that are several orders of magnitude smaller the LQGI and PI controllers.

Transient Analysis

In this section we compare the transient behavior of the WHR under the NMPC, PI and LQGI strategies discussed above. For the NMPC we have considered a configuration consistent on setting the number of multiple shooting intervals as $N = 3$ and the prediction horizon length as $\Delta t_{\text{NMPC}} = 50$ [s]. This configuration is an acceptable NMPC instance that reaches a very good compromise between constraint violations and objective function value. It is associated with a value of $\Gamma_4 = 1.0393 \cdot 10^{-3}$ [m] and $\Gamma_i = 0$ for all $i \neq 4$. It does not consider the external inputs as fully known. Additionally, for the LQGI and PI strategies we have taken those trajectories corresponding to setting the reference superheating to $y^{\text{SH}*} = 1.2$ [K] into account. The corresponding results are shown in Fig. 5.8. Therein the dashed line is used for indicating limits to the trajectories plotted, such as the control upper and lower bounds, the saturated vapor enthalpy and the minimum third zone length.

A first observation that can be made is the undeniable influence of the external inputs on the controllers' dynamic behavior. In particular, the transients of the exhaust gas inlet massflow of Fig. 5.1 are clearly reflected on all curves in Fig. 5.8.

In contrast to the results obtained with the optimal control strategy (see Fig. 5.6(a)), all three controllers start with the maximum massflow. After a transient between around $t = 25$ [s] and around $t = 300$ [s], all three controllers reach similar operating conditions, which are characterized by a very small value of the third zone length and very slow changes. In particular, for

---

[2]Where the subscript 'NMPC+FK' refers to the NMPC scheme under the assumption of full external input knowledge

(a) Working fluid massflow (control). Dashed: upper bound.

(b) Evaporator pressure.

(c) Working fluid enthalpy at the evaporator outlet. Dashed: saturated vapor enthalpy.

(d) Evaporator vapor zone length. Dashed: minimum zone length.

(e) Net generated power.

(f) Working fluid temperature at the evaporator outlet.

Legend: NMPC ── PI ── LQG
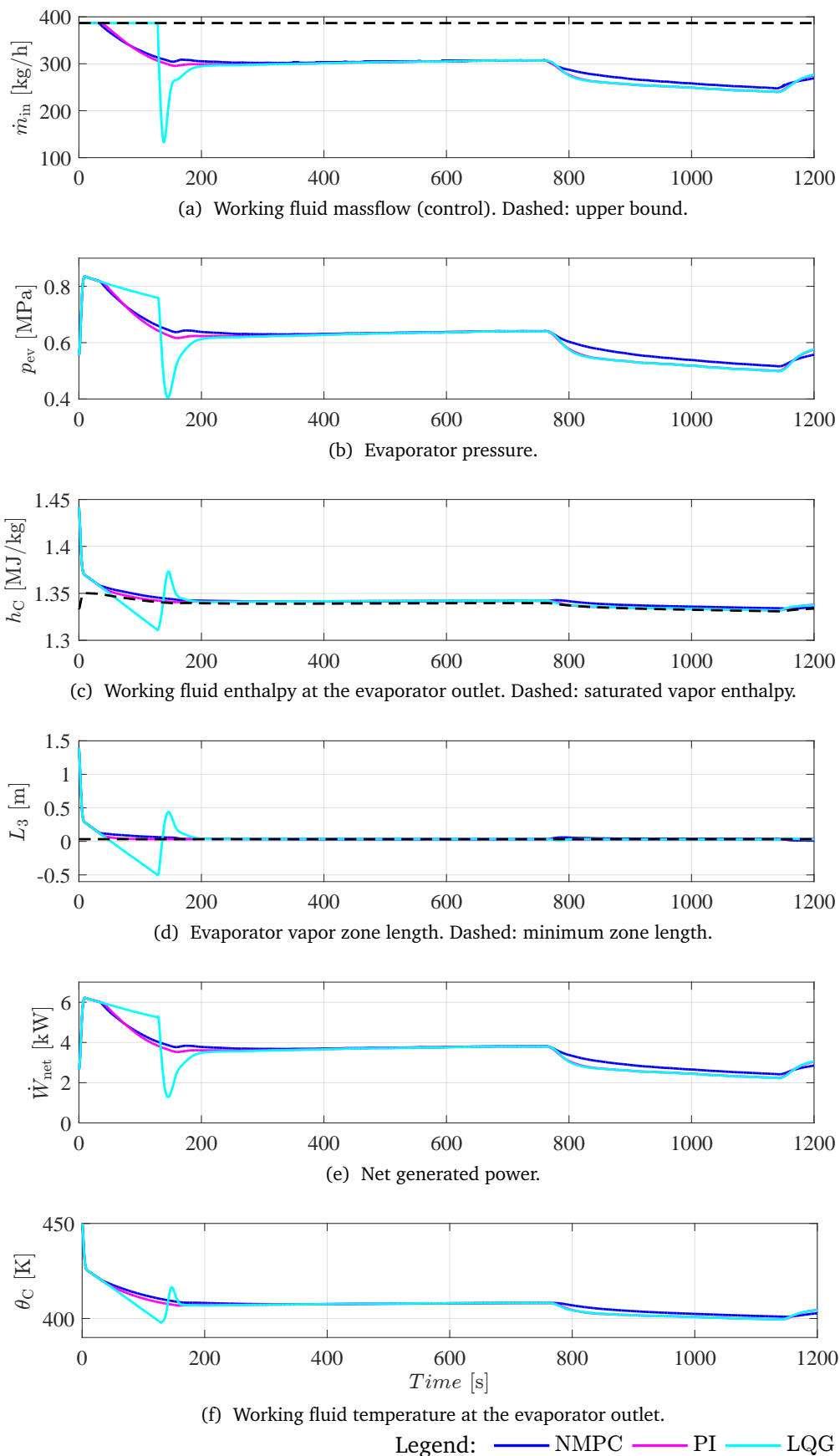
Figure 5.8: Comparison of the transient behavior of selected quantities obtained by using NMPC, LQGI and PI controllers.

the NMPC the minimum third zone length becomes active. During this stage the minor variations of the exhaust gas massflow do not importantly affect the plotted magnitudes. Shortly before $t = 800$ [s] the exhaust gas massflow shows once again an important change, and a new transient is started during which both the PI and the LQGI react almost identically and the NMPC produces clearly different trajectories. At approximately $t = 1150$ [s] the exhaust gas massflow changes once again, and the last transient of our analysis begins.

After approximately $t = 25$ [s] the third zone length remains having a small value for the rest of the operation for all controllers. Furthermore, during the whole operation the evaporator outlet temperature remains in safe values.

Comment on the trajectories' transient behavior: At the beginning of the interval, the control corresponding to the LQGI controller remains at its maximum value during an amount of time that is considerably longer than their counterparts. During this time the LQGI controller clearly suffers from an *integral windup* phenomenon: since the superheating error (i.e. the difference between the current superheating and the target superheating, see Section 4.3) remains big for a long period of time, the integral term of Eq. (4.65) becomes big until the effect is countered by adding negative superheating errors during a sufficiently long time lapse. For this reason, the evaporator outlet temperature for the LQGI reaches the smallest value in comparison to the other strategies at around $t = 120$ [s] and exhibits an oscillatory behavior afterwards. The integral windup causes the LQGI controller to importantly violate the constraints on the third zone length and the output enthalpy (constraints (3.87) and (3.86), respectively), which invalidates its higher power production during this transient. It is precisely the LQGI controller's poor dynamic behavior the responsible for a low power generation between the moment the control leaves its maximum and $t = 200$ [s].

In contrast to the PI controller, the anti-windup mechanism of the PI controller deactivates its integral part when the pump delivers a maximum massflow, and the proportional part can readily start decreasing the control value in a gradual manner as the superheating error approaches zero. It better dynamic behavior gives it clear advantages over the LQGI controller with respect to contraint satisfaction and power generation until $t = 200$ [s], instant after which both controllers have already reached similar operating conditions that will remain so until the end of the interval.

The predictive characteristics of the NMPC are reflected on the fact that its control always shows changes several seconds before its counterparts. This allows the controller's make a better use of the transients to maximize the power generation. In fact, the power generation of the WHR under the NMPC is higher than those under the PI and LQGI controllers for most of the time interval, in particular between approximately $t = 75$ [s] and near $t = 1150$ [s]. Moreover, from Tables 5.7 and 5.9 it becomes clear that for the whole interval the energy recovered by the NMPC is greater than that recovered by the two other controllers.

In summary, the analysis above highlights that due to the fact that the NMPC considers the nonlinear WHR dynamics using them to predict the WHR's future behavior and takes the operational constraints into account, it is able to profit from the transients to achieve a higher energy recovery while exhibiting an increased robustness in the sense of feasibility in comparison to its counterparts.

5.4 Moving Horizon Estimation

In this section, we continue our study by relaxing the exact knowledge of the differential state vector that was assumed until now. In this context we employ the MHE scheme introduced in Section 3.5.3 to estimate the state from practical sensor measurements and the use of the

Table 5.10: MHE Estimation Error

Statistic	Estimated State						
	L_1 [%]	L_2 [%]	p_{ev} [%]	$\theta_{W,1}$ [%]	$\theta_{W,2}$ [%]	$\theta_{W,3}$ [%]	h_C [%]
m_{e_i}	0.01	0.01	<0.01	<0.01	0.01	0.17	<0.01
$\bar{e}_i$	0.37	1.67	0.03	<0.01	0.19	29.92	<0.01
σ_{e_i}	0.18	2.71	0.05	0.01	0.63	3.55	<0.01
M_{e_i}	11.82	89.88	2.51	0.46	6.69	40.41	0.47

nonlinear WHR model of Chapter 3. In Section 5.4.1, the MHE scheme's accuracy is evaluated. Next, in Section 5.4.2, the performance of the NMPC scheme in which the state is estimated by the MHE scheme is compared to that of the NMPC scheme in which the state is perfectly known. Finally, in Section 5.4.3, the scheme in which the NMPC and MHE work together is compared to the PI and LQGI controllers of Section 4.3.

In all our experiments we consider the schematic of Fig. 4.1, in which the proposed NMPC-MHE scheme interacts with a real WHR, which we simulate by means of the DAE model Eq. (3.53). For this simulated WHR, the parameters and initial state of Section 5.1.3 are considered, and its differential and algebraic state vectors at the instant $k \in \mathcal{K}$ are denoted as $\boldsymbol{x}^{(k)}$ and $\boldsymbol{z}^{(k)}$. The DAE system is integrated between adjacent sample times using the controls obtained by the NMPC block as they become available and the curves of Section 5.1.4. The estimates of the differential and algebraic state produced by the MHE are denoted as $\hat{\boldsymbol{x}}^{(k)}$ and $\hat{\boldsymbol{z}}^{(k)}$, respectively. Additionally, the NMPC and MHE are initialized as described in Section 4.2.3. For the initialization of the MHE, the initial differential and algebraic states are the ones of Section 5.1.3. For both the NMPC and the MHE, the controls and external inputs correspond to those of Section 5.1.4. The initial algebraic state for the NMPC is chosen as that of Section 5.1.3.

5.4.1 MHE Performance

Under the aforementioned conditions the MHE and the NMPC control the WHR so that real plant trajectories are generated. For each state $\boldsymbol{x}_i^{(k)}$, $i \in \{1, \ldots, n_x\}$, $k \in \mathcal{K}$; we make the component-wise definition of the percentage estimate relative error $e_i^{(k)}$, and its time statistics: minimum m_{e_i}, maximum M_{e_i}, mean $\bar{e}_i$ and standard deviation σ_{e_i} as

$$e_i^{(k)} = 100\,[\%] \cdot |\hat{\boldsymbol{x}}_i^{(k)} - \boldsymbol{x}_i^{(k)}|/|\boldsymbol{x}_i^{(k)}|, \tag{5.3a}$$

$$m_{e_i} = \min_{k \in \mathcal{K}} e_i^{(k)}, \qquad\qquad \bar{e}_i = \frac{1}{K}\sum_{k \in \mathcal{K}} e_i^{(k)}, \tag{5.3b}$$

$$M_{e_i} = \max_{k \in \mathcal{K}} e_i^{(k)}, \qquad\qquad \sigma_{e_i} = \sqrt{\frac{1}{K-1}\sum_{k \in \mathcal{K}}(e_i^{(k)} - \bar{e}_i)^2}. \tag{5.3c}$$

The definition is analogous for $\boldsymbol{z}^{(k)}$. These time statistics for the performed experiments are shown in Table 5.10.

The most accurate estimations are obtained for p_{ev}, which is measured, and h_C. The latter can be directly translated from the measurements of p_{ev} and θ_C in accordance with Gibbs' phase rule (see Section 2.5.1). Additionally, from Eq. (3.14), when L_1 is big enough, $\theta_{G,\text{out}} \approx \theta_{W,1}$, which explains the good accuracy on $\theta_{W,1}$. For all of these variables, the mean relative error is less than 2 [%].

The estimates of $\theta_{W,3}$ are more sensitive to estimation errors. This is due to the fact that, when L_3 is small, $\dot{Q}_{WF,3}$ is almost zero (cf. Eq. (3.6)), causing the conditioning of Eq. (3.52)
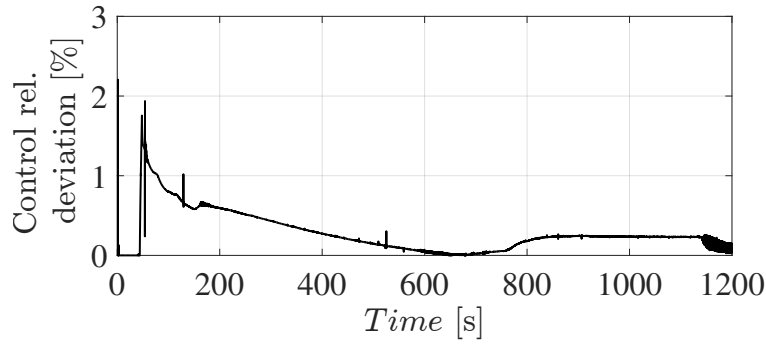
Figure 5.9: Relative deviation in the control control between NMPC-MHE and O-NMPC. $m_{e_u} = 0.00$ [%], $\bar{e}_u = 0.28$ [%], $\sigma_{e_u} = 0.26$ [%], $M_{e_u} = 2.21$ [%].

to become poorer. As analyzed in Section 5.3.2, the WHR operates most of the time precisely in these conditions when the numerical realization of the NMPC strategy considered in this section is used.

5.4.2 Comparison with the Omniscient NMPC

In order to quantify the effect that the loss of certainty has in the controller's performance, the results obtained with the proposed NMPC-MHE scheme are compared with those obtained with an NMPC instance where the state is perfectly known. We call such instance the *omniscient* NMPC instance and denote it as O-NMPC. For the control trajectories the relative deviation sequence is defined as

$$e_u^{(k)} = 100 \ [\%] \cdot |u_{\text{NMPC-MHE}}^{(k)} - u_{\text{O-NMPC}}^{(k)}|/|u_{\text{O-NMPC}}^{(k)}|, \ k \in \mathcal{K}, \tag{5.4}$$

and the corresponding statistics are analogous to those of Eq. (5.3). The trajectory of $e_u^{(k)}$ is shown in Fig. 5.9. It can be seen that the control trajectories of both the NMPC-MHE and the O-NMPC are very similar. The peak deviation is at around $t = 48$ [s], where an active set change takes place (the minimum third zone length constraint becomes active, i.e. $L_3 = L_{3,\min}$). The NMPC-MHE is able to detect it and react accordingly shortly after.

The energy recovery from the exhaust gas is almost the same in both cases: at t_f, the WHR with the O-NMPC recovered 4.2648 [MJ] while with the NMPC-MHE it recovered 4.2232 [MJ], which makes up only a 0.97 [%] difference.

5.4.3 Comparison of the NMPC-MHE Scheme with the LQGI and PI controllers

We can compare the proposed NMPC-MHE Scheme to the LQGI and PI controllers of Section 4.3. Revisiting the results of Table 5.9 and those of Section 5.4.2, we can observe that, if we consider the energy harvested by the energy harvested by the LQGI with target superheating $y^{\text{SH}*} = 10$ [K] as a reference, the proposed scheme recovers 1.90 [%] more energy. Otherwise, if we consider the energy harvested by the LQGI with target superheating $y^{\text{SH}*} = 1.2$ [K] as a reference, our scheme recovers 2.25 [%] more energy.

5.4.4 Influence of Measurement Noise

In order to evaluate the influence that measurement noise has on the proposed NMPC-MHE scheme's performance, in this subsection we consider the measurements $\begin{bmatrix} p_{\text{ev}}, & \theta_C, & \theta_{G,\text{out}} \end{bmatrix}^T$ to be distorted by means of the addition of a Gaussian white noise vector whose components
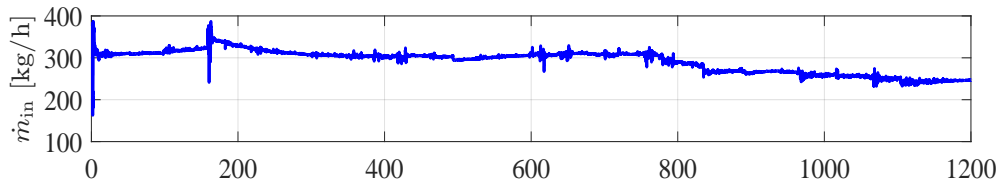
Figure 5.10: Control applied by the NMPC-MHE scheme in the presence of noise.

have standard deviations of 1.0 [kPa], 0.33 [K] and 0.1 [K], respectively. These standard deviations are chosen so that Ψ_k yields measurement errors with amplitudes less or equal than 0.5 [kPa], 1.0 [K] and 0.3 [K] with a probability of 99.73 [%], respectively, which corresponds to a realistic setting.

The obtained results are plotted in Figs. 5.10 to 5.12. Therein we have used the blue line for the real states and the measurements (i.e. those magnitudes associated with the WHR), and the red line for the estimated states and the *filtered* measurements[3] (i.e. those magnitudes associated with the MHE). Notice that the noise for the measured state p_{ev} is included in Fig. 5.11.

The statistics corresponding to the state estimation error are summarized in Table 5.11. The symbols used therein are defined as in Eq. (5.3). Analogous definitions can be used for the measurement estimation error, i.e. the difference between the noisy and the *filtered* measurements[4], with the results included in Table 5.12.

(a) Evaporator pressure.

(b) Working fluid temperature at the evaporator outlet.

(c) Exhaust gas temperature at the evaporator outlet.

Legend: ——— Estimated ——— Real
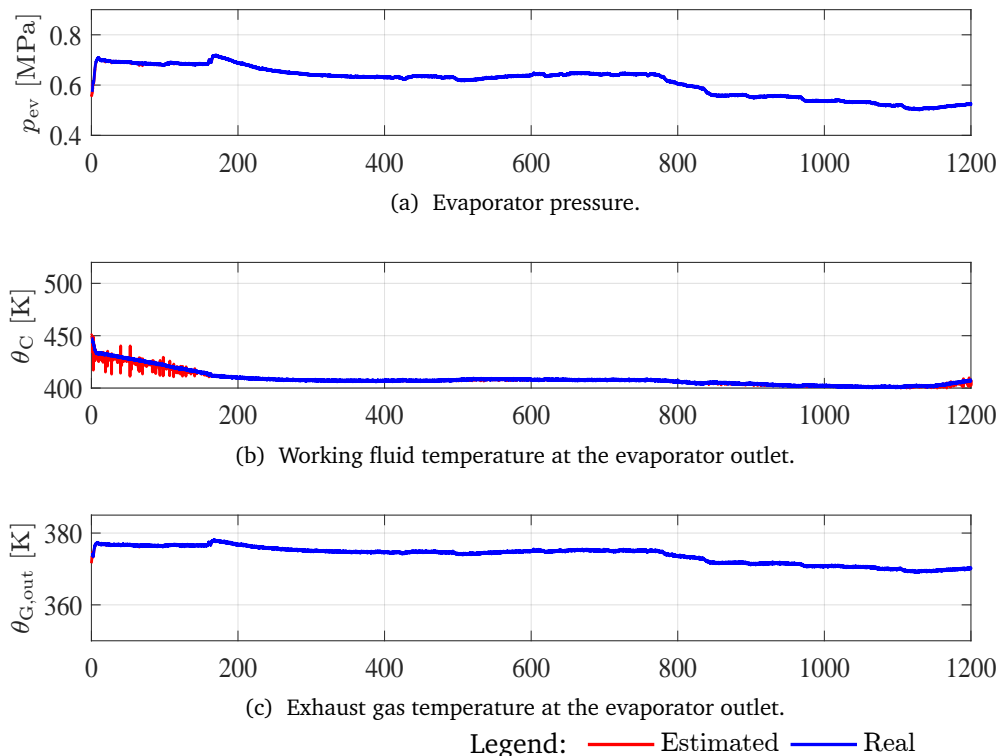
Figure 5.11: Comparison between the actual and filtered measurements.

The results confirm that, in spite the noise's influence, the proposed scheme is able to effectively perform its estimation and control tasks. The results of Tables 5.11 and 5.12 resemble those of

---

[3]With *filtered measurements* we refer to those obtained by evaluating the measurement function $y(\cdot)$ at the differential and algebraic states predicted by the MHE, the measured external inputs and the model parameters.

Table 5.11: State estimation error for the NMPC-MHE scheme in the presence of noise

Statistic	Estimated State						
	L_1 [%]	L_2 [%]	p_{ev} [%]	$\theta_{W,1}$ [%]	$\theta_{W,2}$ [%]	$\theta_{W,3}$ [%]	h_C [%]
m_{e_i}	0.00	0.00	0.00	0.00	0.00	0.00	0.00
$\bar{e}_i$	1.11	9.23	0.07	0.01	0.92	25.23	0.03
σ_{e_i}	0.91	8.89	0.06	0.01	1.54	6.09	0.11
M_{e_i}	12.51	92.71	1.75	0.15	26.69	46.96	4.13

Table 5.12: Measurement estimation error for the NMPC-MHE scheme in the presence of noise

Statistic	Measurement		
	p_{ev} [%]	θ_C [%]	$\theta_{G,\text{out}}$ [%]
m_{e_i}	0.00	0.00	0.00
$\bar{e}_i$	0.15	0.09	0.02
σ_{e_i}	0.12	0.17	0.02
M_{e_i}	2.38	6.05	0.16

Table 5.10 and thus the same analysis of Section 5.4.1 can be done, taking into account that the presence of noise increases the mean estimation errors by a small amount.

The influence of the noise can be seen on the estimates of $\theta_{W,3}$, whose higher sensitivity to estimation errors has been previously discussed. A consequence of this higher sensitivity is that the associated estimates tend to be located close to the border of Eq. (3.92), i.e. such that $\theta_{W,3} \approx \theta_{W,2}$ and $\theta_{W,3} \geqslant \theta_{W,2}$. Additionally, it is observable that the estimation errors of both states and measurements tend to be greater during approximately the first 200 [s] and considerably decrease afterwards. Consistently, during that time interval the control and thus the evaporator pressure do not reach values as high as those obtained in the noise-free, which is though compensated between close to $t = 200$ [s] and around $t = 760$ [s]. After these transients, the values both magnitudes reach resemble those of the noise-free case. With respect to the constraint satisfaction, the only component of the vector $\boldsymbol{\Gamma}$ different than zero corresponds to $\Gamma_4 = 2.83 \cdot 10^{-3}$ [m], which is associated to the limitation of the evaporator's third zone to a lower bound. As before, the violations are much smaller than the value chosen for $L_{3,\text{min}}$. Further, in the presence of noise, the WHR is able to make a net recovery of 4.2241 [MJ] when equipped with the proposed scheme.

In summary, the previous analyses underline the proposed scheme's ability to yield good results also in noisy enviroments.

(a) Liquid zone length.

(b) Two-phase zone length.

(c) Evaporator pressure.

(d) Working fluid enthalpy at the evaporator outlet.

(e) Wall temperature at the liquid.

(f) Wall temperature at the two-phase zone.

(g) Wall temperature at the vapor zone.

Legend: —— Estimated —— Real
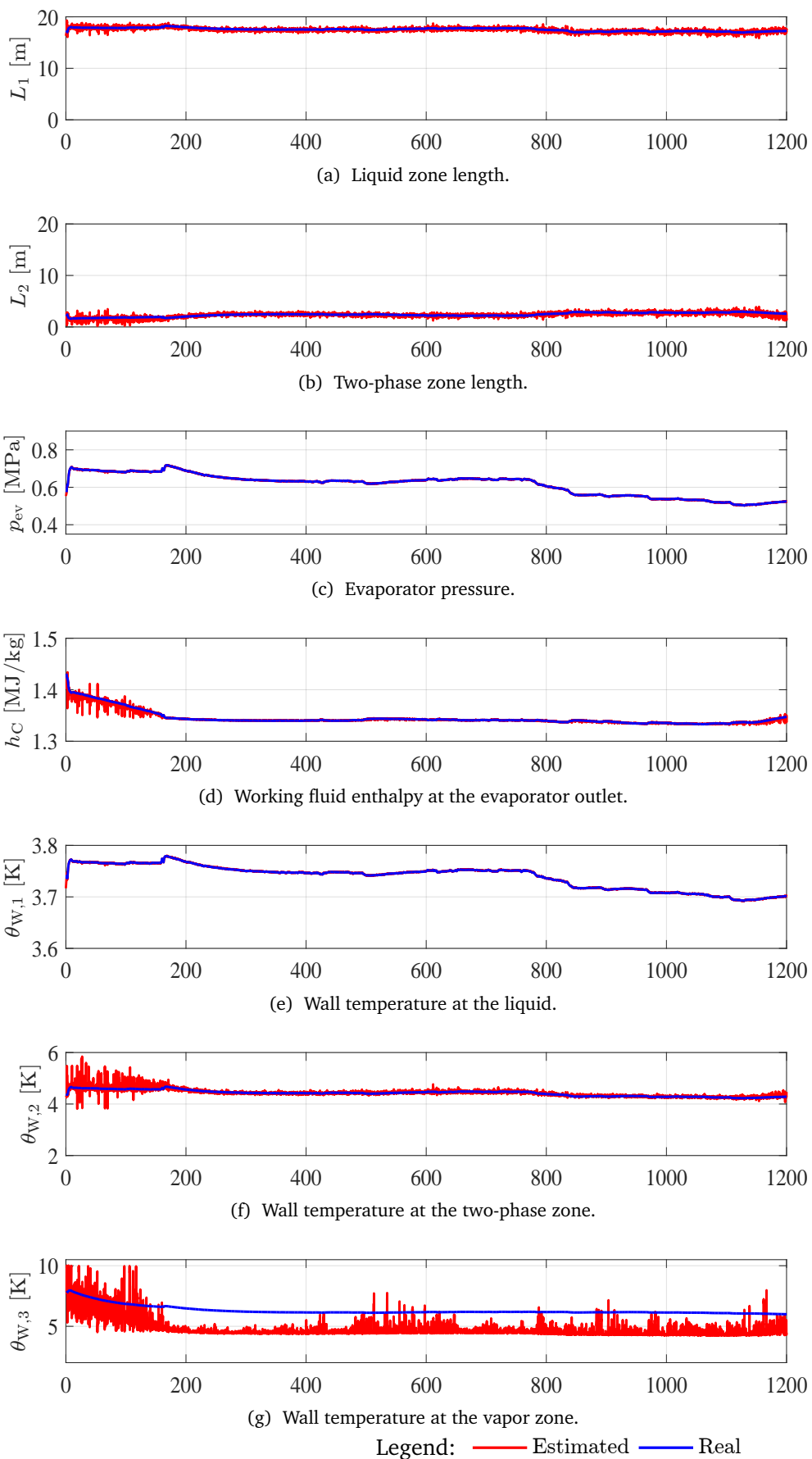
Figure 5.12: Comparison between the actual states and the states estimated by the NMPC-MHE scheme.

6 Conclusions and Future Research Directions

This thesis' main conclusions are summarized in this chapter. Additionally, an overview of appealing research directions for future research is included.

6.1 Conclusions

In this thesis, different ways of controlling a heavy-duty truck's waste heat recovery system (WHR) have been implemented and compared. Tests have been performed on a scenario corresponding to real exhaust gas temperature and massflow data measured at the evaporator inlet on a given time horizon. These data have been recorded and kindly handed over by our industry cooperation partner Daimler AG.

The first important step in our thesis has been the formulation of an optimal control problem (OCP) for the given scenario. To this end, a first-principles model of the WHR has been proposed. This is a challenging task as the involved physical processes (namely, phase change inside the evaporator) are best modelled through the use of curves and surfaces that may not be continuous at all in their whole evaluation domain, and our methods of choice, which are derivative-based, work best with highly differentiable models. To handle this, a tailored partition of the evaluation domain and an adequate extrapolation technique have been introduced in order to yield a model that is continuously differentiable in the whole evaluation domain. According to our numerical experience, the fulfillment of this condition brings satisfactory results. The resulting model consists of a DAE that, under realistic assumptions, is of index 1. Based on the direct multiple shooting method for optimal control and efficient numerical techniques, approximations to the OCP solution for the considered scenario were calculated offline using different numbers of intervals. We have observed the influence of this choice in the computational times, objective function values and constraint satisfaction. As expected, we observe that the higher the number of intervals is, the better the results are with respect to objective function values and constraint satisfaction. On the other hand, the computational costs increase very fast. Nevertheless, very good approximations to the optimum can be obtained in moderate computational times for an offline analysis.

The experience with the numerical solution of the OCP has paved the way for the formulation of a Nonlinear Model-Predictive Control (NMPC) strategy that is grounded in the same efficient numerical techniques and the Real-time iteration (RTI) scheme. Numerical results have been obtained using different numbers of intervals, prediction horizons and knowledge level of the exhaust gas conditions. With regard to the influence of the number of multiple shooting intervals and the prediction horizon length on the NMPC strategy's performance, and in the light of our application's practical requirements, the best results in the sense of a compromise between computational speed, constraint satisfaction and objective function value were obtained using a low number of multiple shooting intervals and relatively short prediction horizons. With respect to the knowledge of future exhaust gas conditions, gains due to accurate prediction of those quantities are only relevant when the prediction horizon is long enough.

In comparison to the energy recovered through the use of Proportional-Integral (PI) and Linear-Quadratic-Gaussian controllers with integral action (LQGI) controllers, the energy recovery obained with the proposed NMPC strategy was about 2.9 [%] higher. With respect to

the computation time, the proposed NMPC strategy exhibits an appealing speed for this application's considered real-time contexts, specially after showing good performance under the considered sample time of 100 [ms]. This outperforms the results reported by other NMPC schemes found in the literature. With respect to the operational constraints, the proposed NMPC strategy yielded successful results for the considered scenario, in the sense that only superheated vapor enters the expander and the working fluid temperatures are kept under their thermal decomposition limit. This good behavior is shared by the PI controller, but the LQGI controller could not fulfill these constraints for a particular target superheating. In summary, we conclude that the proposed NMPC strategy is to be preferred over the rest if it is properly set up.

The aforementioned results motivate the implementation of the proposed scheme on a real testbench. For these means a necessary first step consist on the implementation of a suitable nonlinear state estimator. For these means we have chosen an MHE formulation. In our formulation, realistic WHR measurements are considered to perform the state estimation. The resulting scheme is tested in a simulated noisy environment. Therein, almost all states were accurately estimated, with average relative errors lesser than 2 [%]. Afterwards, the MHE estimator is coupled to our NMPC scheme in order to produce a closed control loop. The proposed scheme's generated control trajectories and recovered energy closely resemble those of an NMPC strategy with full state knowledge. The proposed NMPC-MHE scheme allows the WHR to recover roughly 2 [%] more energy than the tested PI and LQGI alternatives. We conclude that the implemented control loop appears as an appealing alternative for actual implementation on a heavy duty truck.

6.2 Future Research Directions

The success obtained in the experiments performed in the course of this thesis inspire new directions in the optimization-based control of the WHR. These opportunities and challenges are briefly described in this section.

Implementation on an experimental testbench:

The promising results achieved in this thesis make it appealing to test an implementation of the NMPC-MHE scheme on a real testbench, and comparisons to other control strategies similar to those presented in this thesis could be performed in that environment. Since real-time feasible results have been obtained even with moderate computational capabilities, the possibility of executing first tests on a real heavy duty truck seems to be realistic.

Uncertain parameters and/or predictions:

As we have seen in Chapter 5, our NMPC-MHE scheme takes full advantage of the exhaust gas predictions and the knowledge of the model parameters in order to control the system. The scheme can be further extended in order to take into account the uncertainty associated to these quantities and thus produce more robust results. In our concrete case, the results indicate that certain constraints are expected to become active or close to active during the WHR operation, such as the prevention of droplets entering the expander and the prevention of the working fluid's thermal decomposition Eqs. (3.86) and (3.88). At the expander inlet, the working fluid state depends strongly on the values of the convection heat transfer coefficients (see Chapter 2) and the exhaust gas conditions. A good estimation of these coefficients is thus of critical importance, since the working fluid or the expander may suffer damage or accelerated wear if the aforementioned constraints become violated.

Dual control methods: In order to achieve the *robustification* explained above, we can make use of a dual control approach as described in e.g. [87]. The central idea behind it is that the choice of the control not only influences the objective function, but also the measurements' statistical significance for the purpose of the state estimation. The control can thus be chosen in a way that reaches an adequate compromise between a high-quality state estimation (which implies a higher robustness of the solution) and an optimum objective function value.

Inclusion of further operational modes:

The results obtained in this thesis support the explicit consideration of transients in the control of the WHR. It is thus expected that further gains in efficiency can be obtained if a detailed consideration of operational modes other than the one treated in this thesis is included. Examples of this are start-up and shut-down processes, or transient modes in which the warm exhaust gas production is low, such as when the truck is driven by the electrical powertrain, if it is hybrid, or the motor is idle. In this case, the expander is bypassed since the heat recovered from the exhaust gas is not enough to evaporate the working fluid, but nevertheless the question that arises is how to operate the WHR in order to take maximum advantage of the available heat and keep the working fluid as warm as possible in order to allow a fast reconnection of the expander in case the heat is suddenly enough to do so. In order to expand our NMPC-MHE scheme to cover the aforementioned operational modes, new mathematical challenges are to be faced.

Modelling: Bypass valves for the expander and eventually other components should be incorporated into the model. This can be done by introducing *controls taking binary values*.

In addition, the evaporator model should be expanded in order to represent situations in which the working fluid is not in a thermodynamic state corresponding to saturated vapor at the evaporator outlet. The resulting model is likely to be associated to a *switching function* relating the state and the operating mode.

Methods for mixed-integer, switched systems: In summary, the addition of the aforementioned features results in a model with *mixed-integer controls* and *state-dependent switches*. The associated OCP, NMPC and MHE formulations represent challenges for the current state of the art. For their solution, approaches based on the techniques described in [82] can be developed.

Multi-level iterations:

In this thesis we have made use of the RTI scheme for both NMPC and MHE, and therewith we have achieved computational times shorter than the sampling time. This scheme has been extended in the recent years by the Multi-level iterations scheme (MLI), which exploits the fact that the different components of the QP (4.27) are usually valid for different periods of time and thus can be updated with different frequencies. Different levels are thus introduced according to which components of the QP are updated. For a detailed description, see e.g. [83, 165]. This approach can further reduce our already very good computational times, enabling us to consider longer prediction horizons, a bigger number of shooting nodes and additional data in the numerical instances of our MHE and NMPC schemes. Further, MLI can as well be applied to the extensions mentioned in the paragraphs above, which entail higher computational burdens.

Numerical evaluation of WHR performance and the design problem:

If the data for several exhaust gas scenarios are available, the optimal control can be calculated for each one of them by means of the tools described in this thesis. This can be used to perform

a numerical evaluation of the highest practical energy recovery potential for a given WHR topology. The advantage of this kind of procedure over a classical thermodynamic analysis of the kind of the Carnot cycle (see Chapter 2) is that a tighter upper bound for the system's performance can be obtained if the WHR dynamics are taken into account. Moreover, different WHR topologies (i.e. the choice of the component classes that are to be included in the cycle and of the connections between them, see e.g. [155] for a brief overview), components (i.e. the concrete members of the chosen components classes with which the cycle is to be built) and working fluids can be tested in order to evaluate the best combination for a given truck type according to specific criteria, which can be economic. The approaches found in the literature do not include dynamics and pick up a very limited number of possible combinations of topologies and working fluid into account each time.

Formulation of a two-layer optimization problem and a structure-exploiting algorithm: A novel approach would be to formulate this as a two-layer optimization problem. In the upper layer, a *combinatorial optimization problem* can be posed in which the decision variables are the presence or absence of certain components or cycle branches, or the use of a specific working fluid; and the objective function can be e.g. the aggregate component costs. In the lower layer, an *optimal control problem* can be posed in which the WHR's energy recovery is maximized for the aforementioned exhaust gas scenarios under consideration of the topology, components and working fluid from the upper level. The development of an efficient, *structure-exploiting* algorithm to solve this two-layer optimization problem constitutes a challenging task.

Comprehensive truck dynamic optimization:

The success of our NMPC-MHE scheme in the control of the WHR suggests the inclusion of additional truck subsystems in a comprehensive optimization-based control strategy. These subsystems can be e.g. the engine, further energy recovery subsystems and the truck's electrical powertrain. At this point we stress that the solution of this problem results challenging due to the fact that the use of energy recovery systems and the electrical powertrain reduce the internal combustion engine's heat production, which is in turn the energy source of at least some of the recovery systems present on the vehicle. A consequence of that is that it might be desirable to *switch* on or off some of the subsystems and/or the internal combustion engine during the truck's drive.

In order to implement a comprehensive optimization control strategy for the truck, the following developments are to be done.

Modelling: The accurate modelling of the engine, the electrical powertrain and each additional energy recovery subsystem needs to be addressed with particular emphasis on the energy flows between these systems, which is not a trivial task. The model can be also expanded with the inclusion of the vehicle's dynamics to allow for predicting its whole energy usage if a route with known slopes is provided. As before, the resulting model is likely to be associated to *state-dependent switching functions* and *mixed-integer controls*.

Mixed-integer, distributed NMPC: due to the presence of an interconnected network of subsystems to be controlled, an appealing approach consists on implementing individual controllers for each subsystem and an adequate coordination strategy between them, with the aim to take the maximum advantage of the interactions existing between each subsystem to guarantee a stable operation of the truck's energy system as a whole while pursuing the maximization of a collective objective function under consideration of the corresponding operational constraints. In addition, the activation and deactivation of some subsystems requires an adequate incorporation of *mixed-integer optimal control* techniques capable of handling *vanishing constraints*.

Bibliography

[1] J. Albersmeyer. Effiziente Ableitungserzeugung in einem adaptiven BDF-Verfahren. Diploma thesis, Heidelberg University, 2005.

[2] J. Albersmeyer. *Adjoint based algorithms and numerical methods for sensitivity generation and optimization of large scale dynamic systems*. PhD thesis, Heidelberg University, 2010. URL http://www.ub.uni-heidelberg.de/archiv/11651/.

[3] A. Alleyne, B. Rasmussen, M. Keir, and B. Eldredge. Advances in Energy Systems Modeling and Control. In *2007 American Control Conference*, pages 4363–4373, July 2007. doi: 10.1109/ACC.2007.4282747.

[4] Y. Ammar, S. Joyce, R. Norman, Y. Wang, and A. P. Roskilly. Low Grade Thermal Energy Sources and Uses From the Process Industry in the UK. *Applied Energy*, 89(1):3 – 20, 2012. ISSN 0306-2619. doi: 10.1016/j.apenergy.2011.06.003. Special issue on Thermal Energy Management in the Process Industries.

[5] J. Andersson. *A General-Purpose Software Framework for Dynamic Optimization*. PhD thesis, Faculty of Engineering, K.U. Leuven, 2013. URL https://lirias.kuleuven.be/handle/123456789/418048.

[6] K. J. Åstrom and T. Håglund. *PID Controllers: Theory, Design, and Tuning*. Instrument Society of America, second edition, 1995.

[7] S. Bari and S. N. Hossain. Waste Heat Recovery from a Diesel Engine Using Shell and Tube Heat Exchanger. *Applied Thermal Engineering*, 61(2):355 – 363, 2013. ISSN 1359-4311. doi: 10.1016/j.applthermaleng.2013.08.020.

[8] I. Bauer. *Numerische Verfahren zur Lösung von Anfangswertaufgaben und zur Generierung von ersten und zweiten Ableitungen mit Anwendungen bei Optimierungsaufgaben in Chemie und Verfahrenstechnik*. PhD thesis, Heidelberg University, 1999.

[9] I. Bauer, F. Finocchi, W. Duschl, H.-P. Gail, and J. P. Schlöder. Simulation of Chemical Reactions and Dust Destruction in Protoplanetary Accretion Discs. *Astron. Astrophys.*, 317:273–289, 1997.

[10] S. Bendapudi, J. E. Braun, and E. A. Groll. Dynamic Modeling of Shell-and-Tube Heat-Exchangers: Moving Boundary vs. Finite Volume. In *International Refrigeration and Air Conditioning Conference*, 2004.

[11] T. L. Bergman, A. S. Lavine, F. P. Incropera, and D. P. Dewitt. *Fundamentals of Heat and Mass Transfer*. John Wiley & Sons, 7th edition, 2006.

[12] G. Birkhoff and C. de Boor. Error Bounds for Spline Interpolation. *Journal of Mathematics and Mechanics*, 13(5):827–835, 1964. ISSN 00959057, 19435274. URL http://www.jstor.org/stable/24901235.

[13] G. Birkhoff and C. de Boor. Piecewise Polynomial Interpolation and Approximation. *Approximation of Functions*, pages 164–190, 1965.

[14] G. Birkhoff and H. L. Garabedian. Smooth surface interpolation. *Journal of Mathematics and Physics*, 39(1-4):258–268, 1960. ISSN 1467-9590. doi: 10.1002/sapm1960391258.

[15] H. G. Bock. Numerical Treatment of Inverse Problems in Chemical Reaction Kinetics. In K. Ebert, P. Deuflhard, and W. Jäger, editors, *Modelling of Chemical Reaction Systems*, volume 18 of *Springer Series in Chemical Physics*, pages 102–125. Springer, Heidelberg, 1981. URL `http://www.iwr.uni-heidelberg.de/groups/agbock/FILES/Bock1981.pdf`.

[16] H. G. Bock. Recent Advances in Parameter Identification Techniques for ODE. In P. Deuflhard and E. Hairer, editors, *Numerical Treatment of Inverse Problems in Differential and Integral Equations*, pages 95–121. Birkhäuser, Boston, 1983. URL `http://www.iwr.uni-heidelberg.de/groups/agbock/FILES/Bock1983.pdf`.

[17] H. G. Bock. *Randwertproblemmethoden zur Parameteridentifizierung in Systemen nichtlinearer Differentialgleichungen*, volume 183 of *Bonner Mathematische Schriften*. Universität Bonn, 1987.

[18] H. G. Bock and K. Plitt. A Multiple Shooting Algorithm for Direct Solution of Optimal Control Problems. In *Proceedings of the 9th IFAC World Congress*, pages 242–247, Budapest, 1984. Pergamon Press. URL `http://www.iwr.uni-heidelberg.de/groups/agbock/FILES/Bock1984.pdf`.

[19] H. G. Bock, M. Diehl, D. Leineweber, and J. P. Schlöder. A direct multiple shooting method for real-time optimization of nonlinear DAE processes. In F. Allgöwer and A. Zheng, editors, *Nonlinear Predictive Control*, volume 26 of *Progress in Systems Theory*, pages 246–267, Basel Boston Berlin, 2000. Birkhäuser.

[20] J. Bonilla, S. Dormido, and F. E. Cellier. Switching Moving Boundary Models for Two-phase Flow Evaporators and Condensers. *Communications in Nonlinear Science and Numerical Simulation*, 20(3):743 – 768, 2015. ISSN 1007-5704. doi: 10.1016/j.cnsns.2014.06.035.

[21] J. Bonilla Cruz, L. J. Yebra Muñoz, S. Dormido Bencomo, and E. Zarza Moya. *Modeling and Simulation of Two-phase Flow Evaporators for Parabolic-trough Solar Thermal Power Plants*. CIEMAT, 2013. URL `http://documenta.ciemat.es/handle/123456789/195`.

[22] A. E. Bryson and Y.-C. Ho. *Applied Optimal Control: Optimization, Estimation, and Control*. Blaisdell Publishing Company, Waltham,Mass., Toronto, London, 1969.

[23] D. Cakallik. Modellierung eines Abwärmerückgewinnungssystems für Lastkraftwagen. Diplomarbeit, Universität Stuttgart, 2011.

[24] G. W. Castellan. *Physical Chemistry*. Addison-Wesley Publishing Company, 1983.

[25] T. Cheng, X.-D. He, and H. H. Asada. Nonlinear Observer Design for Two-Phase Flow Heat Exchangers of Air Conditioning Systems. In *Proceedings of the 2004 American Control Conference*, volume 2, pages 1534–1539 vol.2, June 2004.

[26] F. Chiara and M. Canova. A Review of Energy Consumption, Management, and Recovery in Automotive Systems, with Considerations of Future Trends. *Proceedings of the Institution of Mechanical Engineers, Part D: Journal of Automobile Engineering*, 227(6): 914–936, 2013. doi: 10.1177/0954407012471294.

[27] D. W. Clarke. Application of Generalized Predictive Control to Industrial Processes. *IEEE Control Systems Magazine*, 8(2):49–55, April 1988. ISSN 0272-1708. doi: 10.1109/37. 1874.

[28] H. Cox. On the Estimation of State Variables and Parameters for Noisy Dynamic Systems. *IEEE Transactions on Automatic Control*, 9(1):5–12, Jan 1964. ISSN 0018-9286. doi: 10.1109/TAC.1964.1105635.

[29] M. Crialesi Esposito, N. Pompini, A. Gambarotta, and M. Canova. *A Switching Moving Boundary Model for the Simulation of ORC Plants in Automotive Applications*, pages 735–753. Springer Fachmedien Wiesbaden, Wiesbaden, 2015. ISBN 978-3-658-08844-6. doi: 10.1007/978-3-658-08844-6_49.

[30] M. Crialesi Esposito, N. Pompini, A. Gambarotta, V. Chandrasekaran, J. Zhou, and M. Canova. Nonlinear Model Predictive Control of an Organic Rankine Cycle for Exhaust Waste Heat Recovery in Automotive Engines. *IFAC-PapersOnLine*, 48(15):411–418, 2015. ISSN 2405-8963. doi: 10.1016/j.ifacol.2015.10.059.

[31] C. Cuevas, J. Lebrun, V. Lemort, and P. Ngendakumana. Development and Validation of a Condenser Three Zones Model. *Applied Thermal Engineering*, 29(17):3542 – 3551, 2009. ISSN 1359-4311. doi: 10.1016/j.applthermaleng.2009.06.007.

[32] C. Curtiss and J. Hirschfelder. Integration of Stiff Equations. *Proc. Nat. Acad. Sci*, 38: 235–243, 1952.

[33] C. de Boor. Bicubic Spline Interpolation. *J. Math. Phys.*, 41(3):212–218, 1962.

[34] C. de Boor. Best Approximation Properties of Spline Functions of Odd Degree. *Journal of Mathematics and Mechanics*, 12(5):747–749, 1963. ISSN 00959057, 19435274. URL http://www.jstor.org/stable/24900881.

[35] A. Desideri, B. Dechesne, J. Wronski, M. van den Broek, S. Gusev, V. Lemort, and S. Quoilin. Comparison of Moving Boundary and Finite-Volume Heat Exchanger Models in the Modelica Language. *Energies*, 9(5), 2016. ISSN 1996-1073. doi: 10.3390/en9050339.

[36] M. Diehl. *Real-Time Optimization for Large Scale Nonlinear Processes*. PhD thesis, Heidelberg University, 2001. URL http://www.ub.uni-heidelberg.de/archiv/1659/.

[37] M. Diehl. *Real-Time Optimization for Large Scale Nonlinear Processes*, volume 920 of *Fortschritt-Berichte VDI Reihe 8, Meß-, Steuerungs- und Regelungstechnik*. VDI Verlag, Düsseldorf, 2002. URL http://www.ub.uni-heidelberg.de/archiv/1659/.

[38] M. Diehl, H. G. Bock, and J. P. Schlöder. A Real-Time Iteration Scheme for Nonlinear Optimization in Optimal Feedback Control. *SIAM Journal on Control and Optimization*, 43(5):1714–1736, 2005.

[39] M. Diehl, R. Findeisen, F. Allgöwer, H. G. Bock, and J. P. Schlöder. Nominal Stability of the Real-Time Iteration Scheme for Nonlinear Model Predictive Control. *IEE Proc.-Control Theory Appl.*, 152(3):296–308, 2005.

[40] M. Diehl, R. Findeisen, F. Allgower, H. G. Bock, and J. P. Schlöder. Nominal stability of real-time iteration scheme for nonlinear model predictive control. *IEE Proceedings - Control Theory and Applications*, 152(3):296–308, May 2005. ISSN 1350-2379. doi: 10.1049/ip-cta:20040008.

[41] M. Diehl, R. Findeisen, and F. Allgöwer. A Stabilizing Real-time Implementation of Nonlinear Model Predictive Control. In L. Biegler, O. Ghattas, M. Heinkenschloss, D. Keyes, and B. van Bloemen Waanders, editors, *Real-Time and Online PDE-Constrained Optimization*. SIAM, 2006.

[42] M. Diehl, P. Kuehl, H. G. Bock, and J. P. Schlöder. Schnelle Algorithmen für die Zustands- und Parameterschätzung auf bewegten Horizonten. *Automatisierungstechnik*, 54(12): 602–613, 2006.

[43] H. E. Dillon and S. G. Penoncello. A fundamental equation for calculation of the thermodynamic properties of ethanol. *International Journal of Thermophysics*, 25(2):321–335, Mar 2004. ISSN 1572-9567. doi: 10.1023/B:IJOT.0000028470.49774.14.

[44] I. Duff and J. Reid. The design of MA48: A code for the direct solution of sparse unsymmetric linear systems of equations. *ACM Trans. on Math. Soft.*, 22:187–226, 1996.

[45] E. Eich. Numerische Behandlung semi-expliziter differentiell-algebraischer Gleichungssysteme vom Index I mit BDF Verfahren. Diploma thesis, Universität Bonn, 1987.

[46] E. Feru, F. Willems, C. Rojer, B. de Jager, and M. Steinbuch. Heat Exchanger Modeling and Identification for Control of Waste Heat Recovery Systems in Diesel Engines. In *2013 American Control Conference*, pages 2860–2865, June 2013. doi: 10.1109/ACC. 2013.6580268.

[47] E. Feru, B. de Jager, F. Willems, and M. Steinbuch. Two-phase Plate-Fin Heat Exchanger Modeling for Waste Heat Recovery Systems in Diesel Engines. *Applied Energy*, 133: 183–196, 2014. ISSN 0306-2619. doi: 10.1016/j.apenergy.2014.07.073.

[48] E. Feru, F. Willems, B. de Jager, and M. Steinbuch. Modeling and Control of a Parallel Waste Heat Recovery System for Euro-VI Heavy-Duty Diesel Engines. *Energies*, 7(10): 6571–6592, Oct 2014. ISSN 1996-1073. doi: 10.3390/en7106571.

[49] E. Feru, F. Willems, B. de Jager, and M. Steinbuch. Model Predictive Control of a Waste Heat Recovery System for Automotive Diesel Engines. In *System Theory, Control and Computing (ICSTCC), 2014 18th International Conference*, pages 658–663, Oct 2014. doi: 10.1109/ICSTCC.2014.6982492.

[50] E. Feru, F. P. T. Willems, G. C. Rascanu, A. G. de Jager, and M. Steinbuch. Control of Automotive Waste Heat Recovery Systems with Parallel Evaporators. In *Proceedings of the FISITA World Automotive Congress 2014, 2-6 June 2014, Maastricht, The Netherlands*. Technische Universiteit Eindhoven., 2014.

[51] E. Feru, F. Willems, B. de Jager, and M. Steinbuch. Control of a Waste Heat Recovery System with Decoupled Expander for Improved Diesel Engine Efficiency. In *2015 European Control Conference (ECC)*, pages 148–153, July 2015. doi: 10.1109/ECC.2015. 7330537.

[52] R. W. Fox, A. T. McDonald, and P. J. Pritchard. *Introduction to Fluid Mechanics*. John Wiley & Sons, 6th edition, 2004.

[53] G. Frison and J. B. Jørgensen. A Fast Condensing Method for Solution of Linear-quadratic Control Problems. In *52nd IEEE Conference on Decision and Control*, pages 7715–7720, Dec 2013. doi: 10.1109/CDC.2013.6761114.

[54] C. Gear. Simultaneous Numerical Solution of Differential-Algebraic Equations. *IEEE Transactions on Circuit Theory*, 18(1):89–95, January 1971. ISSN 0018-9324. doi: 10.1109/TCT.1971.1083221.

[55] C. Gear and T. Vu. Smooth numerical solutions of ordinary differential equations. In P. Deuflhard and E. Hairer, editors, *Numerical Treatment of Inverse Problems in Differential and Integral Equations*. Birkhäuser, Boston, 1983.

[56] P. Gill, W. Murray, M. Saunders, and M. Wright. *User's guide for SOL/QPSOL: a Fortran package for quadratic programming*, volume SOL 83-7 of *Technical Report*. Stanford University, Systems Optimization Laboratory, Department of Operations Research, 1983.

[57] M. Gräber, N. C. Strupp, and W. Tegethoff. Moving Boundary Heat Exchanger Model and Validation Procedure. In *EUROSIM Congress on Modelling and Simulation, Prague*, 2010.

[58] M. Gräber, C. Kirches, J. P. Schlöder, and W. Tegethoff. Nonlinear Model Predictive Control of a Vapor Compression Cycle based on First Principle Models. *IFAC Proceedings Volumes*, 45(2):258–263, 2012. ISSN 1474-6670. doi: 10.3182/20120215-3-AT-3016. 00045.

[59] V. Grelet, P. Dufour, M. Nadri, T. Reiche, and V. Lemort. Modeling and Control of Rankine Based Waste Heat Recovery Systems for Heavy Duty Trucks. *IFAC-PapersOnLine*, 48(8): 568–573, 2015. ISSN 2405-8963. doi: 10.1016/j.ifacol.2015.09.028.

[60] V. Grelet, T. Reiche, V. Lemort, M. Nadri, and P. Dufour. Transient Performance Evaluation of Waste Heat Recovery Rankine Cycle Based System for Heavy Duty Trucks. *Applied Energy*, 165(Supplement C):878 – 892, 2016. ISSN 0306-2619. doi: 10.1016/j.apenergy.2015.11.004.

[61] L. Grüne and J. Pannek. *Nonlinear Model-Predictive Control*. Springer-Verlag London, 2011.

[62] E. Guerrero Merino, C. Kirches, and J. P. Schlöder. Nonlinear Optimal Control of a Heavy Duty Truck Exhaust Heat Recovery System. In H. G. Bock, H. X. Phu, and J. P. Schlöder, editors, *Modeling, Simulation, and Optimization of Complex Processes. Proceedings of the Sixth International Conference on High Performance Scientific Computing, March 16-20, 2015, Hanoi, Vietnam*. Springer Verlag, 2017.

[63] E. Guerrero Merino, J. P. Schlöder, and C. Kirches. A Nonlinear Model-Predictive Control Scheme Together with Moving Horizon Estimation for Waste Heat Recovery System For a Heavy Duty Truck. In *2018 American Control Conference*, March 2018. (accepted).

[64] E. Guerrero Merino, D. Seitz, C. Kirches, J. P. Schlöder, M. Brunschier, C. Bunz, and O. Gehring. Optimal Control and NMPC for Organic Rankine Cycle in Heavy Duty Trucks. *Optimization and Engineering*, 2018. (submitted).

[65] E. Hairer and G. Wanner. *Solving Ordinary Differential Equations II: Stiff and Differential-Algebraic Problems*. Springer Series in Computational Mathematics. Springer-Verlag, second revised edition, 2002.

[66] E. Hairer, S. P. Nørsett, and G. Wanner. *Solving Ordinary Differential Equations I: Nonstiff Problems*. Springer-Verlag Berlin Heidelberg GmbH, secon edition, 2008.

[67] C. A. Hall and W. Meyer. Optimal error bounds for cubic spline interpolation. *Journal of Approximation Theory*, 16(2):105 – 122, 1976. ISSN 0021-9045. doi: 10.1016/0021-9045(76)90040-X.

[68] M. Hatami, D. Ganji, and M. Gorji-Bandpy. A Review of Different Heat Exchangers Designs for Increasing the Diesel Exhaust Waste Heat Recovery. *Renewable and Sustainable Energy Reviews*, 37(Supplement C):168 – 181, 2014. ISSN 1364-0321. doi: 10.1016/j.rser.2014.05.004.

[69] K. Holkar and L. Waghmare. An Overview of Model Predictive Control. *International Journal of Control and Automation*, 3(4):47–63, December 2010.

[70] J. C. Holladay. A Smoothest Curve Approximation. *Mathematical Tables and Other Aids to Computation*, 11(60):233–243, 1957. ISSN 0891-6837. URL `http://www.jstor.org/stable/2001941`.

[71] K. Holmberg, P. Andersson, N.-O. Nylund, K. Mäkelä, and A. Erdemir. Global Energy Consumption Due to Friction in Trucks and Buses. *Tribology International*, 78:94–114, Oct 2014. ISSN 0301-679X. doi: 10.1016/j.triboint.2014.05.004.

[72] *Stainless Steel Media Isolated Pressure Sensors Line Guide*. Honeywell, November 2009.

[73] *Temperature Sensors Line Guide*. Honeywell, March 2016.

[74] T. A. Horst, H.-S. Rottengruber, M. Seifert, and J. Ringler. Dynamic Heat Exchanger Model for Performance Prediction and Control System Design of Automotive Waste Heat Recovery Systems. *Applied Energy*, 105:293–303, May 2013. ISSN 0306-2619. doi: 10.1016/j.apenergy.2012.12.060.

[75] T. Hung, T. Shai, and S. Wang. A Review of Organic Rankine Cycles (ORCs) for the Recovery of Low-grade Waste Heat. *Energy*, 22(7):661–667, 1997. ISSN 0360-5442. doi: 10.1016/S0360-5442(96)00165-X.

[76] A. H. Jazwinski. *Stochastic Processes and Filtering Theory*. Academic Press, Inc., 1970.

[77] J. Jensen. *Dynamic Modeling of ThermoFluid Systems*. PhD thesis, Technical University of Denmark, 2003.

[78] J. Jensen and H. Tummescheit. Moving Boundary Models for Dynamic Simulations of Two-Phase Flows. In M. Otter, editor, *Proceedings of Modelica 2002, Deutsches Zentrum für Luft- und Raumfahrt e.V., Oberpfaffenhofen, Germany, March 2002*, pages 235–244. The Modelica Association and Institut für Robotik und Mechatronik, Deutsches Zentrum für Luft- und Raumfahrt e.V., March 2002.

[79] R. E. Kalman. A New Approach to Linear Filtering and Prediction Problems. *Journal of Basic Engineering*, 82(1):35–45, March 1960.

[80] M. Kane, D. Larrain, D. Favrat, and Y. Allani. Small Hybrid Solar Power System. *Energy*, 28(14):1427 – 1443, 2003. ISSN 0360-5442. doi: 10.1016/S0360-5442(03)00127-0.

[81] H. K. Khalil. *Nonlinear Systems*. Prentice Hall, Upper Saddle River, NJ 07458, third edition, 2002.

[82] C. Kirches. *Fast Numerical Methods for Mixed-Integer Nonlinear Model-Predictive Control*. PhD thesis, Heidelberg University, 2010.

[83] C. Kirches, L. Wirsching, S. Sager, and H. G. Bock. Efficient Numerics for Nonlinear Model Predictive Control. In M. Diehl, F. Glineur, E. Jarlebring, and W. Michiels, editors, *Recent Advances in Optimization and its Applications in Engineering*, pages 339–359. Springer, 2010. URL http://mathopt.de/PUBLICATIONS/Kirches2010c.pdf. ISBN 978-3-6421-2597-3.

[84] V. Klee and G. Minty. How Good is the Simplex Algorithm? In O. Shisha, editor, *Inequalities*, volume III, pages 159–175. Academic Press, New York, 1972.

[85] T. Kraus, P. Kühl, L. Wirsching, H. G. Bock, and M. Diehl. A Moving Horizon State Estimation algorithm applied to the Tennessee Eastman benchmark process. In *Proc. of IEEE Robotics and Automation Society conference on Multisensor Fusion and Integration for Intelligent Systems*, 2006.

[86] P. Kühl, M. Diehl, T. Kraus, J. P. Schlöder, and H. G. Bock. A real-time algorithm for moving horizon state and parameter estimation. *Computers & Chemical Engineering*, 35:71–83, 2011.

[87] H. C. La. *Dual Control for Nonlinear Model Predictive Control*. PhD thesis, Heidelberg University, 2016.

[88] J. Larjola. Electricity from Industrial Waste Heat Using High-speed Organic Rankine Cycle (ORC). *International Journal of Production Economics*, 41(1):227–235, 1995. ISSN 0925-5273. doi: 10.1016/0925-5273(94)00098-0.

[89] S. Lecompte, S. Lemmens, H. Huisseune, M. van den Broek, and M. De Paepe. Multi-Objective Thermo-Economic Optimization Strategy for ORCs Applied to Subcritical and Transcritical Cycles for Waste Heat Recovery. *Energies*, 8(4):2714–2741, Apr 2015. ISSN 1996-1073. doi: 10.3390/en8042714.

[90] D.-S. Lee, T.-C. Hung, J.-R. Lin, and J. Zhao. Experimental Investigations on Solar Chimney for Optimal Heat Collection to be Utilized in Organic Rankine Cycle. *Applied Energy*, 154:651–662, 2015. ISSN 0306-2619. doi: 10.1016/j.apenergy.2015.05.079.

[91] D. Leineweber. Analyse und Restrukturierung eines Verfahrens zur direkten Lösung von Optimal-Steuerungsproblemen. Diploma thesis, Heidelberg University, 1995.

[92] D. Leineweber. *Efficient Reduced SQP Methods for the Optimization of Chemical Processes Described by Large Sparse DAE Models*, volume 613 of *Fortschritt-Berichte VDI Reihe 3, Verfahrenstechnik*. VDI Verlag, Düsseldorf, 1999.

[93] E. W. Lemmon, M. L. Huber, and M. O. McLinden. *NIST Standard Reference Database 23: Reference Fluid Thermodynamic and Transport Properties - REFPROP*. National Institute of Standards and Technology, Standard Reference Data Program, Gaithersburg, MD, 9.0 edition, 2010.

[94] V. Lemort, S. Quoilin, C. Cuevas, and J. Lebrun. Testing and Modeling a Scroll Expander Integrated into an Organic Rankine Cycle. *Applied Thermal Engineering*, 29(14-15): 3094–3102, 2009. ISSN 1359-4311. doi: 10.1016/j.applthermaleng.2009.04.013.

[95] J. Li, A. Kazakov, and F. L. Dryer. Experimental and numerical studies of ethanol decomposition reactions. *The Journal of Physical Chemistry A*, 108(38):7671–7680, 2004. doi: 10.1021/jp0480302.

[96] X.-L. Li, J.-G. Park, and H.-B. Shin. Comparison and Evaluation of Anti-Windup PI Controllers. *Journal of Power Electronics*, 11(1):45–50, Jan 2011. ISSN 1598-2092. doi: 10.6113/jpe.2011.11.1.045.

[97] B.-T. Liu, K.-H. Chien, and C.-C. Wang. Effect of Working Fluids on Organic Rankine Cycle for Waste Heat Recovery. *Energy*, 29(8):1207 – 1217, 2004. ISSN 0360-5442. doi: 10.1016/j.energy.2004.01.004.

[98] L. Ljung. Black-Box Models from Input-Output Measurements. In *IMTC 2001. Proceedings of the 18th IEEE Instrumentation and Measurement Technology Conference. Rediscovering Measurement in the Age of Informatics (Cat. No.01CH 37188)*, volume 1, pages 138–146 vol.1, May 2001. doi: 10.1109/IMTC.2001.928802.

[99] L. Ljung. *System Identification: Theory for the User*. Prentice Hall, second edition, 2007.

[100] D. G. Luenberger. Observing the State of a Linear System. *IEEE Transactions on Military Electronics*, 8(2):74–80, April 1964. ISSN 0536-1559. doi: 10.1109/TME.1964. 4323124.

[101] J. Lunze. *Regelungstechnik 2: Mehrgrößensysteme, Digitale Regelung*. Springer Vieweg, ninth edition, 2016.

[102] D. Luong. *Modeling, Estimation, and Control of Waste Heat Recovery Systems*. PhD thesis, Department of Mechanical and Aerospace Engineering, University of California, Los Angeles, 2013.

[103] D. Luong and T. C. Tsao. Linear Quadratic Integral Control of an Organic Rankine Cycle for Waste Heat Recovery in Heavy-Duty Diesel Powertrain. In *2014 American Control Conference*, pages 3147–3152, June 2014. doi: 10.1109/ACC.2014.6858907.

[104] D. Luong and T.-C. Tsao. Model Predictive Control of Organic Rankine Cycle for Waste Heat Recovery in Heavy-Duty Diesel Powertrain. In D. M. Bevly, editor, *Proceedings of the ASME Dynamic Systems and Control Conference, Volume 2: Dynamic Modeling and Diagnostics in Biomedical Systems; Dynamics and Control of Wind Energy Systems; Vehicle Energy Management Optimization; Energy Storage, Optimization; Transportation and Grid Applications; Estimation and Identification Methods, Tracking, Detection, Alternative Propulsion Systems; Ground and Space Vehicle Dynamics; Intelligent Transportation Systems and Control; Energy Harvesting; Modeling and Control for Thermo-Fluid Applications, IC Engines, Manufacturing*, pages V002T21A001–. ASME, October 2014. doi: 10.1115/DSCC2014-5881.

[105] J. M. Maciejowski. *Multivariable Feedback Design*. Addison-Wesley Publishing Company, Inc., 1989.

[106] G. Manente, A. Toffolo, A. Lazzaretto, and M. Paci. An Organic Rankine Cycle Off-Design Model for the Search of the Optimal Control Strategy. *Energy*, 58:97–106, Sep 2013. ISSN 0360-5442. doi: 10.1016/j.energy.2012.12.035.

[107] D. Mayne, J. Rawlings, C. Rao, and P. Scokaert. Constrained Model Predictive Control: Stability and Optimality. *Automatica*, 36(6):789 – 814, 2000. ISSN 0005-1098. doi: 10.1016/S0005-1098(99)00214-9.

[108] D. Q. Mayne. Model Predictive Control: Recent Developments and Future Promise. *Automatica*, 50(12):2967 – 2986, 2014. ISSN 0005-1098. doi: 10.1016/j.automatica. 2014.10.128.

[109] T. L. McKinley and A. G. Alleyne. An Advanced Nonlinear Switched Heat Exchanger Model for Vapor Compression Cycles Using the Moving-boundary Method. *International Journal of Refrigeration*, 31(7):1253 – 1264, 2008. ISSN 0140-7007. doi: 10.1016/j. ijrefrig.2008.01.012.

[110] H. Michalska and D. Q. Mayne. Moving horizon observers and observer-based control. *IEEE Transactions on Automatic Control*, 40(6):995–1006, 1995.

[111] D. Mikielewicz and J. Mikielewicz. A Thermodynamic Criterion for Selection of Working Fluid for Subcritical and Supercritical Domestic Micro CHP. *Applied Thermal Engineering*, 30(16):2357 – 2362, 2010. ISSN 1359-4311. doi: 10.1016/j.applthermaleng.2010. 05.035. Selected Papers from the 12th Conference on Process Integration, Modelling and Optimisation for Energy Saving and Pollution Reduction.

[112] B. Moore. Principal Component Analysis in Linear Systems: Controllability, Observability, and Model Reduction. *IEEE Transactions on Automatic Control*, 26(1):17–32, Feb 1981. ISSN 0018-9286. doi: 10.1109/TAC.1981.1102568.

[113] M. J. Moran and H. N. Shapiro. *Fundamentals of Engineering Thermodynamics*. John Wiley and Sons Inc., New York, NY, 6th edition, 2009.

[114] K. Ogata. *Discrete-Time Control Systems*. Prentice-Hall, second edition, 1995.

[115] K. Ogata. *Modern Control Engineering*. Prentice-Hall, fifth edition, 2010.

[116] V. Pandiyarajan, M. C. Pandian, E. Malan, R. Velraj, and R. Seeniraj. Experimental investigation on heat recovery from diesel engine exhaust using finned shell and tube heat exchanger and thermal storage system. *Applied Energy*, 88(1):77 – 87, 2011. ISSN 0306-2619. doi: 10.1016/j.apenergy.2010.07.023.

[117] W. Pankiewicz. Algorithms: Algorithm 337: Calculation of a Polynomial and Its Derivative Values by Horner Scheme. *Commun. ACM*, 11(9):633–, Sept. 1968. ISSN 0001-0782. doi: 10.1145/364063.364089.

[118] D.-Y. Peng and D. B. Robinson. A new two-constant equation of state. *Industrial & Engineering Chemistry Fundamentals*, 15(1):59–64, 1976. doi: 10.1021/i160057a011.

[119] J. Peralez, P. Tona, A. Sciarretta, P. Dufour, and M. Nadri. Towards Model-Based Control of a Steam Rankine Process for Engine Waste Heat Recovery. In *2012 IEEE Vehicle Power and Propulsion Conference*, pages 289–294, Oct 2012. doi: 10.1109/VPPC.2012. 6422718.

[120] J. Peralez, P. Tona, O. Lepreux, A. Sciarretta, L. Voise, P. Dufour, and M. Nadri. Improving the Control Performance of an Organic Rankine Cycle System for Waste Heat Recovery from a Heavy-Duty Diesel Engine Using a Model-Based Approach. In *52nd IEEE Conference on Decision and Control*, pages 6830–6836, Dec 2013. doi: 10.1109/CDC.2013.6760971.

[121] J. Peralez, M. Nadri, P. Dufour, P. Tona, and A. Sciarretta. Control Design for an Automotive Turbine Rankine Cycle System Based on Nonlinear State Estimation. *53rd IEEE Conference on Decision and Control*, Dec 2014. doi: 10.1109/cdc.2014.7039902.

[122] J. Peralez, P. Tona, M. Nadri, P. Dufour, and A. Sciarretta. Optimal Control for an Organic Rankine Cycle on Board a Diesel-Electric Railcar. *Journal of Process Control*, 33:1–13, Sep 2015. ISSN 0959-1524. doi: 10.1016/j.jprocont.2015.03.009.

[123] J. Peralez, M. Nadri, P. Dufour, P. Tona, and A. Sciarretta. Organic Rankine Cycle for Vehicles: Control Design and Experimental Results. *IEEE Transactions on Control Systems Technology*, 25(3):952–965, May 2017. ISSN 1063-6536. doi: 10.1109/TCST.2016. 2574760.

[124] K. Plitt. Ein superlinear konvergentes Mehrzielverfahren zur direkten Berechnung beschränkter optimaler Steuerungen. Diploma thesis, Rheinische Friedrich–Wilhelms–Universität Bonn, 1981.

[125] L. S. Pontryagin, V. G. Boltianski, R. V. Gamkrelidze, and E. F. Mishchenko. *The Mathematical Theory of Optimal Processes*. International series of monographs in pure and applied mathematics. Pergamon Press, London, Paris, 1964. A Pergamon Press book. Translated by Brown, D. E.

[126] A. Potschka. Handling Path Constraints in a Direct Multiple Shooting Method for Optimal Control Problems. Diploma thesis, Heidelberg University, 2006. URL `http://apotschka.googlepages.com/APotschka2006.pdf`.

[127] M. Powell. A Fast Algorithm for Nonlinearly Constrained Optimization Calculations. In G. Watson, editor, *Numerical Analysis, Dundee 1977*, volume 630 of *Lecture Notes in Mathematics*, Berlin, 1978. Springer.

[128] H. Qiao, V. Aute, and R. Radermacher. An Improved Moving Boundary Heat Exchanger Model with Pressure Drop. In *15th International Refrigeration and Air-Conditioning Conference at Purdue*, July 2014. URL `https://www.conftool.com/2014Purdue/`.

[129] S. Quoilin and V. Lemort. Technological and Economical Survey of Organic Rankine Cycle Systems. In *European Conference on Economics and Management of Energy in Industry*, 2009.

[130] S. Quoilin, V. Lemort, and J. Lebrun. Experimental Study and Modeling of an Organic Rankine Cycle using Scroll Expander. *Applied Energy*, 87(4):1260 – 1268, 2010. ISSN 0306-2619. doi: 10.1016/j.apenergy.2009.06.026.

[131] S. Quoilin, R. Aumann, A. Grill, A. Schuster, V. Lemort, and H. Spliethoff. Dynamic Modeling and Optimal Control Strategy of Waste Heat Recovery Organic Rankine Cycles. *Applied Energy*, 88(6):2183–2190, 2011. ISSN 0306-2619. doi: 10.1016/j.apenergy. 2011.01.015.

[132] S. Quoilin, S. Declaye, B. F. Tchanche, and V. Lemort. Thermo-Economic Optimization of Waste Heat Recovery Organic Rankine Cycles. *Applied Thermal Engineering*, 31(14-15): 2885–2893, 2011. ISSN 1359-4311. doi: 10.1016/j.applthermaleng.2011.05.014.

[133] S. Quoilin, M. Orosz, H. Hemond, and V. Lemort. Performance and Design Optimization of a Low-Cost Solar Organic Rankine Cycle for Remote Power Generation. *Solar Energy*, 85(5):955–966, 2011. ISSN 0038-092X. doi: 10.1016/j.solener.2011.02.010.

[134] S. Quoilin, M. V. D. Broek, S. Declaye, P. Dewallef, and V. Lemort. Techno-Economic Survey of Organic Rankine Cycle (ORC) Systems. *Renewable and Sustainable Energy Reviews*, 22:168–186, 2013. ISSN 1364-0321. doi: 10.1016/j.rser.2013.01.028.

[135] C. Rao, J. Rawlings, and J. Lee. Constrained linear state estimation - a moving horizon approach. *Automatica*, 37(2):1619–1628, 2001.

[136] C. V. Rao, J. B. Rawlings, and D. Q. Mayne. Constrained state estimation for nonlinear discrete-time systems: Stability and moving horizon approximations. *IEEE Transactions on Automatic Control*, 48(2):246–258, 2003.

[137] J. Reid and I. Duff. MA48, A Fortran Code for Direct Solution of Sparse Unsymmetric Linear Systems of Equations. Technical Report RAL 93 072, Rutherford Appleton Laboratory, 1993.

[138] D. Robertson and J. Lee. A least squares formulation for state estimation. *Journal of Process Control*, 5(4):291–299, 1995.

[139] J. Roy and A. Misra. Parametric Optimization And Performance Analysis of a Regenerative Organic Rankine Cycle Using R-123 for Waste Heat Recovery. *Energy*, 39(1): 227–235, 2012. ISSN 0360-5442. doi: 10.1016/j.energy.2012.01.026. Sustainable Energy and Environmental Protection 2010.

[140] J. Roy, M. Mishra, and A. Misra. Parametric Optimization and Performance Analysis of a Waste Heat Recovery System Using Organic Rankine Cycle. *Energy*, 35(12):5049–5062, 2010. ISSN 0360-5442. doi: 10.1016/j.energy.2010.08.013. The 3rd International Conference on Sustainable Energy and Environmental Protection, {SEEP} 2009.

[141] J. Roy, M. Mishra, and A. Misra. Performance Analysis of an Organic Rankine Cycle with Superheating under Different Heat Source Temperature Conditions. *Applied Energy*, 88 (9):2995–3004, 2011. ISSN 0306-2619. doi: 10.1016/j.apenergy.2011.02.042.

[142] B. Saleh, G. Koglbauer, M. Wendland, and J. Fischer. Working Fluids for Low-temperature Organic Rankine Cycles. *Energy*, 32(7):1210 – 1221, 2007. ISSN 0360-5442. doi: 10.1016/j.energy.2006.07.001.

[143] I. J. Schoenberg. Contributions to the Problem of Approximation of Equidistant Data by Analytic Functions: Part A.—On the Problem of Smoothing or Graduation. A First Class of Analytic Approximation Formulae. *Quarterly of Applied Mathematics*, 4(1):45–99, 1946. ISSN 1552-4485.

[144] D. Seitz, O. Gehring, C. Bunz, M. Brunschier, and O. Sawodny. Design of a Nonlinear, Dynamic Feedforward Part for the Evaporator Control of an Organic Rankine Cycle in Heavy Duty Vehicles. *IFAC-PapersOnLine*, 49(11):625–632, 2016. ISSN 2405-8963. doi: 10.1016/j.ifacol.2016.08.091.

[145] H. Späth. *Zweidimensionale Spline-, Interpolations- Algorithmen*. R. Oldenbourg, 1991. ISBN 9783486218077.

[146] H. Späth and J. Meier. *Eindimensionale Spline- Interpolations- Algorithmen*. R. Oldenbourg, 1990. ISBN 9783486213034.

[147] C. Sprouse III and C. Depcik. Review of Organic Rankine Cycles for Internal Combustion Engine Exhaust Waste Heat Recovery. *Applied Thermal Engineering*, 51(1-2):711–722, 2013. ISSN 1359-4311. doi: 10.1016/j.applthermaleng.2012.10.017.

[148] Statistical Office of the European Union (Eurostat). *Energy, Transport and Environment Indicators – 2017 Edition*. Publications Office of the European Union, Luxembourg, 2017.

[149] Statistical Office of the European Union (Eurostat). *Energy Balance Sheets – 2017 Edition*. Publications Office of the European Union, 2017.

[150] L. Sun and J. F. Ely. Universal equation of state for engineering application: algorithm and application to non-polar and polar fluids. *Fluid Phase Equilibria*, 222–223:107 – 118, 2004. ISSN 0378-3812. doi: 10.1016/j.fluid.2004.06.028. Proceedings of the Fifteenth Symposium on Thermophysical Properites.

[151] B. F. Tchanche, G. Papadakis, G. Lambrinos, and A. Frangoudakis. Fluid Selection for a Low-temperature Solar Organic Rankine Cycle. *Applied Thermal Engineering*, 29(11): 2468 – 2476, 2009. ISSN 1359-4311. doi: 10.1016/j.applthermaleng.2008.12.025.

[152] B. F. Tchanche, G. Lambrinos, A. Frangoudakis, and G. Papadakis. Low-grade Heat Conversion into Power Using Organic Rankine Cycles – A Review of Various Applications. *Renewable and Sustainable Energy Reviews*, 15(8):3963 – 3979, 2011. ISSN 1364-0321. doi: 10.1016/j.rser.2011.07.024.

[153] B. F. Tchanche, M. Pétrissans, and G. Papadakis. Heat Resources and Organic Rankine Cycle Machines. *Renewable and Sustainable Energy Reviews*, 39:1185–1199, 2014. ISSN 1364-0321. doi: 10.1016/j.rser.2014.07.139.

[154] J. R. Thome. *Engineering Data Book III*. Wolverine Tube, Inc, 2004.

[155] P. Tona and J. Peralez. Control of Organic Rankine Cycle Systems on Board Heavy-Duty Vehicles: a Survey. *IFAC-PapersOnLine*, 48(15):419–426, 2015. ISSN 2405-8963. doi: 10.1016/j.ifacol.2015.10.060.

[156] P. Tona, J. Peralez, and A. Sciarretta. Supervision and Control Prototyping for an Engine Exhaust Gas Heat Recovery System Based on a Steam Rankine Cycle. In *2012 IEEE/ASME International Conference on Advanced Intelligent Mechatronics (AIM)*, pages 695–701, July 2012. doi: 10.1109/AIM.2012.6266053.

[157] VDI-Gesellschaft. *VDI-Wärmeatlas*. Springer Berlin Heidelberg, 2006. doi: 10.1007/978-3-540-32218-4.

[158] R. von Schwerin. *Numerical methods, algorithms, and software for higher index nonlinear differential-algebraic equations in multibody system simulation*. PhD thesis, Heidelberg University, 1997.

[159] J. L. Walsh, J. H. Ahlberg, and E. N. Nilson. Best Approximation Properties of the Spline Fit. *Journal of Mathematics and Mechanics*, 11(2):225–234, 1962. ISSN 1943-5274. URL http://www.jstor.org/stable/24900920.

[160] E. Wang, H. Zhang, B. Fan, M. Ouyang, Y. Zhao, and Q. Mu. Study of Working Fluid Selection of Organic Rankine Cycle (ORC) for Engine Waste Heat Recovery. *Energy*, 36 (5):3406 – 3418, 2011. ISSN 0360-5442. doi: 10.1016/j.energy.2011.03.041.

[161] J. Wang, Y. Dai, and L. Gao. Exergy Analyses and Parametric Optimizations for Different Cogeneration Power Plants in Cement Industry. *Applied Energy*, 86(6):941–948, 2009. ISSN 0306-2619. doi: 10.1016/j.apenergy.2008.09.001.

[162] T. Wang, Y. Zhang, Z. Peng, and G. Shu. A Review of Researches on Thermal Exhaust Heat Recovery with Rankine Cycle. *Renewable and Sustainable Energy Reviews*, 15(6): 2862–2871, 2011. ISSN 1364-0321. doi: 10.1016/j.rser.2011.03.015.

[163] D. Wei, X. Lu, Z. Lu, and J. Gu. Performance Analysis and Optimization of Organic Rankine Cycle (ORC) for Waste Heat Recovery. *Energy Conversion and Management*, 48 (4):1113 – 1119, 2007. ISSN 0196-8904. doi: 10.1016/j.enconman.2006.10.020.

[164] D. Wei, X. Lu, Z. Lu, and J. Gu. Dynamic Modeling and Simulation of an Organic Rankine Cycle (ORC) System for Waste Heat Recovery. *App. Therm. Eng.*, 28(10):1216–1224, 2008.

[165] L. Wirsching. *Multi-Level Iteration Schemes with Adaptive Level Choice for Nonlinear Model Predictive Control*. PhD thesis, Heidelberg University, 2018.

[166] A. Wynn, M. Vukov, and M. Diehl. Convergence Guarantees for Moving Horizon Estimation Based on the Real-Time Iteration Scheme. *IEEE Transactions on Automatic Control*, 59(8):2215–2221, Aug 2014. ISSN 0018-9286. doi: 10.1109/TAC.2014.2298984.

[167] H. Xie and C. Yang. Dynamic Behavior of Rankine Cycle System for Waste Heat Recovery of Heavy Duty Diesel Engines under Driving Cycle. *Applied Energy*, 112:130–141, 2013. ISSN 0306-2619. doi: 10.1016/j.apenergy.2013.05.071.

[168] T. Yamamoto, T. Furuhata, N. Arai, and K. Mori. Design and Testing of the Organic Rankine Cycle. *Energy*, 26(3):239–251, 2001. ISSN 0360-5442. doi: 10.1016/S0360-5442(00)00063-3.

[169] P. Young and J. Willems. An Approach to the Linear Multivariable Servomechanism Problem. *International Journal of Control*, 15(5):961–979, 1972. doi: 10.1080/00207177208932211.

[170] J. Zhang, W. Zhang, G. Hou, and F. Fang. Dynamic Modeling and Multivariable Control of Organic Rankine Cycles in Waste Heat Utilizing Processes. *Computers & Mathematics with Applications*, 64(5):908–921, 2012.

[171] J. Zhang, Y. Zhou, S. Gao, and G. Hou. Constrained Predictive Control Based on State Space Model of Organic Rankine Cycle System for Waste Heat Recovery. In *24th Chinese Control and Decision Conference (CCDC)*, pages 230–234, May 2012. doi: 10.1109/CCDC.2012.6244032.

[172] J. Zhang, Y. Zhou, Y. Li, G. Hou, and F. Fang. Generalized Predictive Control Applied in Waste Heat Recovery Power Plants. *Applied Energy*, 102:320–326, Feb 2013. ISSN 0306-2619. doi: 10.1016/j.apenergy.2012.07.038.

[173] J. Zhang, M. Lin, F. Shi, J. Meng, and J. Xu. Set Point Optimization of Controlled Organic Rankine Cycle Systems. *Chin. Sci. Bull.*, 59(33):4397–4404, Aug 2014. ISSN 1861-9541. doi: 10.1007/s11434-014-0590-1.

[174] J. Zhang, Y. Zhou, R. Wang, J. Xu, and F. Fang. Modeling and Constrained Multivariable Predictive Control for ORC (Organic Rankine Cycle) Based Waste Heat Energy Conversion Systems. *Energy*, 66:128–138, Mar 2014. ISSN 0360-5442. doi: 10.1016/j.energy.2014.01.068.

Nomenclature

Throughout this thesis, lowercase roman and greek letter in boldface ($\boldsymbol{x}$, $\boldsymbol{y}$, $\boldsymbol{\lambda}$, $\boldsymbol{\mu}$) are used for vectors. Matrices use uppercase roman letters in boldface ($\boldsymbol{A}$, $\boldsymbol{B}$, $\boldsymbol{C}$). Scalars are denoted by lowercase roman and greek letters (f, g, λ, μ). In this thesis concepts and ideas belonging to thermodynamics, chemistry, heat transfer, optimization, differential equations and control systems coexist, and thus the choice of a set of symbols that respects existing conventions, results intuitive to understand and remains consisten throughout the text has been a task far from trivial. In cases where a symbol unavoidably has been assigned more than a meaning, we are confident that the reader will be able to distinguish the adequate meaning from the context. In the list of symbols included below the character "/" is used to separate the alternative meanings some symbols have.

In this thesis, vector values are printed in lowercase boldface and are assumed to be column vectors. A vector $\boldsymbol{v}$ can be defined by extensions by means of the notation $[v_1, \ldots, v_n]^T$, which is equivalent to the notation $[v_1; \ldots; v_n]$. This is expanded to the vertical concatenation of vectors, we $\boldsymbol{v}_1, \ldots, \boldsymbol{v}_n$, as in $[\boldsymbol{v}_1; \ldots; \boldsymbol{v}_n]$. Notice that the notation $[\boldsymbol{v}_1, \ldots, \boldsymbol{v}_n]$ denotes a matrix of n columns and $[v_1, \ldots, v_n]$ explicitly denotes a row vector, i.e. both notations are intended for horizontal concatenations.

Matrices are denoted by uppercase boldface symbols. We also make use of brackets to define matrices by extension. If $\boldsymbol{A}$, $\boldsymbol{B}$, $\boldsymbol{C}$ and $\boldsymbol{D}$ have appropriate dimensions, we resort to the notation

$$\begin{pmatrix} A & B \\ C & D \end{pmatrix}$$

to describe the block matrix constituted by matrices $\boldsymbol{A}$, $\boldsymbol{B}$, $\boldsymbol{C}$ and $\boldsymbol{D}$ in the usual convention. In such context, a 0 denotes a block of consistent dimensions whose elements are all zero. The same holds for vectors. In order to emphasize the structure, we proceed to add vertical and/or horizontal lines such as in

$$\left[\begin{array}{c|c} A & B \\ \hline C & D \end{array} \right].$$

Another use for brackets is to designate units of measure, such as "[kg]". Transposition of a vector $\boldsymbol{v}$ or a matrix $\boldsymbol{a}$ is indicated by $\boldsymbol{v}^T$.

The gradient of a scalar valued function $f : \mathbb{R}^n \to \mathbb{R}$ with respect to a vector valued unknown $\boldsymbol{x}$ is denoted both by

$$\nabla_{\boldsymbol{x}} f(\boldsymbol{x}) \text{ and } \frac{\partial f}{\partial \boldsymbol{x}}$$

and is understood as a *column vector*,

$$\nabla_{\boldsymbol{x}} f(\boldsymbol{x}) \text{ and } \left. \frac{\partial f}{\partial \boldsymbol{x}} \right|_{(\boldsymbol{x})} \stackrel{\text{def}}{=} \left[\begin{array}{ccc} \frac{\partial f(\boldsymbol{x})}{\partial x_1}; & \cdots; & \frac{\partial f(\boldsymbol{x})}{\partial x_n} \end{array} \right].$$

The notation is extended to the Jacobian of a vector valued function $\boldsymbol{f} : \mathbb{R}^n \to \mathbb{R}^m$ as follows: the $n \times m$ matrix made up of the horizontal concatenation of the m gradients of the component

functions $f_i : \mathbb{R}^n \to \mathbb{R}$ is denoted as

$$\nabla_{\boldsymbol{x}} \boldsymbol{f}(\boldsymbol{x}) = \left.\frac{\partial \boldsymbol{f}}{\partial \boldsymbol{x}}\right|_{(\boldsymbol{x})} \stackrel{\text{def}}{=} [\nabla_{\boldsymbol{x}} f_1 \mid \cdots \mid \nabla_{\boldsymbol{x}} f_m]$$

List of Symbols

$:=$	Assigned as
$\stackrel{\text{def}}{=}$	Defined to be equal
$\odot$	Thermodynamic state
$(\cdot)$	Wildcard notation for the omitted list of function arguments
$\lfloor \cdot \rfloor$	Component-wise mapping of a real number to the next smallest integer value
$\lvert \cdot \rvert$	Mapping of a real number to its absolute value / Maximum distance between meshpoints
$\{\,\}$	Set delimiters / Sequence
$\cup$	Set–theoretic union ("unified with")
$\cap$	Set–theoretic intersection ("intersected with")
$\subseteq, \subset$	Subset of a set ("is a (proper) subset of")
$\supseteq, \supset$	Superset of a set ("is a (proper) superset of")
$\in, \notin$	Set membership ("is (not) an element of")
$\times$	Cartesian product of sets, multiplication in literal numbers
$\otimes$	Tensor product of sets
$\emptyset$	The empty set
$\forall$	Universal quantifier ("for all")
$\exists$	Existential quantifier("there exists")
$[\,]$	Units of measurement delimiters
$[a, b]$	Closed interval between quantities a and b
$[a_1, \ldots, a_n]^T$	A column vector whose components are $a_1, \ldots, a_n$ in that order
$[\boldsymbol{x}_1, \ldots, \boldsymbol{x}_n]$	A matrix in $\mathbb{R}^{n_{\mathrm{x}} \times n}$ whose columns are the column vectors $\boldsymbol{x}_1, \ldots, \boldsymbol{x}_n$ in that order
$[\boldsymbol{x}_1; \ldots ; \boldsymbol{x}_n]$	If column vectors $\boldsymbol{x}_i$ have n_i components each, this represents a column vector of $\sum_{i=1}^n n_i$ components obtained by vertically concatenating vectors $\boldsymbol{x}_1, \ldots, \boldsymbol{x}_n$ in that order
$[\boldsymbol{X}_1 \mid \ldots \mid \boldsymbol{X}_m]$	If matrices $\boldsymbol{X}_i$ belong each to $\mathbb{R}^{n_{\mathrm{x}} \times n_i}$, this represents a matrix in $\mathbb{R}^{n_{\mathrm{x}} \times \sum_{i=1}^m n_i}$ obtained by horizontally concatenating $\boldsymbol{X}_1, \ldots, \boldsymbol{X}_m$ in that order
$0_{n_1 \times n_2}$	Matrix in $\mathbb{R}^{n_1 \times n_2}$ whose elements are all zero
(a, b)	Open interval between a and b, function arguments, ordered pair
$\boldsymbol{A}_{i,j}$	Element (i, j) of matrix $\boldsymbol{A}$, a scalar value
$\boldsymbol{a}_i$	The i–th element of vector $\boldsymbol{a}$, a scalar value
$\boldsymbol{A}_{\cdot,j}$	j–th column of matrix $\boldsymbol{A}$, a column vector
$\boldsymbol{A}_{\mathcal{I}}$	Submatrix of rows of $\boldsymbol{A}$ whose indices are contained in $\mathcal{I} \subset \mathbb{N}$
$\boldsymbol{A}_{\star \mathcal{J}}$	Submatrix of columns of $\boldsymbol{A}$ whose indices are contained in $\mathcal{J} \subset \mathbb{N}$
$\boldsymbol{A}_{\mathcal{I}\mathcal{J}}$	Submatrix of rows of $\boldsymbol{A}$ in $\mathcal{I}$ and columns of $\boldsymbol{A}$ in $\mathcal{J}$
$\boldsymbol{A}^T, \boldsymbol{x}^T$	Transpose of matrix or vector
$\boldsymbol{A}^{-1}$	Inverse of regular matrix $\boldsymbol{A}$
$\boldsymbol{A}^{-T}$	Inverse of transposed regular matrix $\boldsymbol{A}$
$f\rvert_{(\cdot)}$	Function f evaluated at the arguments indicated by $(\cdot)$
$\mathrm{d}f/\mathrm{d}t$	Function f's total time derivative
$\mathrm{diag}(\boldsymbol{x})$	If vector $\boldsymbol{x}$'s dimension is n_{x}, a diagonal matrix in $\mathbb{R}^{n_{\mathrm{x}} \times n_{\mathrm{x}}}$ whose diagonal

	correpsonds to the elements of x
$(\partial f / \partial x)_y$	Function f's partial derivative with respect to variable x while keeping variable y constant
$\mathrm{d}^{(r)} f / \mathrm{d} t^{(r)}$	Function f's r–th–order total derivative
$\nabla_{\boldsymbol{v}} f, \partial f / \partial \boldsymbol{v}$	Gradient or Jacobian of the scalar or vector function f w.r.t. variable $\boldsymbol{v}$
$\nabla_{\boldsymbol{v}}^2 f$	Hessian of the scalar function f w.r.t. variable $\boldsymbol{v}$
$\int_{t_1}^{t_2} f(t) \mathrm{d}t$	Integral of the function f w.r.t. its argument between t_1 and t_2.
$\int_{①}^{②} \mathrm{d}f$	Integral of the function f along a given trajectory between thermodynamic states ① and ②
$\oint \mathrm{d}f$	Integral of the function f along a given thermodynamic cycle
$\lim_{x \to y}$	Limit of the expression when variable x approaches the value y
$\sum_j f_{\mathrm{i},j}$	Sum along all quantities f coming into a system
$\sum_j f_{\mathrm{o},j}$	Sum along all quantities f going out of a system
$\tilde{\boldsymbol{u}}(t; \boldsymbol{q})$	Value of the representation of control function $\boldsymbol{u}$ by means of the finite-dimensional parameter $\boldsymbol{q}$ at time t
$\boldsymbol{x}(t; t_i, \boldsymbol{s}_i^x, \boldsymbol{s}_i^z, \boldsymbol{q}_i, \boldsymbol{p})$	Value of the differential state vector at time t that results from solving the relaxed initial value problem on multiple shooting interval i

Latin Symbols

A	Cross section area
ACC	NLP solver accuracy
$\boldsymbol{B}$	Approximation of the partially reduced Hessian of the Lagrangian function
C	Number of components of a simple compressible system
$\boldsymbol{C}_i^q, \boldsymbol{C}_i^x, \boldsymbol{C}_i^z$	Jacobians of the constraint function at node i w.r.t. control, differential state and algebraic state at node i
$\boldsymbol{D}_i^q, \boldsymbol{D}_i^x$	Null-space basis of the linearized consistency constraints on the z–subspace
$\boldsymbol{D}_i$	Basis for the null-space of the linearized consistency constraints of node i
F	Force, degrees of freedom of a simple compressible system
$\mathbf{F}$	Objective function of the NLP resulting from the DMS method
$\mathbf{G}$	Equality constraint function of the NLP resulting from the DMS method
$\boldsymbol{G}_i^q, \boldsymbol{G}_i^x, \boldsymbol{G}_i^z$	Jacobians of the consistency conditions at node i w.r.t. control, differential state and algebraic state at node i
H	Enthalpy
$\mathbf{H}$	Inequality constraint function of the NLP resulting from the DMS method
ITMAX	Maximum number of iterations of the SQP solver
I	Error integral
K	Index of the last considered sample / PI controller constant
L	Evaporator length / Zone length / OCP objective function Lagrange term integrand
L_j^-	Longitudinal coordinate of the upstream end of zone j (w.r.t. the working fluid)
L_j^+	Longitudinal coordinate of the downstream end of zone j (w.r.t. the working fluid)
$\overline{L_3}$	Terminal cost third-zone length
$L_i(\boldsymbol{s}_i^x, \boldsymbol{s}_i^z, \boldsymbol{q}_i, \boldsymbol{p})$	Multiple shooting objective function contribution on interval i
$\boldsymbol{M}$	DAE or ODE left-hand side matrix
M	Number of past measurements considered for the MHE

N	Dimension of the data mesh used for the spline interpolation, number of multiple shooting intervals
P	Number of phases in thermal equilibrium within a simple compressible system / Generic ordered pair / Infinite-dimensional optimization problem
$\boldsymbol{P}$	Condensing permutation matrix
PM	Phase margin
$\dot{Q}$	Heat transfer rate
$\boldsymbol{Q}$	Covariance matrix
Q	Heat transfered during a process
QPMAX	Maximum number of iterations allowed by the QP solver
R	Universal gas constant, tube radius
S	Entropy
$S(\tau; \pi)$	Set of functions $f \in \mathcal{C}[\tau_0, \tau_n]$ that are equal to cubic polinomials on the subintervals of mesn π
T	Temperature
T_s	Sampling time (sampling period)
TOL	DAE solver tolerance
$\boldsymbol{T}$	Condensing matrix
U	Internal energy
$\boldsymbol{U}_i^q, \boldsymbol{U}_i^x, \boldsymbol{U}_i^g$	Directional derivatives of the objective function contribution at node i
V	Volume
V	Fluid velocity
$\boldsymbol{V}_i^q, \boldsymbol{V}_i^x, \boldsymbol{V}_i^g$	Directional derivatives of the relaxed IVP solution at node $i+1$
$\dot{W}$	Mechanical power
W	Work exerted during a process
$\boldsymbol{W}_i^q, \boldsymbol{W}_i^x, \boldsymbol{W}_i^g$	Directional derivatives of the inequality constraints at node i
X	Generic property
$\boldsymbol{X}_i^q, \boldsymbol{X}_i^x, \boldsymbol{X}_i^z$	Jacobians of the relaxed IVP solution at node $i+1$ w.r.t. control, differential state and algebraic state at node i
a	HELMHOLTZ's free energy
a^{ij}	Bicubic spline coefficient corresponding to quadrant ij
a^i	Cubic spline coefficient corresponding to interval i
$\boldsymbol{b}$	DAE or ODE differential right-hand side
c	Specific heat capacity
$\boldsymbol{c}$	OCP Path constraint function
d	Diameter
d	Exact differential
đ	Inexact differential
$\boldsymbol{d}_i^g$	Range-space step component on the range-space of the linearized consistency constraints on the z–subspace
$\boldsymbol{d}_i$	Range-space step component on the range-space of the linearized consistency constraints of node i
e	Superheating error
f	Frequency
$\boldsymbol{f}$	Mapping of a differential state vector at a sample time to its value at the next one
$\boldsymbol{g}$	DAE or ODE algebraic right-hand side
h	Specific enthalpy
ℓ	Number of steps considered for the limited-memory implementation

m	Mass contained on a volume
$\dot{m}$	Massflow
n	Angular speed
n_{x}	Dimension of the vector space of x
o	Bachmann–Landau's small-o notation
p	Pressure
$\boldsymbol{p}$	Parameter vector
$\dot{q}$	Heat flux (heat transfer rate per unit area per unit time)
$\boldsymbol{q}$	Control vector (finite-dimensional)
r	Radial cylindrical coordinate
s	Specific entropy
$\boldsymbol{s}^{x}$	Node differential state vector
$s(\tau; \pi, f)$	Spline representation of function f using the data of mesh π
$\boldsymbol{s}^{z}$	Node algebraic state vector
t	Time
t_{k}	k–th sample time
$\boldsymbol{t_{c}}$	computation time vector
$\boldsymbol{t}$	condensing transformation vector
u	Specific internal energy
$\boldsymbol{u}$	Control vector function (infinite-dimensional)
v	Specific volume
$\boldsymbol{v}$	Decision variable vector of the NLP generated from the DMS method
$\boldsymbol{w}$	External input vector
x	Quality of a two-phase liquid-vapor mixture
$\boldsymbol{x}$	Differential state vector
$\boldsymbol{y}$	Model measurement vector
$\boldsymbol{y}^{\mathrm{SH}}$	Superheating
z	Longitudinal cylindrical coordinate
$\boldsymbol{z}$	Algebraic state vector

Greek Symbols

$\boldsymbol{\Gamma}$	Constraint violation vector
$\Delta \pi$	Difference between consecutive meshpoints
Δt	Prediction horizon or estimation window length
$\Delta \boldsymbol{x}$	In an iterative method, step vector associated to $\boldsymbol{x}$
$\Theta_{i,k}$	Powell's damping factor corresponding to block i of iterate k of the high rank updating scheme for the partially reduced Hessian
$\boldsymbol{\Lambda}$	LQGI objective function weights
Ξ_{k}	Vector of all measurements considered on the k–th MHE problem
Φ	OCP Objective function Net generated energy
Ψ	Noise term
α	Helmholtz's free energy, dimensionless / Newton's convection coefficient / Step length
γ	Void fraction
$\boldsymbol{\gamma}_{i,k}$	Lagrangian gradient difference vector corresponding to block i of iterate k of the high rank updating scheme for the partially reduced Hessian
δ	Reduced density
δ_{b}	Hydrodynamic boundary layer region radial width
δx	Small perturbation in variable x
$\delta^{(k)}$	Estimation and control time delays at sample k

$\boldsymbol{\delta}_{i,k}$	Displacement vector corresponding to block i of iterate k of the high rank updating scheme for the partially reduced Hessian
ϵ	Small reminder / Small perturbation
ϵ_{mach}	Machine precision
ζ_i	Relaxed initial value problem factor function on multiple shooting interval i
η	Efficiency
$\boldsymbol{\eta}_{i,k}$	POWELL's damped Lagrangian gradient difference corresponding to block i of iterate k of the high rank updating scheme for the partially reduced Hessian
θ	Temperature (numerical value in the KELVIN scale)
κ_R	PLITT's reciprocal initial Hessian factor
$\boldsymbol{\lambda}$	Lagrange multiplier associated to an NLP's equality constraints
μ	Density ratio
$\boldsymbol{\mu}$	Lagrange multiplier associated to an NLP's inequality constraints
$\boldsymbol{\xi}_j$	Measurement vector at the j–th sample
ξ	PI controller's anti-windup indicator
π	Ratio of a circumference's perimeter to its diameter / Mesh
ϱ	Density
σ	Entropy production due to irreversibilities within the system
$\dot{\sigma}$	Rate of entropy production due to irreversibilities within the system per unit time
$\sigma_p, \sigma_{\theta_F}, \sigma_{\theta_G}$	Standard deviations associated to p_B, θ_C and $\theta_{G,\text{out}}$, respectively
σ_L	Terminal cost standard deviation
τ	Reciprocal reduced temperature / Interpolation meshpoint
φ	Angular cylindrical coordinate
ω	Acentric factor
ω_c	Crossover frequency

Subscripts, Superscripts and Accents

$\dot{(\cdot)}$	Transfer or change rate per unit time
$\bar{(\cdot)}$	Zone mean value / Correction term for real gases / Relative to an equilibrium state
$\tilde{(\cdot)}$	At the spline data mesh's nearest border, deviation from the equilibrium
$\breve{(\cdot)}$	Estimated value
$\hat{(\cdot)}$	Estimated value
$(\cdot)'$	At the sat. liquid curve
$(\cdot)''$	At the sat. vapor curve
$(\cdot)_j^-$	At the upstream end of zone j (w.r.t. the working fluid)
$(\cdot)_j^+$	At the downstream end of zone j (w.r.t. the working fluid)
$(\cdot)^0$	Ideal gas / Part associated with the initial state constraint
$(\cdot)_0$	Initial / Arbitrary reference
$(\cdot)_\infty$	Far away from the surface
$(\cdot)^\diamond$	QP solution
$(\cdot)^\star$	Approximated OCP solution
$(\cdot)_i$	Multiple shooting node i
$(\cdot)_j$	Inside the evaporator, zone j ($j \in \{1, 2, 3\}$)
$(\cdot)_{A \to B}$	Between states Ⓐ and Ⓑ
$(\cdot)_A$	Working fluid at condenser outlet
$(\cdot)_B$	Working fluid at pump outlet

$(\cdot)_{\mathrm{C}}$	Cold thermal reservoir
$(\cdot)_{C}$	Working fluid at evaporator outlet
$(\cdot)_{D}$	Working fluid at expander outlet
$(\cdot)_{F}$	Working fluid (inside evaporator)
$(\cdot)_{G}$	Exhaust gas
$(\cdot)_{GW}$	From exhaust gas to wall
$(\cdot)_{\mathrm{H}}$	Hot thermal reservoir
$(\cdot)^{L}$	Coordinate associated with the subcooled liquid region
$(\cdot)_{\mathrm{MHE}}$	Moving Horizon Estimation
$(\cdot)^{\mathcal{N}}$	Null-space of the linearized consistency constraints
$(\cdot)_{\mathrm{NMPC}}$	Nonlinear Model-Predictive Control
$(\cdot)_{\mathrm{OCP}}$	Moving Horizon Estimation
$(\cdot)^{\mathrm{PI}}$	Proportional–integral controller
$(\cdot)_{\mathrm{PR}}$	PENG-ROBINSON equation of state
$(\cdot)_{\mathrm{Rankine}}$	RANKINE cycle
$(\cdot)_{\mathrm{TH}}$	Thermal
$(\cdot)_{\mathrm{V}}$	Volumetric
$(\cdot)^{V}$	Coordinate associated with the superheated vapor region
$(\cdot)_{W}$	Wall
$(\cdot)_{WF}$	From wall to working fluid
$(\cdot)_{\mathrm{boundary}}$	Transferred across the system's boundary
$(\cdot)_{\mathrm{b}}$	Hydrodynamic boundary layer
$(\cdot)_{\mathrm{b,T}}$	Thermal boundary layer
$(\cdot)_{c}$	At the critical point
$(\cdot)^{\mathrm{c}}$	Associated to the condensing step
$(\cdot)_{\mathrm{conv.}}$	Due to convection
$(\cdot)_{\mathrm{cv}}$	Control volume
$(\cdot)_{\mathrm{cycle}}$	Transfered during a whole cycle
$(\cdot)_{e}$	Hydrodynamic entrance
$(\cdot)_{e,\mathrm{T}}$	Thermal entrance
$(\cdot)^{\epsilon}$	Perturbed quantity
$(\cdot)_{\mathrm{el}}$	Electric
$(\cdot)_{\mathrm{ev}}$	Evaporator
$(\cdot)_{\mathrm{ex}}$	Expander
$(\cdot)_{\mathrm{f}}$	Final
$(\cdot)_{i}$	Incoming / PI integral term
$(\cdot)_{\mathrm{i}}$	Inner
$(\cdot)^{(i)}$	i–th block matrix of the partially reduced Hessian approximation
$(\cdot)^{(i,j)}$	Block matrix of the partially reduced Hessian approximation corresponding to vectors $\Delta \boldsymbol{v}_i^{\mathrm{c}}$ and $\Delta \boldsymbol{v}_j^{\mathrm{c}}$
$(\cdot)_{\mathrm{in}}$	Input
$(\cdot)_{\mathrm{int.\ rev.}}$	Internally reversible process
$(\cdot)_{\mathrm{is}}$	Isentropic
$(\cdot)^{(k)}$	Value associated with the k–th NMPC subproblem
$(\cdot)_{k}$	Value at the k–th sample or iteration
$(\cdot)_{\mathrm{liquid}}$	Corresponding to the liquid phase in a two-phase liquid-vapor mixture
$(\cdot)_{m}$	Mapped point mesh
$(\cdot)_{\mathrm{max}}$	Upper bound / Maximum mesh value
$(\cdot)_{\mathrm{min}}$	Lower bound / Minimum mesh value
$(\cdot)_{o}$	Outgoing

$(\cdot)_\text{o}$	Outer
$(\cdot)_\text{out}$	Output
$(\cdot)_\text{p}$	Pump
$(\cdot)_p$	At constant pressure,PI proportional term
$(\cdot)_\text{pre}$	Before truncation and offset
$(\cdot)_{qq}$	Partially reduced Hessian block corresponding to the second derivatives w.r.t. q
$(\cdot)_\text{rev. cycle}$	Reversible power cycle
$(\cdot)_\text{sat}$	Evaluated at the two-phase liquid-vapor mixture states
$(\cdot)_{sq}$	Partially reduced Hessian block corresponding to the crossed derivatives w.r.t. s and q
$(\cdot)_{ss}$	Partially reduced Hessian block corresponding to the second derivatives w.r.t. s
$(\cdot)_\text{subc.liq.}$	Subcooled liquid state
$(\cdot)_\text{suph.vap.}$	Superheated vapor state
$(\cdot)_\text{surf.}$	At the surface
$(\cdot)_\text{vapor}$	Corresponding to the vapor phase in a two-phase liquid-vapor mixture
$(\cdot)^x$	Part associated to the differential state vector or the continuity constraints
$(\cdot)^z$	Part associated to the algebraic state vecto or the consistency constraintsr

Calligraphic Symbols

$\mathcal{C}$	Class of a function
$\mathcal{C}^k[a,b]$	Set of the k–times continuously differentiable functions on interval $[a,b]$
$\mathcal{K}$	Sample index set
$\mathcal{L}$	Lagrangian function of an NLP
$\mathcal{N}(\mu,\sigma)$	Normal distribution with mean μ and standard deviation σ
$\mathcal{O}$	BACHMANN–LANDAU's big-O notation
$\mathcal{T}$	Time horizon $\mathcal{T}=[t_0,t_\text{f}]\subset\mathbb{R}$ for an ODE

Blackboard Symbols

$\mathbb{E}\{\cdot\}$	Expected value
$\mathbb{I},\mathbb{I}_n$	Identity matrix, identity matrix of dimension n
$\mathbb{N},\mathbb{N}_0$	Set of natural numbers excluding (including) zero
$\mathbb{R}$	Set of real numbers
$\mathbb{R}^n$	Space of n–vectors with elements from the set $\mathbb{R}$
$\mathbb{R}^{m\times n}$	Space of $m\times n$–matrices with elements from the set $\mathbb{R}$

List of Figures

List of Tables

List of Acronyms

BDF   Backward Differentiation Formulae
BFGS   Broyden–Fletcher–Goldfarb–Shanno
CARIMA Controller Auto-Regressive Integrated Moving-Average
DAE   Differential Algebraic Equation
DMS   Direct Multiple Shooting
DP   Dynamic Programming
EKF   Extended Kalman Filter
END   External Numerical Differentiation
FK   Full Knowledge
FV   Finite–Volume
FOPTD First–Order–Plus–Time–Delay
GPC   Generalized Predictive Control
IND   Internal Numerical Differentiation
IVP   Initial Value Problem
KKT   Karush–Kuhn–Tucker
LMPC   Linear Model Predictive Control
LQGI   Linear–Quadratic–Gaussian with Integral Action
LQR   Linear–Quadratic Regulator
MB   Moving Boundary
MHE   Moving Horizon Estimation
MIMO   Multi–Input, Multi–Output
MLI   Multi–Level Iteration
MPC   Model Predictive Control
NLP   Nonlinear Programming Problem
NMPC   Nonlinear Model Predictive Control
OCP   Optimal Control Problem
ODE   Ordinary Differential Equation
ORC   Organic Rankine Cycle
PDE   Partial Differential Equation
PI   Proportional–Integral
PID   Proportional–Integral–Derivative
QP   Quadratic Programming Problem
RTI   Real–Time Iteration
SISO   Single–Input, Single–Output
SQP   Sequential Quadratic Programming
TIP   Turbine Inlet Pressure
TIT   Turbine Inlet Temperature
TITO   Two–Input, Two–Output
WHR   Waste Heat Recovery System